Caractérisation de l'endommagement dans les aciers Dual-Phase à l'aide de la tomographie aux rayons X

Caroline Landron

N°d'ordre : 2011-ISAL-0147 Année 2011

Thèse

Ductile damage characterization in Dual-Phase steels using X-ray tomography

Présentée devant

L'**I**nstitut **N**ational des **S**ciences **A**ppliquées de **Lyon**

Pour obtenir

Le grade de docteur

Formation doctorale : Matériaux
École doctorale : École doctorale matériaux de Lyon

Par

Caroline LANDRON
(Ingénieur)

Thèse dirigée par
Eric Maire, Jérôme Adrien (INSA de Lyon) et Olivier Bouaziz (ArcelorMittal)

Soutenue le 21 décembre 2011 devant la Commission d'examen

Jury

Président	A. PINEAU	Professeur (Mines ParisTech)
Rapporteur	X. FEAUGAS	Professeur (Université La Rochelle)
Rapporteur	T. PARDOEN	Professeur (Université Catholique de Louvain)
Examinateur	O. BOUAZIZ	Docteur Ingénieur (ArcelorMittal)
Directeur	E. MAIRE	Directeur de recherche (INSA de Lyon)
Co-directeur	J. ADRIEN	Ingénieur de recherche (INSA de Lyon)

Laboratoire de recherche : MATEIS–UMR 5510

INSA Direction de la Recherche - Ecoles Doctorales – Quinquennal 2011-2015

SIGLE	ECOLE DOCTORALE	NOM ET COORDONNEES DU RESPONSABLE
CHIMIE	**CHIMIE DE LYON** **http://www.edchimie-lyon.fr** Insa : R. GOURDON	M. Jean Marc LANCELIN Université de Lyon – Collège Doctoral Bât ESCPE 43 bd du 11 novembre 1918 69622 VILLEURBANNE Cedex Tél : 04.72.43 13 95 directeur@edchimie-lyon.fr
E.E.A.	**ELECTRONIQUE, ELECTROTECHNIQUE, AUTOMATIQUE** **http://edeea.ec-lyon.fr** Secrétariat : M.C. HAVGOUDOUKIAN eea@ec-lyon.fr	M. Gérard SCORLETTI Ecole Centrale de Lyon 36 avenue Guy de Collongue 69134 ECULLY Tél : 04.72.18 60 97 Fax : 04 78 43 37 17 Gerard.scorletti@ec-lyon.fr
E2M2	**EVOLUTION, ECOSYSTEME, MICROBIOLOGIE, MODELISATION** **http://e2m2.universite-lyon.fr** Insa : H. CHARLES	Mme Gudrun BORNETTE CNRS UMR 5023 LEHNA Université Claude Bernard Lyon 1 Bât Forel 43 bd du 11 novembre 1918 69622 VILLEURBANNE Cédex Tél : 04.72.43.12.94 e2m2@biomserv.univ-lyon1.fr
EDISS	**INTERDISCIPLINAIRE SCIENCES-SANTE** **http://ww2.ibcp.fr/ediss** Sec : Safia AIT CHALAL Insa : M. LAGARDE	M. Didier REVEL Hôpital Louis Pradel Bâtiment Central 28 Avenue Doyen Lépine 69677 BRON Tél : 04.72.68 49 09 Fax :04 72 35 49 16 Didier.revel@creatis.uni-lyon1.fr
INFOMATHS	**INFORMATIQUE ET MATHEMATIQUES** http://infomaths.univ-lyon1.fr	M. Johannes KELLENDONK Université Claude Bernard Lyon 1 INFOMATHS Bâtiment Braconnier 43 bd du 11 novembre 1918 69622 VILLEURBANNE Cedex Tél : 04.72. 44.82.94 Fax 04 72 43 16 87 infomaths@univ-lyon1.fr
Matériaux	**MATERIAUX DE LYON** Secrétariat : M. LABOUNE PM : 71.70 –Fax : 87.12 Bat. Saint Exupéry Ed.materiaux@insa-lyon.fr	M. Jean-Yves BUFFIERE INSA de Lyon MATEIS Bâtiment Saint Exupéry 7 avenue Jean Capelle 69621 VILLEURBANNE Cédex Tél : 04.72.43 83 18 Fax 04 72 43 85 28 Jean-yves.buffiere@insa-lyon.fr
MEGA	**MECANIQUE, ENERGETIQUE, GENIE CIVIL, ACOUSTIQUE** Secrétariat : M. LABOUNE PM : 71.70 –Fax : 87.12 Bat. Saint Exupéry mega@insa-lyon.fr	M. Philippe BOISSE INSA de Lyon Laboratoire LAMCOS Bâtiment Jacquard 25 bis avenue Jean Capelle 69621 VILLEURBANNE Cedex Tél :04.72.43.71.70 Fax : 04 72 43 72 37 Philippe.boisse@insa-lyon.fr
ScSo	**ScSo*** M. OBADIA Lionel Sec : Viviane POLSINELLI Insa : J.Y. TOUSSAINT	M. OBADIA Lionel Université Lyon 2 86 rue Pasteur 69365 LYON Cedex 07 Tél : 04.78.69.72.76 Fax : 04.37.28.04.48 Lionel.Obadia@univ-lyon2.fr

*ScSo : Histoire, Geographie, Aménagement, Urbanisme, Archéologie, Science politique, Sociologie, Anthropologie

Les devises Shadok

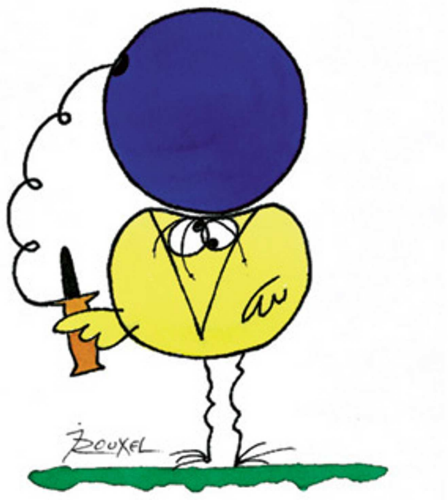

EN ESSAYANT CONTINUELLEMENT
ON FINIT PAR RÉUSSIR. DONC:
PLUS ÇA RATE, PLUS ON A
DE CHANCES QUE ÇA MARCHE.

Acknowledgements

Je tiens en premier lieu à remercier ceux gâce à qui cette thèse a été rendue possible, mes directeurs de thèse Eric, Jérôme et Olivier. Nos caractères complémentaires nous ont permis de mener à bien cette thèse dans une ambiance très agréable et propice à la réflexion.

Merci à toutes les personnes rencontrées au laboratoire MATEIS, les jeunes et les moins jeunes (dédicace spéciale à JYB), ceux qui ont terminé avant moi et ceux qui sont arrivés aprés (bon courage à ceux qui sont encore en rédaction!), ceux qui m'ont accompagnée lors des footings aux parcs de la Feyssine ou de la Tête d'or, ceux qui ont travaillé avec moi lors des nuits à l'ESRF et ceux qui ont partagé mon bureau pendant ces trois années. Vous allez me manquer et je compte toujours sur vous pour des sorties ski et randonnée!

Je remercie également les personnes extérieures au laboratoire qui ont contribué à ce travail: le staff des lignes ESRF ID15, ID19 et ID22 pour leur aide, les personnes du SIMAP porteuses du long term project ma560, et celles des belles rencontres à l'UCL et à la TU de Vienne.

Une pensée particulière pour ma famille et Matthieu (mieux connu sous le nom de Chouch') qui m'ont toujours soutenue et réconfortée lorsqu'il le fallait.

Pour terminer, je ne félicite pas la SNCF pour sa ponctualité sur la ligne TER Lyon-Grenoble et je pense aux personnes que j'ai croisées dans le train et qui continuent les trajets quotidiens.

Ductile damage characterization in Dual-Phase steels using X-ray tomography

Abstract

As part of the current context of requiring ever more efficient grades of steels in terms of resistance to stress and to damage, the Dual-Phase steels (DP) present an acceptable strength/ductility compromise. It is nevertheless necessary to have a better understanding of the mechanisms leading to the fracture of such steels. Damage mechanisms were studied in this PhD using X-ray tomography. In-situ tensile tests were carried out on several grades of DP steel, a ferritic steel and a martensitic steel in order to characterize each step of ductile damage. Qualitative observations and quantitative data on the nucleation of damage, the void growth and the coalescence of cavities were collected during these tests. This quantitative data was then used for the development and/or the validation of damage models. A prediction of the kinetic of nucleation was proposed and the Huang's correction of the void growth model of Rice and Tracey accounting for the triaxiality was experimentally validated. For the first time, the step of void coalescence leading to fracture of materials was quantitatively characterized in an industrial material and coalescence criteria were locally applied on couples of neighboring cavities present in the studied specimen. The use of analytical models enabled a better understanding of the properties influencing the studied damage phenomena. The effect of the kinematic part of the strain hardening on void nucleation and void growth was notably emphasized and validated by performing complex loading tests.

Keywords: ductile damage, Dual-Phase steel, X-ray tomography, void nucleation, void growth, void coalescence, analytical modeling

Caractérisation de l'endommagement dans les aciers Dual-Phase à l'aide de la tomographie aux rayons X

Résumé

Dans le cadre du développement de nuances d'aciers toujours plus performantes en termes de résistance à l'effort et à l'endommagement, les aciers Dual-Phase (DP) présentent un bon compromis résistance/ductilité. Cependant, il est nécessaire de disposer de meilleures connaissances concernant les mécanismes menant à la rupture de tels aciers. Les mécanismes d'endommagement ont ainsi été étudiés dans cette thèse à l'aide de la tomographie aux rayons X. Des essais de traction in-situ ont été réalisés sur plusieurs nuances d'aciers DP, un acier ferritique et un acier martensitique afin de caractériser chaque étape de l'endommagement ductile. Des observations qualitatives et des données quantitatives concernant la germination de l'endommagement, la croissance des cavités et la coalescence ont été recueillies lors de ces essais. Ces données quantitatives ont ensuite été utilisées pour le développement et/ou la validation de modèles d'endommagement. Une prédiction de la cinétique de germination a ainsi été proposée et la version du modèle de croissance de cavités de Rice et Tracey corrigée par Huang et prenant mieux en compte l'effet de la triaxialité a été validée expérimentalement. L'étape de coalescence des cavités menant à la rupture des matériaux a pour la première fois été caractérisée de façon quantitative dans un matériau industriel et des critères de coalescence ont été appliqués localement sur les couples de cavités présentes dans le matériau. L'utilisation de ces modèles analytiques a permis une meilleure compréhension des propriétés agissant sur les phénomènes mis en jeu. L'effet de la part cinématique de l'écrouissage sur la germination et la croissance de l'endommagement a notamment été souligné et validé par des essais de chargements complexes.

Mots-clés: Endommagement ductile, acier Dual-Phase, Tomographie aux rayons X, germination de cavités, croissance de cavités, coalescence, modélisation analytique

Contents

List of Figures

List of Tables

Introduction

High strength steels commonly constitute the major material involved in the structural parts of automotive products. Among these grades, the dual-phase steels (DP) are characterized by their bi-phased microstructure consisting of a soft phase, the ferrite, and a hard phase, the martensite. This specific microstructure gives interesting mechanical properties to these steels, in particular a strong work hardening rate and a high tensile strength. Figure 1 shows typical applications of DP steels in an automotive body-in-white (BIW).

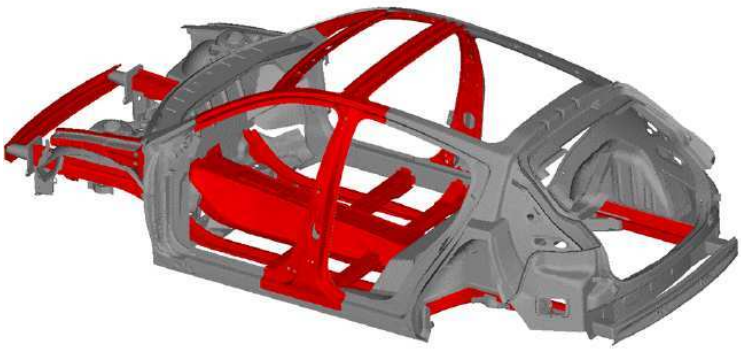

Figure 1: Parts of the automotive BIW made of DP steels grades (appearing in red –ArcelorMittal credit).

The current environmental concerns lead automotive manufacturers to provide even lighter vehicles. It is therefore advantageous to decrease the final weight of components by using materials with a higher strength. Steel grades with higher strength were thus developed to match this requirement. However, as it can be noticed on the graph given in Figure 2, an increase of the tensile strength leads to a decrease of the ductility. The material aptitude for deforming is necessary to the forming step of such parts by rolling or bending. DP steels stand as an attractive compromise between strength and resistance to damage. A better understanding and a prediction of damage mechanisms leading to the fracture of such a material would give the possibility to design new grades of DP steels with an increased tensile strength and an improved ductility.

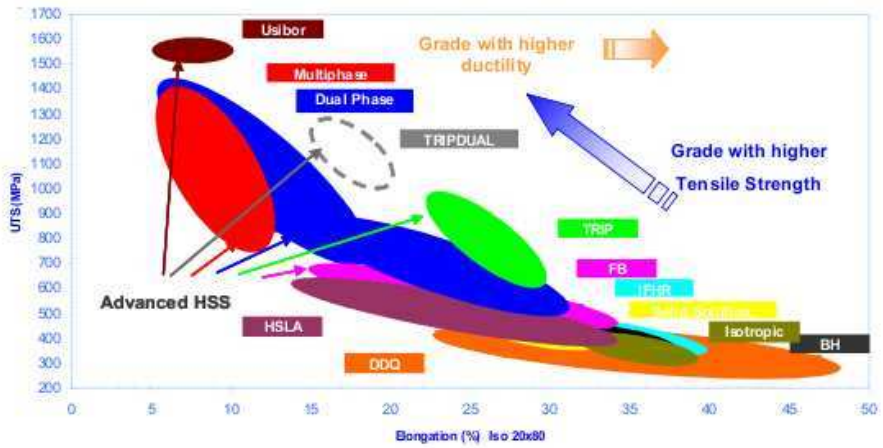

Figure 2: Ultimate tensile strength (UTS)–Elongation map of the main grades of high strength steels (ArcelorMittal credit).

Ductile damage mechanisms involved in the fracture of steels have been widely studied since the sixties. From a physical point of view, one can divide ductile damage in three steps. First, voids nucleate, the more frequently because of the microstructural heterogeneities of the materials. These cavities then grow until the coalescence occurs, leading to the final fracture of the material. Models for these three steps of ductile damage were developed. However, the acquisition of quantitative data characterizing void nucleation, growth and coalescence was difficult and few models were experimentally validated.

Recent development of new techniques of characterization have brought a light into the research on ductile damage. Indeed, X-ray tomography provides three-dimensional (3D) images of a scanned sample with a spatial resolution up to the micrometer relevant with the characterization of cavities present in damaged specimens. Moreover, X-ray tomography is particularly effective to get 3D quantitative information concerning each step of the ductile damage.

The present work is dedicated to the characterization of damage in DP steels using X-ray tomography. It is divided in the following way:

- The first chapter is devoted to the description of the investigated steels and to the techniques of characterization, mainly X-ray tomography, used in this work.
- The study of the three steps of ductile damage introduced herein, *i.e.* void nucleation, void growth and void coalescence, are respectively the subjects of the three next chapters. Each chapter starts with a literature overview of available research

on the subject. A second section concerns the experimental characterization of the damage step mainly using X-ray tomography. In the last part of these chapters, models previously described in the literature are adapted or applied as-is on the experimental data. These models are implemented in order to have a better understanding of the influence of the microstructural parameters on damage and to have a prediction of the damage kinetics.

- The work achieved in the previous chapters underlines the influence of the kinematic hardening on damage evolution. Because the kinematic part of strain hardening is strongly dependent of the loading path applied to the specimen and because tensile tests are not fully representative of the forming steps, *in-situ* tests with complex loading paths were also carried out in this work. Chapter 5 is devoted to the results of these tests.

- Two appendices complement this study. The first one describes the macroscopic measurement of mechanical parameters using the volumes acquired by X-ray tomography. These parameters (true strain, true stress, triaxiality) are involved in damage modeling. The second appendix presents some results on the effect of banded martensitic microstructure on ductile damage in DP steels.

Chapter 1

Experimental methods

The selection of steels used in this study is described in this chapter. Three DP steels presenting different microstructures and their two single-phased constituents were investigated. Ductile damage was widely characterized in qualitative and quantitative ways by X-ray tomography. Optical micrographs were also performed as complementary way of characterization.

1.1 Experimental characterization techniques

1.1.1 X-ray tomography

X-ray tomography was first used in the medical field 40 years ago. Tomography has brought the possibility to better locate the position of features of interest (*e.g.* tumor etc ...) which was not accessible using only 2D radiographies. The benefits of 3D maps to characterize internal structures led to a rapid adaptation of this technique in other fields including materials science.

1.1.1.1 X-ray tomography principle

The principle of X-ray tomography is given in Figure 1.1. The object to characterize rotates about a single axis while a series of 2D X-ray absorption images is recorded. Using mathematical principles of tomography, this series of images is reconstructed to produce a 3D digital image where each voxel (volume element or 3D pixel) represents the X-ray absorption at that point [Herm 80].

Two kinds of contrasts can be found in the acquired projections:

- X-ray attenuation as it passes through a material is a logarithmic function of the absorptivity of the material, and the distance through which the rays must travel. The true absorptivity of the material depends on the number and the type of atoms along the path of the beam. In most cases, the atomic absorption decreases as the energy of the X-ray photons increases (the wavelength decreases).

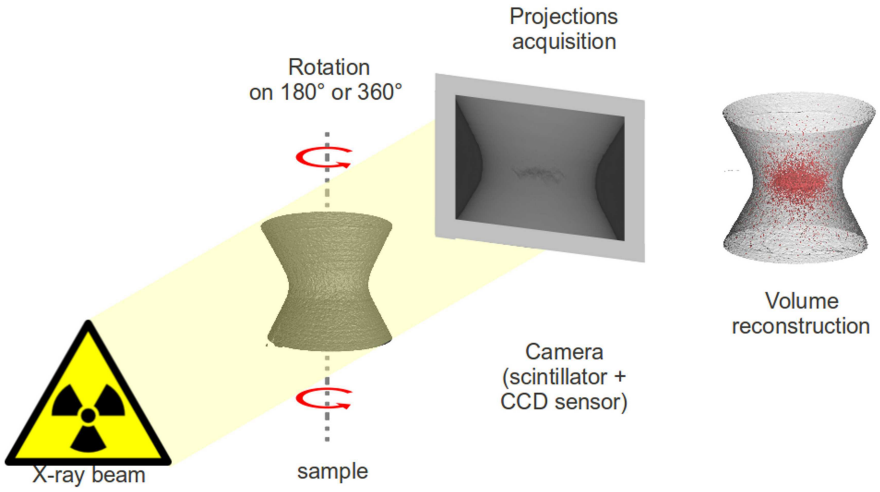

Figure 1.1: X-ray tomography principle.

In general, for a fixed X-ray photon energy, lower-Z (fewer electrons) elements absorb less than higher-Z elements. Extensive tables of X-ray mass attenuation coefficients μ (as a function of the type of element and of the X-ray photon energy) have been produced [Henk 93]. Typical values of μ are given in Figure 1.2. The X-ray intensity I, measured at a point (x, z), can be related to the incident X-ray intensity, $I_0(x, z)$, by:

$$I(x, z) = I_0(x, z) \exp(-\tau) \tag{1.1}$$

where $\tau = \mu\rho t$ is the total absorption along the X-ray path depending on the material density ρ and the material thickness t.

- The second origin of the contrast is linked to the phase of the X-rays. Because the refractive index for hard X-rays is slightly different from unity, the optical phase of a beam is affected by transmission through an object [Ando 72]. Phase images can be obtained using a spatially coherent beam and holographic reconstruction. Indeed, the phase is not simply related to the brightness of the image unlike attenuation. Holographic reconstruction consists of retrieving the value of the phase using images taken at different distances D from the specimen, the phase contrast being different on each image (see Figure 1.3). Associated with the principle of tomography, the holographic reconstruction procedure allows the complete 3D mapping of the phase in a sample [Cloe 99]. This specific technique of tomography is named holotomography and its principle is summarized in Figure 1.3.

The spatial resolution of X-ray tomography is typically limited by the geometry of the X-ray beam along with the characteristics of the detector. For a point source, the

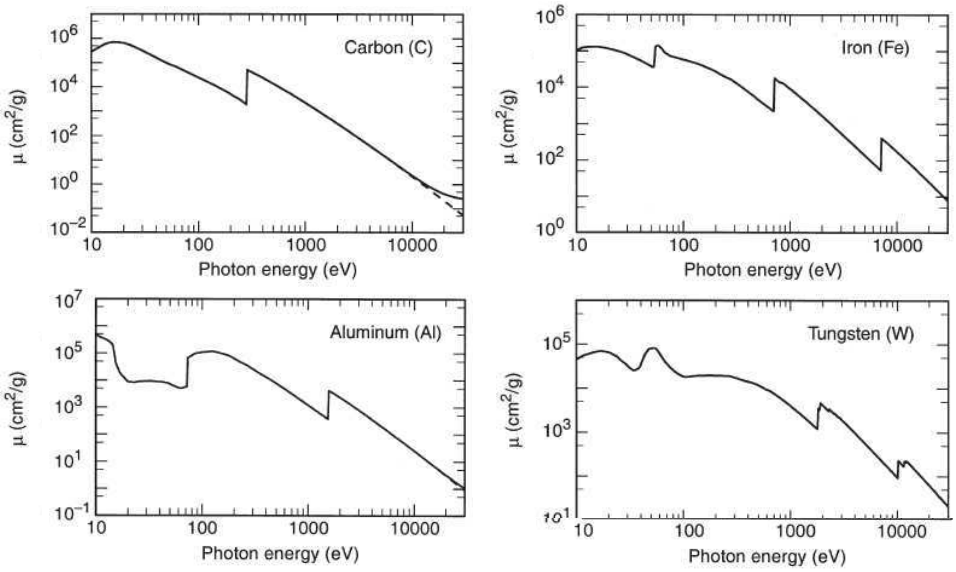

Figure 1.2: Typical values of μ for common elements [Henk 93].

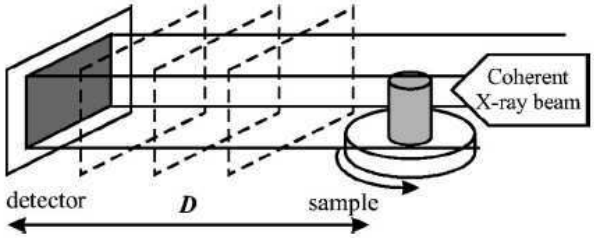

Figure 1.3: Schematic drawing of the holotomography technique setup [Cloe 99].

spot size of the X-ray source plays an important role. The smaller the spot size, the smaller the penumbral blurring, helping to produce a more accurate projected image. The use of synchrotron radiation as an X-ray source brought significant enhancements in X-ray tomography. Synchrotron radiation results from the bending of a high-energy electron beam due to a magnetic field. The emitted light is many orders of magnitude greater in brightness than that emitted by conventional X-ray sources. The high flux of synchrotron sources allows one to resolve very subtle variations in absorptivity and therefore in internal structure. Additional advantages of synchrotron radiation include X-ray beam collimation (the parallel beam shown in Figure 1.5(a)), which simplifies the tomographic reconstruction algorithm, and the tunability of the X-ray energy to a narrow energy band. In case of parallel beam, the final voxel size only depends on the CCD camera composing the detector.

1.1.1.2 *In-situ* / *Ex-situ* tensile tests

Because X-ray tomography is a non-destructive technique, many scans of the same sample can be made under different conditions. Several kinds of tensile tests coupled to X-ray tomography characterization can thus be performed [Suer 10]. They are listed in Figure 1.4.

- Post-mortem characterization: the material is pulled for a given deformation; it is thereafter unloaded and imaged. In order to follow the evolution of the material, as many specimens as necessary are deformed for different times. This procedure assumes that the material does not change from one specimen to another.

- *Ex-situ* characterization: one specimen is pulled for a given deformation. It is thereafter unloaded and imaged. This procedure is repeated as many times as necessary. The advantage of this procedure compared with the previous one is that only one specimen is used. However it is assumed that the interruption of the deformation and the unloading does not influence the test.

- *In-situ* characterization with interruption of the deformation: the procedure is similar to the previous one but the specimen is not unloaded; the tensile device is placed on the beam line. During imaging, the deformation is stopped but maintained constant.

- *In-situ* continuous characterization: in this procedure, imaging is carried out continuously during the deformation without interruption. This procedure is obviously the best one to characterize the evolution of the sample during the tensile test since there is no interruption of the deformation. The main requirement for this procedure is that the scan time has to be small compared to the deformation speed. If not, volume reconstruction leads to blurring of the images which are therefore difficult to analyze.

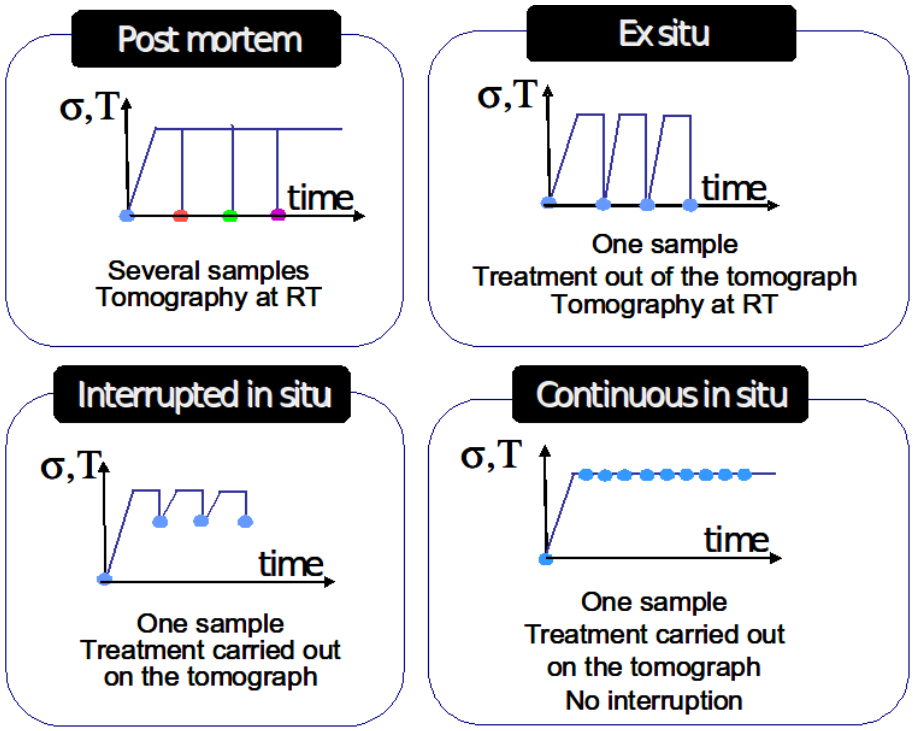

Figure 1.4: Schematic of the various procedures used to perform tomography acquisition during thermomechanical treatments. The ordinate axis is in our case the stress [Suer 10].

We have made comparisons between interrupted *in-situ* tensile test and continuous *in-situ* tensile test [Suer 10]. It was shown that no difference appeared for a kind of test or the other. Interrupted *in-situ* tensile tests were thus mainly performed in this PhD work because they lead to better quality images.

1.1.1.3 Volumes acquisition

Several beamlines of the European Synchrotron Radiation Facility (ESRF) located in Grenoble, France, are dedicated to X-ray tomography. Absorption contrast volumes were acquired on the ID15A beamline where a parallel X-ray beam (see Figure 1.5(a)) with a peak energy set to 50keV was used. The voxel size of this tomograph was between 1.4µm and 1.6µm and the field of view about 1.5×1.5mm. About 800 2D projections were acquired on 180°with a projection time of 0.15s.

Attenuation coefficients of ferrite and martensite are very close to each other. As no contrast between the two components of the DP steel can be detected on the volumes obtained from attenuation contrast, holotomography acquisitions were achieved. Phase contrast volumes, requiring a finer resolution, were acquired on the ID22Ni beamline with a voxel size of 100nm. The set up used combined a KirkpatrickBaez optic system with a focused parallel beam (see Figure 1.5(a)) with an energy of 29 keV. Each holotomography scan was composed of four tomography scans at increasing distances between the sample and the detector. For each scan, 2000 projections were acquired on 360°and the exposure time per frame was 0.25s. The distances z_S between the sample and the focal point for each scan are given in Table 1.1. The final reconstructed volume was a cylinder of 150µm in height and 150µm in diameter.

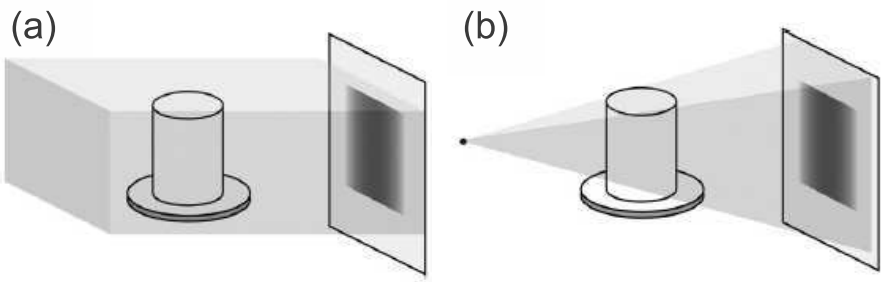

Figure 1.5: Different X-ray tomography acquisition configurations :(a) parallel beam (ID15A), (b) cone beam [Land 10a].

In the next chapters, experimental data used in the damage characterization comes from volume acquisition on the ID15 beamline, except noted differently.

To achieve *in-situ* tensile tests, a dedicated tensile machine described in [Buff 10]

z_{S1}	z_{S2}	z_{S3}	z_{S4}
74.4	75.4	79.4	89.4

Table 1.1: Distances between the sample and the focal point for each scan composing the holotomography acquisition (mm).

was used. It was mounted on the rotation stage of the tomograph as seen in Figure 1.6. The applied displacement speed was chosen to be between 1 µm $\cdot s^{-1}$ and 5 µm$\cdot s^{-1}$.

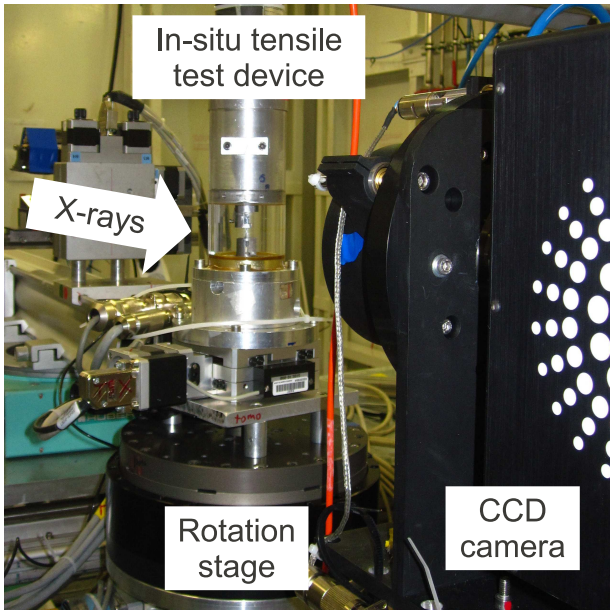

Figure 1.6: *In-situ* experimental device at the ID15A beamline (ESRF).

Specimens with adapted dimensions were machined. Two parameters limit the maximal dimension of the specimen section :

- the field of view of the detector, depending on the voxel size and the CCD camera dimension,
- the absorption coefficient of the studied material.

On the ID15A beamline, the main limiting parameter is the field of view of the detector equal to 1.5mm. A section of 1mm per 1mm was thus chosen. On ID22Ni, because of the weaker achieved energy and the high absorption of steel, specimens with 300×300µm section were used. Smooth and notched axisymmetric specimens inspired from [Bron 04] are machined in the steel sheet when a sufficient thickness permitted it. In the case of thin sheets, flat square smooth specimens were machined. The shapes of these

samples are given in Figure 1.7 (axisymmetric samples) and Figure 1.8 (square samples).

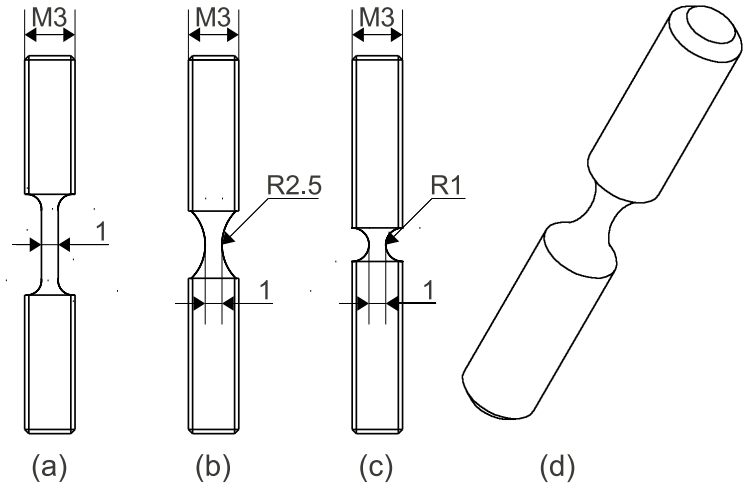

Figure 1.7: Smooth and notched axisymmetric specimens. This design requires a thickness of the sheet of 3mm at least.

On ID22Ni, *ex-situ* tensile tests were carried out because of the high precision of the rotation stage required for the scan does not allow us to place the tensile device inside the tomograph. On the initial volumes, acquired before applying deformation, a phase contrast between the ferrite and the martensite can be detected (Figure 1.9(a)). Unfortunately, when deformation proceeds, this contrast is lost because of the strong interference fringes induced by the appearing cavities (Figure 1.9(b)).

1.1.1.4 Processing of the raw volumes

The raw volumes obtained from the reconstructions of the tomography scans need to be processed in order to be used for the characterization of ductile damage. All the processing work is performed using ImageJ, a specific freeware dedicated to the image processing [Abra 04].

Filtering and thresholding

The first processing consists in filtering the volume to decrease the noise induced by the experimental method. We used a median filter. Figure 1.10 shows the effect of a median filter with a radius of one voxel (Figure 1.10(b)) and with a radius of two voxels (Figure 1.10(c)) applied on an initial raw volume (Figure 1.10(a)). The median filter effectively reduces the noise in the volume but also induces blur: some smallest voids are no longer detectable in the section filtered with a median filter with a radius of two voxels. For volumes acquired at ESRF, a median filter with a radius of one voxel is

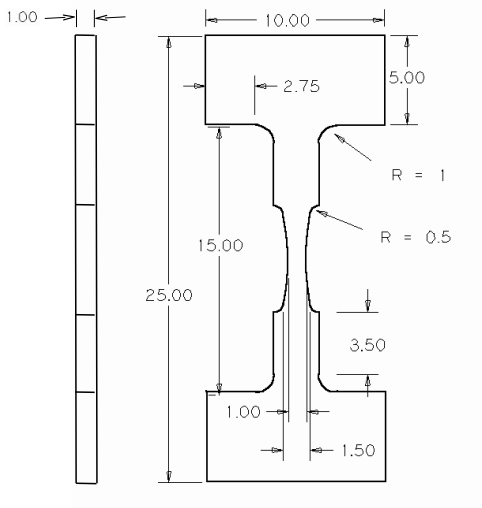

Figure 1.8: Smooth square specimen used for thin sheets.

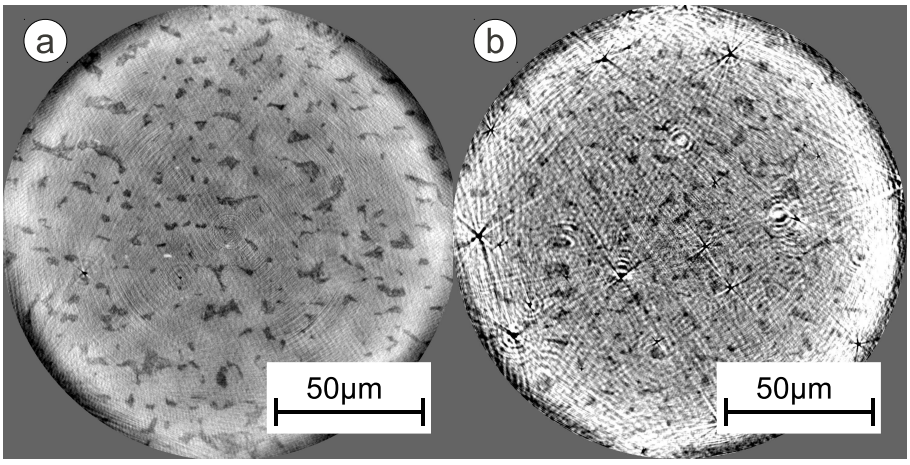

Figure 1.9: Slice of the reconstructed volume acquired by holotomography: (a) initial volume acquired before deformation, (b) volume acquired after proceeding deformation.

sufficient to satisfactorily reduce the noise.

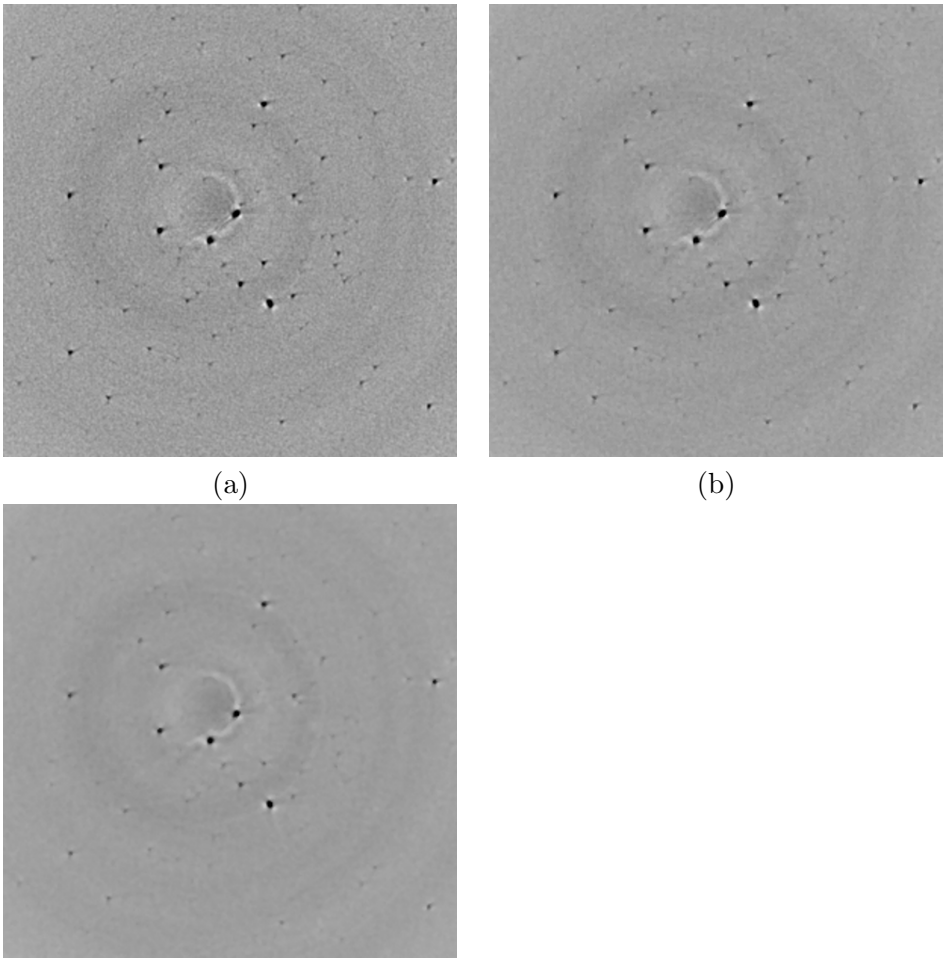

(a) (b)

(c)

Figure 1.10: Focused view of a section inside a volume undergoing different filtering : (a) no filtering, (b) 1 voxel radius median filtering, (c) 2 voxels radius median filtering.

The median-filtered volume is thereafter thresholded to separate the material phase from the "void phase". The "void phase" includes cavities inside the material and the air outside the specimen. A simple threshold automatically calculated from the histogram of the gray levels (given in Figure 1.11(a)) is used. The result of the threshold applied on the filtered section of Figure 1.10(b) is given in Figure 1.11(b).

3D visualization

Using the thresholded volumes, damaged specimens can be visualized in 3D using

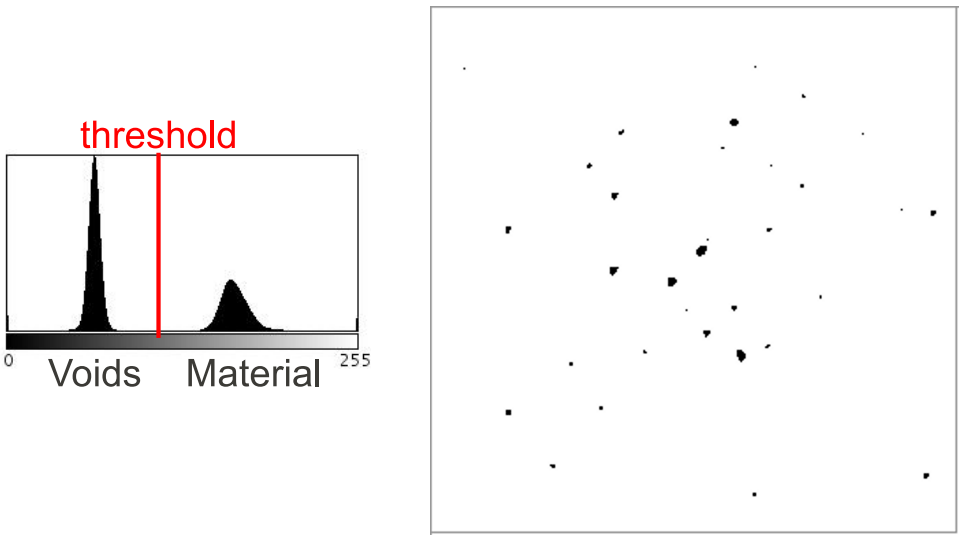

(a) (b)

Figure 1.11: (a) Automatic detection of the threshold using the histogram of the gray levels, (b) Result of the applied threshold on the section already shown in Figure 1.10(b).

the software Aviso®. In this work, the outer shape of the specimen always appear in transparent gray and the porosity inside the sample in red.

Damage characterization

Only the central area of the tensile specimen, where damage is mainly concentrated, was selected for damage quantification [Mair 08]. This sub-region was chosen to be a cubic volume of $(300\ \mu m)^3$, as indicated in Figure 1.12. It can be assumed that this central sub-region undergoes the highest stress triaxiality state and the highest strain during the tensile test. The size was chosen to be sufficiently large for the elementary volume to be representative but also sufficiently small for the strain and triaxiality to be spatially constant inside this sub-volume. Each pore of the volume was then detected and labeled using a dedicated image processing plug-in implemented in ImageJ freeware. To be detected, a cavity needs to be a clusters of at least three connected voxels. This volume threshold prevents from considering noises present in the volume as porosity.

1.1.2 Optical microscopy

1.1.2.1 Samples preparation

Representative samples were cut and mounted in Bakelite. They were polished with SiC grinding paper for the coarse steps (600 to 2400 SiC paper) and using diamond paste (3µm and 1µm diamond) for the last steps. The samples were dipped in a solution of

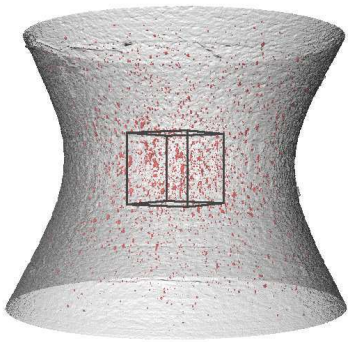

Figure 1.12: 3D visualization of the chosen volume to study damage.

ethanol and placed into a ultrasound cleaner for 30 minutes after polishing to eliminate as many fragments blunting the cavities as possible. After polishing, samples were etched using Nital 2% in order to reveal the microstructure. The optical observations were done on a Zeiss Axioplan microscope which allows magnifications up to 1000. Typical micrographs of investigated steels are given in Section 1.2.1.2.

1.1.2.2 Serial sectioning

The reconstruction of the microstructure of damaged DP11 sample was achieved by serial sectioning and optical microscopy. This study was carried out at the Institute of Material Science and Technology in TU Vienna (Austria). The distance between two successive observations was measured using Vickers indentations like in [Asgh 09]. An average value of 0.65 ± 0.3µm was found. Sequential slices were realigned using the StackReg plugin from the ImageJ freeware [Thev 98]. Views in the three directions of the reconstructed volume are given in Figure 1.13. This technique of characterization allows us to visualize in 3D the damage due to the applied deformation and the microstructure of the DP steel at the same time.

1.2 Investigated materials

1.2.1 Dual-phase steels

1.2.1.1 General aspects

The typical microstructure of a DP steel consists of ferrite α and martensite α'. This bi-phased microstrucure is produced by intercritical heat treatment of an initial ferrite/pearlite ($\alpha + Fe_3C$) microstructure followed by an accelerated cooling (see Figure 1.14). During the heating, the austenitic phase γ appears for a temperature $\theta > A_1$. The amount of austenite, being later the amount of martensite, is controlled by the temperature level comprised between A_1 and A_3. The final quenching allows the transformation

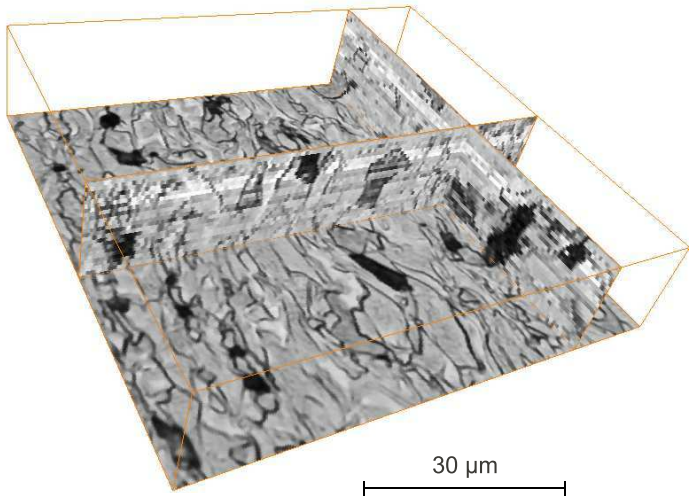

Figure 1.13: Serial sectioning on a fractured DP steel specimen.

$\gamma \rightarrow \alpha'$ to take place, leading to the final microstructure of the DP steel.

1.2.1.2 Studied DP steels

In this study, three different DP microstructures were employed:

- The first one is a commercial grade named DP11 in this work. A micrography of the microstructure is given in Figure 1.15. The global composition of the steel is given in Table 1.2. This grade contains a volume fraction of martensite F_M=11%. Assuming that all carbon atoms present in the material are located within the martensite, the carbon concentration inside the martensitic phase C_M is about 0.72%. According to the work of Grange *et al.* [Gran 77], the Vickers hardness of the martensite is about HV_M=830MPa. This martensite is quite hard and thus rather fragile.

C	Mn	Si	Cr
0.08	0.8	0.23	0.68

Table 1.2: Chemical composition of DP11 (wg%).

  In the DP11 samples, the ferritic phase is majority and the islands of martensite appear to be isotropic and surrounded by the ferrite. To analyze this further, the

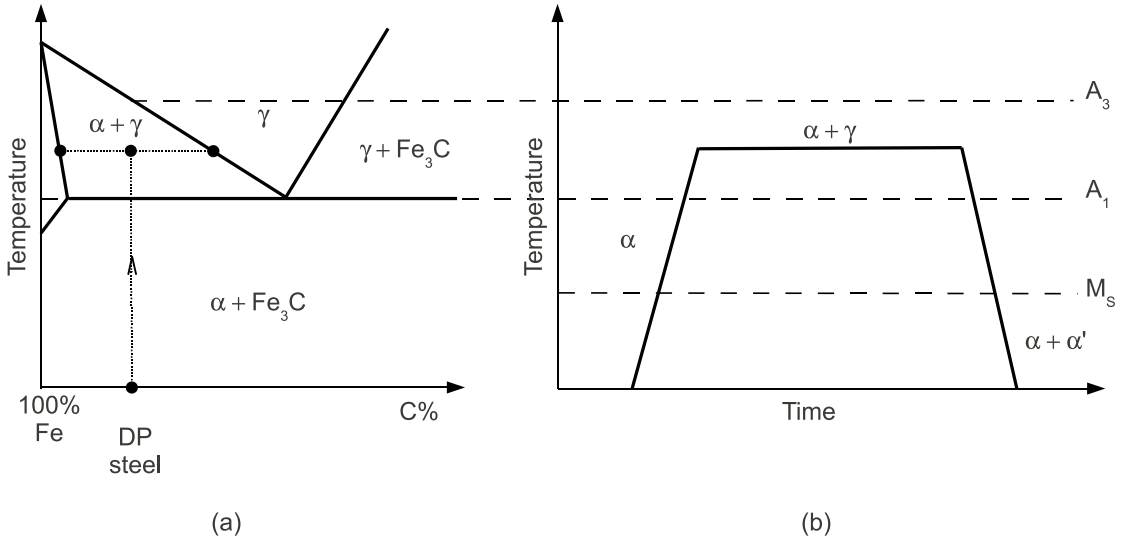

Figure 1.14: Thermal treatment to obtain a DP microstructure: (a) schematic Fe-C diagram, (b) applied heat treatment.

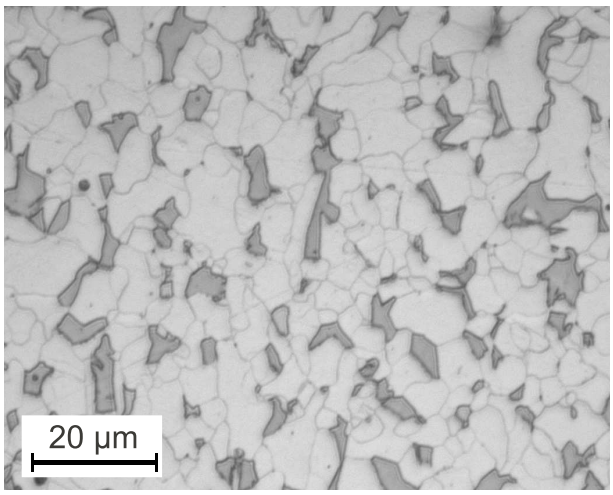

Figure 1.15: Optical micrograph of the DP11's microstructure. Ferrite and martensite respectively appear in light gray and in dark gray.

microstructure of the DP11 was imaged in 3D using the holotomography technique (see Section 1.1.1). A part of the scanned volume is represented in Figure 1.16. This reveals that martensite islands are actually connected as previously observed by Goune *et al.* [Goun 06]. This particular arrangement of the martensitic phase is due to the history of the microstructure: the austenite transformation occurs first at the boundary of the ferrite grains. A more or less continuous network of austenite is then created, leading to a final network of martensite.

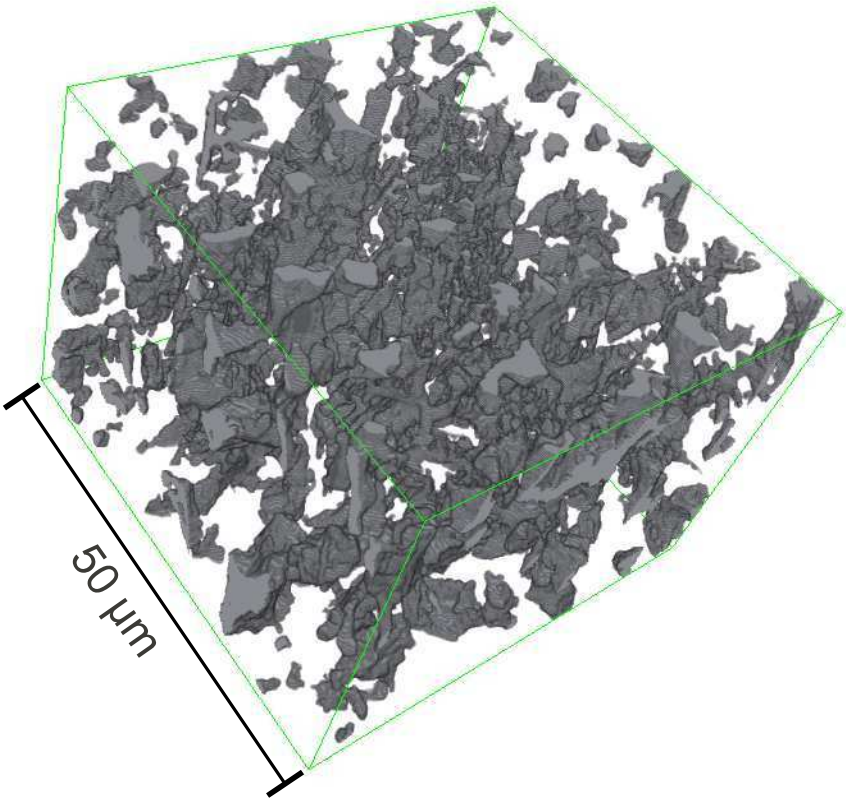

Figure 1.16: Reconstructed volume of the DP11 microstructure using holotomography: martensitic phase appears in gray and ferrite is transparent.

- The second DP microstructure is the same that the first one described in this section, but subjected to a tempering treatment of 30 minutes at 400°C. The tempering has an effect on the martensitic phase: a softening is observed because of the carbide precipitation. The final Vickers hardness of the martensite within the tempered DP11 sample was measured to be 415MPa. To include this steel to this present work permits to study the effect on damage of changing the properties of the martensitic phase while keeping the same microstructure.

- A third DP microstructure very different from the ones described before was also studied here. Its global chemical composition, given in Table 1.3, is close to the DP11's one but the main difference lies in the volume fraction of martensite being much higher than previously: F_M=62%. This microstructure is then referred to as DP62. Using the same assumption, *i.e.* all carbon atoms present in the material are located in the martensite, the carbon concentration inside the martensitic phase C_M is then about 0.24% leading to a ductile martensite with a Vickers hardness measured to be about 530MPa [Gran 77]. A micrography of the DP62's microstructure is given in Figure 1.17. The phase arrangement is different: the two phases are interlocked with no preferential matrix phase or inclusion phase.

C	Mn	Si	Cr
0.15	0.215	1.9	0.195

Table 1.3: Chemical composition of DP62 (wg%).

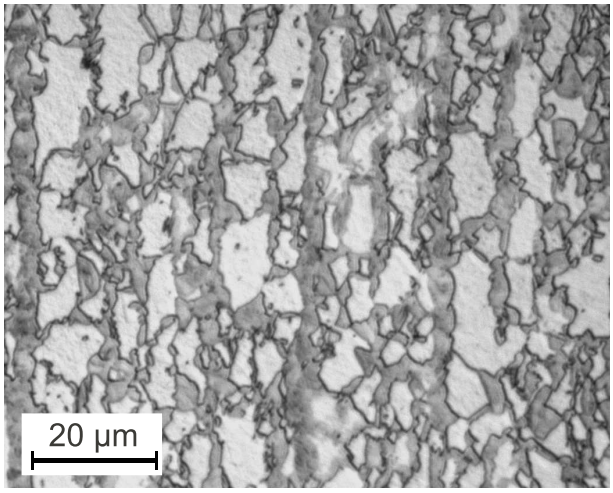

Figure 1.17: Optical micrograph of the DP62's microstructure. Ferrite and martensite respectively appear in light gray and in dark gray.

1.2.2 Single-phased steels

To have a better understanding of the damage phenomena involved in the DP steels, the two constituents, *i.e.* the ferrite and the martensite were also investigated separately. A fully ferritic steel and a fully martensitic steel were thus included in this study. The martensite, with a carbon content of 0.1% was chosen to be sufficiently soft to have a ductile behavior.

1.2.3 Investigated steels designation

The five steels described before are summarized in Table 1.4. Every steel was provided by ArcelorMittal in the form of a sheet with a thickness from 1mm to 3mm obtained by rolling. A summarization of the studied microstructures can be found in Table 1.5 and the tensile curve of each material can be found in Appendix A.

Designation	Vickers Hardness (20 kgf)	Kind of microstructure	F_M	C_M (%wg)	HV_M
DP11	180	bi-phased	11%	0.73	830
DP11T	165	bi-phased	11%	0.73	415
DP62	315	bi-phased	62%	0.24	530
Ferrite	150	single-phased	0%	-	-
Martensite	330	single-phased	100%	0.1	330

Table 1.4: A summary of the microstructure of the investigated steels.

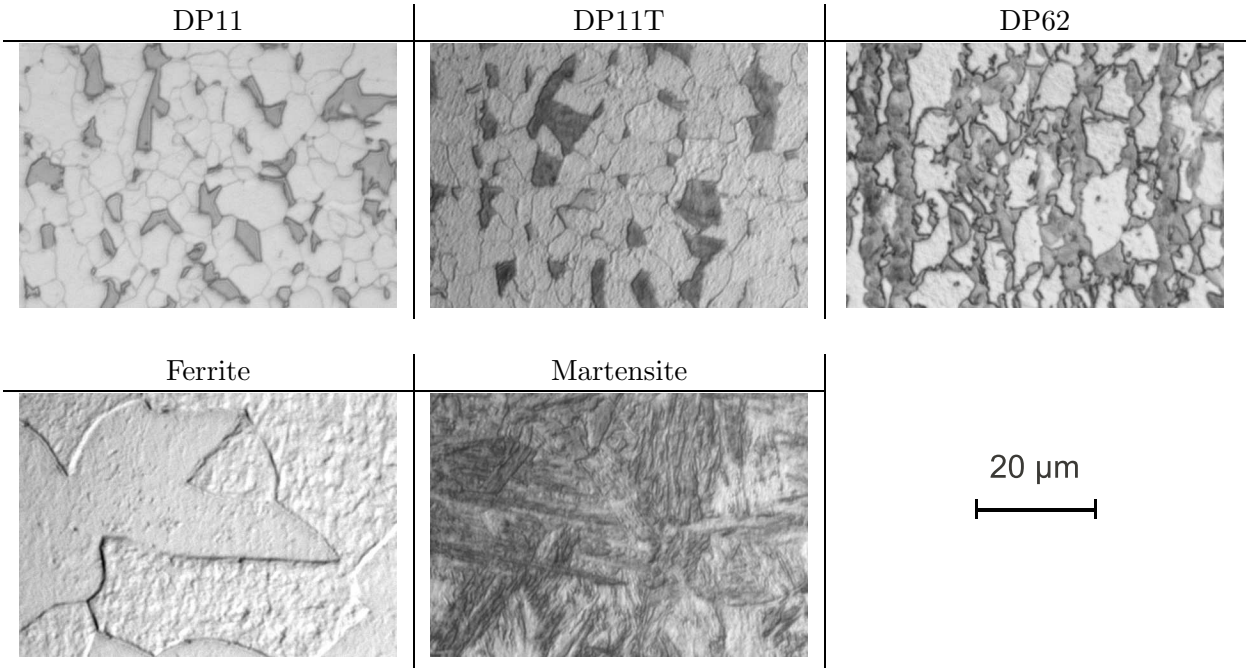

Table 1.5: A summary of the microstructure of the investigated steels as seen using optical microscopy.

1.3 Summary and conclusion

This chapter presented the materials and experimental methods used in this PhD work

→ Ductile damage is characterized in fives different steels: two different DP microstructures, a tempered DP steel and the two components of the DP steels *i.e.* a ferritic and a martensitic steels. The effect of the DP microstrucure and of the tempering on damage evolution were thus investigated.

→ Ductile damage is mainly studied using X-ray tomography. This recent technique permits to obtain qualitative and quantitative data concerning each step of damage. However, X-ray tomography presents some inconveniences such the absence of contrast between the ferrite and the martensite. Optical microscopy is thus used as complementary way of characterization.

Chapter 2

Void nucleation

The mechanisms of void nucleation in the studied DP steels are investigated in this chapter. The kinetic of nucleation, related to the steel microstructure, is quantified in 3D using the volumes acquired by X-ray tomography during in-situ tensile tests. The different mechanisms of nucleation are modeled using several criteria. A part of this work has been published in [Land 10b].

2.1 Literature review

2.1.1 Experimental evidences

First observations of ductile damage showed that void nucleation can be classified as homogeneous or heterogeneous [Good 79]. Homogeneous nucleation occurs inside the grain and is not associated to the presence of an heterogeneity or a second phase in the microstructure while heterogeneous nucleation happens because of the heterogeneous deformation close to inclusions, the grain boundaries or precipitates [Putt 59, Argo 75b, Good 79, Fish 81, Bere 81]. Homogeneous nucleation was observed in very pure single phase metals [Thom 77] but as materials frequently exhibit a multiphased microstructure, heterogeneous nucleation is the most encountered mode of nucleation. In this latter case, voids appear either by fracture of the second phase inclusion, either by decohesion at the interface or by cavitation in the matrix next to the particle. The most frequent nucleation mechanisms, *i.e.* the inclusion fracture and the interface decohesion, are illustrated in Figure 2.1. Babout *et al.* showed that the nucleation mechanism depends on the flow properties of the components of the microstructure itself [Babo 04a]. Using metal matrix composites, where the properties of the inclusion and the matrix can be easily controlled, they experimentally proved that a soft matrix favors interface decohesion while a hard matrix leads to particle fracture.

Furthermore, all voids do not nucleate at the same time but void nucleation rather occurs in a continuous way during progressive straining [Cox 74]. The main reason is probably the inhomogeneity in the particle distribution causing local stress concentra-

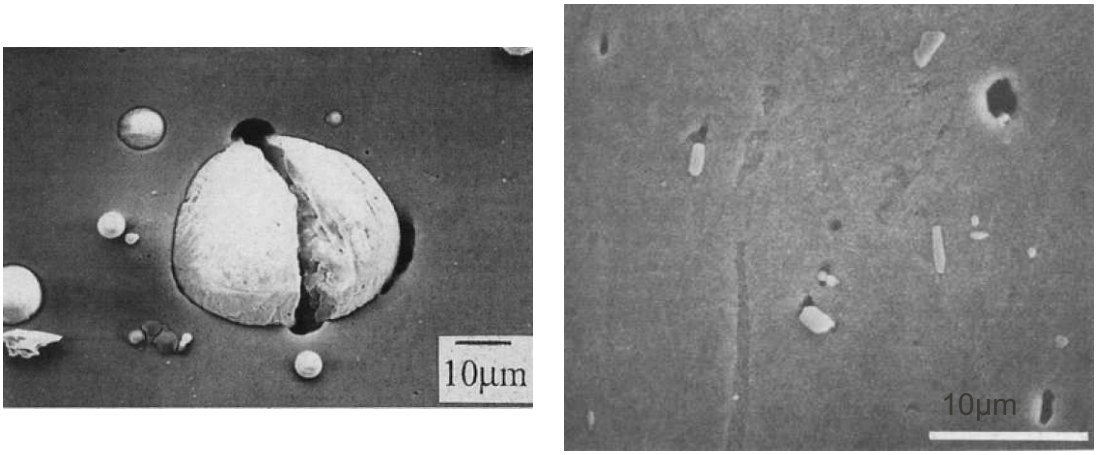

(a) (b)

Figure 2.1: (a) Particle fracture in an aluminum 6061 matrix reinforced with Al2O3 particles [Kane 95], (b) interface decohesion in a copper matrix containing CuCr particles [Argo 75a].

tion. Voids also first nucleate on largest inclusions presenting statistically more defects inside the particle or at the interface.

2.1.2 Measurements of damage nucleation

The first observations of damage were conducted on 2D metallographic sections such as the ones exhibited in Figure 2.1. This technique of characterization, easy to implement, allows one to identify the nucleation mechanisms. Damage nucleation can be observed by SEM during *in-situ* tensile tests. Two examples of such experiments performed on aluminum alloys and DP steels can be found in [Deyb 05, Mair 08]. However 2D methods of observation of damage face some limitation when quantitative measurements is needed. On metallographic sections, a broken particle appearing small may actually be larger in the bulk. Concerning *in-situ* observations, they are performed on free surfaces where stress conditions are different from the ones in the center of the specimens (see, for example, Fougères and coworkers [Buff 99, Babo 04a]).
The first 3D quantifications of damage were performed using indirect methods such as the change of the elastic stiffness[Schm 82, Corb 94], change of resistivity or change of density [Pard 98b, El G 01]. An example of the measure of the porosity using density measurements is given in Figure 2.2. The main inconvenience of these indirect methods is that only the void volume fraction can be measured. These methods do not provide any information on the number, the shape or the distribution of cavities.

The recent technique of X-ray tomography brought the possibility to obtain more accurate quantitative data about damage. First studies of damage using tomography was performed on metal matrix composites (MMC) [Buff 99, Babo 01, Babo 04b]. An

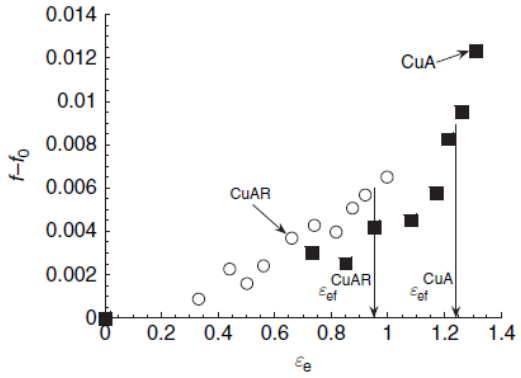

Figure 2.2: Variation of the porosity estimated from density measurements from samples of as-received (CuAR) and annealed copper bars (CuA) [Pard 98b].

example of 3D rendering of the reconstructed volume is given in Figure 2.3(a). Data from tomography are not only dedicated to damage observations. It can also be used for the quantitative analysis of damage. Figure 2.3(b) exhibits an example of the comparison of the quantified porosity from interface decohesion and from particle fracture in different MMCs [Babo 04a]. The ability of X-ray tomography to quantitatively characterize damage in 3D led many people to use this technique to study damage in composite materials [Babo 01, Babo 04a], in steels [Mair 08, Lort 10] or in other metallic materials [Dzie 11, Toda 11, Kuro 11, Mair 11].

2.1.3 Void nucleation criteria

Void nucleation criteria frequently involve that some critical stress, strain or energy level is reached. The energy criterion is necessary for the creation of the new surfaces inside the inclusion or at the interface. For inclusions larger than 1 µm, this energy criterion is satisfied at the very beginning of the plastic deformation [Tana 70]. In the case of smaller particles, an analysis based on the dislocation theory is required [Good 79]. The energy criterion being necessary but not sufficient in most of the studied cases, critical stress or strain criteria were also developed. Four of those are described hereafter:

- Argon *et al.* proposed a critical stress condition for void nucleation by interface decohesion [Argo 75b]. This phenomenological criterion involves a contribution of the hydrostatic stress σ_H and the equivalent stress σ_{eq}:

$$\sigma_{eq} + \sigma_H = \sigma_C \tag{2.1}$$

  where σ_C is the critical stress of the interface *e.g.* , the maximum stress that the interface can undergo without breaking.
  This criterion was then successfully applied on a spheroidized 1045 steel, a copper with Cu-Cr particles and a maraging steel [Argo 75a]. Note that this criterion has

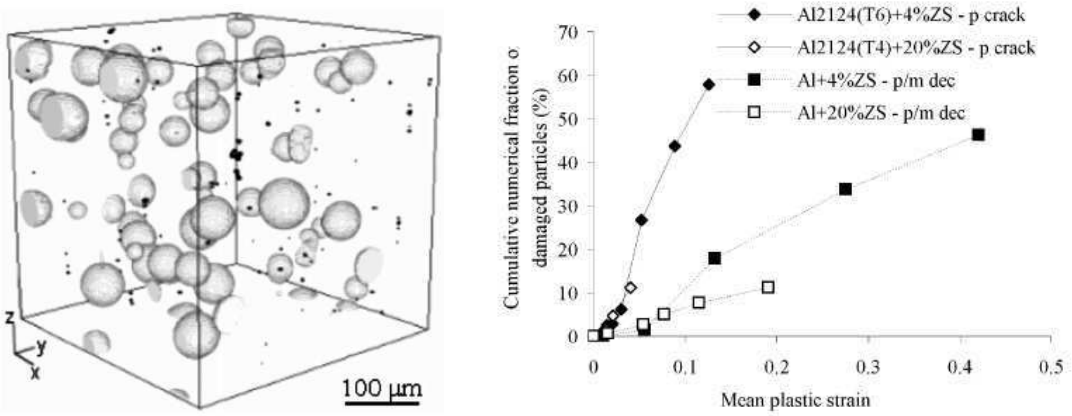

(a) (b)

Figure 2.3: (a) 3D rendering of the reconstructed volume for the model material Al2124(T6) +4ZS. (The matrix has been removed, particles appear in gray and cavities in black). (b) Quantification of the porosity coming from the interface decohesion and from the particles fracture in different MMC [Babo 04b].

later been used by Le Roy *et al.* associated to a void growth model and a void coalescence criterion in order to predict the fracture strain [LeRo 81].

- Few years later, the Beremin team proposed a stress criterion based on the Eshelby theory [Bere 81, Eshe 57]. This criterion was assessed in samples of A508 steel containing MnS inclusions responsible for void nucleation either by interface decohesion or particle fracture. The Beremin criterion states that the void nucleation occurs when the stress inside the particle reaches the critical value σ_C (being either the critical stress for the interface decohesion or the critical stress for the particle fracture). For a fragile particle inside a perfectly plastic matrix, the criterion's expression is:

$$\sigma_I^{max} + k_s \left(\sigma_{eq} - \sigma_0\right) = \sigma_C \tag{2.2}$$

where σ_I^{max} is the maximal principal stress, σ_{eq} the equivalent stress inside the material, σ_0 the equivalent stress inside the matrix and k_s a stress concentration factor depending on the particle shape.

- Guillemer-Neel *et al.* developed a critical stress condition of nucleation where hydrostatic stress σ_H and equivalent plastic deformation ε_{eq}^p were involved [Guil 00]:

$$A\sigma_H + B\varepsilon_{eq}^p = \sigma_C \tag{2.3}$$

Note that in these three stress criteria, the value of the critical stress σ_C is intrinsic to the nature of the interface or the inclusion material, *i.e.* the shape or the size of the particle is not involved in the criterion.

- In the famous ductile damage analysis of Gurson [Gurs 77] and of Goods and Brown [Good 79], a strain criterion was used. This simpler void nucleation criterion based on the deformation states that voids appear when the critical plastic strain ε_N is reached inside the material.
  Later, Chu and Needleman used this criterion to predict the evolution of the void density with the deformation [Chu 80]. They expressed the rate of void nucleating per unit area dN_a/N_a as being:

$$\frac{dN_a}{N_a} = f\,(T)\,d\varepsilon \tag{2.4}$$

  where T is the stress triaxiality.
  This expression was successfully used to fit the kinetic of nucleation in α/β titanium alloys [Helb 98] and in DP steels [Mair 08].

Void nucleation criteria were thus integrated in numerical simulations using cohesive zones. One of the first numerical application was the work of Needleman, see Figure 2.4.

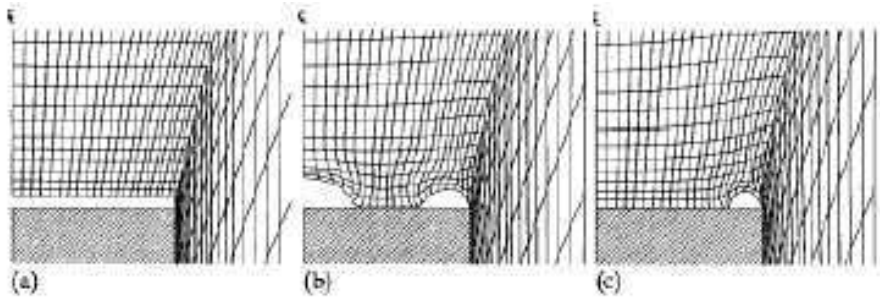

Figure 2.4: Interface decohesion using cohesive zone in finite elements simulation [Need 87].

2.1.4 Previous studies on void nucleation in DP steels

Damage nucleation in DP steels was previously investigated in the literature [Stei 88, Han 89, Mazi 07, Mair 08, Avra 09b, Avra 09a, Kadk 11]. All these studies showed that void nucleation is linked to the presence of the martensitic phase and that cavities appear either because of the ferrite/martensite interface decohesion or because of the fracture of the martensite islands. Figure 2.5 exhibits micrographs of both nucleation mechanisms.

Several studies [Stei 88, Avra 09b, Avra 09a] showed that the morphology and the distribution of the martensitic phase had a significant influence in the location of the cavities. In particular, banded microstrutures and elongated particles of martensite

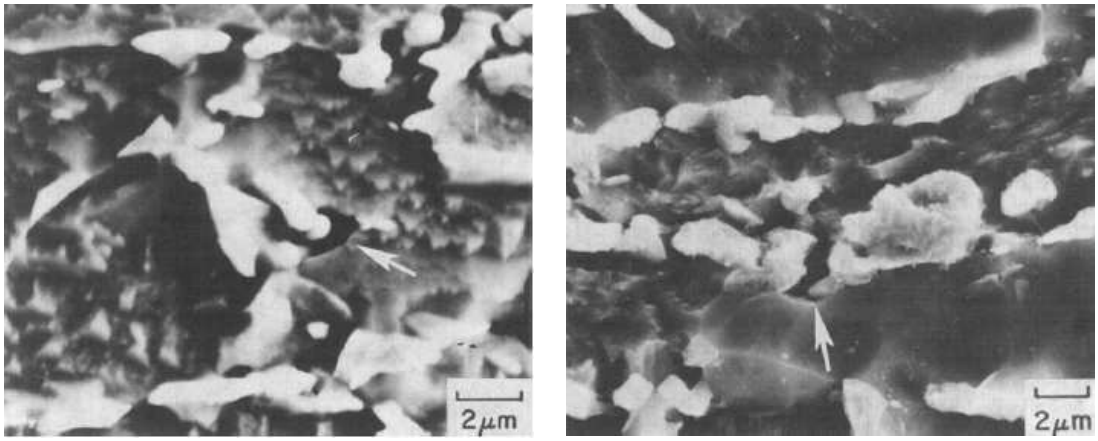

(a) (b)

Figure 2.5: SEM investigation of the nucleation mechanisms in DP steels, (a) ferrite/martensite interface decohesion, (b) fracture of the martensitic island [Stei 88].

promoted the void nucleation inside the martensitic phase. 2D and 3D quantitative measurements of the void density were respectively performed in [Avra 09b] and in [Mair 08]. Figure 2.6 exhibits the results of these two studies.

SEM *in-situ* tensile tests on DP steels were also carried out in [Mair 08]. Observations were performed on the surface of the specimen although tomography characterization showed that damage mainly appear in the center of the necked specimen. Imaged volume of the studied specimen is given in Figure 2.7(a) and the porosity measured along the main directions of the specimen are exhibited in Figure 2.7(b).

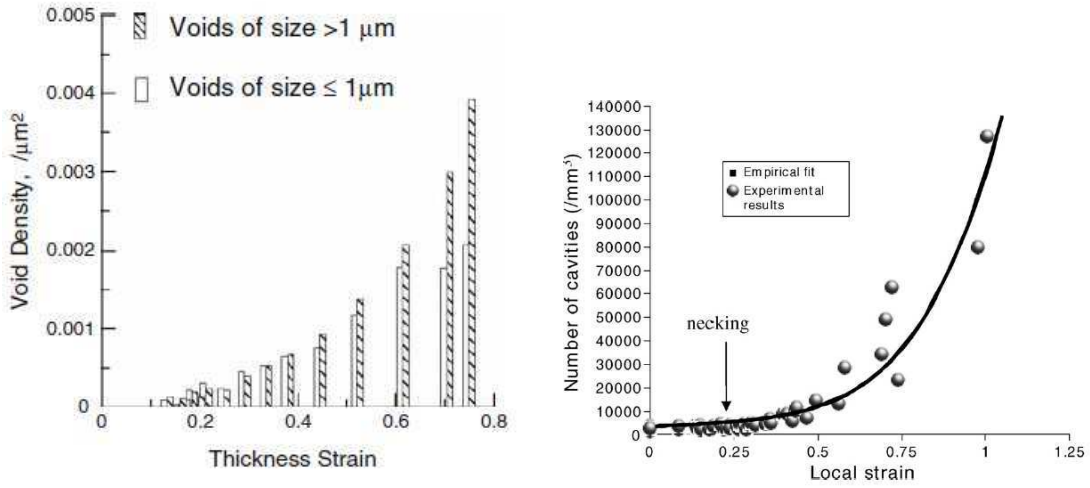

(a) (b)

Figure 2.6: Quantification of the void density in DP steels: (a) from 2D measurements [Avra 09b], (b) from 3D measurements [Mair 08].

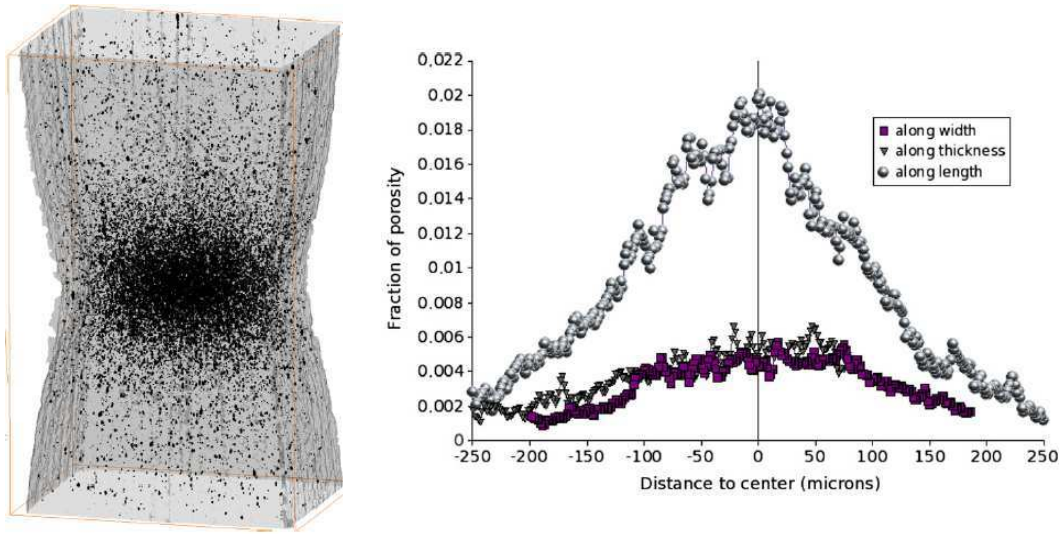

(a) (b)

Figure 2.7: Porosity distribution in the DP specimen studied in [Mair 08]:(a) qualitative observations, (b) quantitative measurements.

2.2 Void nucleation characterization

2.2.1 Qualitative observations

Damage nucleation has been investigated in the present PhD using X-ray tomography associated to *in-situ* tensile tests. Figure 2.8 shows the voids appearing during the tensile tests of the five studied materials. The number of cavities clearly increases with the applied deformation as previously observed in [Mair 08, Avra 09b]. Theses pictures show that the void density is highly different from a material to another. In particular, more cavities appear in the bi-phased microstructures (DP11, DP11T and DP62 samples) than in monophased steels (ferrite and martensite). This qualitative observation is confirmed by the quantitative characterization presented in the next section. A very low level of porosity (0.03%) could be detected before the tensile test, possibly due to the fabrication process. The use of these 3D pictures is really important in this work to account for all nucleating voids: Figure 2.9 shows that in 2D, only a small part of cavities present on the imaged section is seen.

2.2.2 Quantification of void nucleation

To quantify the void nucleation during the tensile test, the number of detected cavities in the studied sub-volume is counted and the void density N is calculated:

$$N = \frac{\text{number of cavities}}{\text{studied volume}} \tag{2.5}$$

The evolution of the void density with the applied tensile deformation is plotted in Figure 2.10 for each steels studied here. This figure confirms that the kinetic of void nucleation is really different from a material to another. The main remarks that can be formulated from these quantitative measurements are:

- The void density becomes particularly high in the deformed DP11 sample.
- In homogeneous materials, *i.e.* the fully ferritic steel and the fully martensitic steel, void nucleation is less important than in bi-phased steels.
- The microstructure has an effect on the void nucleation kinetic.
- The tempering decreases the void nucleation rate.

Thanks to the specimens with different geometries employed in this study, the effect of triaxiality on the void nucleation was examined. Figure 2.11 shows the effect of triaxiality in DP11 samples. As expected, a higher triaxiality leads to a faster increase of the void density during the tensile test.

2.2.3 Effect of the voxel size on the void nucleation characterization

In order to quantify the influence of the used resolution on the damage measurements performed for this work, we have compared the experimental data acquired on the ID15

DP11		
$\varepsilon_{loc} = 0$	$\varepsilon_{loc} = 0.4$	$\varepsilon_{loc} = 0.7$
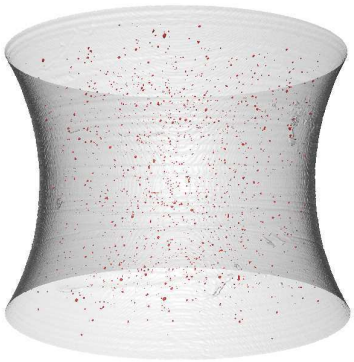	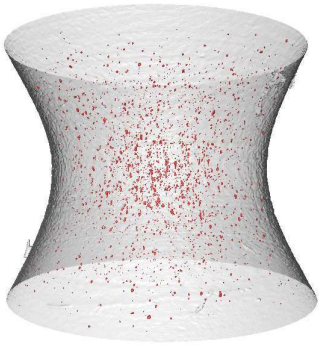	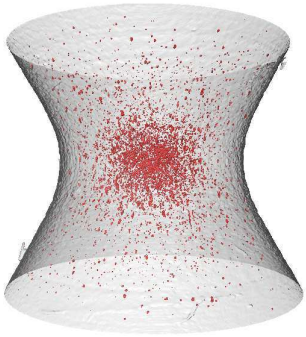
DP11T		
$\varepsilon_{loc} = 0$	$\varepsilon_{loc} = 0.9$	$\varepsilon_{loc} = 1.4$
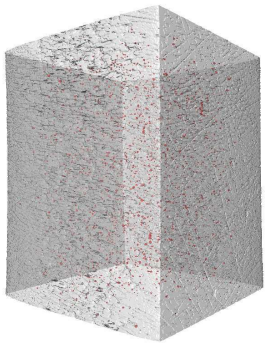	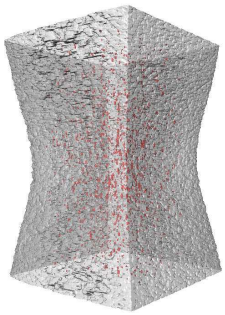	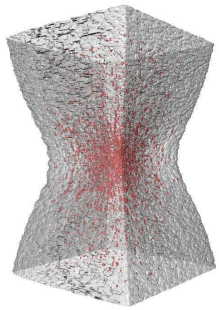
DP62		
$\varepsilon_{loc} = 0$	$\varepsilon_{loc} = 0.27$	$\varepsilon_{loc} = 0.35$
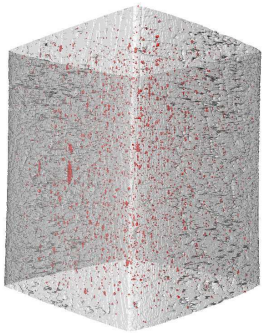	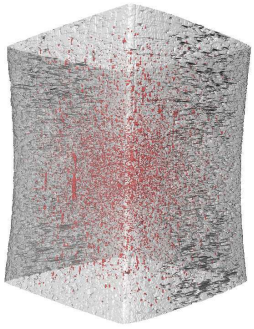	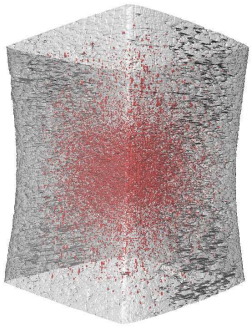

Ferrite		
$\varepsilon_{loc} = 0$	$\varepsilon_{loc} = 0.55$	$\varepsilon_{loc} = 1.9$
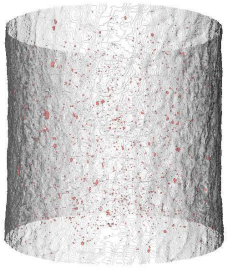	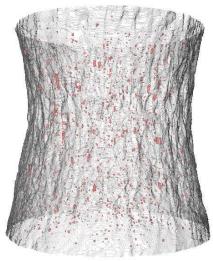	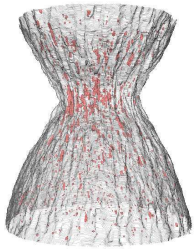
Martensite		
$\varepsilon_{loc} = 0$	$\varepsilon_{loc} = 0.25$	$\varepsilon_{loc} = 0.6$
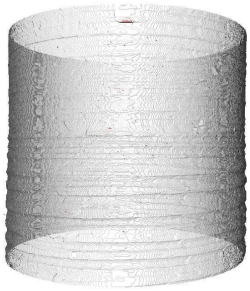	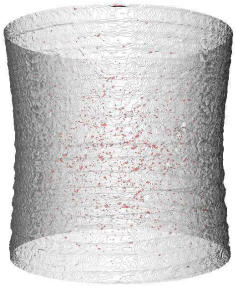	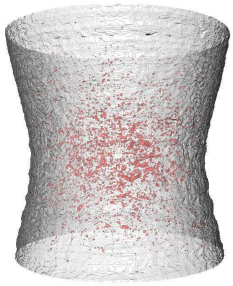

Figure 2.8: 3D views of the specimens of the studied steels at various steps of deformation.

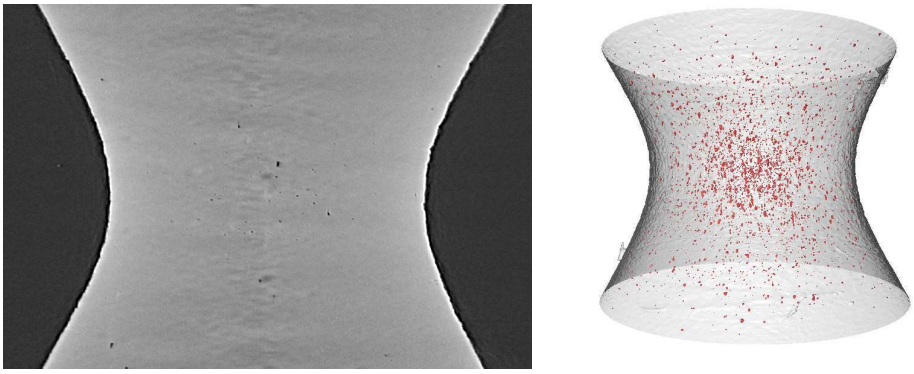

(a) (b)

Figure 2.9: Views of the same specimen (notched DP11 sample) coming from the acquired tomogramm: (a) 2D view of a section inside the volume, (b) 3D view of the entire volume.

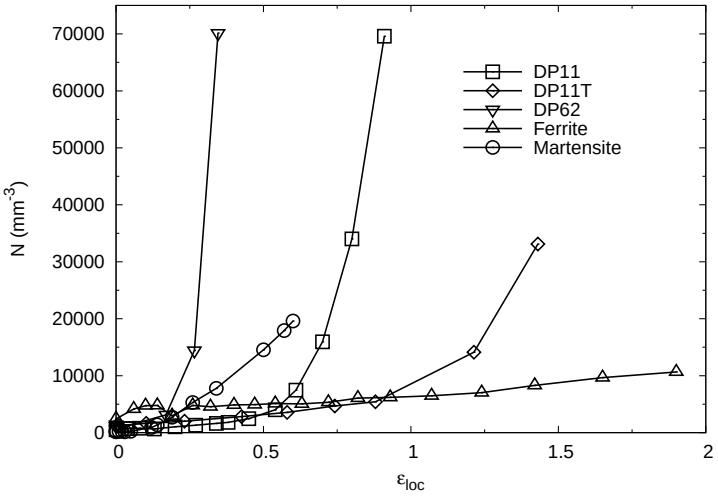

Figure 2.10: Evolution of the void density in each studied steel.

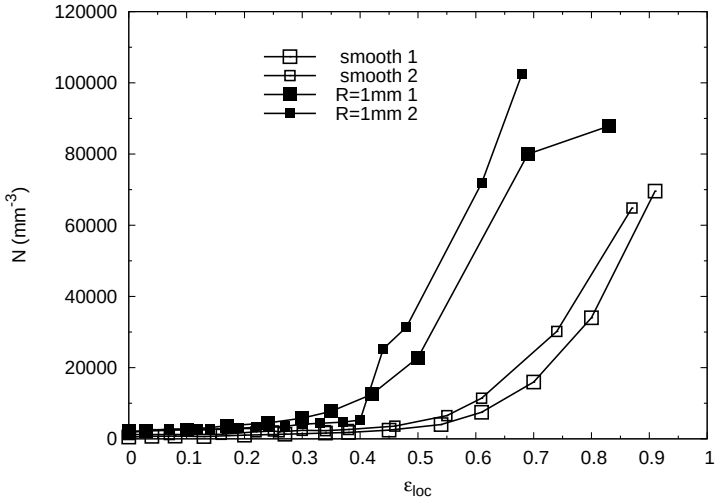

Figure 2.11: Triaxiality effect on void nucleation in DP11 sample.

beamline with a voxel size of 1.6µm and the data acquired on the ID22 beamline with a voxel size of 100nm. *Ex-situ* tensile tests performed on DP11 specimens at very high resolution show that a much large part of damage is not detected at low resolution. It can be qualitatively seen in Figure 2.12 which compares for the two resolution used similar central sub-regions extracted from DP11 specimens with a similar state of deformation and triaxiality. The quantitative evolution of the void density measured in the sub-volumes with the two different voxel sizes is given in Figure 2.13. As a confirmation of the qualitative observations, the number of detected cavities is much higher at high resolution. The volumes of the smallest detected cavities are almost $8\mu m^3$ in the case at low resolution and $2.10^{-3}\mu m^3$ at high resolution, these minimal volumes leading to a critical void size respectively of 2µm and 150nm. The frequency distributions of the equivalent diameter of the cavities measured in the similar volumes are given in Figure 2.14 for the two used resolutions. This graph shows that a substantial part of the cavities appearing during the tensile test have an equivalent diameter inferior to 2µm. This confirms that these small voids can only be seen at high resolution. Because of the *ex-situ* nature of the tensile tests performed at high resolution, only a few steps of deformation are available. This data is not sufficiently substantial to be used in the modeling section. However, the presence of the very small cavities will have to be taken into account.

2.2.4 Mechanisms of voids nucleation in DP steels

As mentioned in Section 1.1.1, attenuation X-ray tomography does not allow to distinguish the ferritic phase from the martensitic one because the attenuation coefficients of the two phases are very close. In order to obtain information on the location of the cav-

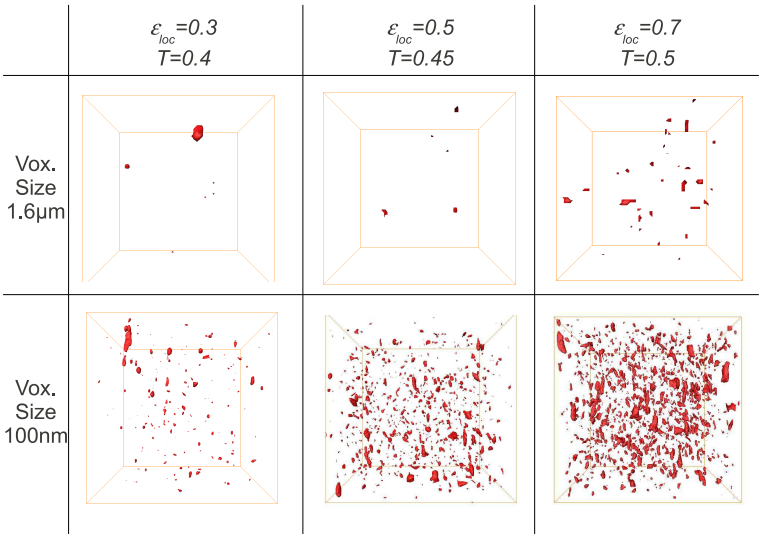

Figure 2.12: Qualitative comparison of visualized damage in central cubes (volume=$(100\mu m)^3$) coming from tomograms acquired with different resolutions.

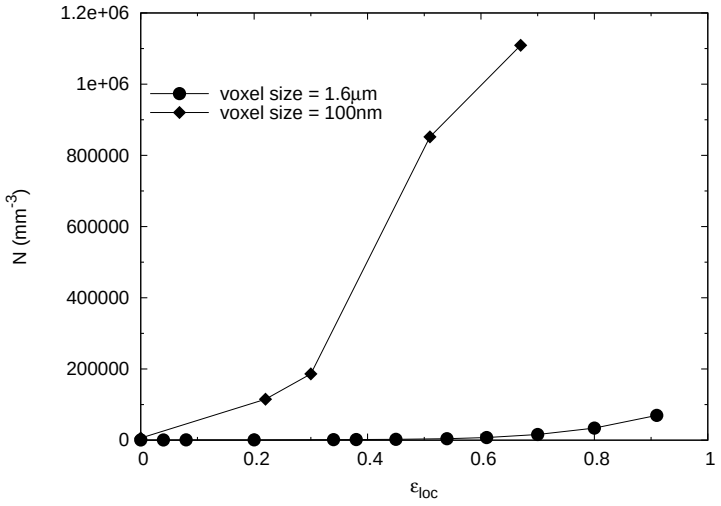

Figure 2.13: Evolution of the void density in the studied sub-volumes acquired with different voxel sizes in smooth DP11 specimens.

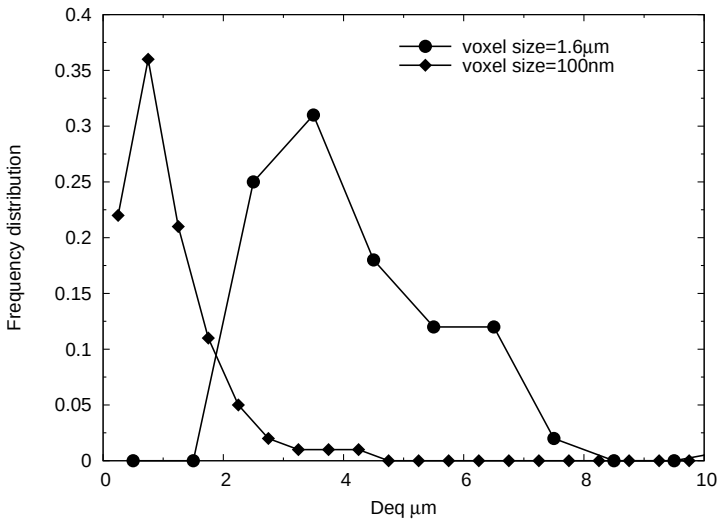

Figure 2.14: Comparison of the frequency distribution of the equivalent diameter of the cavities measured at high resolution and at low resolution in smooth specimens of DP11.

ities, being either at the ferrite/martensite interface or in the martensite as observed in previous studies (presented in Section 2.1.4), optical micrographs of polished and etched longitudinal sections of fractured specimens were performed. Micrographs of bi-phased materials are shown in Figures 2.15, 2.17, 2.18. In the DP11 sample, where the ferritic matrix is soft and the inclusions of martensite are hard, voids mainly appear by decohesion of the interface ferrite/martensite (Figure 2.15). This 2D observation is confirmed by the volume obtained by serial sectioning given in Figure 2.16. In the DP62 sample, where the martensite is softer, cavities appear inside the martensitic phase like in the tempered DP11T sample (Figures 2.17 and 2.18).

2.3 Void nucleation modeling

Several nucleation mechanisms were observed in the studied steels, *i.e.* interface decohesion, martensite fracture and void nucleation in the ferritic phase (for the fully ferritic steel). Each mechanism contribute to the total nucleation rate $\frac{dN}{d\varepsilon}$ and thus has to be accounted for.

$$\frac{dN}{d\varepsilon} = \frac{dN_D}{d\varepsilon} + (1 - F_M)\frac{dN_F}{d\varepsilon} + F_M\frac{dN_M}{d\varepsilon} \tag{2.6}$$

where $\frac{dN_D}{d\varepsilon}$ is the rate of nucleation by decohesion of the interface ferrite / martensite, $\frac{dN_M}{d\varepsilon}$ the rate of nucleation by fracture of the martensite islands and $\frac{dN_F}{d\varepsilon}$ in ferrite and F_M is the volume fraction of martensite.

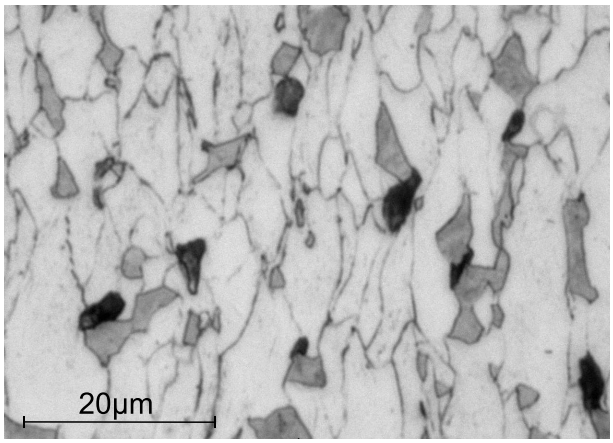

Figure 2.15: Optical micrograph of a fractured sample of DP11. White is ferrite, gray martensite, black cavities.

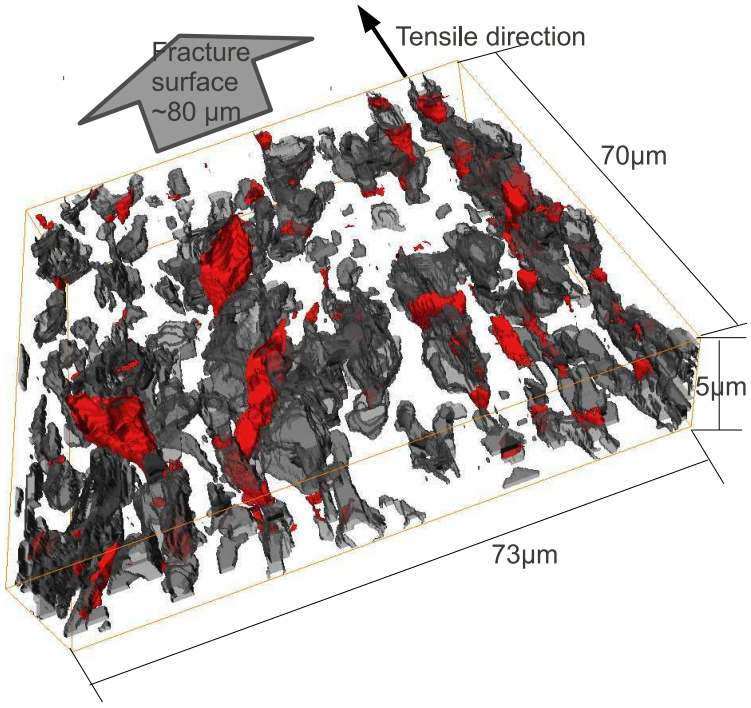

Figure 2.16: Volume of a fractured sample of DP11 reconstructed from serial sectioning. Gray is martensite, red cavities and ferrite is removed.

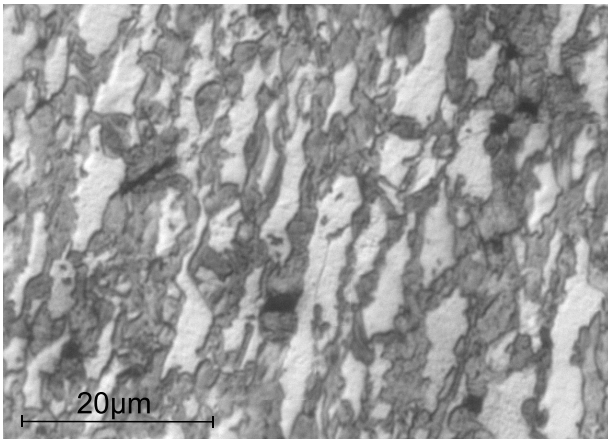

Figure 2.17: Optical micrograph of a fractured sample of DP62.

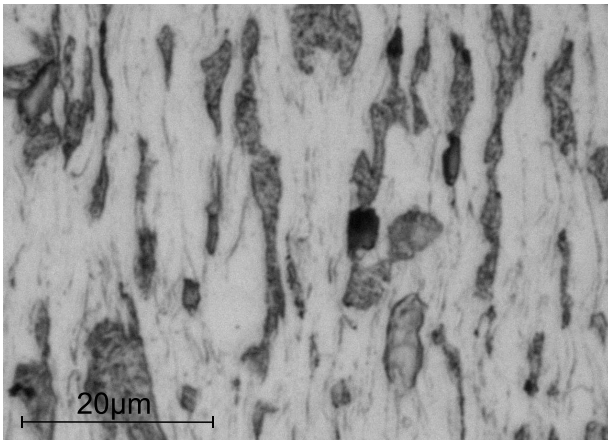

Figure 2.18: Optical micrograph of a fractured sample of DP11T.

In DP11 samples, cavities appear mainly at the ferrite/martensite interface. This experimental data was thus used in Section 2.3.1 to model the rate of nucleation by decohesion. Quantitative data concerning the other steels (DP11T, DP62, ferrite and martensite) where void nucleation mainly occurs in the martensitic phase or in the ferritic phase, were employed in the modeling of the rate of nucleation in martensite and in ferrite performed in Section 2.3.2.

2.3.1 Modeling the interface decohesion

As demonstrated by Tanaka *et al.* [Tana 70], the energy criterion necessary for the creation of new surfaces at the inclusion/matrix interface is satisfied at the onset of the plastic deformation in materials containing inclusions larger than about 25nm in diameter. Martensitic islands having a size about 10µm, only a stress criterion is therefore used to model interface decohesion in DP steels. The Argon criterion and the Beremin criterion are used in this section.

2.3.1.1 The Argon criterion

The interest in using the Argon criterion presented in Section 2.1.3 lies in the fact that it accounts for the triaxiality T being the ratio between σ_{eq} and σ_H:

$$T = \frac{\sigma_H}{\sigma_{eq}} \tag{2.7}$$

Combining Eqs. (2.1) and (2.7), the criterion is expressed as:

$$\sigma_{eq}\,(1+T) = \sigma_C \tag{2.8}$$

In the original Argon criterion the triaxiality used is the macroscopic triaxiality. However, decohesion is a local phenomenon which occurs at the interface of ferrite and martensite islands. In Helbert *et al.* [Helb 98] it was demonstrated that local triaxiality is higher at the interface because of the kinematic hardening X generated by the difference in the mechanical behavior of the two phases. In DP steels the difference between the mechanical behavior of ferrite and martensite is quite high. Therefore, it would be better to use the local triaxiality at the interface T_{loc}. We proposed in [Land 10b] that T_{loc} could be estimated using the following expression from [Helb 98]:

$$T_{loc} = T\frac{\sigma_{eq}}{\sigma_{eq} - X} \tag{2.9}$$

The modified expression of the Argon criterion to obtain local decohesion then becomes:

$$\sigma_{eq}\,(1+T_{loc}) = \sigma_C \tag{2.10}$$

The left side of the equation in this local version of the Argon criterion is termed ξ_{Argon} below.

$$\xi_{Argon} = \sigma_{eq}\,(1+T_{loc}) \tag{2.11}$$

An estimation of the value of the kinematic hardening X is necessary at this stage to calculate T_{loc}. The value of X increases with the applied deformation. The maximum value is reached from the very beginning of the tensile test. This maximum value is thus used in the present modeling and is estimated from the formula given by Allain and Bouaziz [Alla 08] and expressed as a function of the respective hardness of ferrite HV_F and martensite HV_M :

$$X = F_M\,(1 - F_M)\,3|HV_M - HV_F| \tag{2.12}$$

where F_M is the volume fraction of martensite.
The values of the hardness of ferrite and martensite in DP11 were given in Section 1.2.1.2. $HV_M = 830$MPa and $HV_F = 150$MPa. This leads to a value of $X = 199$MPa for this particular steel.

2.3.1.2 The Beremin criterion

The Beremin criterion, also presented in Section 2.1.3, was tested here to model the decohesion of the interface ferrite/martensite. In our case, σ_I^{max} is the applied tensile stress σ_{zz}, σ_{eq} the equivalent stress and σ_0 the equivalent stress measured in the ferrictic specimen. The left side of the expression of the Beremin criterion is further termed $\xi_{Beremin}$:

$$\xi_{Beremin} = \sigma_{zz} + k_s\,(\sigma_{eq} - \sigma_F) \tag{2.13}$$

k_s is chosen to be equal to 1 because martensite islands are roughly isotropic.

2.3.1.3 A rough estimation of the critical stress of the ferrite/martensite interface

Both criteria, *i.e.* the modified Argon developed in this work and the classical Beremin, are used to estimate the value of the stress at the ferrite/martensite interface. These stresses can be seen as the driving forces available to break the interface. The evolution of their respective values in a smooth specimen and a notched specimen of DP11 are plotted in Figure 2.19. Concerning the smooth specimen, $\xi_{Beremin}$ and ξ_{Argon} are really close although in the notched specimen case the difference between the two criteria increases with the deformation. In every cases, the Argon criterion predicts a stress value superior to the one predicted by the Beremin criterion.

By calculating the value of the stress at the interface ξ at the experimentally observed nucleation strain ε_N, an average value of σ_C can be estimated in the case of the ferrite/martensite interface:

$$\xi\,(\varepsilon_N) = \sigma_C \tag{2.14}$$

Two values of ε_N are determined from the void density measurements on the smooth and the notched samples. These values are taken at the point when the void density started to increase. Focusing on the low strain region given in Figure 2.20, values for nucleation

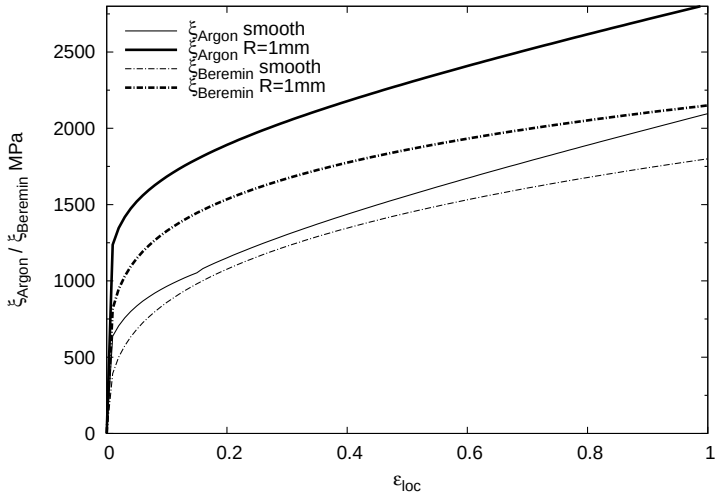

Figure 2.19: Comparison of $\xi_{Beremin}$ and ξ_{Argon} in a smooth specimen and in a notched specimen of DP11.

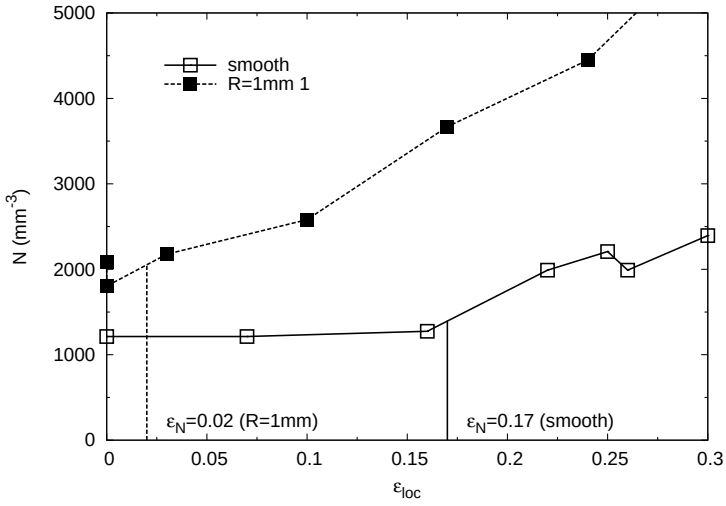

Figure 2.20: Focus on the low strain region of the evolution of the void density in the DP11 samples.

strain of 0.17 for the smooth specimen and 0.02 for the notched specimen can be inferred.

Figures 2.21 and 2.22 show the estimation of σ_C using both criteria. The interface strengths found here for the particular values of strain when nucleation started to increase was about 1100MPa using the modified expression of Argon and about 1000MPa using the Beremin criterion. This strength probably depends on the carbon content in the martensite and on the eventual tempering. The value determined here is a lower bound and is thus valid only for the studied DP11 steel.

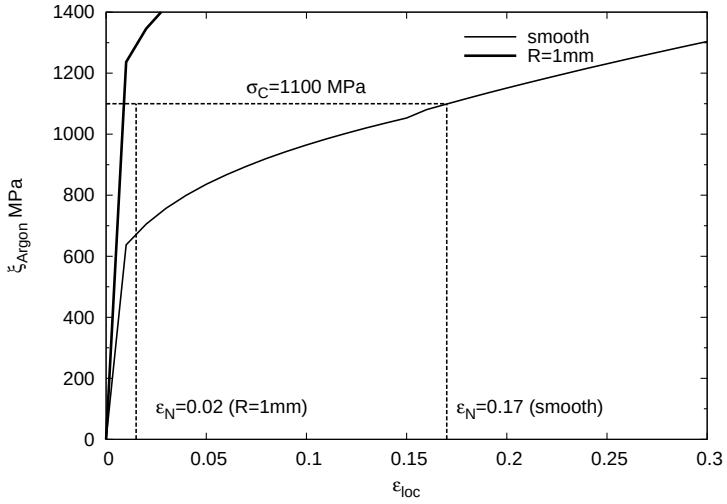

Figure 2.21: Estimation of σ_C using the modified expression of Argon.

A compilation of several values for the interface strength between other particles and ferrite found by different authors is listed in Table 2.1. The order of magnitude is the same as the one calculated using our approach, our estimation being situated in the lower range of these values. Note that our estimation is valid for the very beginning of nucleation (*i.e.* when the number of voids starts to increase as seen in the tomography images). The other values were obtained with other methods and probably other definitions, however, a direct comparison is not the aim of the table. We simply underline here that the order of magnitude provided by the calculation seems physically right.

2.3.1.4 Modeling of the void nucleation kinetic

As observed by Avramovic-Cingara *et al.* [Avra 09b], void nucleation in DP steels is progressive during the entire deformation process. Each void nucleates for a different value of the plastic strain. This is because each single interface probably exhibits a different value of ε_N and is also possibly subjected to a different value of ξ. Interface decohesion is thus a progressive phenomenon, starting for a strain of 0.17 but continuing

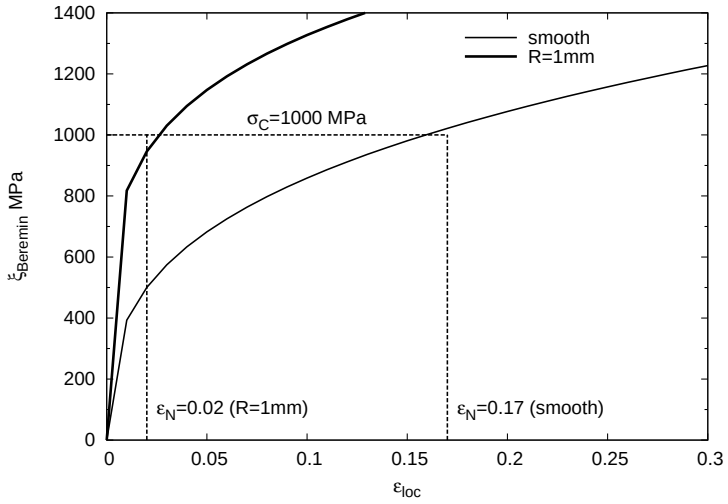

Figure 2.22: Estimation of σ_C using the Beremin expression.

Particle	Interface Strength (MPa)	Ref.
Y2O3	1000 - 1600	[Kosc 93]
MnS	1100 - 1400	[Qiu 99]
Fe3C	1200 - 2000	[LeRo 81] [Kwon 88]

Table 2.1: Values of other ferrite/particle interface strength.

after this value of strain, and the evolution of the cavity density has to be predicted as a function of the local strain. Figure 2.11 shows two different nucleation regimes at low and high strains. We have proposed a possible approach to model the kinetic of interface decohesion in DP steel in [Land 10b]. It is observed experimentally (see Figure 2.11) that the number of cavities increases slowly and linearly in a first regime. In a second regime many voids appear exponentially. This experimental observation led us to propose the following empirical equation based on the local criterion of decohesion and involving the parameters ξ and σ_C, ξ being calculated from the modified Argon expression given in Eq (2.11) or from the Beremin expression given in Eq (2.13):

$$\frac{dN}{d\varepsilon} = A\frac{\xi}{\sigma_C}\left(1 + \frac{N}{N_0}\right) \tag{2.15}$$

A and N_0 being two constants (expressed in the same unit as N, for instance, mm^{-3}). The two extreme regimes are well described by this empirical expression. When $N \ll N_0$ the following approximation is applicable:

$$\frac{dN}{d\varepsilon} \approx A\frac{\xi}{\sigma_C} \tag{2.16}$$

Interface decohesion is then linearly controlled by the local stress ξ, which increases with the applied strain. In the second step, when $N \gg N_0$ the approximation becomes:

$$\frac{dN}{d\varepsilon} \approx A\frac{\xi}{\sigma_C}\frac{N}{N_0} \tag{2.17}$$

The evolution of the rate of nucleation with the strain is proposed to depend on N itself, thus describing a self-catalytic effect and the exponential acceleration of the number of cavities. This self-catalytic effect could for example be due to the interaction between cavities when they come close together. A distance between cavities around 35 µm is calculated from the void density at which exponential increase starts.

The assessment of the model using ξ_{Argon} and $\xi_{Beremin}$ was first done using experimental data from smooth specimens. The values of A and N_0 giving the best fit between the model and experimental data for the smooth sample were $A = 4500\text{mm}^3$ and $N_0 = 1300\text{mm}^3$ whatever the calculation method of ξ. These values were then applied to the notched samples and also showed satisfactory agreement, as shown in Figures 2.23 and 2.24. Equation 2.15 was also used to model the void density measured at high resolution (see Figure 2.25). It leads to $A = 450000\text{mm}^3$ and $N_0 = 130000\text{mm}^3$. This validates the use of the stress at the ferrite/martensite interface as the driving force in the interface fracture criterion.

2.3.2 Modeling of the void nucleation inside the martensitic phase

2.3.2.1 Using the Beremin criterion

The stress criterion of Beremin can be used to model either the interface decohesion (as the case presented in the last section) or the particle fracture. This stress criterion was

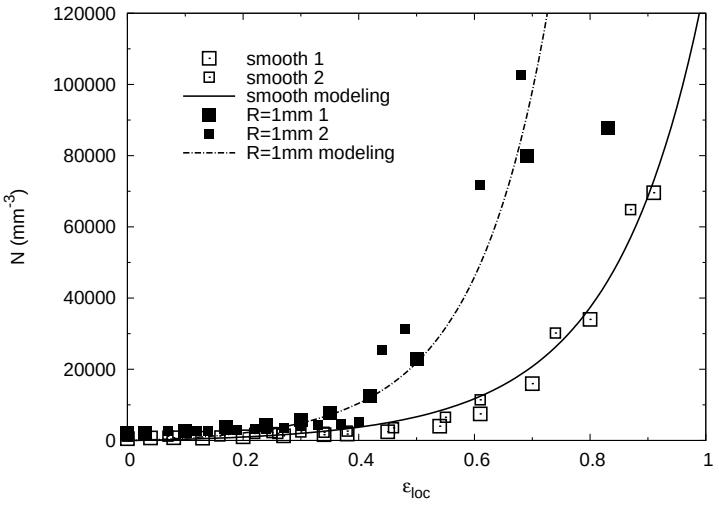

Figure 2.23: Comparison of the prediction of the nucleation model using ξ_{Argon} and experimental data.

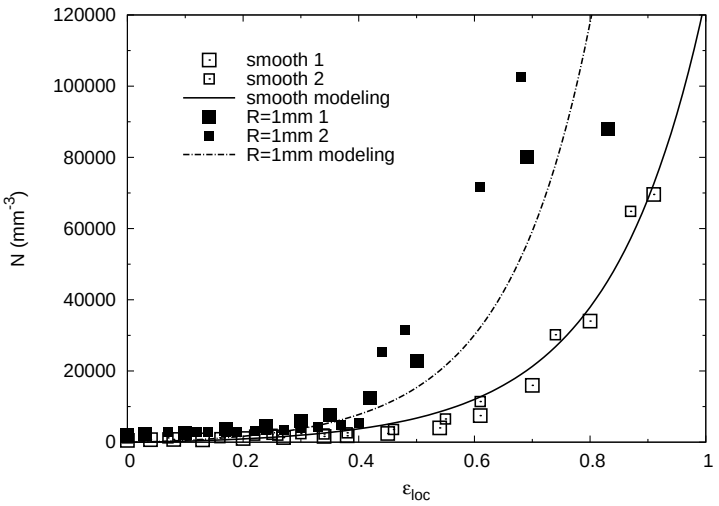

Figure 2.24: Comparison of the prediction of the nucleation model using $\xi_{Beremin}$ and experimental data.

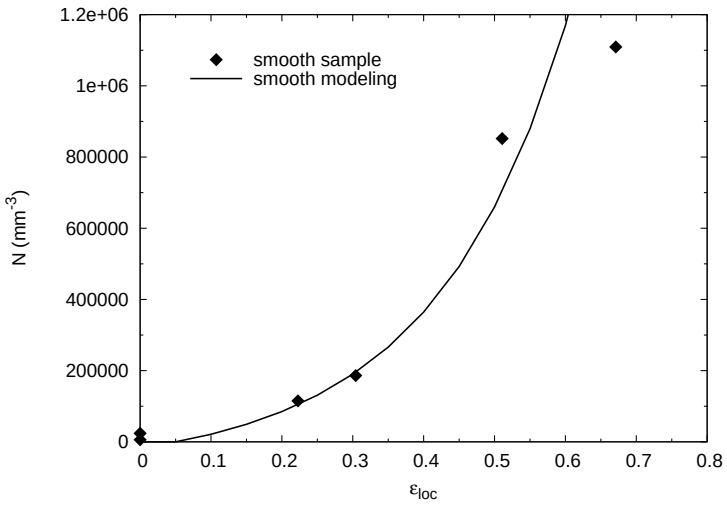

Figure 2.25: Comparison of the prediction of the nucleation model using ξ_{Argon} and experimental data acquired with high resolution.

then used in this section to predict the fracture of the martensitic phase in the DP62 sample and in the tempered DP11T sample.

The same approach as the one developed in Section 2.3.1.4 is used here. Equation (2.13) is used to calculate the value of the stress inside the martensite. In the DP11T specimen, k_s is taken equal to 1 because the martensite island are roughly isotropic (no elongated shape stress concentration) and in the DP62 sample, this shape parameter is taken equal to 0.1 because martensite islands are elongated. The evolution of $\xi_{Beremin}$ with the deformation is given for both materials in Figure 2.26.

The value of σ_C, being in this case the critical stress for the fracture of the martensitic phase is calculated as being the value of $\xi_{Beremin}$ for $\varepsilon_{loc} = \varepsilon_N$. The strain at the onset of nucleation ε_N in the DP11T and DP62 samples were experimentally measured using curves like the ones in Figure 2.10 and the values are given in Table 2.2. Determination of the values of σ_C performed in Figure 2.26 leads to $\sigma_C = 1750$MPa for the DP62 steel and $\sigma_C = 700$MPa for the tempered DP11T steel.

Material	Experimentally measured values of ε_N
DP11T	0.1
DP62	0.03

Table 2.2: Values of ε_N experimentally measured in the DP11T and DP62 samples.

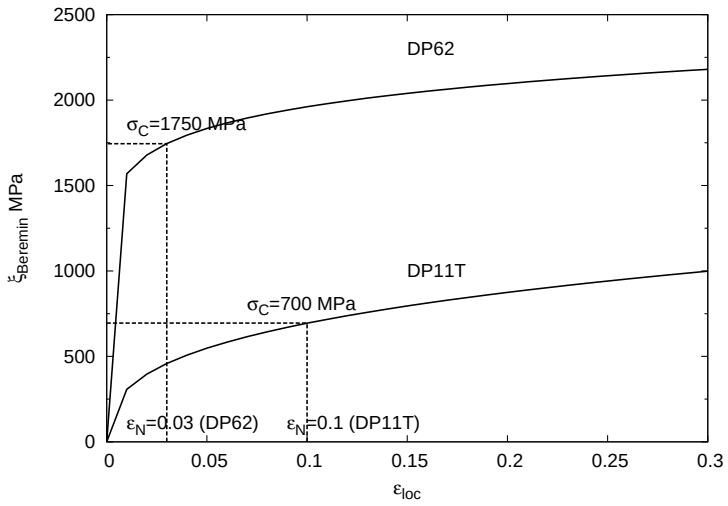

Figure 2.26: Values of $\xi_{Beremin}$ calculated in the DP11T and the DP62 specimen and estimation of σ_C for both materials.

The value $\sigma_C = 1750$MPa found for the DP62 is relevant because it corresponds to the fracture stress of the martensite composing this steel. The kinetic of nucleation in this steel is then predicted using Eq (2.15) with $\sigma_C = 1750$MPa, $A = 4500\text{mm}^3$ and $N_0 = 250\text{mm}^3$. The experimental data and the prediction are given in Figure 2.27.

On the contrary, The value $\sigma_C = 700$MPa found for the DP11T seems to be really low to be compared with the the fracture stress of the tempered martensite. Moreover the kinetic of nucleation cannot be modeled from Eq. (2.15). This discrepancy may be due to the fact that a high plastic deformation is induced in the islands of martensite during the tensile test. The Beremin criterion does not take into account this plastic deformation. It is then not adapted to predict this void nucleation. A strain criterion is then tested in the next section.

2.3.2.2 Using a strain criterion

In the cases where damage appears in the martensitic phase, *i.e.* the fully martensitic steel, the tempered DP11T sample and the DP62 sample, or in the ferritic phase, *i.e.* the fully ferritic steel, the approach developed by Chu and Needleman [Chu 80] was preferred to model the kinetic of void nucleation. This approach, based on the attainment of a critical strain level ε_N inside the concerned phase, was successfully applied on a bi-phased titanium in [Helb 98]. We have then used a similar expression of the evolution of the density of voids appearing inside the martensitic phase N:

$$N = N_0 \left(\exp\left(\frac{\varepsilon}{\varepsilon_N} \right) - 1 \right) \tag{2.18}$$

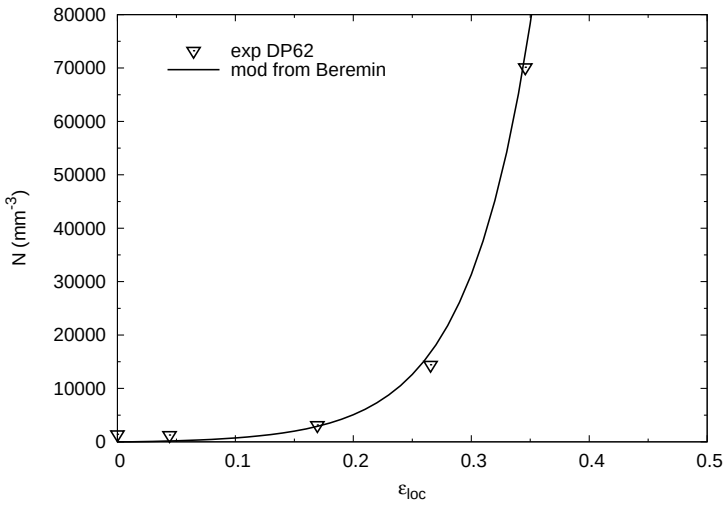

Figure 2.27: Experimental data and prediction from Eq.(2.15) for the DP62 steel.

with

$$\varepsilon_N = A \exp\left(-\beta T\right) \tag{2.19}$$

where N_0, A and β are constants used as fitting parameters for each steel.
For the single-phase steels, the deformation employed in the model is the measured local strain while in the bi-phased steels, the used one is the deformation inside the martensite ε_M.
ε_M is estimated using the isoW homogenizing equations presented in [Boua 04]:

$$d\varepsilon = F_M d\varepsilon_M + (1 - F_M)\, d\varepsilon_F \tag{2.20}$$

$$\sigma_F d\varepsilon_F = \sigma_M d\varepsilon_M \tag{2.21}$$

where ε_F, σ_F and σ_M are respectively the deformation and the stress in the ferritic phase and the stress in the martensite. Combining equations (2.20) and (2.21), we obtain:

$$d\varepsilon_M = \frac{d\varepsilon}{F_M + \left(1 - F_M \frac{\sigma_M}{\sigma_F}\right)} \tag{2.22}$$

Using the approximation $\sigma \approx 3HV$ valid for the steel materials, the stress ratio $\frac{\sigma_M}{\sigma_F}$ is substituted by the known hardness ratio $\frac{HV_M}{HV_F}$.
The results of the fitting procedure of Eq. (2.18) on experimental data are given in Figure 2.28 and in Table 2.3.

- The parameter β controlling the effect of the triaxiality on ε_N was chosen to be the same for all materials. $\beta = 2$ gave good fitting results in particular for samples where different notched specimens were tested.

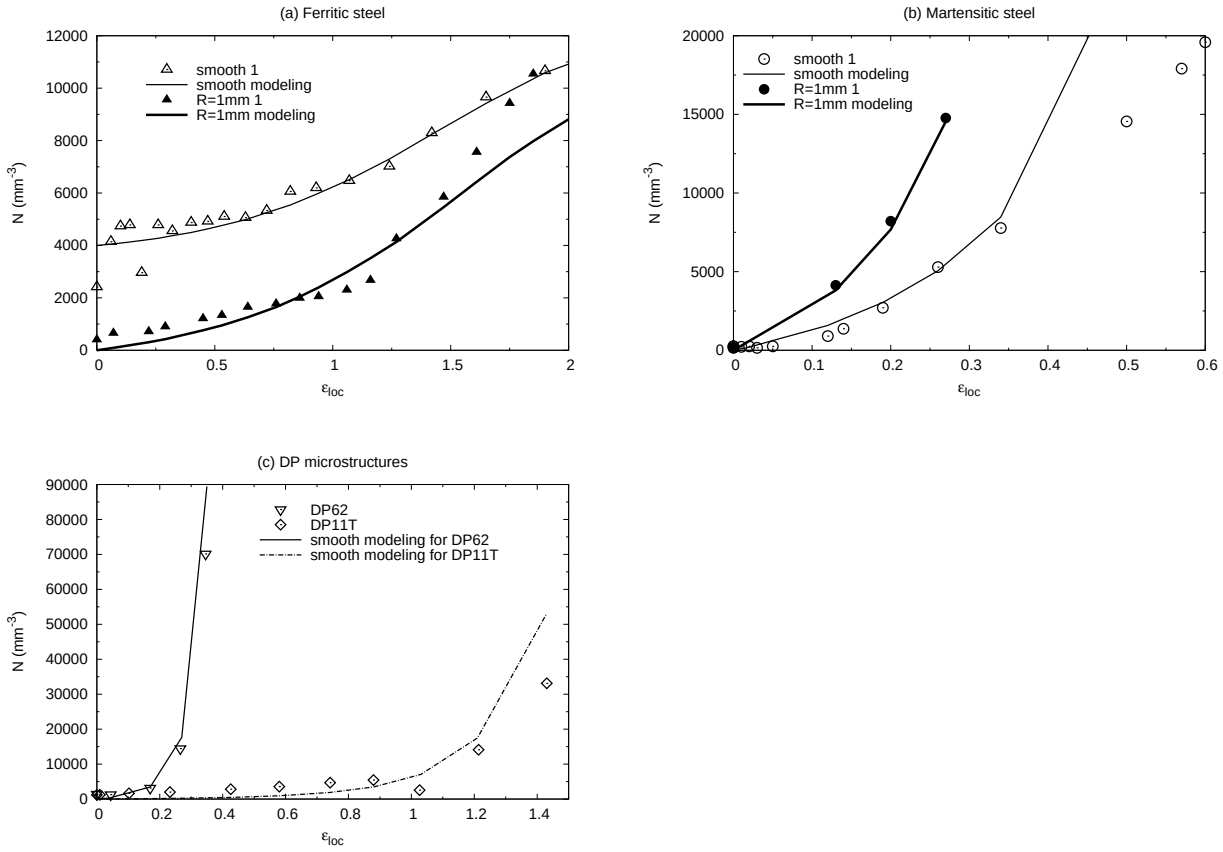

Figure 2.28: Comparison between the prediction of the nucleation model from Eq. 2.18 and experimental data.

Material	HV_M (MPa)	$N_0(\text{mm}^{-3})$	A	β
Ferritic steel	150	5000	13	2
Martensitic steel	370	5000	1	2
DP62	530	500	0.09	2
DP11T	415	500	0.6	2

Table 2.3: Values of the parameters used in Eq.(2.18) to fit the experimental evolution of $N = f(\varepsilon)$.

- The parameter A also influencing ε_N was used to fit the prediction on experimental data for each material. A particular attention was paid to have appropriate values of ε_N. A relationship linking A and the hardness of the phase where cavities appear can be observed in Figure 2.29. This relationship suggests that the harder the phase, the lower the value of ε_N and then the faster the void nucleation.

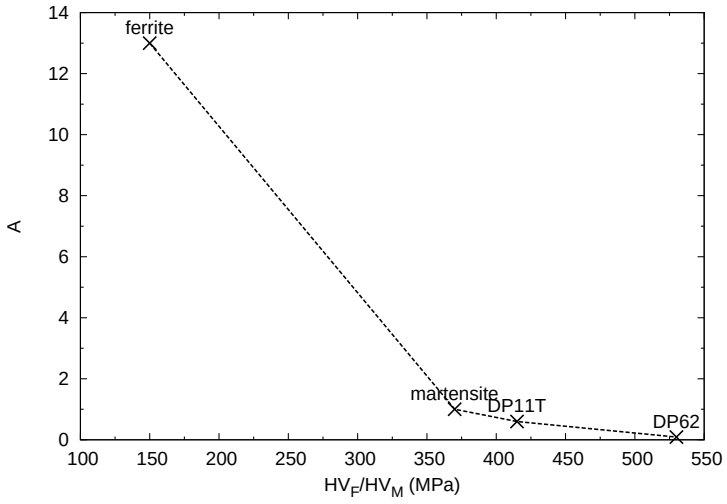

Figure 2.29: Relationship between the parameter A and the hardness (HV_F or HV_M) of the phase where cavities appear.

- The last parameter, N_0 was also used to fit the prediction on experimental data. Only two value were found for all the specimens: $N_0 = 5000\text{mm}^{-3}$ for the single-phased steels and $N_0 = 500\text{mm}^{-3}$ for the bi-phased steels.

2.4 Summary

The mechanisms of void nucleation in the investigated DP steels were studied using optical micrographs of fractured specimens. Void nucleation kinetic were quantified using X-ray tomography. The important conclusion drawn are:

→ The bi-phased microstructure of DP steels is the origin of a much faster void nucleation compared with single-phase steels.

→ The mechanisms of void nucleation strongly depend on the steel microstructure: in the case where the interface strength is weak, voids appear because of the decohesion of the interface and when the interface is stronger and the martensite softer, voids appear in the martensite.

→ The void nucleation kinematic at the interface and within the martensitic phase were modeled using samples where damage nucleates either by interface decohesion or fracture of martensite islands.

To complete this study, void nucleation kinetic in a DP steel exhibiting both nucleation mechanisms could be quantified. Such data would validate the global equation of the nucleation kinetic and may show that a correlation between the different mechanisms of nucleation exists.

The limitations of X-ray tomography used to characterize damage in DP steels were also underlined in this chapter. First the fact that the two components of DP steels, *i.e.* ferrite and martensite, cannot be visualized is a problem to identify the nucleation mechanisms. Optical micrographs were thus required to analyze this very important parameter. Then a really fine resolution is needed to detect all voids appearing in the specimen. Tomograms can be acquired with fine resolution but the achievement of images at such high resolution is difficult and requires further development.

Chapter 3

Void growth

After the nucleation, cavities instantly start to grow by plastic deformation, this is the second step of the ductile damage process. In this chapter, the void growth in the different studied steels is studied. Quantitative results are compared to the void growth models developed in the literature. The microstructure parameters influencing the void growth mechanisms are investigated through the use of these models. A part of this work has been published in [Land 11].

3.1 Literature review

3.1.1 Experimental observations of void growth

The void growth is doubtlessly the most widely studied step of ductile damage. This is likely because it is the most easily observable. The growth of cavities was first investigated using metallographic observation of longitudinal sections of fractured specimens as done by Puttick [Putt 59], Floreen and Hayden [Flor 70], Cox and Low [Cox 74] and Park and Thompson [Park 88]. Examples of optical and SEM micrographs are respectively given in Figure 3.1(b) and (e) and 3.1(a). The relevance of these 2D measures very much depends on the quality of the polishing in order to avoid smearing out of the voids. Void growth can be directly observed at the surface of specimen during *in-situ* tensile test. Figure 3.1(c) shows the growth of void at the surface of a steel specimen during such a test.

3D indirect methods introduced page 42 are not adapted to study cavity growth. Only the growth of the global porosity fraction including void nucleation and void growth can be measured using these global methods. The recent technique of X-ray microtomography provided more complete quantitative information, particularly concerning the 3D morphology of the cavities [Ever 01, Babo 01, Babo 04a, Weck 08b, Bouc 08, Lort 10, Mair 11]. Buffiere *et al.* [Buff 99] and Babout *et al.* [Babo 04b] pointed out the interest of using tomography to avoid the artifacts of surface observation in the study of damage. Figure 3.1(d) shows voids appearing in a MMC specimen [Weck 08b]. The 3D

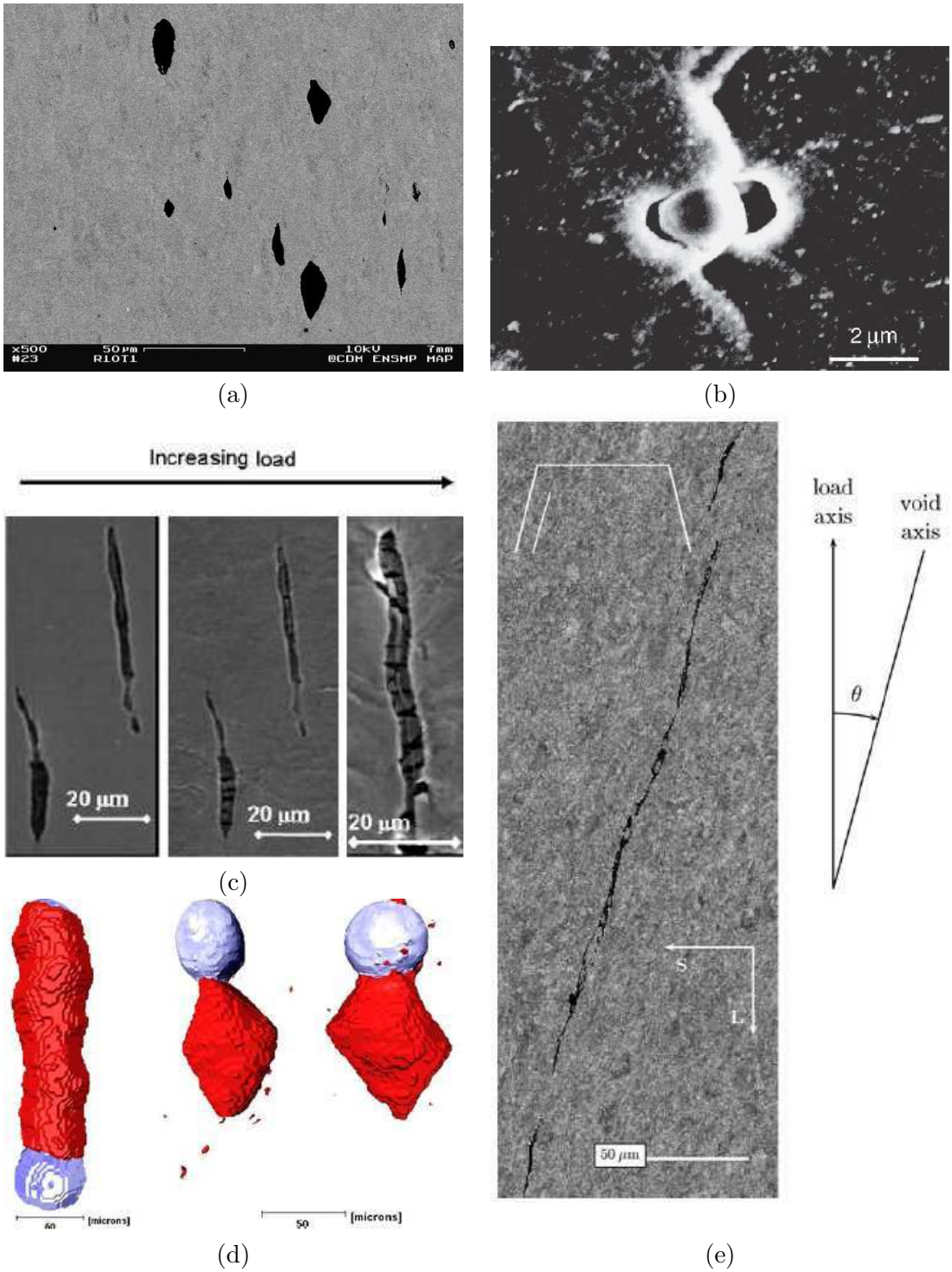

Figure 3.1: Experimental observation of void growth: (a) SEM micrograph of fractured tensile bar [Benz 10] , (b) Micrograph of voids originating from the decohesion of the interface matrix (copper) / particle (copper oxide inclusion)[Pard 98c], (c) SEM observations during the *in-situ* tensile test of ductile steel[Bouc 08], (d) Tomographic reconstruction of voids (dark colors) nucleated at zirconia particles (light colors) [Weck 08b], (e) evidence of void rotation in metallographic observation of longitudinal section of medium carbon low alloy steel [Benz 04a].

characterization allows to distinguish voids growing where deformation is homogeneous (elongated void) or localized (diamond-shape void).

These experimental observations of void growth showed that cavities tend to become elongated in the tensile direction. Examples are given in Figure 3.1(a) (c) or (d). In the case where void axis are not aligned with the principal deformation, Benzerga *et al.* showed that a rotation of the void was observed [Benz 04a] (see Figure 3.1(e)).

3.1.2 Parameters influencing void growth

Parameters having an influence on the void growth were investigated using this technique of characterization. The stress triaxiality was widely studied by McClintock [McCl 68], Marini *et al.* [Mari 85], Pardoen and Delannay [Pard 98b], Chae and Koss [Chae 04], Geni and Kikuchi [Geni 99] etc... All these studies concluded that an increasing triaxiality induces a significant increase of the void growth rate. During its numerous quantitative investigation of void growth, Marini *et al.* observed some differences in the growth kinetic linked to the void density [Mari 85]. They attributed these differences to the interactions between cavities leading to an acceleration of the void growth.

The effect of isotropic strain hardening and of voids interactions were as well earlier examined. Barnby *et al.* [Barn 84] and Pardoen *et al.* [Pard 98c] showed that isotropic strain hardening reduces the void growth rate. More recently, Tanguy and Besson [Tang 05] investigated the influence of kinematic hardening inducing the opposite effect, e.i. an increase in the cavity growth.

3.1.3 Void growth models

3.1.3.1 Simple analytic models for isolated voids

The first developed family of void growth models was based on a simple analytical approach for isolated voids in a perfectly plastic infinite matrix. The first model developed by McClintock predicted the growth of cylindrical voids [McCl 68]. One year later, Rice and Tracey proposed an equation for the growth of an initially spherical cavity in an infinite, rigid, perfectly plastic material subjected to a uniform remote strain field [Rice 69]. Assuming a fully isotropic void growth, the variational analysis of Rice and Tracey leads to the following expression:

$$\frac{dR}{R} = 0.272 \exp\left(\frac{3}{2}T\right) d\varepsilon \tag{3.1}$$

Where R is the void radius, ε the plastic equivalent strain and T the stress triaxiality. The Rice and Tracey model was widely used in the literature to predict the ductile void growth [Pard 98b, Pard 98c, Stra 03, Imad 03, Chae 04, Miro 04, Mair 08, Weck 08c, Kuma 09, Takt 09].

This model has later been revisited by Huang [20] who calculated the pre-exponential term, accounting for its dependence on the triaxiality T:

$$\begin{aligned} &\text{for } T \leq 1 \qquad \frac{dR}{R} = 0.427 T^{0.25} \exp\left(\frac{3}{2}T\right) d\varepsilon \\ &\text{for } T > 1 \qquad \frac{dR}{R} = 0.427 \exp\left(\frac{3}{2}T\right) d\varepsilon \end{aligned} \tag{3.2}$$

Successful applications of the Huang's correction on experimental data can be found in [Hamm 07, Garr 07, Wei 07, Mair 11, Land 11].

The general analysis of Rice and Tracey took also into account the void shape evolution [Rice 69, Thom 90]. Assuming an ellipsoidal shape, the expression of the void radii in the principal directions R_k was calculated as follows:

$$\frac{dR_k}{R} = \frac{dR}{R} + (1 + E_V)\, d\varepsilon_k \tag{3.3}$$

where $1 + E_V$ is a void shape parameter initially calculated to be equal to 5/3.
The first term, $\frac{dR}{R}$ is the void growth rate assuming a spherical cavity. Its initial expression is given in Eq.(3.1). The void shape change is controlled by the second term of the Eq.(3.3) $(1 + E_V)\, d\varepsilon_k$. Worswick and Pick showed using void cell calculations that the void shape parameter $1 + E_V$ depends on the stress triaxiality, the initial porosity, the strain hardening and the plastic deformation [Wors 90]. Again, it is worth noting that Le Roy *et al.* [LeRo 81] used the general void growth model of Rice and Tracey with the Argon's criterion of nucleation [Argo 75b] and the Brown and Embury coalescence condition [Brow 73] to predict the entire ductile damage process.

The models described previously are suitable for a perfectly plastic matrix. However, the isotropic hardening of the material matrix is taken into account in other void growth models. This is the case of the first model of McClintock for cylindrical voids [McCl 68]:

$$\frac{dR}{R} = \frac{\sqrt{3}}{2(1-n)} sinh\left(\sqrt{3}(1-n)T\right) d\varepsilon \tag{3.4}$$

where n is the hardening exponent determined using the power law $\sigma = k_\sigma \varepsilon^n$.

The initial Rice and Tracey model has also been extended by Tracey [Trac 71] and Budiansky *et al.* [Budi 82] in subsequent studies in order to take into account strain hardening . Others extensions taken into account parameter influencing the void growth such as the void interactions introduced by Marini *et al.* [Mari 85] were also added to the initial equation proposed by Rice and Tracey.

3.1.3.2 Constitutive models for porous media

A second family of more complex void growth models consists of constitutive models for porous elastoplastic or viscoplastic media. These models involve the coupling between

the porosity in the material's response. Their expression gives the equation of a yield function depending on the volume fraction of porosity f. The first of these models is the Gurson model [Gurs 77]. This model is based on a simplified representation a voided material assumed to be represented by a hollow sphere. The matrix is assumed to be rigid, isotropic, perfectly plastic with a yield limit σ_y. The analysis of the void growth is similar to the one performed by Rice and Tracey [Rice 69]. The equation of the yield surface Φ proposed by Gurson is the following:

$$\Phi \equiv \frac{{\sigma_e}^2}{{\sigma_y}^2} + 2f\cosh\left(\frac{1}{2}\frac{\sigma_{kk}}{\sigma_y}\right) - 1 - f^2 = 0 \tag{3.5}$$

Where σ_e is the von Mises stress and σ_{kk} the trace of the stress tensor.
This expression, valid for the assumption mentioned earlier, was many times modified to extend its range of validity. Some of these extensions are quoted in the Table 3.1.

Ref.	Modification
[Tver 81, Kopl 88, Perr 90]	Improve global accuracy
[Lebl 95]	Improved modelling of strain hardening
[Mear 85, Lebl 95, Helb 98, Bess 03]	Kinematic hardening
[Benz 04b]	Plastic anisotropy
[Golo 93, Pard 00]	Void shape effect
[Perr 00]	Two void populations

Table 3.1: Some extensions of the Gurson's model.

3.1.4 Previous experimental studies on void growth in DP steels

In the eighties, the void growth in DP steels was already imaged using optical micrographs of polished longitudinal sections inside specimens [Szew 82, Su 87, Han 89]. Classical ductile void growth was mainly observed (see Figure 3.2(a)). Kadkhodapour *et al.* [Kadk 11] emphasized that in some cases (elongated martensitic islands) cavities grow as the result of the delamination of ferrite grains (see Figure 3.2(b)). Han and Margolin observed a continuous acceleration of the void growth with the strain [Han 89].

Cavity growth was not often quantified in DP steels. However, the effect of microstructure on void growth was quantitatively investigated by Su and Gurland in [Su 87] and Avramovic-Cingara *et al.* [Avra 09b, Avra 09a]. Su and Gurland showed that a higher volume fraction of martensite led to an increase in the void growth rate. Avramovic-Cingara *et al.* studied the effect of the distribution of the martensitic phase in the two DP microstructures shown in Figure 3.3(a) and 3.3(b). Figure 3.3(c) shows that the cavities present in the homogeneous DP microstructure (DP600B) grow more slowly than the cavities in the microstructure with the martensite banded structure.

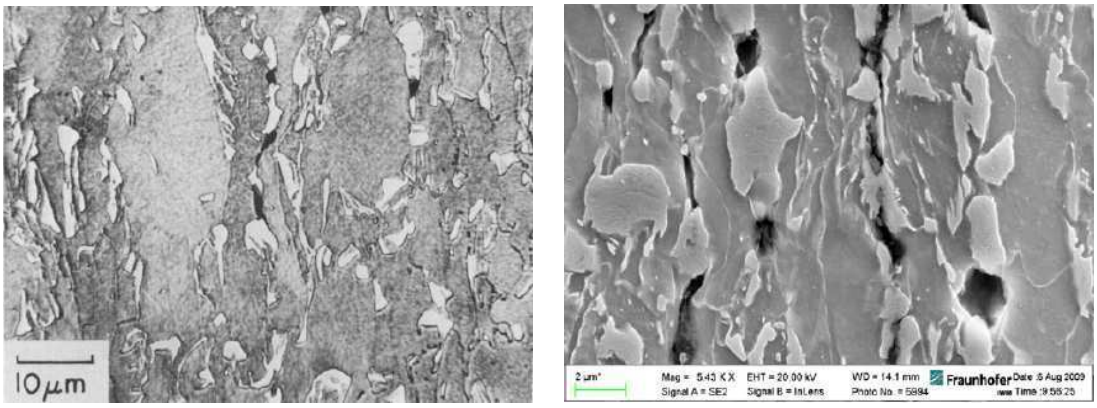

(a) (b)

Figure 3.2: (a)Optical micrograph of etched cross-section inside DP steel specimen, $\varepsilon = 0.89$ [Szew 82]. (b) SEM picture of a fractured DP specimen from [Kadk 11].

Using the recent technique of X-ray tomography, Maire *et al.* performed volume acquisition during *in-situ* tensile tests and quantified in 3D the void growth in DP steels [Mair 08]. They showed that the mean radius calculated over the entire void population remained constant during the tensile test (see Figure 3.4(a)) while the radius of the largest cavities was increasing (see Figure 3.4(b)). The fact that new small nucleating voids was taken into account in the entire population led to this difference in the measurement.

Experimental 3D data from [Mair 08] was also exploited by Ben Bettaieb *et al.* to model the porosity distribution in the DP steel specimens using an advanced coupled approach of the Gurson-Tvergaard-Needleman model [Bett 11]. The result of this numerical simulation, given in Figure 3.5 is in good agreement with the experimental data.

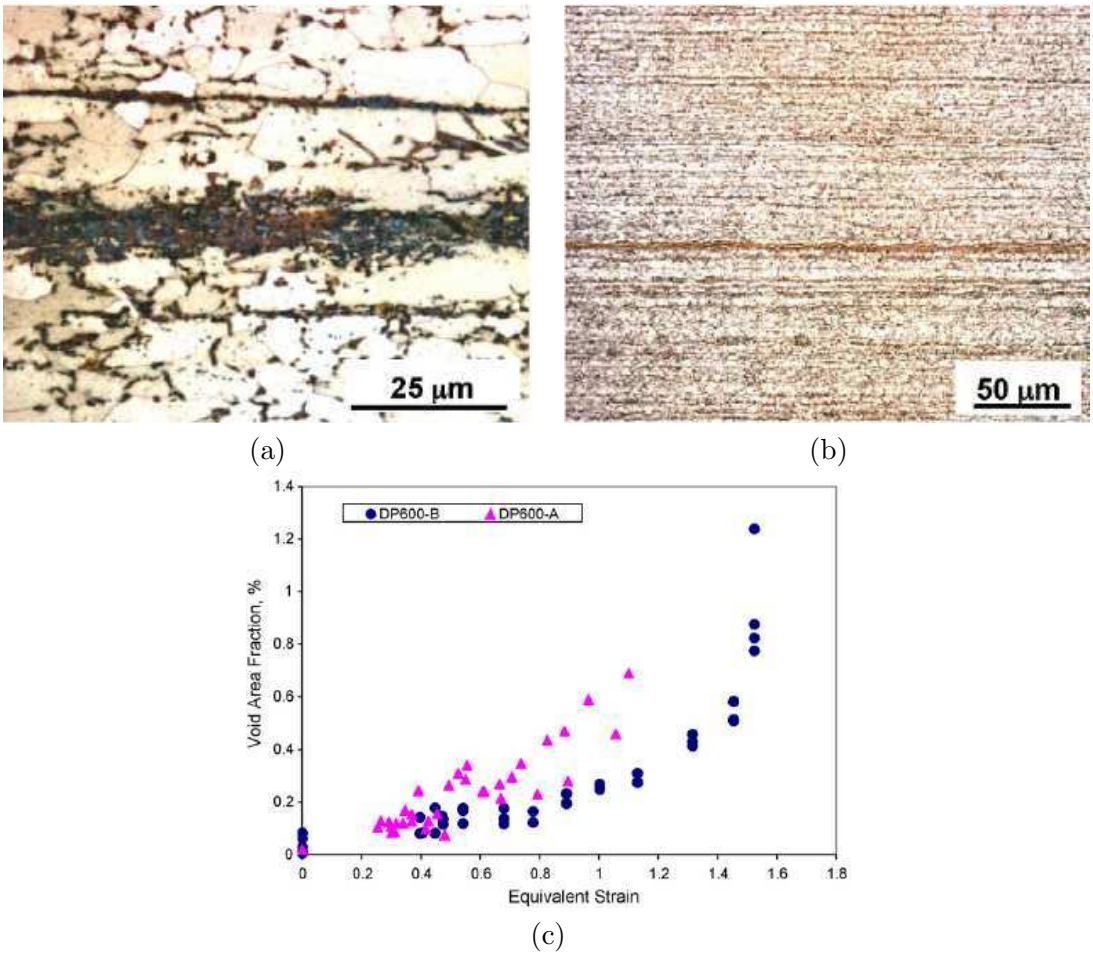

Figure 3.3: (a) DP microstructure of DP600A with a martensite banded structure (martensite is in dark), (b) Homogeneous DP microstructure of DP600B, (c) Void growth comparison in DP600A and DP600B[Avra 09a].

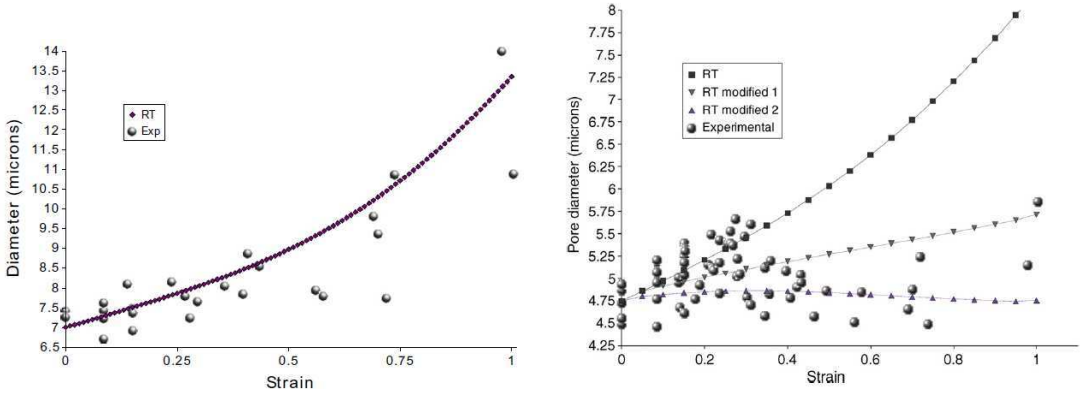

(a) (b)

Figure 3.4: (a) Evolution with the strain of the equivalent diameter of the largest cavities in a DP steel, (b) Evolution with the strain of the equivalent mean radius calculated over the entire void population in the same DP steel [Mair 08].

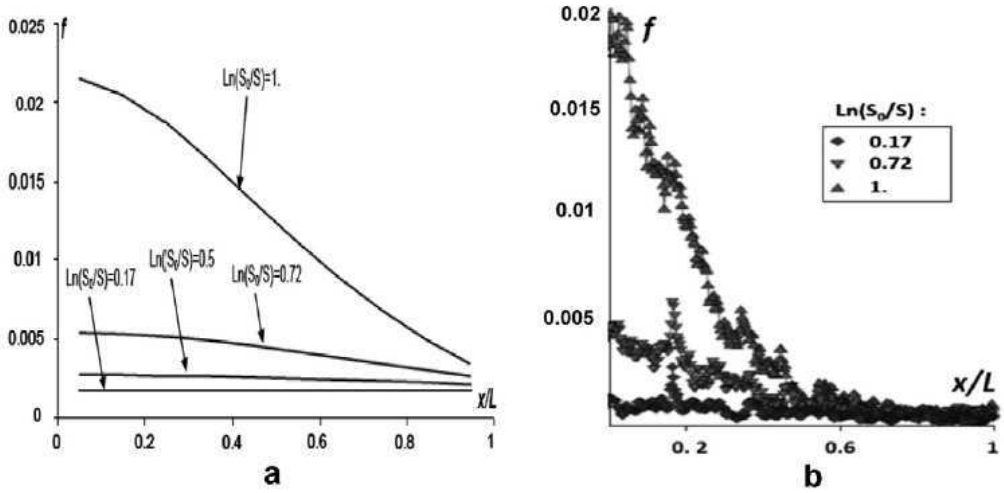

Figure 3.5: (a) Numerical result for the porosity f distribution along the distance from the center of the sample x/L in a DP steel specimen [Bett 11], (b) Experimentally measured distribution of the porosity in a DP steel specimen [Mair 08].

3.2 Void growth characterization

3.2.1 Qualitative observations

The growth of voids nucleating in the studied materials can be observed in 3D following the same cavities at different steps of deformation. The tracked cavities being more easily spotted are among the largest ones. 3D views of a tracked void in the DP11, in the ferritic steel and in the martensitic steel at different strains are respectively given in Figures 3.6, 3.7 and 3.8. These 3D views show that the volume of the voids increases and that the void shape evolves with the applied deformation. In the cases of the DP11 and the ferritic steel, the voids initially seem to be spherical and become more and more prolate with the tensile deformation. In the case of the martensitic steel, the void growth seems to be more isotropic. These tracked cavities being among the largest ones, they are involved in local events of void coalescence at the end of the tensile test as seen at the last step of deformation for the DP11 and the martensitic steel.

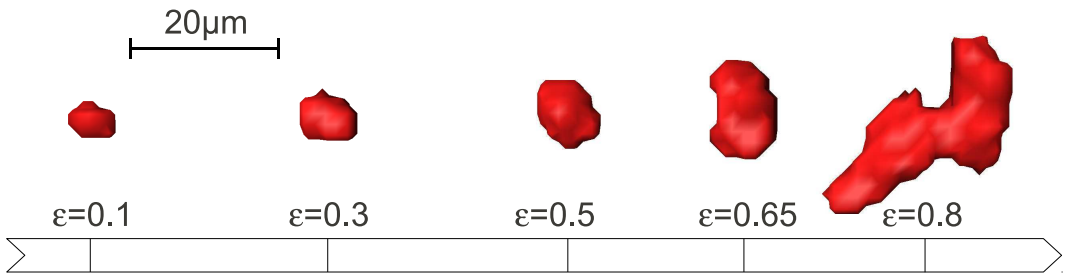

Figure 3.6: 3D visualization of the same cavity at different steps of deformation in the DP11 smooth sample.

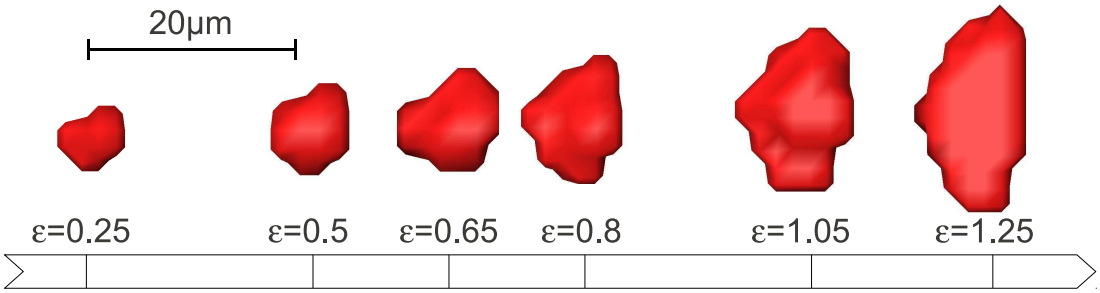

Figure 3.7: 3D visualization of the same cavity at different steps of deformation in the ferritic steel.

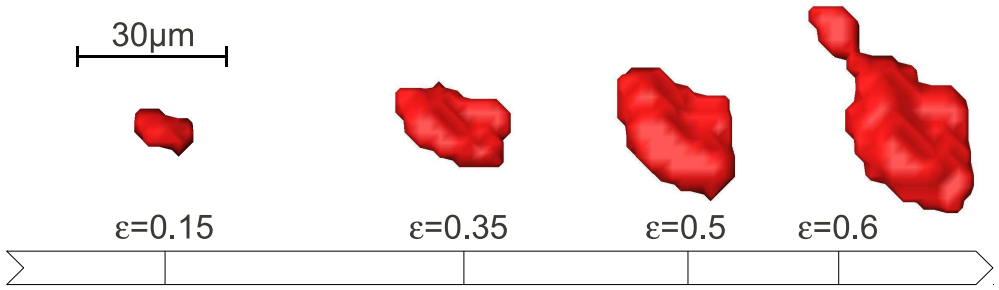

Figure 3.8: 3D visualization of the same cavity at different steps of deformation in the martensitic steel.

3.2.2 Quantification of void growth

3.2.2.1 Measurement of the equivalent diameter

The number of voxels composing each detected cavity is used to calculate the equivalent diameter assuming that voids have a spherical shape. The absolute error on this measurement is constant (of the order of one voxel). As a consequence, the relative error on the measurement of the dimensions depends on the dimensions themselves: it is rather large (100%) when the cavities nucleate (due to the very small size of nucleated cavities) but then it quickly becomes negligible when the cavities grow.
Tracking cavities from one strain step to the next proved to be extremely tedious. It can be achieved automatically when the number of objects is constant. This has been used in [Toda 11, Dzie 11]. In the sub-volume studied in this work, the number of objects to track is constantly changing. Tracking was manually performed but for a few number of selected cavities for one sample of DP11, ferritic steel and martensitic steel. These selected cavities were easier to track than others because these were among the largest in the sub-volume.
Another strategy was then adopted to quantify growth more easily and more extensively for all the samples. The measurement of the size of the N largest cavities of a population is straightforward [Mair 08]. It can be a good measurement of the void growth if these N largest cavities remain the same at each deformation step. This was quantified in the present study, for $N = 20$ and $N = 50$ and this was compared with the evolution of the average diameter of the entire population and with the previously mentioned measurement of the three manually tracked particles. Results for the three investigated steels are plotted in Figure 3.9.

Regarding these results, the following remarks can be done:

- The evolution of the diameter being the closest to the growth measured on single large pores is obtained when using the 20 largest cavities. This is numerically confirmed using the Rice and Tracey model in Section 3.3.1.1.

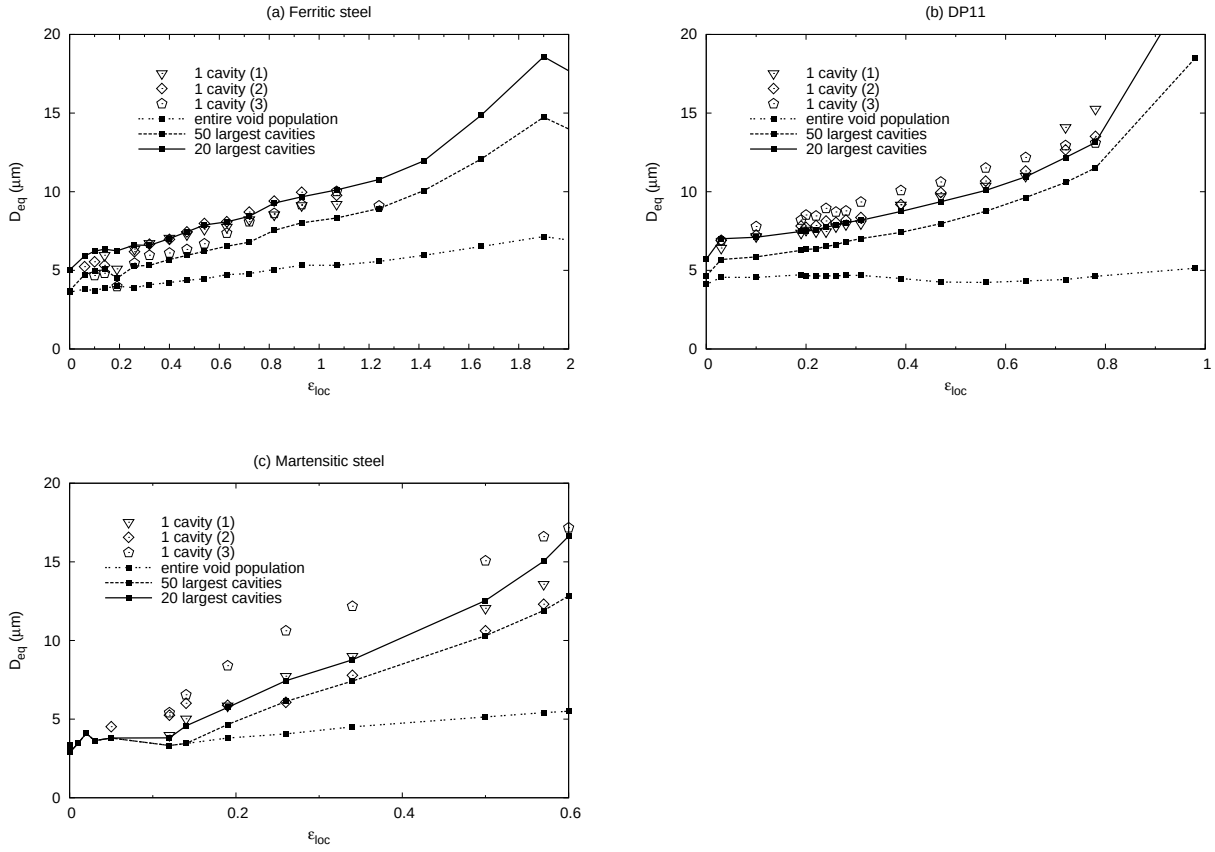

Figure 3.9: Evolution of the average equivalent void diameter for different numbers of examined cavities : 1, the 20 largest, the 50 largest, and the entire population.

- The mean equivalent diameter calculated using the entire population remains almost constant in these steels because of the nucleation of new porosities (this has already been measured and explained for DP steels in [Mair 08]).

- A void growth acceleration is observed close to the end of the tensile test. It is due to void coalescence occurring close to the fracture of the sample. A local coalescence event between two cavities is for example qualitatively observable in Figures 3.6 and 3.8.

This experimental strategy has thus been used to characterize the void growth in all the studied steels (see Figure 3.10). This figure shows that the kinetic of void growth is really different from one microstructure to another as previously observed in the literature [Su 87, Avra 09a]. Note that the tempering induces a deceleration of the void extension in the DP11.

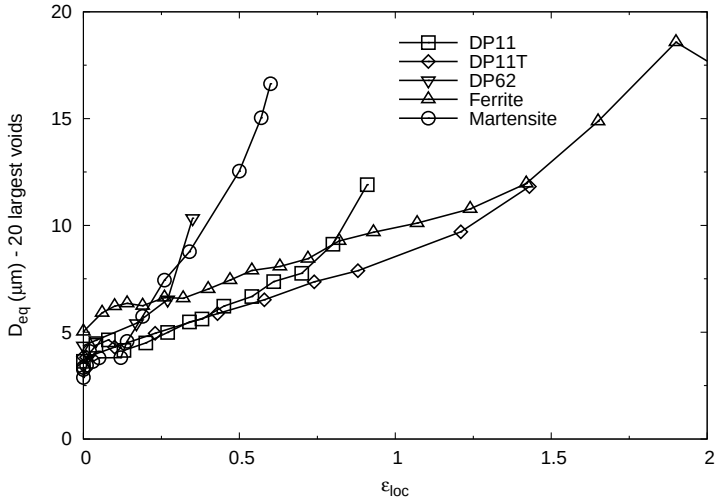

Figure 3.10: Evolution of the average equivalent void diameter over the 20 largest cavities in the studied steels.

The use of specimens with several notches allowed the study of the effect of the triaxiality on the void growth. As expected, Figure 3.11 shows for the case of the cases of the DP11, the ferritic steel and the martensitic steel that a higher triaxiality induces a higher void growth.

3.2.2.2 Characterization of the void shape evolution

As seen on Figures 3.6 and 3.7, voids are initially isotropic but become more elongated in the tensile direction when tensile deformation is applied. To assess this shape change, cavity dimensions of the twenty largest cavities in the tensile direction $D_{tensile}$ and

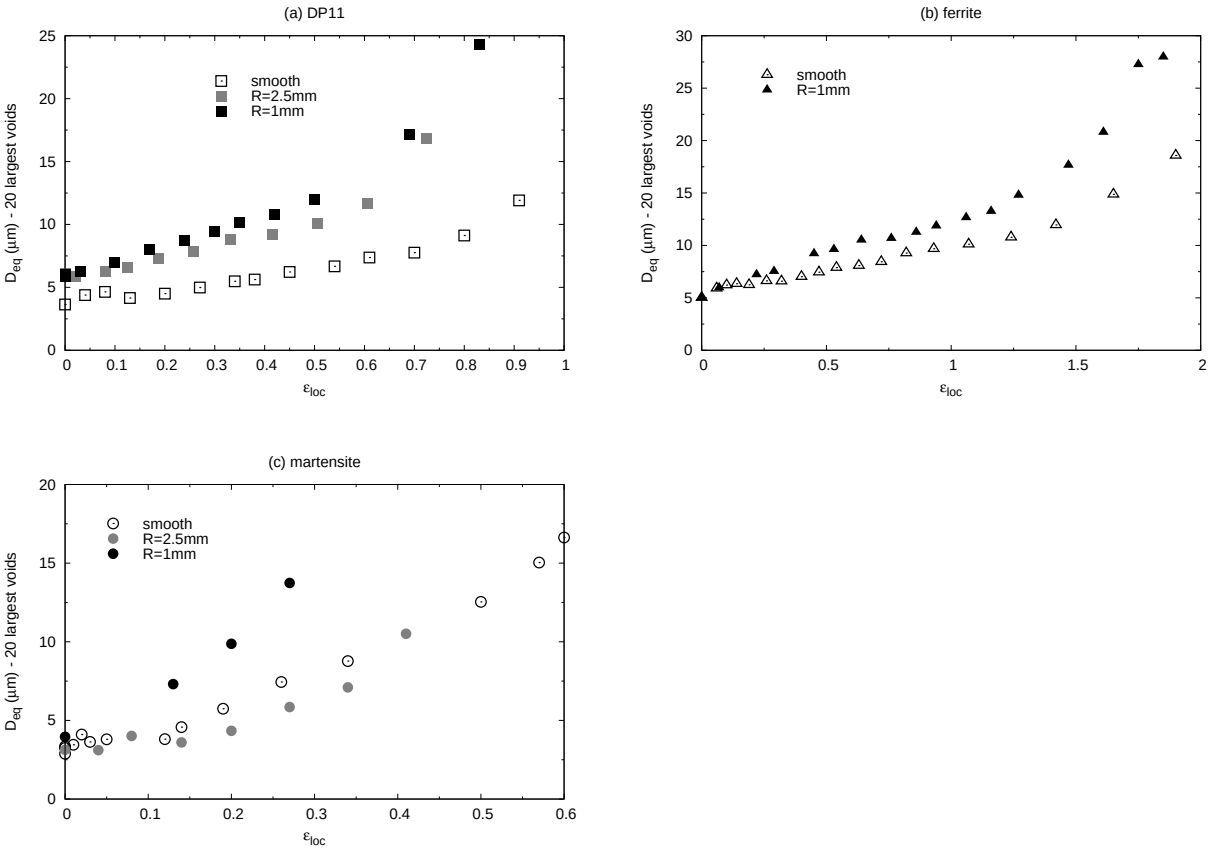

Figure 3.11: Triaxiality effect on the void growth in the DP11 steel, the ferritic steel and the martensitic steel.

transversal direction D_{trans} were also measured and used to calculate the void aspect ratio W:

$$W = \frac{D_{tensile}}{D_{trans}} \tag{3.6}$$

The evolution of W is plotted in Figure 3.12 for the five studied steels. Whatever the steel, voids are initially rather spherical. In the cases of the DP steels and the ferrite specimens, cavities become more and more elongated while voids in the martensite sample remain slightly oblate during the entire tensile deformation.

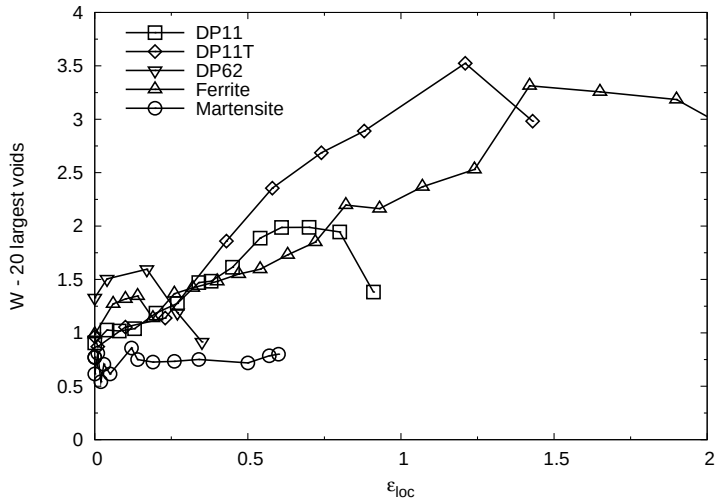

Figure 3.12: Evolution of the void aspect in the studied steels.

Figure 3.13 shows that the triaxiality seems to only affect weakly the evolution of the void shape, voids mainly growing in the tensile direction and W goes from 1 to 2 in 0.5 of strain.

3.2.3 Effect of the voxel size on the void growth characterization

As already observed in Figure 3.9, the mean diameter measured over the entire population, given in Figure 3.14, remains constant during the tensile test. At high resolution, the mean diameter is obviously lower than at low resolution because smallest cavities were taken into account in the average. On the contrary, concerning the growth of the twenty largest cavities, no difference can be seen. The low resolution is then sufficient to investigate the void growth in DP steels.

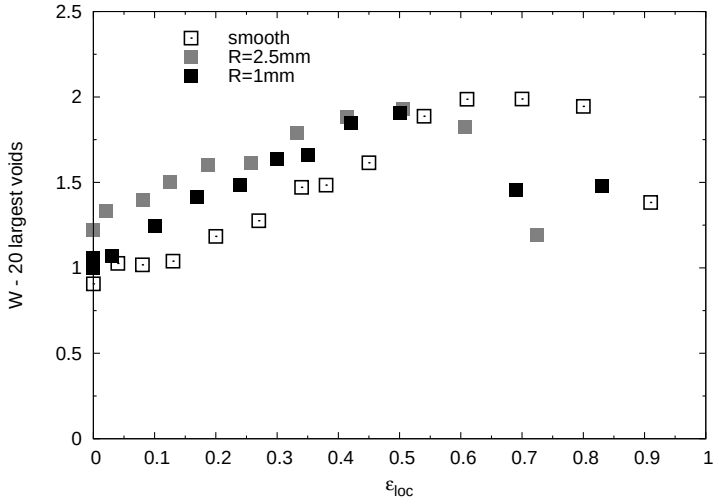

Figure 3.13: Triaxiality effect on the void aspect ratio in DP11 steel.

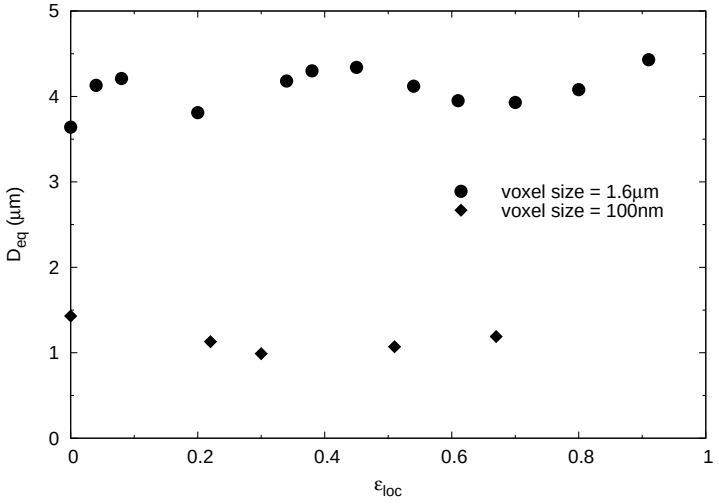

Figure 3.14: Resolution effect on the mean equivalent diameter of the entire void population in the DP11 sample.

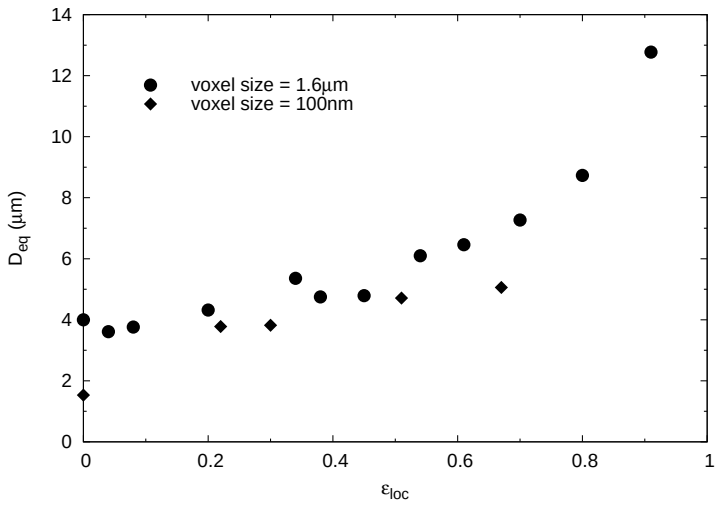

Figure 3.15: Resolution effect on the mean equivalent diameter of the 20 largest cavities in DP11 smooth sample.

3.3 Void growth prediction

3.3.1 Prediction of the equivalent diameter

3.3.1.1 Using the Rice and Tracey's model

The expression of the Rice and Tracey (RT) model [Rice 69] presented in Section 3.1.3.1 and given in equation 3.1 was employed to fit our experimental results. The used values of T and ε were the ones experimentally measured in Appendix A.

$$\frac{dR}{R} = \alpha_{RT} \exp\left(\frac{3}{2}T\right) d\varepsilon \tag{3.7}$$

The RT model was first tested on the DP11 sample on the diameters measured by tracking single cavities, on the diameter of the twenty largest and on the diameter of the fifty largest. A simple fit using equation 3.1 led to a discrepancy between the measured and calculated evolution of R in our studied cases. Thus, we applied a more pragmatic approach where the value of the pre-exponential term α_{RT} is not pre-calculated. This method has already been used in [Pard 98b, Stra 03, Kuma 09, Takt 09]. Table 3.2 gives the values of the α_{RT} parameter required to fit the RT model on the different experimental data measured in the DP11 steel. The same values were found for single cavities, for the 20 largest cavities and for the 50 largest cavities. This confirms that to quantify the void growth using the equivalent diameter of the N largest cavities (N=20 in our case) present in the studied sub-volume is relevant for quantifying the growth phase.

	cavity (1)	cavity (2)	cavity (3)	20 largest	50 largest
α_{RT}	0.5	0.47	0.47	0.47	0.47

Table 3.2: Values of the α_{RT} parameter required to fit the RT model on experimental data measured in the DP11 steel from 1 cavity, the 20 largest ones or the fifty largest one.

The experimental data measured from the 20 largest cavities in the ferritic steel, the martensitic steel and the DP11 with the different initial triaxiality states were then fitted with the RT model of equation 3.7 by changing the value of α_{RT}. The results of this fitting procedure are given in Table 3.3. It is shown that whatever the material, the values of the constant α_{RT} required to fit the experimental values are not equal to the initial value found by Rice and Tracey and values differ for each material and for each specimen geometry (except for the ferrite samples).

	Ferrite	DP11	Martensite
Smooth specimen	0.20	0.47	1.3
Notched specimen R=2.5mm	-	0.50	1.4
Notched specimen R=1mm	0.20	0.52	1.5

Table 3.3: Values of the α_{RT} parameter required to fit the model on experimental data.

3.3.1.2 Using the Huang's model

Validation of the Huang's correction of the RT model

The expression found by Rice and Tracey was later re-assessed by Huang using additional velocity fields [Huan 91]. Huang retrieved the same result but with the pre-exponential term depending on the triaxiality for $T < 1$. The same previous approach was used to fit experimental results:

$$\frac{dR}{R} = \alpha_{Huang} T^{0.25} \exp\left(\frac{3}{2}T\right) d\varepsilon \tag{3.8}$$

The results of the fit are given in Table 3.4. As previously observed, the values of the constant α required to fit the experimental values are not equal to the initial value $\alpha_{Huang} = 0.427$ initially calculated by Huang. However, in the case of the Huang's correction of the model, values differ only for each material but remain the same whatever the sample geometry. It is then demonstrated that the Huang's correction improves the RT model by capturing the effect of triaxiality induced by the change in the specimens geometries. Huang's predictions are plotted in Figure 3.16 in comparison with the equivalent experimental measurements and the RT predictions. The Huang's model is then used to predict the void growth of all the studied steels.

	Ferrite	DP11	Martensite
Smooth specimen	0.22	0.55	1.6
Notched specimen R=2.5mm	-	0.55	1.6
Notched specimen R=1mm	0.22	0.55	1.6

Table 3.4: Values of α_{Huang} parameters required to fit the model on experimental data.

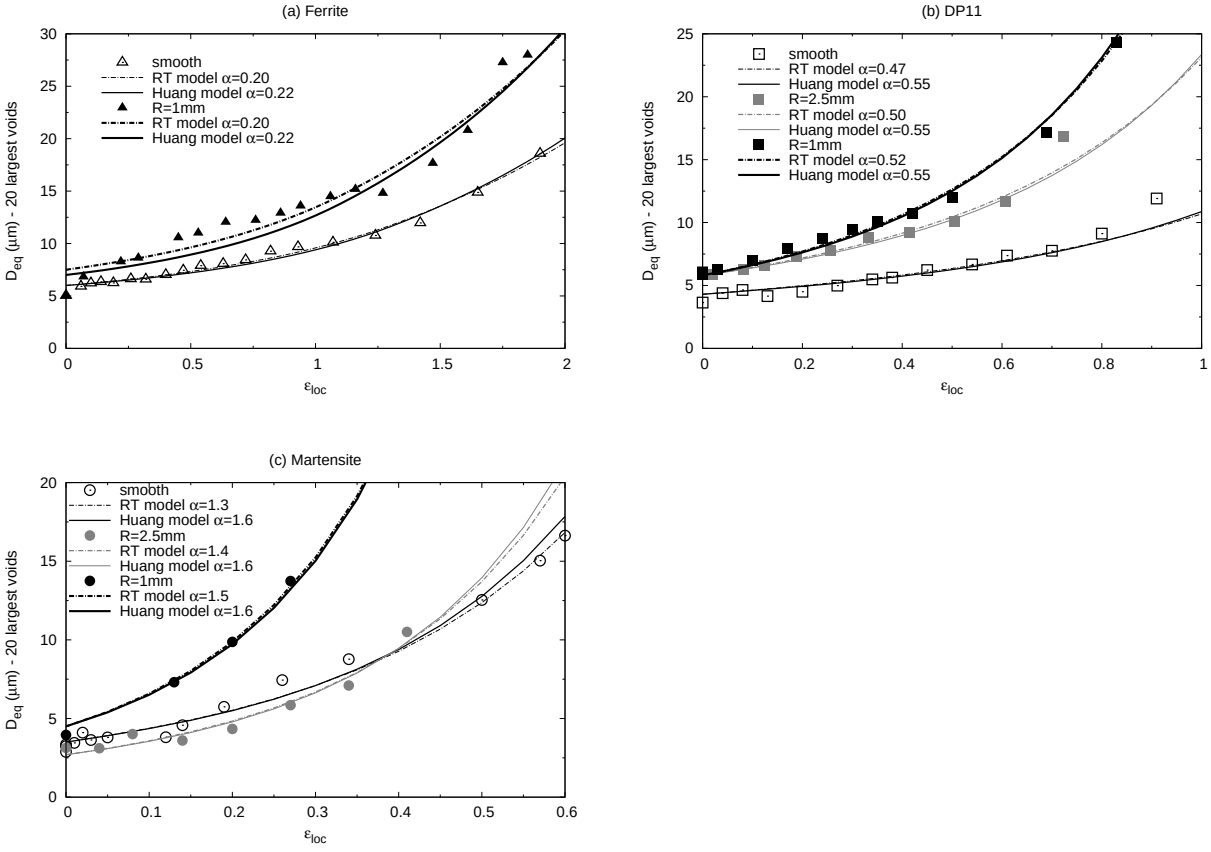

Figure 3.16: Comparison of the predictions of the RT model and the Huang's model and the experimental evolution of the mean diameter of the twenty largest cavities.

Void growth prediction in the studied steels

The Huang's prediction from equation 3.8 was then used to model the growth of cavities in all the smooth specimens of the different studied steels using the pre-exponential term as a fitting parameter. As previously observed, each steel exhibits a different value of α_{Huang}. These values are given in Table 3.5 and the result of the fit is given in Figure 3.17

Steel	α_{Huang}
Ferrite	0.22
DP11	0.55
DP11T	0.45
DP62	1.2
Martensite	1.6

Table 3.5: Values of α_{Huang} parameters required to fit the model on experimental data.

3.3.2 Microstructure influence on the void growth

The differences between the values found for the studied steels and the one initially proposed by Huang can be explained. The underlying assumptions of the Huang's correction are the same that ones of the RT model [Rice 69, Huan 91]. These models predict the isotropic growth of an initially spherical void in a infinite and perfectly plastic matrix. These assumptions was not respected in the investigated materials.

- In the ferritic steel the α_{Huang} value is found to be lower than the theoretical one. The most probable cause is strain hardening, which is not included in the model. The effect of isotropic strain hardening on void growth has already been studied [Pard 98b, Trac 71, Budi 82] where it was shown that strain hardening reduces the void expansion rate.

- In the various DP steels and the fully martensitic steel, a part of strain hardening is kinematic hardening [Cobo 08]. Compared to the isotropic hardening effect, several studies about the kinematic strain hardening [Bess 03, Li 02] show the opposite effect *i.e.* kinematic strain hardening induces a void growth acceleration.

- Other assumptions can be made concerning the higher values of α_{Huang} in the DP steels. First with the void density being higher in DP steels, cavities are closer to one another. Consequently, each cavity undergoes more interactions with its neighbors. Void interaction is another reason for a faster growth [Mari 84, Mari 85]. Furthermore, the martensitic islands prevent the pores from growing in the transverse direction, which is not the case in the ferritic steel samples. Cavities then tend to grow faster in this constrained environment, as shown numerically in [Stau 98].

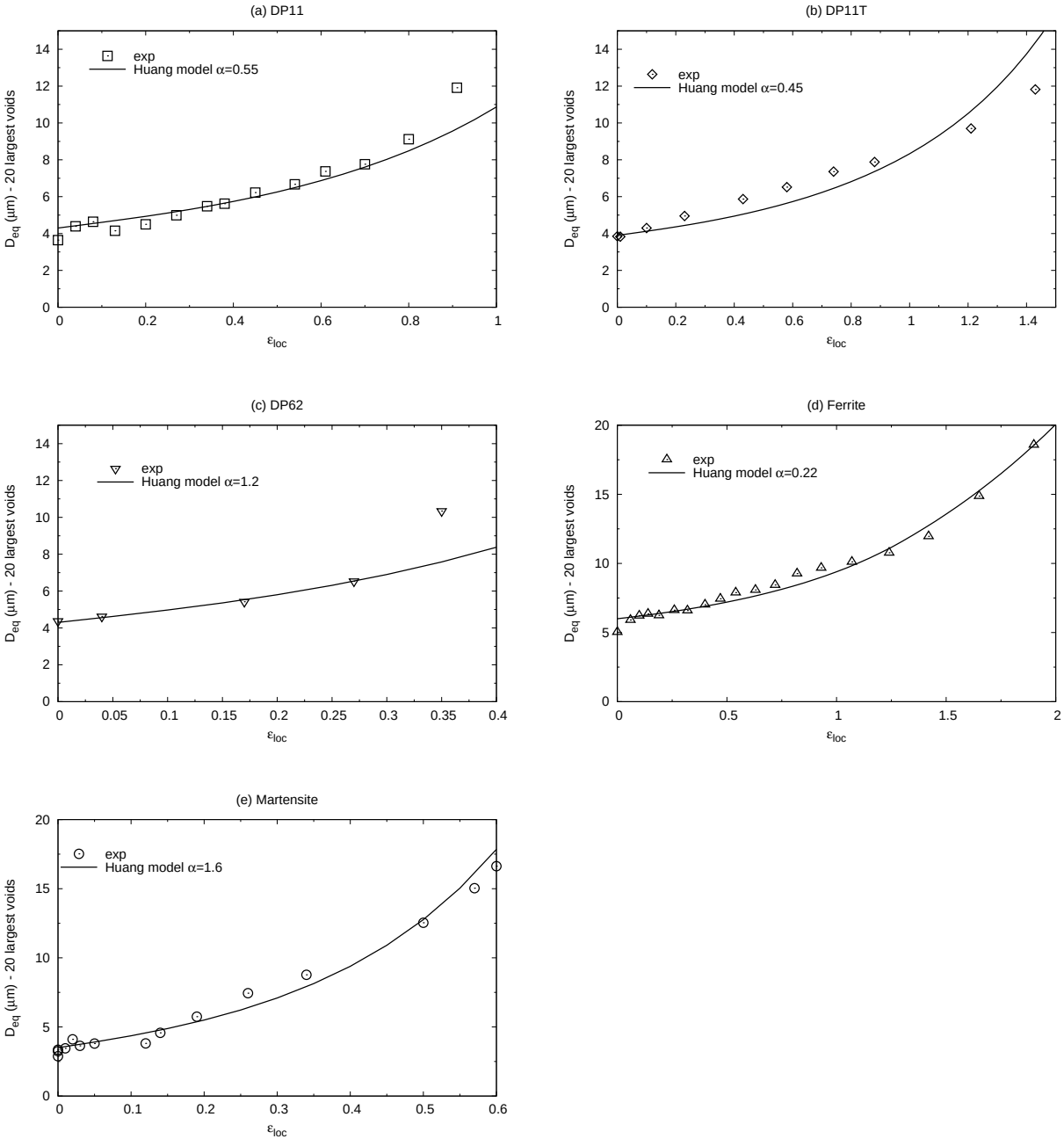

Figure 3.17: Comparison of the experimental data and the Huang prediction of the void growth in the studied steels.

- The initial void shape can also be responsible for a faster void growth. In the martensitic steel, nucleated cavities tend to be more oblate and have the form of microcracks. An aspect ratio of about 0.6 was incidentally measured in Figure 3.12. It has been demonstrated that for geometrical reasons, such a shape leads to a faster void growth [Lass 06].

- The effect of the tempering on the DP microscructure is experimentally observed here: the tempering tends to slow down the void growth. A possible reason to this growth deceleration could be the lower void density inducing less voids interactions.

3.3.3 Relationship between the matrix strength and void growth rate

The models of Rice and Tracey and Huang do not involve the matrix strength. However, we observe that the higher the measured strength in the steels, the higher the value of α_{Huang}. For each studied steel, the experimental curves σ_{eq} vs ε_{loc} were fitted using a traditional power law involving the parameters k_σ and n:

$$\sigma_{eq} = k_\sigma {\varepsilon_{loc}}^n \tag{3.9}$$

Figure 3.18 shows the result of these fits for each studied steel and the determined values of the parameters n and k_σ are given in Table 3.6.

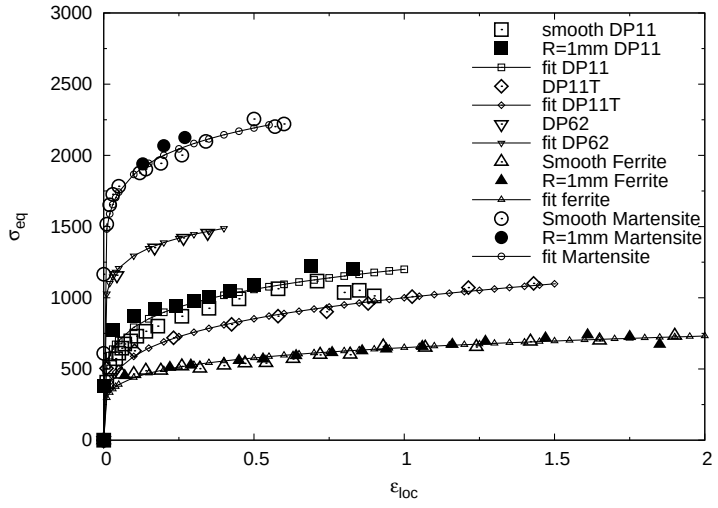

Figure 3.18: σ_{eq} vs ε_{loc} curves for all studied steels.

Referring to equation (3.9), k_σ is representative of the strength of the material. Figure 3.19 shows the evolution of α_{Huang} with k_σ. A linear increase of α_{Huang} is observed with k_σ. The equation of the fitting curve is the following:

$$\alpha_{Huang} = 8.510^{-4} k_\sigma - 0.38 \tag{3.10}$$

Steel	k_σ	n
Ferrite	650	0.17
DP11	1200	0.18
DP11T	1000	0.23
DP62	1630	0.1
Martensite	2350	0.1

Table 3.6: Fitted values of n and k_σ.

This observation is so far rather empirical and we still have no explanation for this linear relationship.

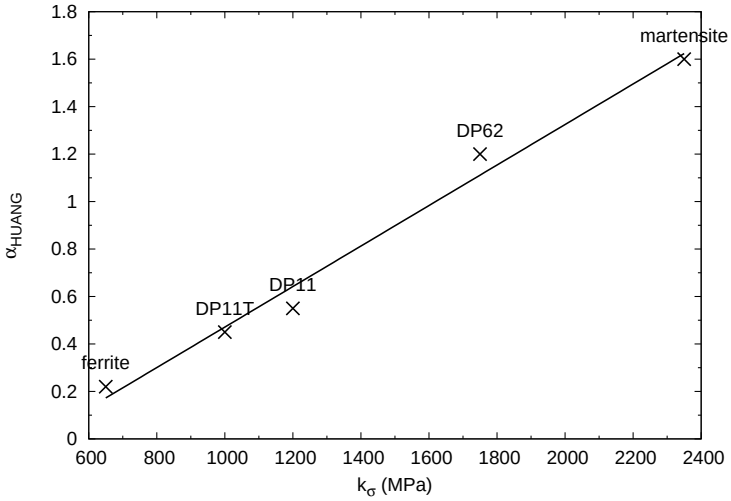

Figure 3.19: Linear relationship between α_{Huang} and k_σ.

3.3.4 Prediction of the shape evolution

As mentioned in Section 3.2.2.2, cavities in DP steels and in ferrite tend to evolve into a more ellipsoidal shape, as opposed to cavities in martensite which remain roughly spherical during the tensile deformation. This modification in the void shape can be taken into account in the modeling using the general analysis of RT [Rice 69, Thom 90] presented in Section 3.1.3.1. This model involves the deformation in the directions perpendicular to the tensile direction ε_{trans}. As mentioned in Appendix A, we have:

$$\varepsilon_{trans} = -\frac{\varepsilon_{loc}}{2} \tag{3.11}$$

Using the Huang's expression of the void growth rate given in Eq.(3.8) and Eq.(3.3), the rate change of the void radii in the tensile and in the transversal direction can be

expressed as:

$$\begin{aligned}\frac{dR_{tensile}}{R} &= \alpha_{Huang} T^{0.25} \exp\left(\frac{3}{2}T\right) d\varepsilon_{loc} + (1+E_V)\, d\varepsilon_{loc} \\ \frac{dR_{trans}}{R} &= \alpha_{Huang} T^{0.25} \exp\left(\frac{3}{2}T\right) d\varepsilon_{loc} - \frac{1}{2}(1+E_V)\, d\varepsilon_{loc}\end{aligned} \tag{3.12}$$

Equation (3.12) was used to predict the void shape change during tensile deformation in the studied materials. The values of α_{Huang} previously determined were used for each steel and the parameter $1+E_V$, assumed to be constant, was taken as a fitting parameter. The predicted evolutions of the void dimensions in the tensile direction and in the transversal direction obtained using this approach are compared to the experimental data in Figure 3.20 and the values of the parameter $1+E_V$ used for the fit are given in Table 3.7. Note that, in every cases, $1+E_V$ is found to be quite smaller than the 1.6667 predicted by the theory, indicating that cavities tend to be less prolate in these steels than in a non-hardening matrix. These experimental observations are in disagreement with numerical results from [Wors 90, Raga 04, Pard 06] which conclude that a higher isotopic strain hardening capacity leads to more prolate cavities.

The values of $1+E_V$ found for the DP steels and the ferritic steel were close to be the same. That can be explained by the fact that in the DP steels, void growth occurs mainly in the soft phase, *i.e.* the ferrite, as numerically shown in [Li 02]. The slight difference might be due to the presence of martensite islands. As mentioned before, the martensite islands prevent the cavities from growing in the transversal direction leading therefore to more prolate voids and inducing a higher value of in the case of the DP steel. In the fully martensitic sample where the cavities remain rather isotropic, $1+E_V$ is found to be equal to 0. Testing this model on specimens with different notches (smooth and R=1mm), we have experimentally seen here that triaxiality does not affect the parameter $1+E_V$.

Steel	$1+E_V$
DP11	1
DP11T	1
DP62	1
Ferrite	0.8
Martensite	0

Table 3.7: Values of $1+E_V$ parameters required to fit the model on experimental data.

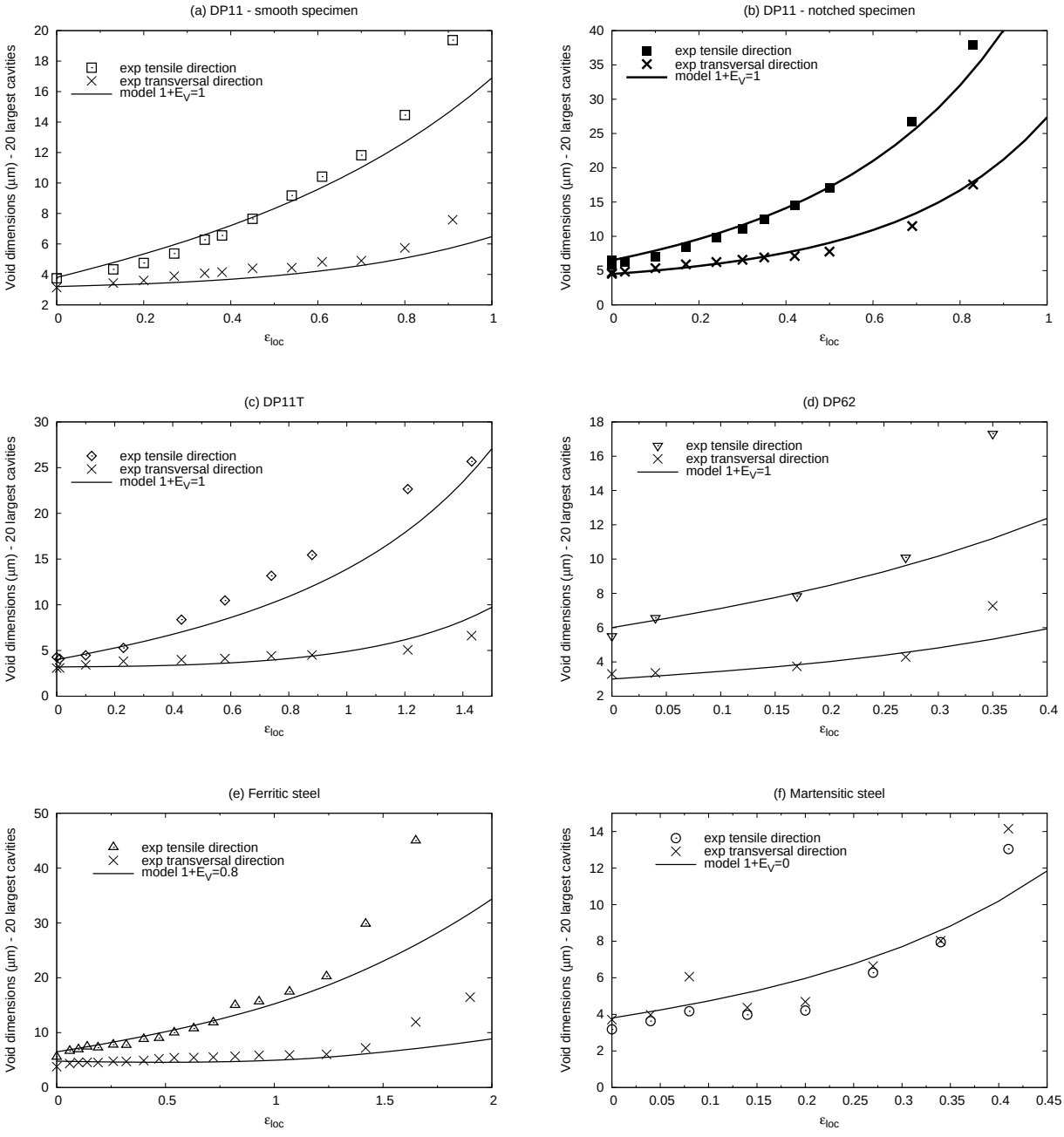

Figure 3.20: Comparison of the prediction of the Huang's model accounting for shape change and the evolution of the dimensions in the tensile and transversal directions of the twenty largest cavities measured in the studied steels.

3.3.5 Prediction of the mean equivalent diameter accounting for void nucleation

As already observed in [Mair 08], the mean equivalent diameter measured over the entire population remains almost constant in DP steels because of the nucleation of new porosities. In this paper, a correction of the RT model was proposed by Bouaziz [Mair 08] to take into account the new nucleating voids:

$$\frac{d\bar{R}}{d\varepsilon} = \frac{dR}{d\varepsilon} + \frac{1}{N}\frac{dN}{d\varepsilon}\left(\bar{R} - R^{\star}\right) \tag{3.13}$$

where $\bar{R}$ is the mean equivalent radius of the void population, N is the void density and $R^{\star}$ is the nucleating radius.

As it has been shown in a preceding section that the Huang's expression of the RT model is more relevant than the RT expression, the Bouaziz's correction is applied here on the Huang's model from eq.(3.8):

$$\frac{d\bar{R}}{d\varepsilon} = \alpha_{Huang} T^{0.25} \exp\left(\frac{3}{2}T\right)\bar{R} + \frac{1}{N}\frac{dN}{d\varepsilon}\left(\bar{R} - R^{\star}\right) \tag{3.14}$$

This analytical approach simply takes into account the density of nucleating voids $\frac{dN}{d\varepsilon}$ assuming to have a radius $R^{\star}$. This expression is applied using the experimentally measured void density N and the values of α_{Huang} previously determined and given in Table 3.5. $R^{\star}$ is chosen to be around 2µm because this is the radius of the smallest detected cavities on the volumes acquired with a voxle size of 1.6µm. The predictions given by the corrected Huang's model are compared to the experimental measurements of the mean equivalent diameter in the studied steels in Figure 3.21. A good agreement between the experimental data and this simple modeling is found whatever the material.

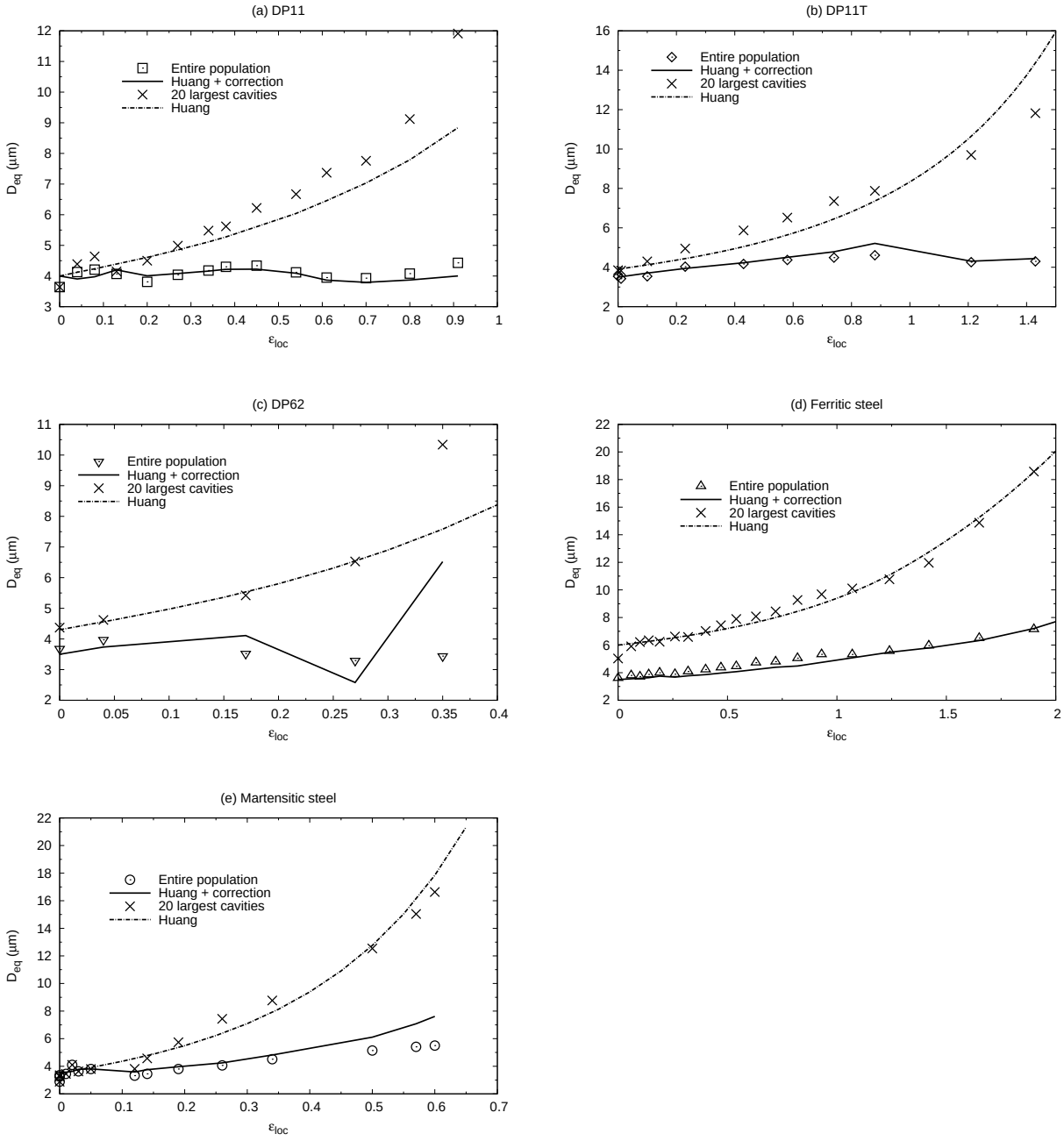

Figure 3.21: Comparison of the prediction of the Bouaziz correction applied to the Huang's model and the evolution of the mean equivalent diameter measured over the entire void population in the studied steels.

3.4 Summary

In this chapter, the growth step of ductile damage process was characterized using tomography data. The evolution of the volume and the shape of the cavities were quantified and this quantitative data on void growth was then used to validate some void growth models. The main outcomes of this work are:

→ By the comparison with careful manual single void measurements, we have shown that the study of the mean diameter of the twenty largest pores in the population gives an accurate measurement of the growth of single voids.

→ Accounting for the triaxiality in the initially constant α_{RT} parameter is a real improvement of this void growth model, thus validating the Huang's correction of the Rice and Tracey's model.

→ The growth kinetics are impacted by the steel microstructure and mechanical behaviors (flow stress and strain hardening mechanisms). In particular, the higher the flow stress, the faster the growth of cavities.

Chapter 4

Void coalescence

The third step of ductile damage leading to the final fracture of the materials is characterized in this chapter. Void coalescence starts when the deformation is localized within the ligament of material between cavities located in the most critical region of the sample. Although void coalescence controls the ductility of material, this is the less investigated step of damage because of the experimental difficulties to observe it. Using X-ray tomography characterization, new quantitative data related to the void coalescence is now available and can help for a better understanding of this final step of ductile damage.

4.1 Literature review

4.1.1 Experimental evidences

Due to the difficulty to experimentally capture coalescence events, few experimental results are available in the literature. Some qualitative images were obtained using metallographical cross-section of deformed specimens (*e.g.* see Figures 4.1 and 4.2). Void coalescence was more easily observed in systems in which holes are drilled into plates (see [Dube 87, Magn 88]. In the recent work of Weck *et al.* [Weck 07, Weck 08c, Weck 08a]), *in-situ* tensile tests were carried out on laser drilled plates with different configurations of voids (holes oriented at 90°as imaged in Figure 4.3 (a), (b) and (d) or at 45 °as imaged in Figure 4.3(c))

These experimental observations leads to three modes of coalescence. They are illustrated in Figure 4.3.

- The first one named internal necking consists in the shrinkage of the ligament between the two voids with a typical shape of a necking process [Thom 87]. This mode of coalescence is observed on Figures 4.1, 4.3(a) and (b). During this coalescence process, the voids evolve towards a diamond shape.
- The second mode of coalescence is a shear localization. Weck and Wilkinson observed it in model materials when closest voids are located at 45°[Weck 08a] (see

Figure 4.1: Internal necking in the central region of an as-rolled copper tensile specimen. ×300 [Putt 59].

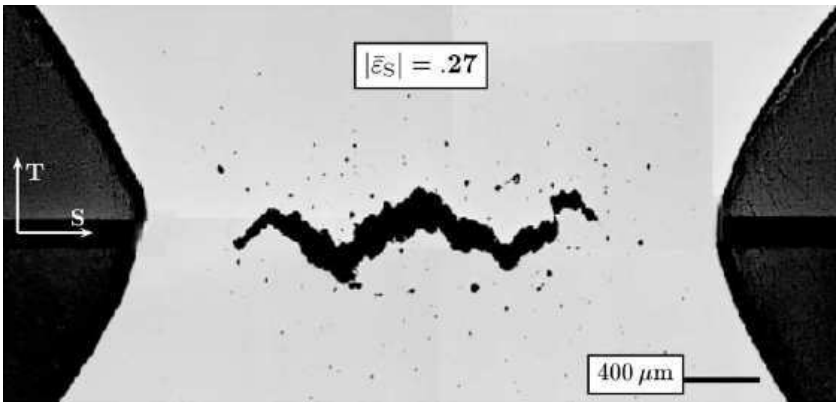

Figure 4.2: Crack growth in round notched bars [Benz 04a].

Figure 4.3(c)).

- The last mode of coalescence is rarely observed. Necklace coalescence consists in the localization of the coalescence in a direction parallel to the main loading axis. It was observed by Pardoen [Pard 98a] in copper containing long clusters of oxyde particles where voids nucleated and Benzerga [Benz 00] in steels (see illustration given in Figure 4.3(d)).

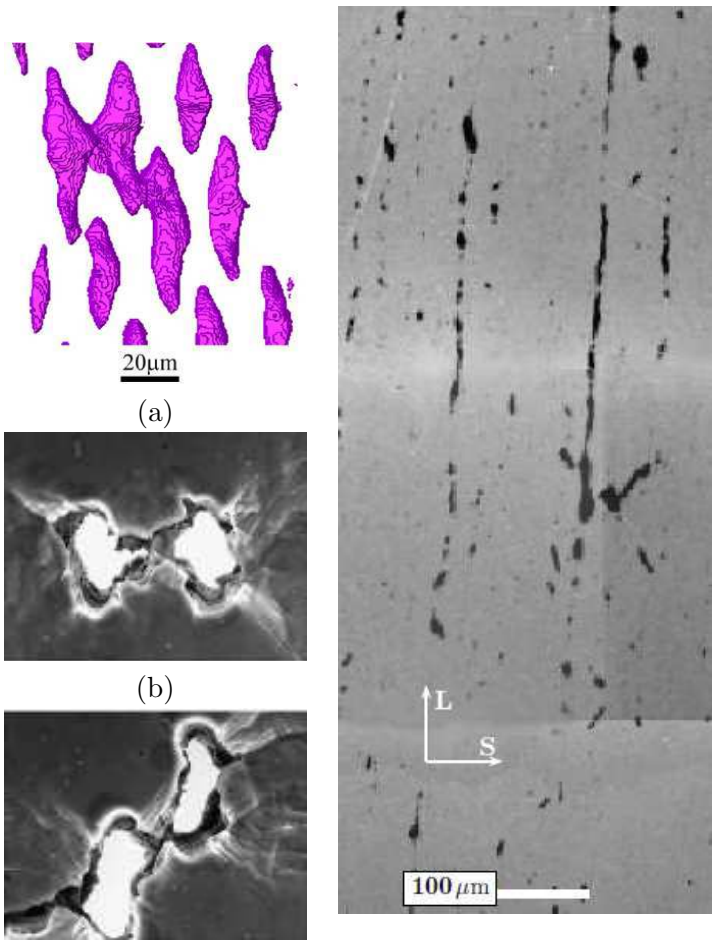

Figure 4.3: Illustration of the three modes of coalescence: (a) coalescence by internal necking (X-ray tomography) [Weck 08c] (b) coalescence by internal necking (SEM observation) [Weck 08a] (c) coalescence by shear localization (SEM observation) [Weck 08a] (d) necklace coalescence (optical metallography) [Benz 00].

4.1.2 Void cell simulations

Because of the difficulty of capturing experimentally void coalescence, quantitative information on void coalescence was often numerically obtained using void cell simulations as the one presented in Figure 4.4. In general, the geometry of the unit cell is characterized by the void volume fraction f, the void aspect ratio W and the cell aspect ration λ. These simulations allowed a better understanding of the parameter influencing coalescence such as the triaxiality or the mechanical properties of the matrix material. Many void coalescence criteria were developed using void cell simulations.

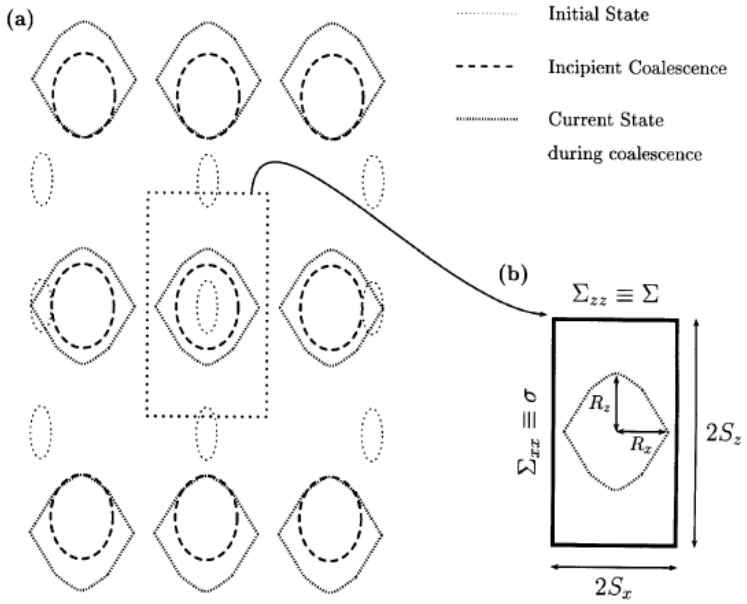

Figure 4.4: (a) Schematic representation of void cell simulations, (b) representative volume element during coalescence [Benz 02].

A pioneering piece of work was performed in this field by Koplik and Needleman [Kopl 88]. These authors studied the effects of the triaxility, of the initial porosity, of the initial void shape ratio, of the initial void spacing ratio and of the strain hardening exponent on void growth and void coalescence using cell simulations.

4.1.3 Void coalescence criteria

A review of the main void coalescence criteria given in Table 4.1 was proposed by Weck in his PhD work [Weck 07]. The Brown and Embury criterion and the Thomason criterion along with their respective improvements are detailed hereafter. These both criteria are later implemented in the present work.

Author	Criteria	Limitations
McClintock [McCl 68]	Hole impingement	Cylindrical holes No interaction between holes No localization
Brown and Embury [Brow 73]	Void length equals intervoid spacing	For regular array of voids No Hydrostatic component No material properties
Tvergaard and Needleman [Tver 84]	Critical porosity and acceleration factor	Model rely on arbitrary parameters No hole geometry (average)
Thomason [Thom 90]	Plastic limit load	No microshear localization possible Only for non-hardening materials
Gammage [Gamm 04]	Stress equals global work hardening rate	Local work hardening = Global work hardening rate

Table 4.1: Coalescence models developed in literature [Weck 07].

The void configuration of most of the coalescence criteria is given in Figure 4.5. Non-dimensional geometrical parameters involved in the criteria are:

- the void aspect ratio $W = \frac{R_z}{R_x}$
- the relative intervoid space $\chi = \frac{R_x}{L_x}$

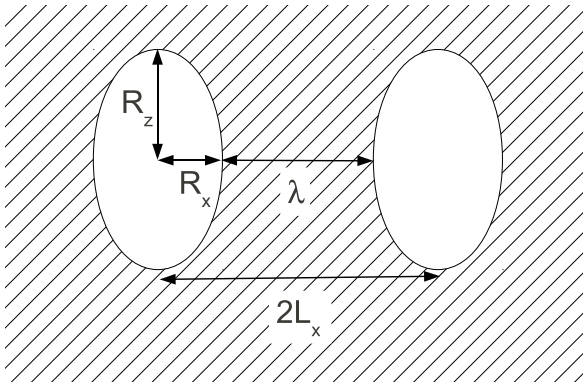

Figure 4.5: Geometrical parameters involved in void coalescence models.

The Brown and Embury criterion [Brow 73]

The criterion developed by Brown and Embury (B&E) is a criterion for void coalescence by internal necking. It is based on the micromechanical fact that internal necking

is considered to occur when 45°microshear bands can connect two neighboring voids. The original criterion states that void coalescence occurs for elongated cavities when the radius is equal to half the distance between the two void centers. For ellipsoidal voids, the criterion writes:

$$\chi\sqrt{1+W^2}=1 \tag{4.1}$$

Later, Le Roy [LeRo 81] associated the void nucleation criterion of Argon [Argo 75b] and the void growth model of Rice and Tracey [Rice 69] to this void coalescence criterion, thus linking the void coalescence to the deformation.

The Thomason criterion [Thom 90]

Like the B&E criterion, the Thomason criterion is for void coalescence by internal necking. It was developed from the analysis of the tensile plastic localization in the intervoid ligaments. The initial condition adapted to rigid-perfectly plastic materials proposed by Thomason is:

$$\frac{\sigma_{zz}}{\sigma_0}=\left(1-\chi^2\right)\left[0.1\left(\frac{1-\chi}{\chi W}\right)^2+1.2\frac{1}{\sqrt{\chi}}\right] \tag{4.2}$$

Equation (4.2) states that void coalescence starts when σ_{zz} reaches a critical value. This critical value decreases as the voids open (W increases) and get closer to each other (χ increases). This initial equation was improved many times in order to adapt the criterion to more realistic strain hardening materials. Zhang and Niemi and Pardoen and Hutchinson proposed to replace the initial yield stress σ_0 by the current overall yield stress of the matrix σ_y [Zhan 95] and accounting for the strain hardening n using the parameter $\alpha(n)=0.1+0.217n+4.83n^2$ with $0\leq n\leq 3$ [Pard 00]:

$$\frac{\sigma_{zz}}{\sigma_y}=\left(1-\chi^2\right)\left[\alpha(n_\varepsilon)\left(\frac{1-\chi}{\chi W}\right)^2+1.24\frac{1}{\sqrt{\chi}}\right] \tag{4.3}$$

Later, Benzerga re-evaluated the equation (4.3) to adjust it for low values of triaxiality [Benz 02]:

$$\frac{\sigma_{zz}}{\sigma_y}=\left(1-\chi^2\right)\left[0.1\left(\frac{\chi^{-1}-1}{W^2+0.1\chi^{-1}+0.02\chi^{-2}}\right)^2+1.3\frac{1}{\sqrt{\chi}}\right] \tag{4.4}$$

Fabregue and Pardoen added a term accounting for a second void population f_2 to the equation (4.3) [Fabr 08a, Fabr 08b]:

$$\frac{\sigma_{zz}}{\sigma_y}=\left(1-f_2\right)\left(1-\chi^2\right)\left[\alpha(n_\varepsilon)\left(\frac{1-\chi}{\chi W}\right)^2+1.24\frac{1}{\sqrt{\chi}}\right] \tag{4.5}$$

Finally, Scheyvaerts *et al.* proposed an alternative form to the equation (4.3) in which the hardening law dependence is no longer included [Sche 11]:

$$\frac{\sigma_{zz}}{\sigma_y^{loc}} = \left(1-\chi^2\right)\left[0.1\left(\frac{1-\chi}{\chi W}\right)^2 + 1.24\frac{1}{\sqrt{\chi}}\right] \tag{4.6}$$

where σ_y^{loc} is the current yield stress next to the void surface.

4.1.4 Previous studies on void coalescence in DP steels

Because of the difficulty to study experimentally the void coalescence, no investigation on the step of coalescence in the DP steels can be found in the literature. The characterization of the void coalescence performed in the present work will then attempt to bring initial responses to this problem.

4.2 Void coalescence characterization

4.2.1 Qualitative observations

As mentioned before, the step of void coalescence is difficult to observe experimentally because of the stochastic nature of the coalescence and the very short time between the beginning of the coalescence and the fracture of the specimen. When tomograms were acquired at the right instant during the tensile test, events of coalescence were observed in volumes. The void coalescence can then be visualized in 2D using a section inside the imaged volume of the specimen (Figure 4.6) or in 3D (Figure 4.7). Figures 4.6(a) and 4.7(a) show the first observed local events of coalescence. These local events of coalescence then lead to the macroscopic coalescence which were observed in Figures 4.6(b) and 4.7(b). The step of deformation where macroscopic coalescence was observed was usually the last one, the final fracture occurring soon after it.

Figure 4.8 shows the modes of coalescence observed in the studied steels. It depended on the position of the voids coalescing. If neighboring voids were side by side, coalescence rather occurred by necking of the internal ligament (see Figure 4.8(a)). In the cases where the angle between the voids was around 45°, coalescence resulted from shear localization (see Figure 4.8(b)). The third mode of necklace coalescence was not observed in the studied samples.

The optical micrograph of a DP11 sample presented in Figure 4.9 shows that in the bi-phased microstructure, coalescence preferentially occurs in the soft phase, *i.e.* the ferrite.

4.2.2 Void coalescence effect on damage quantification

When the void coalescence started to occur in a sufficient amount during an *in-situ* tensile test, the evolution of the measured void density, the equivalent diameter and the

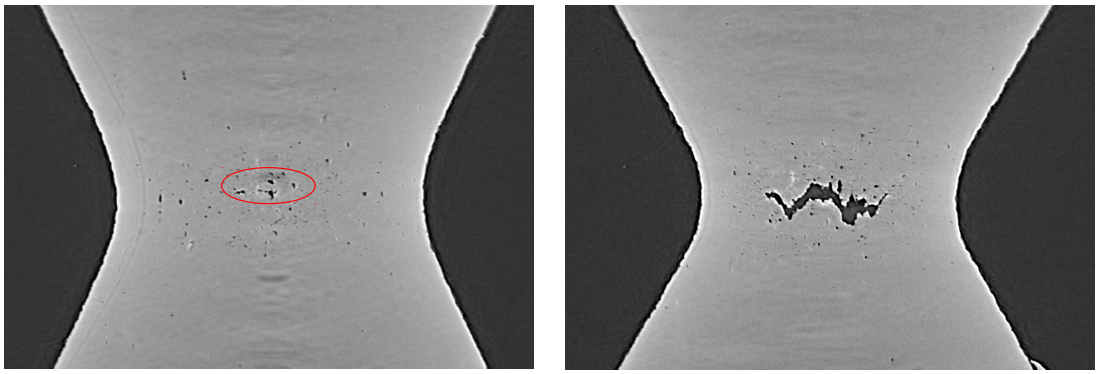

(a) (b)

Figure 4.6: Observation of a longitudinal section inside the imaged specimen of DP11 using X-ray tomography at different deformations: (a)$\varepsilon_{loc} = 0.69$, (b) $\varepsilon_{loc} = 0.83$.

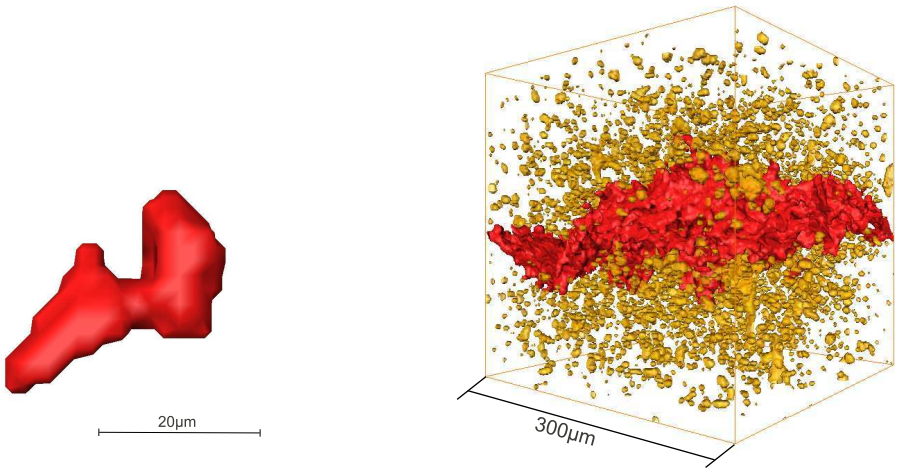

(a) (b)

Figure 4.7: 3D visualization of void coalescence in a DP11 specimen: (a) local event of coalescence at $\varepsilon_{loc} = 0.69$, (b) macroscopic coalescence inside the same specimen at $\varepsilon_{loc} = 0.83$ (a huge cavity induced by the macroscopic coalescence appears in red).

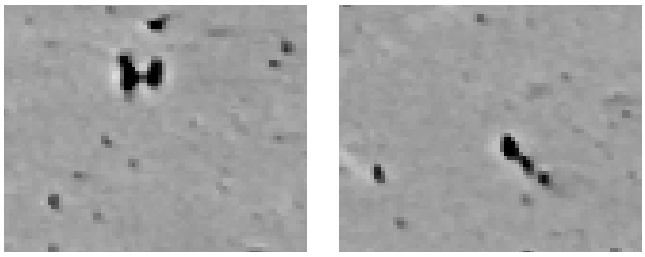

(a) (b)

Figure 4.8: Coalescence mechanisms observed in the DP11 specimen: (a) necking of the internal ligament, (b) shear localization.

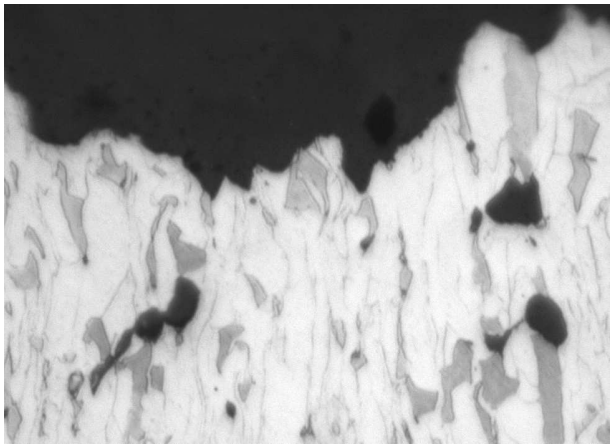

Figure 4.9: Optical micrograph of a DP11 specimen after fracture.

void dimensions were affected:

- As mentioned in Chapter 2, the density of nucleating voids exponentially increases with the deformation. When events of coalescence occur, the number of voids decreases. This has been observed in aluminum alloys in [Mart 00] (superplastic deformation) and in [Mair 11]. In our experimental case, when only few local events of coalescence happen, the change in the evolution of the void density is not enough to be detected. The effect of void coalescence appears for high deformations close to the fracture of the specimen, when macroscopic coalescence occurs. The number of coalescence occurrences is of the same magnitude as the number of nucleating cavities and thus the void density stops to exponentially increase. This phenomenon is illustrated for a notched specimen of DP11 given in Figure 4.10.
- When two cavities coalesce, the volume of the resulting void is almost twice larger than the volume of a non-coalescing cavity. The measurement of the equivalent diameter of the cavity is thus affected by the coalescence. When one of the twenty largest voids studied to quantify the growth is implied in a coalescence occurrence, the calculated equivalent diameter is then impacted by the coalescence. As shown in Figure 4.11, the void growth accelerates as compared with the prediction given by the Huang model.
- As void coalescence occurs either by internal necking or shear localization, the lateral dimensions of the cavities may particularly be concerned by the coalescence. It is confirmed by Figure 4.12 showing the very high increase of the transversal dimension of the cavities at higher strain.

4.2.3 Quantification of void coalescence

4.2.3.1 Measurement of the inter-cavities distance

The key parameter controlling the void coalescence is the distance between closest cavities λ (see Figure 4.5). Besides, this parameter is involved in all the coalescence criteria. An average value of λ can be calculated inside the studied sub-volume using the void density N and the equivalent diameter D_{eq} assuming that the cavities are homogeneously distributed in the studied sub-volume:

$$\lambda_{mean} = \frac{1}{N^{1/3}} - D_{eq} \tag{4.7}$$

The evolution of λ_{mean} calculated from Equation 4.7 with the deformation is given in Figure 4.13 for the five studied steels. The ligament decreases differently from a studied materials to another. The final value of λ_{mean} calculated at the last step of strain before fracture is about 20 µm for the three bi-phase steels and 40 µfor the two single-phase steels.

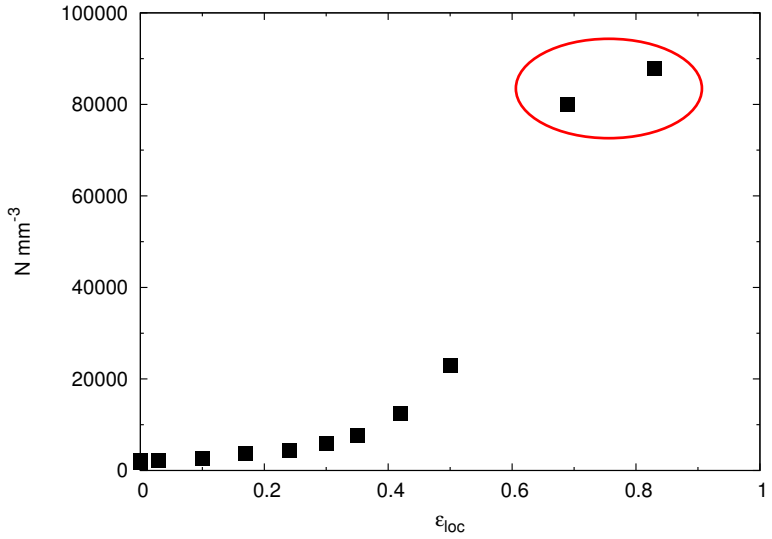

Figure 4.10: Effect of void coalescence on the measurement of the void density in DP11.

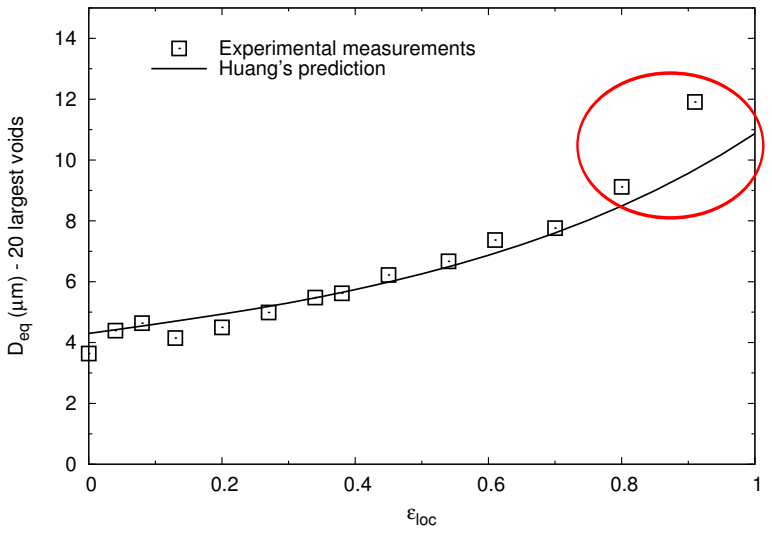

Figure 4.11: Void coalescence effect on the measurement of the equivalent diameter of the 20 largest cavities in DP11.

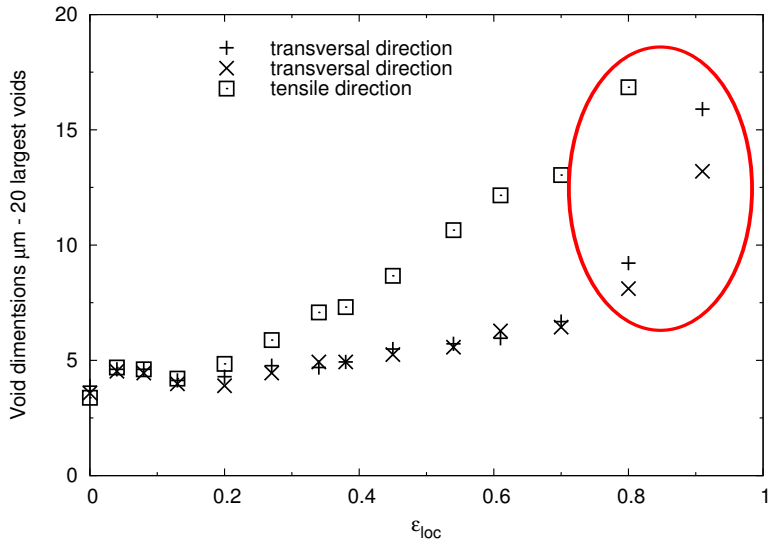

Figure 4.12: Void coalescence effect on the measurement of the voids dimensions in DP11.

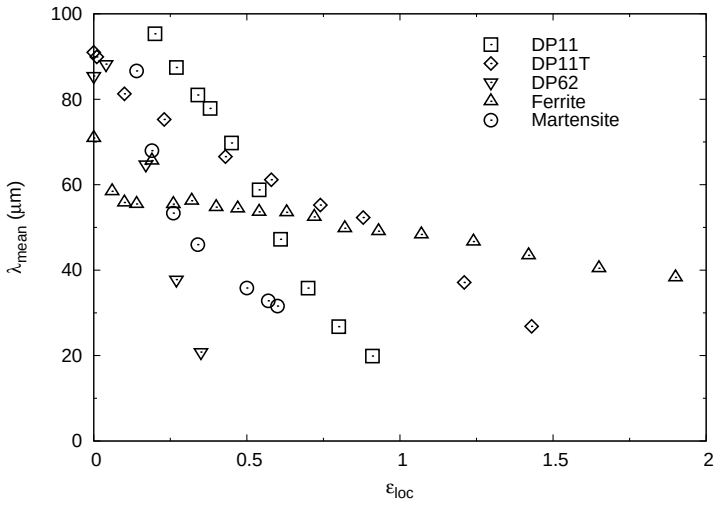

Figure 4.13: Evolution of λ_{mean} with the deformation for the studied steels.

This average value of λ does not give information on local events of coalescence. To obtain a better measurement of the local value of λ, the distance between each couple of neighboring cavities present in the studied sub-volume at each deformation step was measured using an appropriate image processing. Each cavity was first labeled. This labeled image was then dilated . When two cavities start to touch each other, they are marked as neighbors and the distance between them is known using the current number of dilatation steps. The frequency distribution of the measured length of the material ligament is then plotted for each deformation step. Figure 4.14 shows the evolution of this distribution in a smooth specimen of DP11. For low values of strain, the frequency distribution is quite large. It then narrows when deformation increases. At the last step of deformation before fracture, the mean value of λ, λ_{mean}, previously calculated (see Figure 4.13) matches the maximum value of the distribution in Figure 4.14.This is a good evidence of the consistency between the two measurements.

Figure 4.15 compares the frequency distribution of λ in the different investigated specimens at the last step of deformation before fracture. Firstly, the triaxiality does not have an influence on this distribution. Secondly, only the single-phase or the bi-phase nature of the microstructure seems to have an impact: the λ distributions of the DP steels are similar while ones of the homogeneous microstructures, *i.e.* the ferritic and the martensitic steels are also similar but larger and shifted to the higher values of λ. This last remark is already done regarding the average values of the distance inter-cavities calculated at the last strain step of the tensile test of each material.

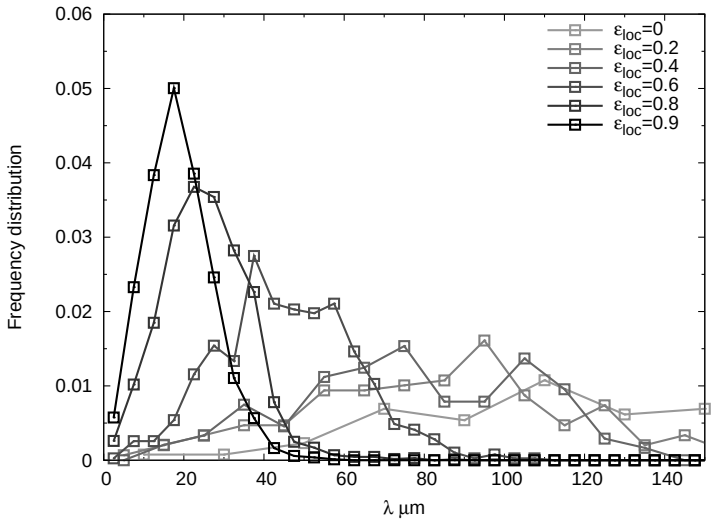

Figure 4.14: Evolution of the frequency distribution of λ with the strain in a smooth specimen of DP11.

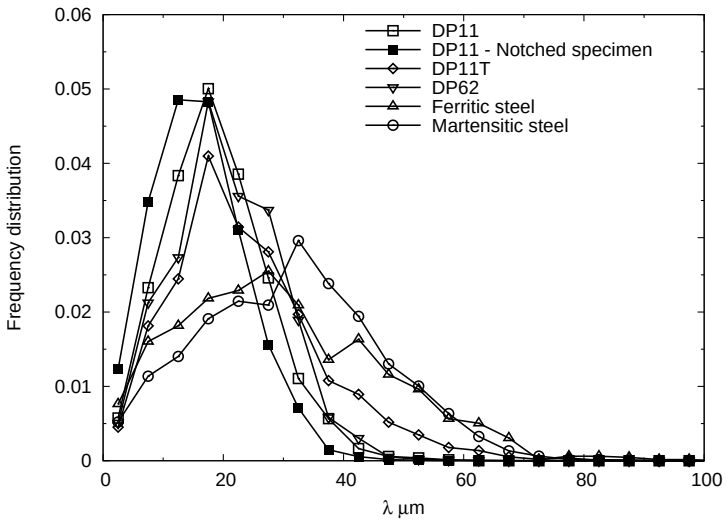

Figure 4.15: Frequency distribution of λ at the last step of deformation in the different studied materials.

4.2.3.2 Effect of the voxel size on the characterization of the void coalescence

In the volumes acquired with a high resolution, more smaller cavities were detected than in the standard volumes. The distance between cavities was thus smaller in the high resolution volume as seen in Figure 4.16. However, few high resolution volumes were available, It is indeed much more difficult to obtain data at this high resolution. Void coalescence cannot practically be investigated using these high resolution volumes. However, the presence of these small cavities, not detected at the standard scale, will be taken into account in Section 4.3.2.4.

4.2.3.3 Experimental configuration of neighboring cavities

Using the image processing procedure introduced in Section 4.2.3.1, the couples of closest neighboring cavities can be determined. Using this information, the geometrical configuration of the neighboring cavities was determined. The orientation of the neighboring voids was calculated from the position of the center of gravity of every cavities of each couple. The ratio of the equivalent diameter of the two neighboring cavities could also easily be calculated. Figures 4.17 and 4.18 respectively show the frequency distribution of the orientation and of the ratio of the equivalent diameter of the neighboring voids. Most of the couples of neighboring cavities are almost horizontally aligned, however, a significant part of the couples have an orientation close to 45°. Concerning, the size of the neighboring voids, few couples consist of two voids with a similar volume.

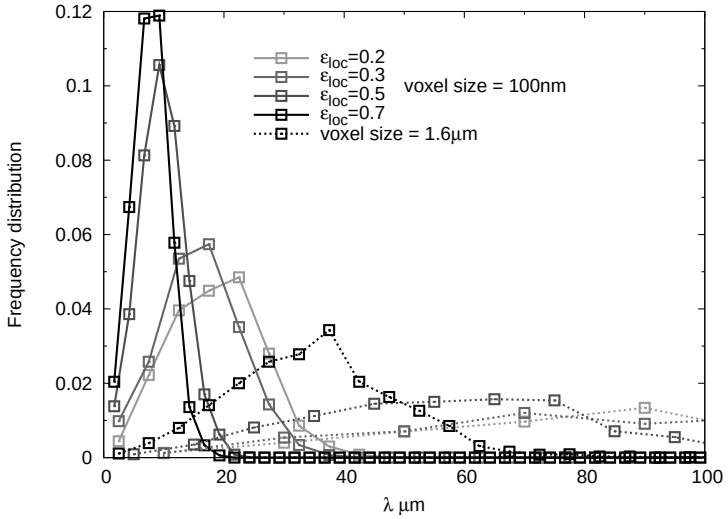

Figure 4.16: Effect of the voxel size on the measurement of the frequency distribution of λ in DP11.

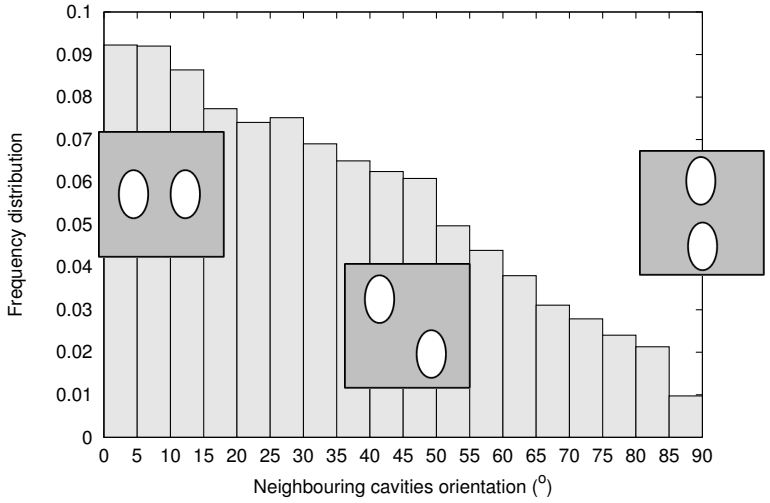

Figure 4.17: Frequency distribution of the orientation of the neighboring cavities.

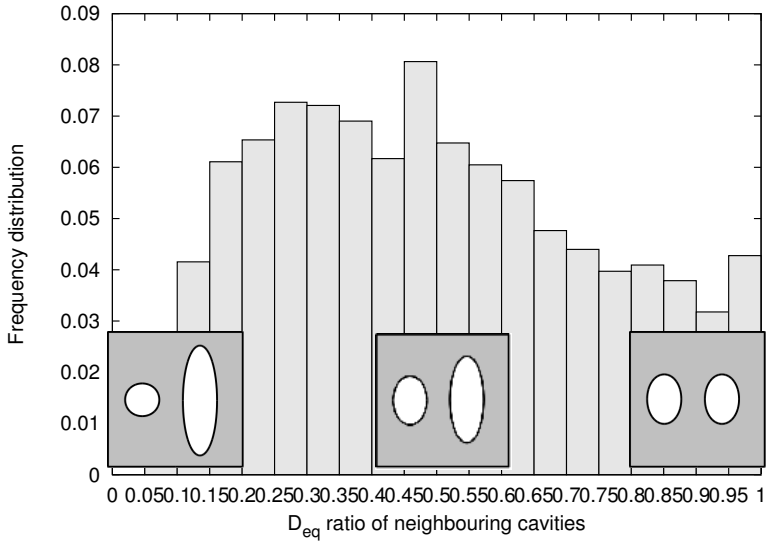

Figure 4.18: Frequency distribution of the equivalent diameter ratio of the neighboring cavities.

In every coalescence criteria presented in Section 4.1.3, the geometrical configuration of the coalescing cavities is the one given in Figure 4.5: voids are horizontally aligned and have the same dimensions. In real specimens we have shown that the geometrical disposition of cavities is quite different. Concerning the prediction of the void coalescence, we have attempted to account for these differences between the real configuration of the neighboring voids and the assumptions of the criteria.

4.3 Void coalescence prediction

Until now, void coalescence criteria have been applied on periodic clusters of cavities either in cell calculations or in model materials. In this work, two ways of implementing these approaches on experimental data from *in-situ* tensile tests are investigated.

- The first one consists in allocating to the specimen a single value of the criterion for a given deformation step. It amounts to assuming a periodic clusters of void coalescing at the same time, like in cell calculations. This macroscopic approach does not take into account the singularity of each couple of voids.

- The second approach is a local application of the criterion. The criterion is applied on each couple of neighboring voids accounting for features of each couple.

Both approaches are applied on the studied steels with the simple criterion of Brown and Embury and an improved criterion of Thomason.

4.3.1 Macroscopic implementation of the coalescence criteria

Like in cell calculations, the coalescence criterion is applied on one single couple of voids. The void parameters are chosen to be the most representative of the experimental system.

4.3.1.1 Macroscopic implementation of the Brown and Embury criterion

The original criterion presented in Section 4.1.3 involves the half distance between the two voids centers Lx and the void radii in the tensile and transversal directions R_x and R_z:

$$Lx^2 = {R_x}^2 + {R_z}^2 \tag{4.8}$$

In the studied specimens, the mean value of the distance between the voids centers $2Lx_{mean}$ is calculated from the measured void density N:

$$2Lx_{mean} = \frac{1}{N^{1/3}} \tag{4.9}$$

Concerning the void radii in the tensile and transversal directions, the used values are the average value calculated over the 20 largest cavities $R^{20}_{tensile}$ and R^{20}_{trans} The criterion can then be implemented from these experimental measurements. Figure 4.19 shows the evolution with the deformation of both parts of the Brown and Embury criterion *i.e.* Lx_{mean} and $\sqrt{{R^{20}_{trans}}^2 + {R^{20}_{tensile}}^2}$ for each studied steel.

Figure 4.19 exhibits quite good agreement between the end of the tensile test and the strain at coalescence predicted by the criterion. However, attributing the average values R^{20}_{trans} and $R^{20}_{tensile}$ to the void dimensions is equivalent to assume that all voids present in the studied sub-volume are as large as the 20 largest ones. It was thus expected that the Brown and Embury criterion should underestimate the deformation at coalescence.

4.3.1.2 Macroscopic implementation of the Thomason criterion

The version of the Thomason criterion used here is the most recently developed in [Sche 11] (see Equation (4.6)). The Brown and Embury criterion is a purely geometrical criterion. The Thomason criterion also accounts for the mechanical parameters σ_{zz} and σ_y^{loc}. The true stress in the tensile direction σ_{zz} is calculated from the data acquired during *in-situ* tensile tests (see Annexe A). Concerning the current yield stress next to the void surface, σ_y^{loc}, it is calculated using the same approach developed in [Sche 11]:

$$\sigma_y^{loc} = \sigma_{eq}\left(\varepsilon_{zz}^{loc}\right) \tag{4.10}$$

where ε_{zz}^{loc} is the local value of the strain next to the void surface. ε_{zz}^{loc} is estimated from the integration of the value of the strain rate $\dot{\varepsilon}_{zz}^{loc}$ given by the equation proposed by Fabregue and Pardoen [Fabr 08a]:

$$\dot{\varepsilon}_{zz}^{loc} \approx \frac{1}{3}\left(\dot{\varepsilon}_{loc} + 2\dot{\varepsilon}_{trans} + \frac{\dot{f}}{f} + 2\frac{\dot{W}}{W}\right)\left(\frac{\pi}{2}\sqrt{\frac{1}{2}\left(\frac{1}{W^2}+1\right)}\right) \tag{4.11}$$

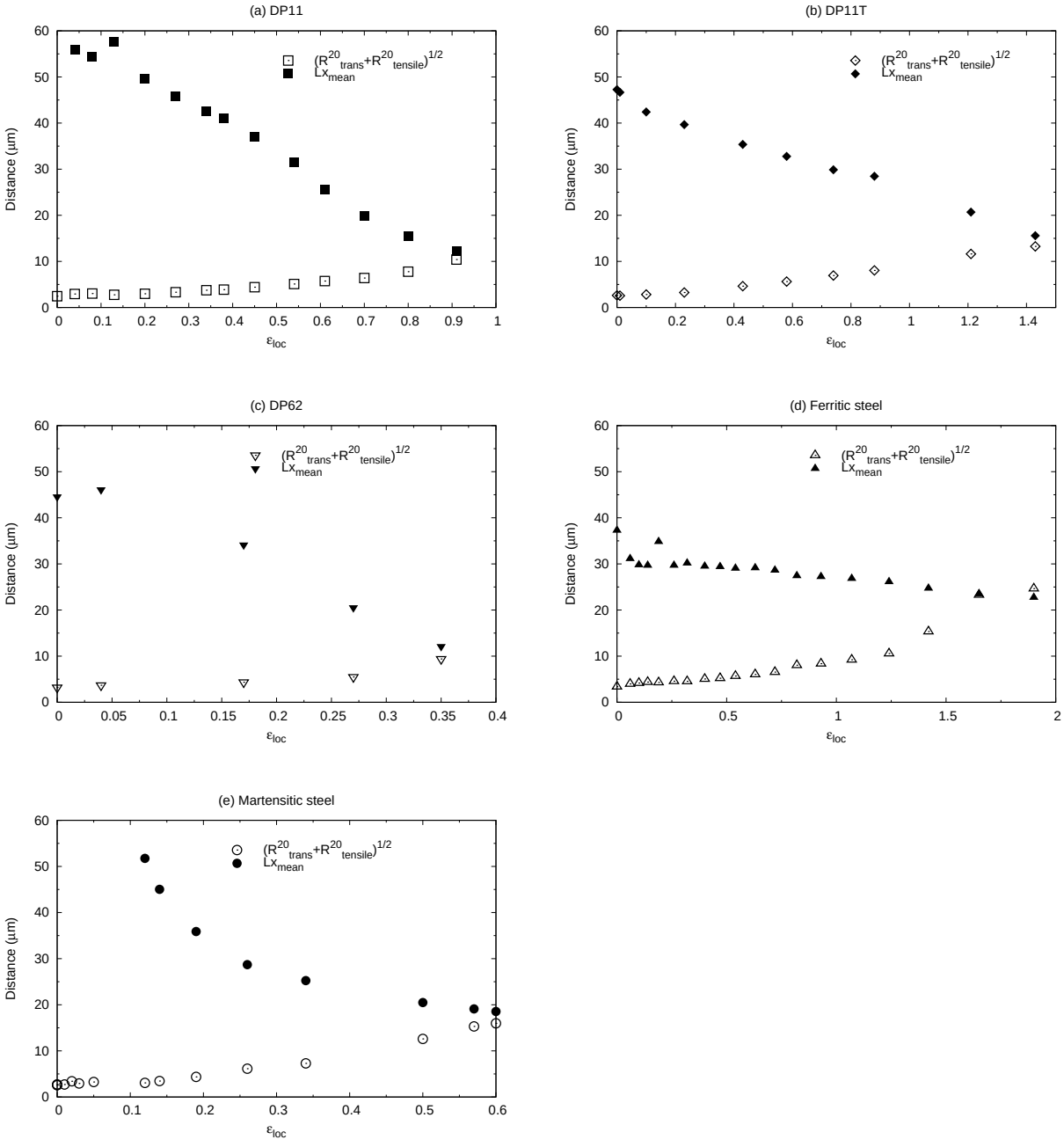

Figure 4.19: Macroscopic implementation of the Brown and Embury criterion on the experimental data.

The evolution of ε_{zz}^{loc} calculated from the integration of this equation is given in Figure 4.20.

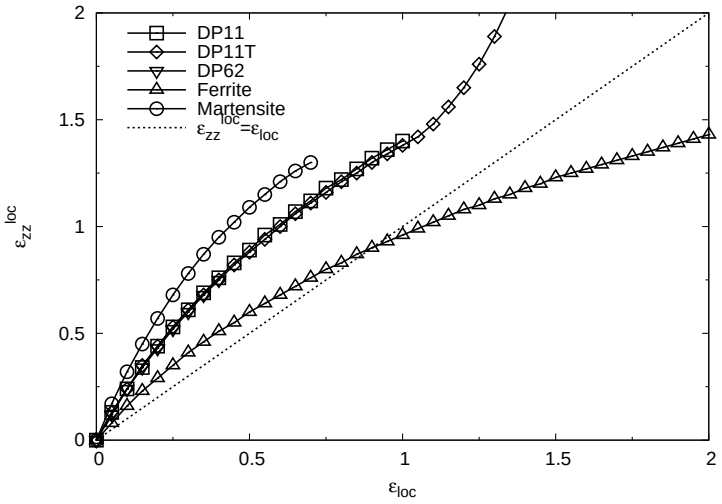

Figure 4.20: Evolution of ε_{zz}^{loc} calculated from Eq.(4.11) for each studied steel.

As in every coalescence criteria, the geometrical parameters concerning voids W and χ are involved. Like in the macroscopic implementation of the Brown and Embury criterion, they are calculated using the average values of $D_{tensile}^{20}$, D_{trans}^{20} and Lx_{mean}. The results of the macroscopic implementation of the Thomason criterion is given in Figure 4.21.

As already mentioned for the Brown and Embury criterion, the use of the average values $D_{tensile}^{20}$ and D_{trans}^{20} should lead to an overestimation of the fracture strain. Figure 4.21 shows that the strain at coalescence predicted by the Thomason criterion is however quite close to the one measured at the end of the tensile test.

4.3.1.3 Prediction of the fracture strain using the macroscopic implementation of the criteria

These later sections show that the macroscopic implementation of the Brown and Embury or the Thomason criteria using the experimental values of D_{trans}^{20} and $D_{tensile}^{20}$ and N leads to a quite good prediction of the fracture of the specimen. The advantage of attributing these values to the criteria lies in the fact that they were modeled in the previous sections so that the criteria can also be expressed from these predictions. Figures 4.22 and 4.23 exhibit the implementation of both tested criteria using the models developed in Section 2 to predict N and in Section 3 to model D_{trans}^{20} and $D_{tensile}^{20}$. The use of these predictions cannot lead to an analytical expression of the value of the rupture strain because N and D are calculated from the integration of the equations

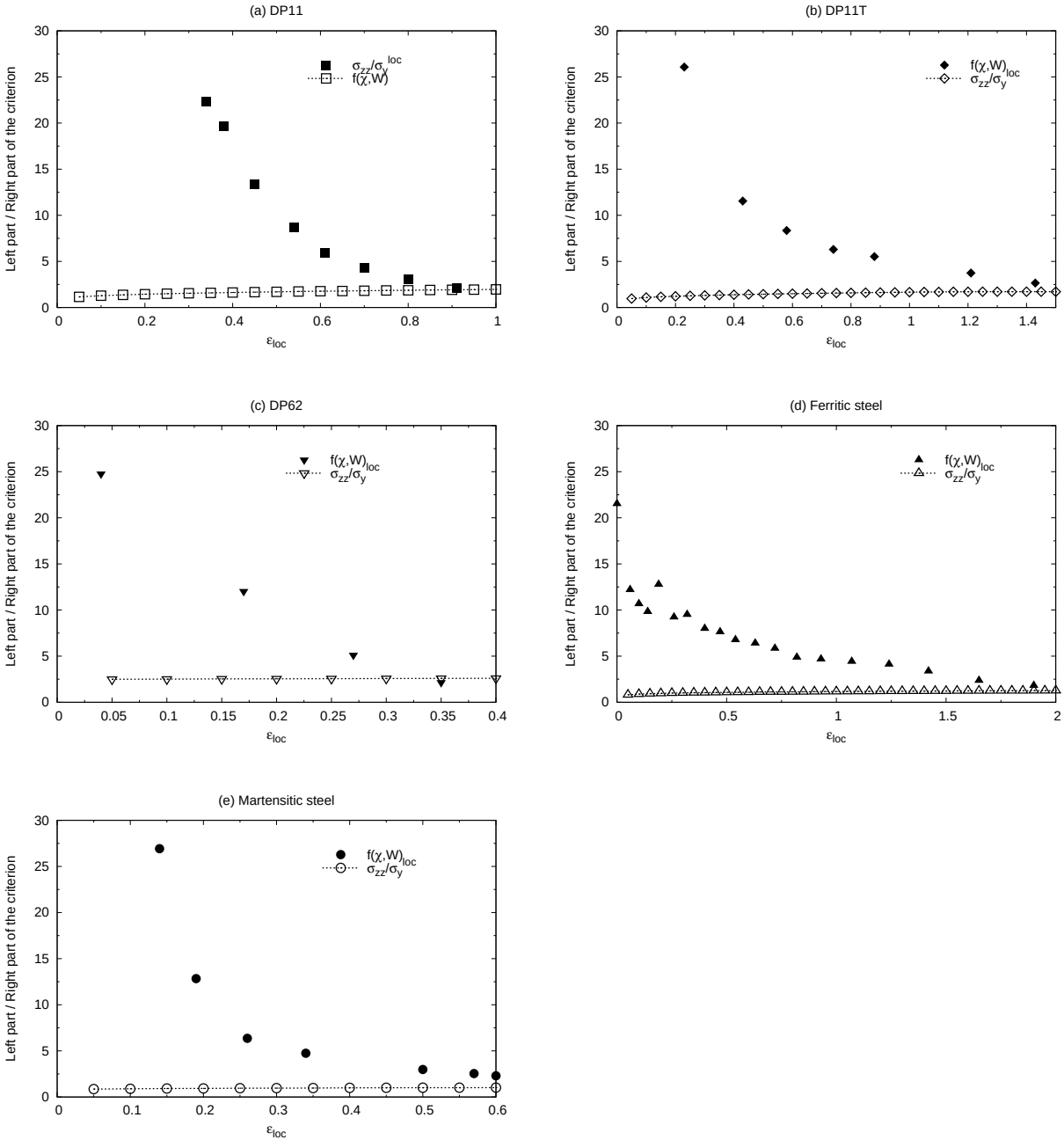

Figure 4.21: Macroscopic implementation of the Thomason criterion on the experimental data.

(2.15) and (3.8) respectively given in pages 62 and 87. However, the numerical implementation permits to determine the value of the fracture strain predicted by the Brown and Embury criterion ε_R^{BE} and the Thomason criterion $\varepsilon_R^{Thomason}$ using the predicting equations. The values of ε_R^{BE} and $\varepsilon_R^{Thomason}$ found for every studied steel are listed in Table 4.2. Globally, the values of ε_R predicted by both criteria are really close to the actual fracture strain observed experimentally (except in the case of the ferritic steel where the Thomason criterion overestimate the fracture strain).

	DP11	DP11T	DP62	ferrite	marteniste
ε_R^{exp}	1	1.43	0.35	2.2	0.6
ε_R^{BE} (error)	1.1 (+0.1)	1.45 (+0.02)	0.41 (+0.06)	2.25 (0.05)	0.6 (0)
$\varepsilon_R^{Thomason}$ (error)	1 (0)	1.4 (-0.03)	0.32 (-0.03)	2.7 (+0.5)	0.55 (-0.05)

Table 4.2: Values of the fracture strain given by the global Brown and Embury criterion ε_R^{BE} and the global Thomason criterion $\varepsilon_R^{Thomason}$.

4.3.2 Local implementation of the coalescence criteria

4.3.2.1 Methodology

In order to account for the local events of coalescence observed experimentally, the Brown and Embury's criterion and the Thomason's criterion were applied on each detected couple of neighboring cavities. The local implementation of the criteria is done using the value of W and of χ specific to each couple of voids. W is calculated as being the average value of the void aspect ratio $W^{cavity1}$ and $W^{cavity2}$ of the two cavities involved in the criterion:

$$W = \frac{W^{cavity1} + W^{cavity2}}{2} \tag{4.12}$$

χ is calculated using the distance between the two cavities λ and both values of the void radius in the transversal direction $R_{trans}^{cavity1}$ and $R_{trans}^{cavity2}$:

$$\chi = \frac{R_{trans}^{cavity1} + R_{trans}^{cavity2}}{\lambda + R_{trans}^{cavity1} + R_{trans}^{cavity2}} \tag{4.13}$$

The local implementation of a criterion leads to the calculation of a parameter δ. This parameter δ is negative when the coalescence condition is reached. More information concerning the calculation of δ for the Brown and Embury's criterion and for the Thomason criterion is given in the next subsections. As many values of δ as the number of couples of neighboring cavities can finally be calculated. The frequency distribution of δ is then determined for each strain step.

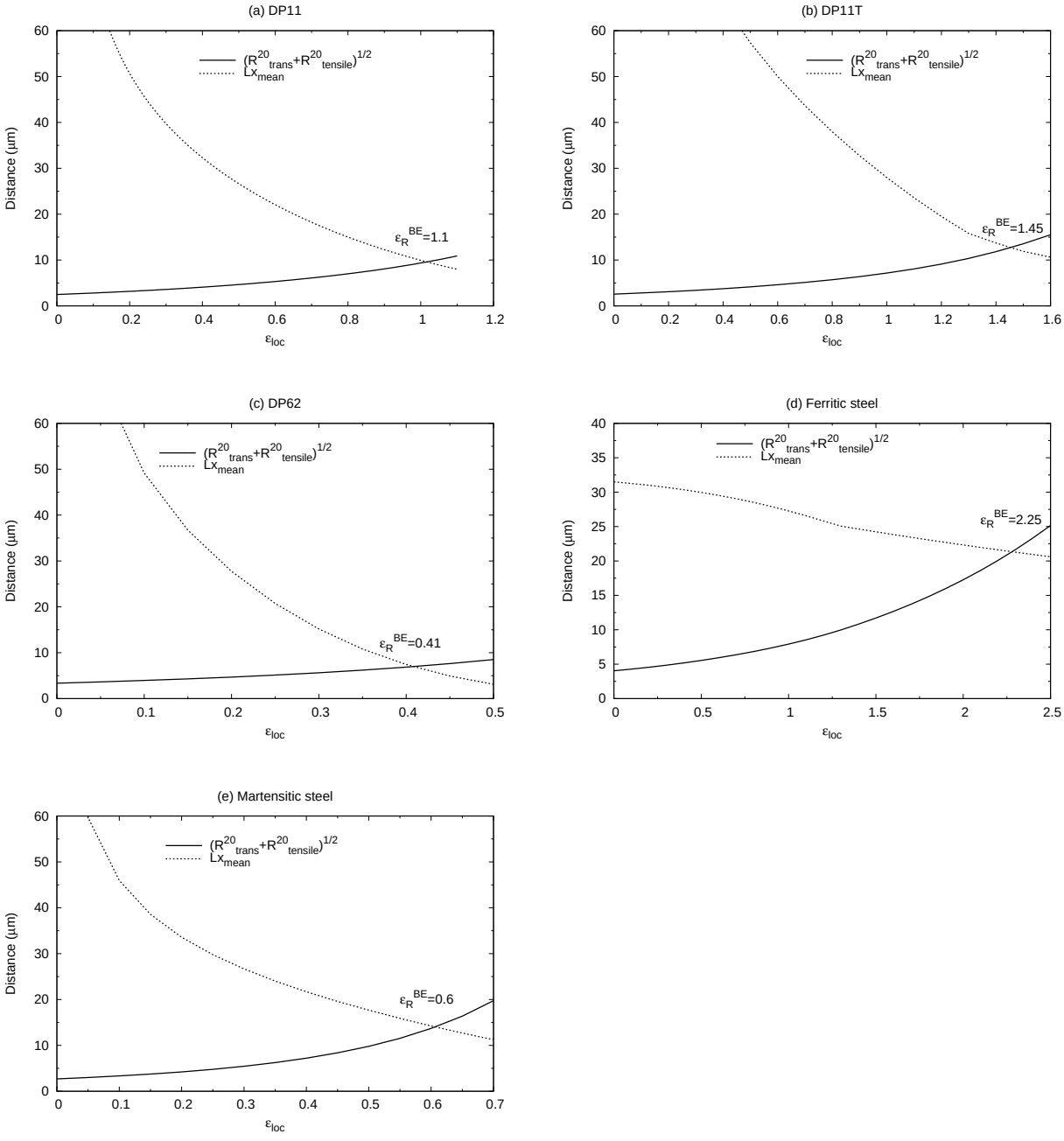

Figure 4.22: Macroscopic implementation of the Brown and Embury criterion using predicted value of N, D^{20}_{trans} and $D^{20}_{tensile}$.

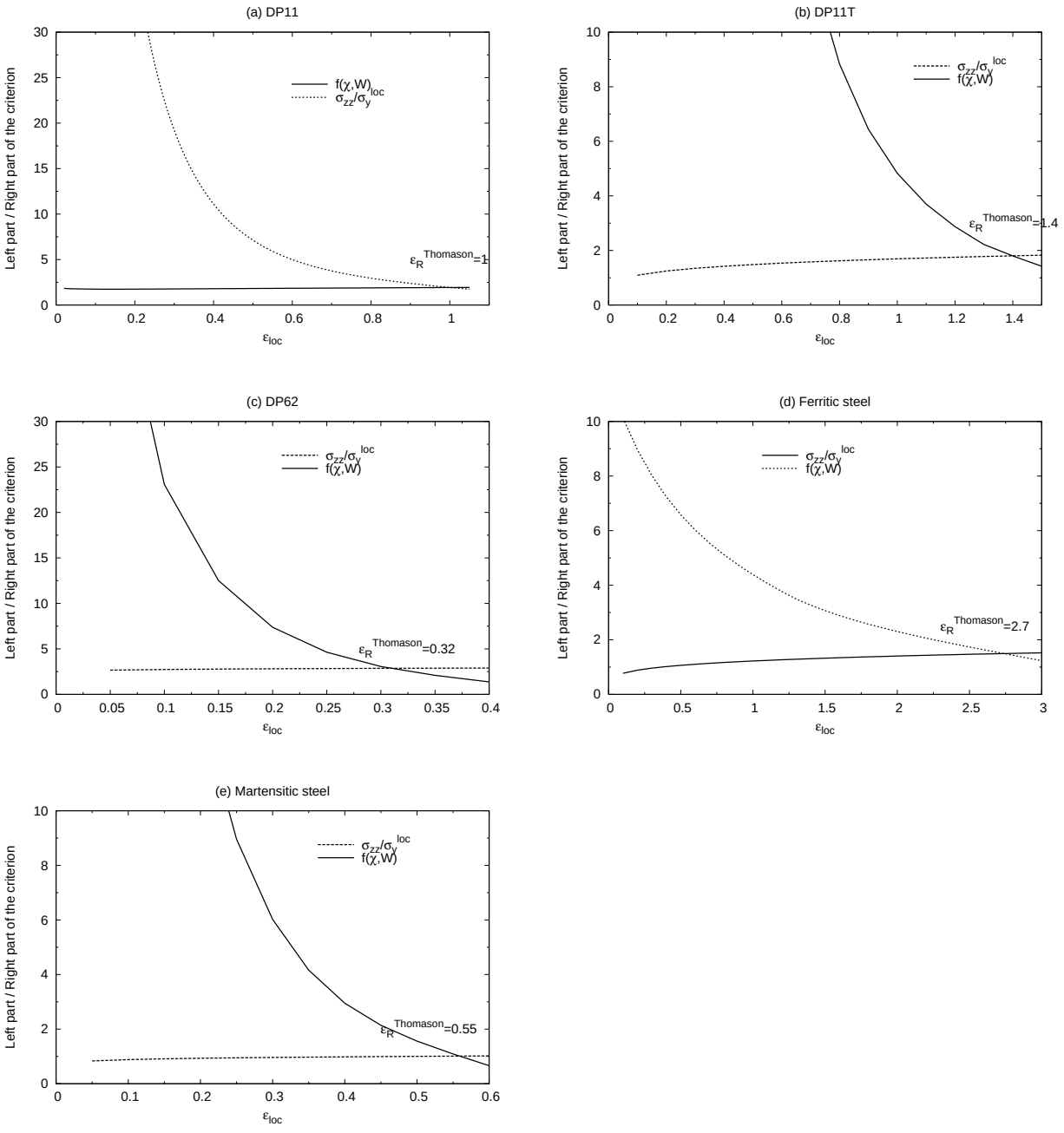

Figure 4.23: Macroscopic implementation of the Thomason criterion using predicted value of N, D^{20}_{trans} and $D^{20}_{tensile}$.

4.3.2.2 Local implementation of the Brown and Embury's criterion

The Brown and Embury criterion was applied to each couple of neighboring cavities without accounting for the orientation and the volume ratio of the two voids involved in the criterion:

$$\frac{1}{\chi} = \sqrt{1+W} \tag{4.14}$$

For each couple of voids, $\delta_{B\&E} = \frac{1}{\chi} - \sqrt{1+W}$ was calculated ($\delta_{B\&E} < 0$ when the criterion is positive).
The evolution of the frequency distribution of $\delta_{B\&E}$ with the strain is given for each studied steel in Figure 4.24.

4.3.2.3 Local implementation of the Thomason's criterion

As shown in Figure 4.17, the neighboring cavities have various orientations and various volumes. The Brown and Embury criterion used in the previous section do not account for these differences. However, the effect of the orientation of the neighboring voids on coalescence γ can be taken into account using the version of the Thomason criterion developed by Scheyvaerts *et al.* [Sche 11]:

$$\frac{\sigma_{zz}(\gamma)}{\sigma_y^{loc}(\gamma)} = \left(1-\chi_{eff}^2(\gamma)\right)\left[0.1\left(\frac{1-\chi_{eff}(\gamma)}{\chi_{eff}(\gamma)W_{eff}(\gamma)}\right)^2 + 1.2\frac{1}{\sqrt{\chi_{eff}(\gamma)}}\right] \text{ for } \gamma \in \left[0:\frac{\pi}{2}\right] \tag{4.15}$$

The geometrical and mechanical parameters involved in this expression are explicitly given in Figure 4.25. In order to have an expression easier to implement, the following assumptions are made:

- $R_x(\gamma) \approx R_x(\gamma=0)$ and $R_z(\gamma) \approx R_z(\gamma=0)$ leading to $W_{eff} \approx W$ and $\chi_{eff} \approx \frac{R_x}{L_x(\gamma)}$.
- $\sigma_y^{loc}(\gamma) = \sigma_y^{loc}(\gamma=0)$

Equation (4.15) becomes then:

$$\frac{\sigma_{zz}(\gamma)}{\sigma_y^{loc}} = \left(1-\chi_{eff}^2\right)\left[0.1\left(\frac{1-\chi_{eff}}{\chi_{eff}W}\right)^2 + 1.2\frac{1}{\sqrt{\chi_{eff}}}\right] \tag{4.16}$$

Like for the Brown and Embury criterion,
$\delta_{Thomason} = \frac{\sigma_{zz}(\gamma)}{\sigma_y^{loc}} - \left(1-\chi_{eff}^2\right)\left[0.1\left(\frac{1-\chi_{eff}}{\chi_{eff}W}\right)^2 + 1.2\frac{1}{\sqrt{\chi_{eff}}}\right]$ is calculated for each couple of neighboring cavities ($\delta_{Thomason} < 0$ when the criterion is positive) and the evolution of the frequency distribution of $\delta_{Thomsaon}$ with the strain is given for each studied steel in Figure 4.26.

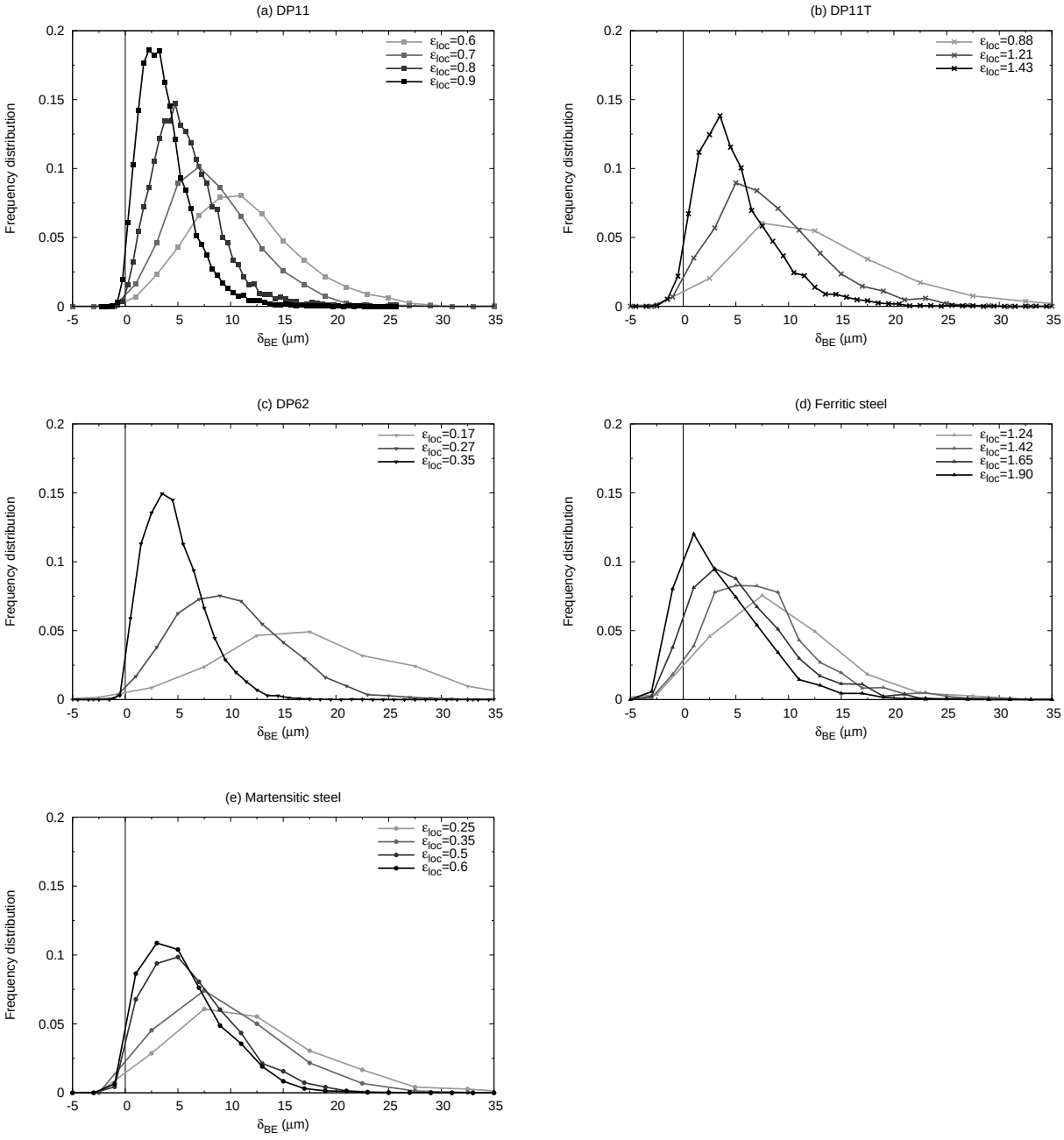

Figure 4.24: Local implementation of the Brown and Embury criterion on the studied steels.

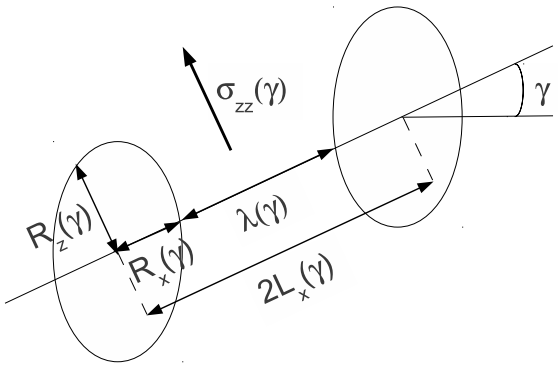

Figure 4.25: Definition of the parameters entering the void coalescence criterion given in equation (4.15).

4.3.2.4 Effect of the secondary voids population detected at high resolution

In-situ tensile test characterized with sub-micrometer resolution tomography showed the presence of very small cavities in the DP11 sample being not detected in the first experiments. In order to account for these voids, the expression of the Thomason criterion developed by Fabregue *et al.* [Fabr 08a] and given in Equation 4.5 is associated to the expression used in the previous subsection (Equation 4.15):

$$\frac{\sigma_{zz}(\gamma)}{\sigma_y^{loc}} = (1-f_2)\left(1-\chi_{eff}^2\right)\left[0.1\left(\frac{1-\chi_{eff}}{\chi_{eff}W_{eff}}\right)^2 + 1.2\frac{1}{\sqrt{\chi_{eff}}}\right] \tag{4.17}$$

where f_2 is the volume fraction of the secondary voids population.
This expression of the Thomason criterion was tested on each couple of neighboring voids present in the DP11 specimen at the last step before fracture with a measured volume fraction of secondary voids $f_2 = 0.003$. The frequency distribution of $\delta_{Thomason}$ obtained with Equations 4.15 and 4.17 are compared in Figure 4.27. This figure shows that the void volume fraction of the secondary voids population is extremely low, the two curves being very close.

4.3.2.5 Comparison of the Brown and Embury and the Thomason criteria

Both local implementation of the Thomason's criterion and the Brown and Embury's criterion gave similar results. The tensile strain shifts the frequency distribution of δ to the smaller values. At the beginning of the tensile test, no couples have a positive coalescence criterion and the number of couples presenting a positive coalescence criterion increases as the tensile test goes along. The number of couples having a positive Brown and Embury's criterion and the number of couples having a positive Thomason's criterion were then counted in the last step before fracture of each investigated specimen.

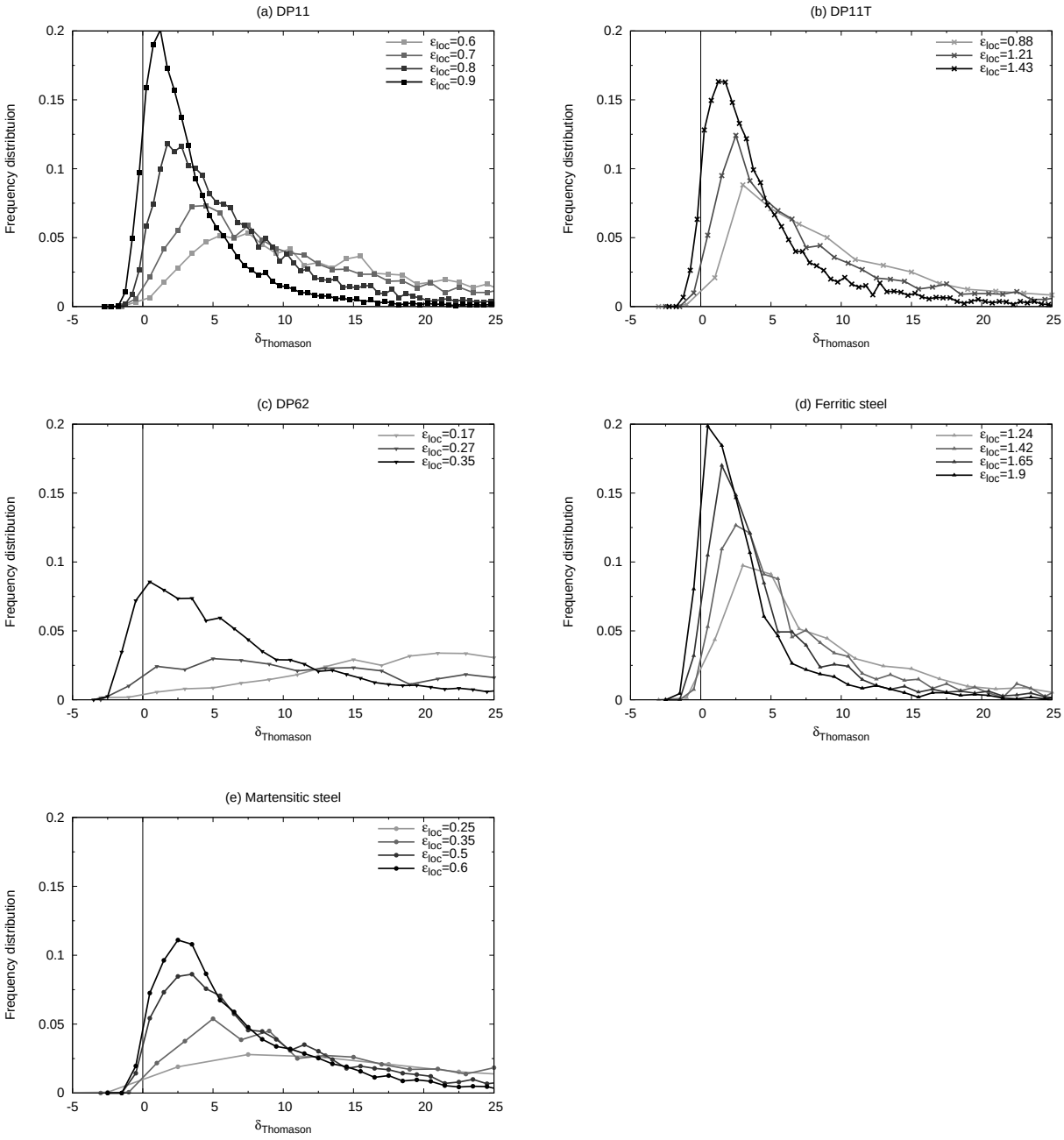

Figure 4.26: Local implementation of the Thomason criterion on the studied steels.

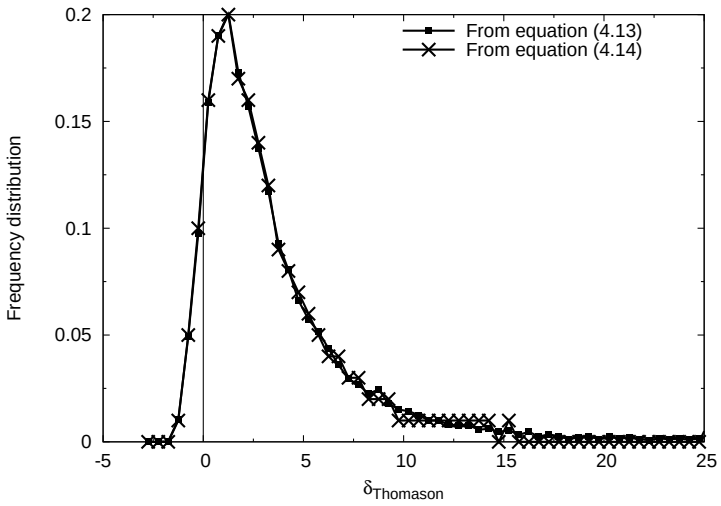

Figure 4.27: Effect of the secondary porosity on the frequency distribution of $\delta_{Thomason}$ in the DP11 specimen at the last strain step.

The results are given in Table 4.3. This comparison shows that the number of couples presenting a positive criterion of Brown and Embury is very inferior to the number of couples presenting a positive criterion of Thomason (except in the ferritic steel case).

	Positive B&E criterion	Positive Thomason criterion
DP11	189	1294
DP11T	148	260
DP62	33	1209
Ferritic steel	268	132
Martensitic steel	64	105

Table 4.3: Number of couples of neighboring cavities having a positive Brown and Embury criterion and a positive Thomason criterion at the last strain step.

To understand the origin of these differences, each couple of neighboring voids present in the imaged specimens were represented on a $\chi - W$ graph given in Figure 4.28. The void coalescence criteria of Brown and Embury and Thomason were also represented. The Brown and Embury criterion is the same whatever the material since it is only a geometrical criterion whereas the Thomason criterion depends on the stress inside the specimen and thus differs from one specimen to another. The couples of voids presenting a positive criterion are located on the top right corner of the graph. Figure 4.28

shows that in every studied steels, except in the ferritic steel, the Brown and Embury's criterion is more limiting that the Thomason's criterion. To be positive, the Brown and Embury's criterion requires couple of cavities with both quite high values of χ and W whereas the Thomason's criteria mainly needs a high value of χ. In the ferritic case, as the voids are very elongated (and thus have a high value of W), some couples give a positive Brown and Embury while their Thomason criterion is negative.

To confirm if the number of couples of voids being coalescing has to be calculated using the criterion of Brown and Embury or the Thomason's one, couples of voids present in the DP11 specimen and in the ferritic steel specimen and actually coalescing at the next studied strain step were prospected in the sub-volumes. These couples of voids are underlined in red in Figure 4.29(a) and (b). Figure 4.29(a) shows that the five couples coalescing in the DP11 sample have a positive Thomason criterion while only two couples also have a positive Brown and Embury criterion. In the ferritic steel (see Figure 4.29(b)), the five underlined couples coalescing at the next step have positive criteria of Thomason and Brown and Embury whereas a lot of couples have a positive Brown and Embury criterion and a negative Thomason criterion. These observations lead to favor the Thomason's criterion to calculate the number of coalescing couples of neighboring voids.

4.3.3 Link between the local events of coalescence and the macroscopic coalescence

The density of couple presenting a positive criterion of Thomason $N_{positiveThomason}$ is thus calculated for each step of deformation. The evolution of $N_{positiveThomason}$ with the strain is given in Figure 4.30 for each studied steel. An increase of $N_{positiveThomason}$ is observed at the end of the tensile test, close to the final fracture. In the bi-phased steels, this increase is really high and exponential whereas in the single-phased materials the increase is moderate and even undetectable for the martensitic steel.

The local events of coalescence thus play a role in the final fracture of the materials although they are not totally linked to the macroscopic coalescence. In the current situation, the more probable way of connecting the local events of coalescence to the macroscopic coalescence consists in the use of the percolation theory. An attempt to predict the macroscopic coalescence from the local events of coalescence using this approach is presented here for the DP11 specimen.

The frequency distribution of the distance between neighboring cavities $p(\lambda)$ measured at each step of deformation was modeled using the tessellation theory [Unde 70]:

$$p(\lambda) = 2CN^{2/3}\lambda \exp(-CN^{2/3}\lambda^{2/3}) \tag{4.18}$$

C being a constant and N the void density measured in Chapter 2.
$C = \frac{\pi}{2}$ was identified to obtain the best fit of the modeled distribution on the experi-

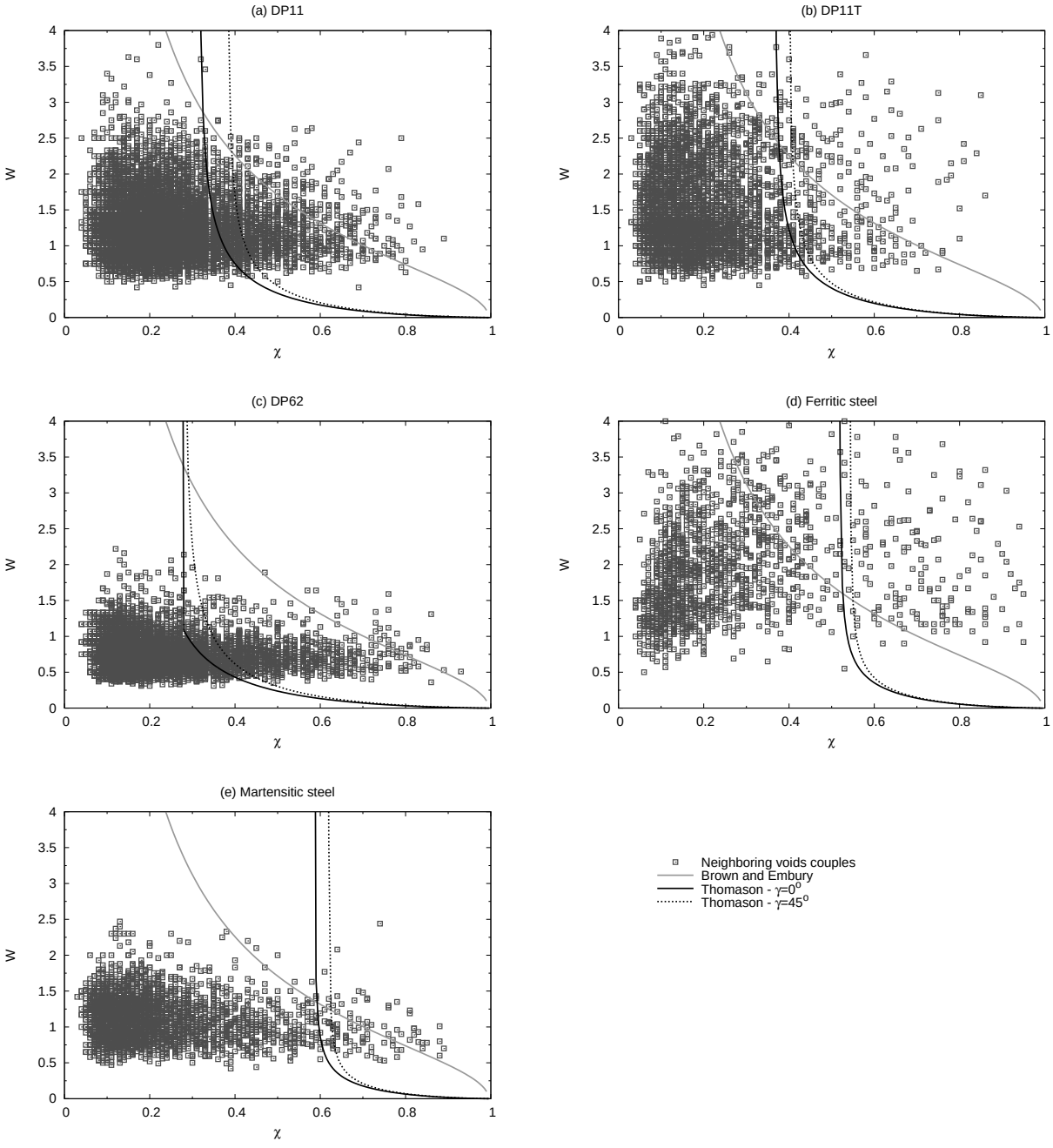

Figure 4.28: Graphical representation of the couples of neighboring voids, the Brown and Embury criterion and the Thomason criterion in the last step of deformation in the different studied materials.

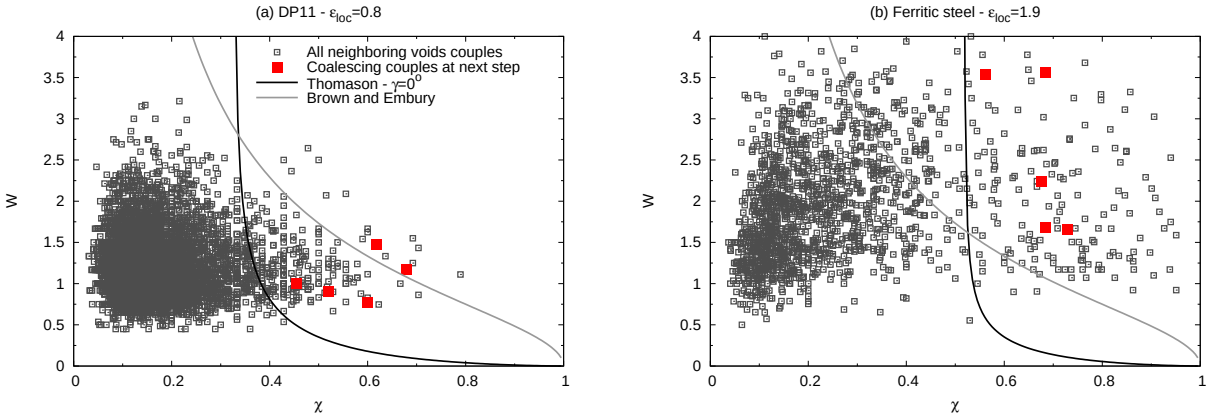

Figure 4.29: Comparison of the predictions of the Brown and Embury criterion, the Thomason criterion and the couples actually coalescing in the DP11 specimen and in the ferritic steel.

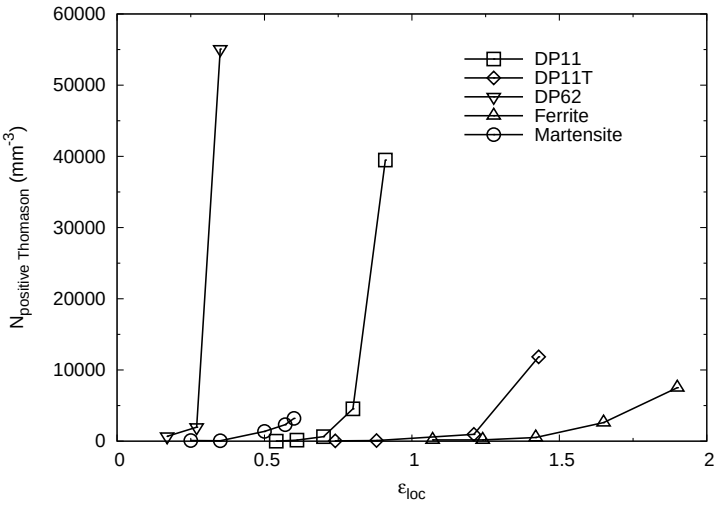

Figure 4.30: Evolution of the density of couple presenting a positive criterion of Thomason with the strain in every investigated materials.

mental data given in Figure 4.31. The actual distribution is slightly underestimated by the modeled distribution.

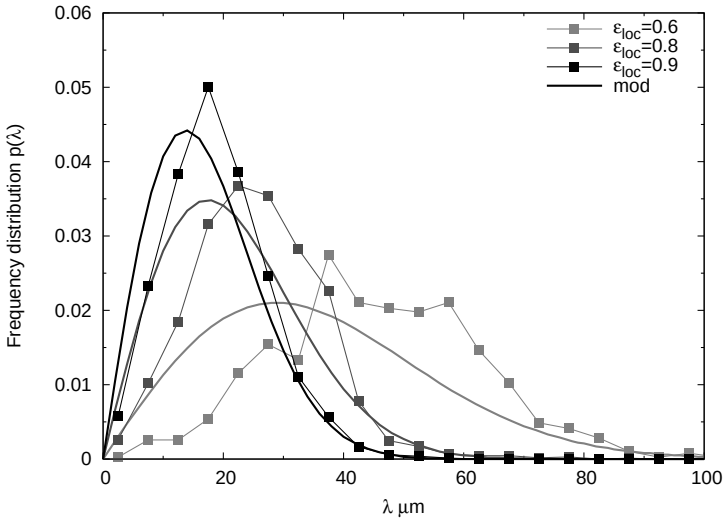

Figure 4.31: Modeling of the frequency distribution of the distance between closest cavities.

Assuming that a local event of coalescence occurs when the distance between the cavities becomes inferior to a critical distance λ_C, the fraction of coalescing couples of void f_C is calculated using the modeled frequency distribution of the distance between neighboring cavities $p(\lambda)$:

$$f_C = \int_0^{\lambda_C} p(\lambda)\,\mathrm{d}\lambda \tag{4.19}$$

$$= 1 - \exp\left(-CN^{2/3}{\lambda_C}^2\right) \tag{4.20}$$

f_C is experimentally known using the void density N and the density of couples having a positive Thomason criterion $N_{positiveThomason}$:

$$f_C = \frac{N_{positiveThomason}}{N + N_{positiveThomason}} \tag{4.21}$$

Combining Equations 4.20 and 4.21, an expression is found for λ_C:

$$\lambda_C = \sqrt{\frac{1}{CN^{2/3}} \ln\left(1 + \frac{N_{positiveThomason}}{N}\right)} \tag{4.22}$$

The values of λ_C depending on the deformation are calculated using Equation 4.22. Figure 4.32 compares λ_C with the mean distance between closest cavities λ^* calculated

for the distribution $p(\lambda)$ [Unde 70]:

$$\lambda^* = \frac{0.554}{N^{1/3}} \tag{4.23}$$

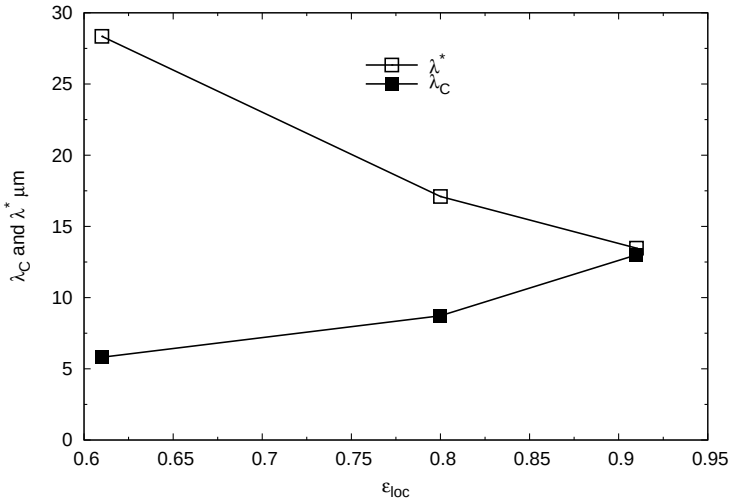

Figure 4.32: Comparison of the critical distance between cavities for local events of coalescence λ_C with the mean distance between closest cavities λ^*.

Figure 4.32 shows that the macroscopic coalescence *i.e.* the percolation of the local events of coalescence occurs when the critical distance leading to a local event of coalescence becomes equal to the mean distance between closest cavities in the case of the DP11 specimen. More investigations in this direction are nevertheless required to validate this approach.

4.4 Summary

→ For the first time, the step of void coalescence was experimentally characterized in an industrial material. This experimental characterization more particularly showed that local events of coalescence between close cavities occurred before the macroscopic coalescence and led to the sample fracture.

→ Two void coalescence criteria, the Brown and Embury's one and the Thomason's one, were tested on the experimental data both in a macroscopic way and in a local way. The macroscopic implementation of the coalescence criteria gave acceptable results. However, the local approach is probably the closest of the real nature of void coalescence in the studied steels because it takes into account the local events of coalescence occurring during the tensile test.

→ The correlation between the actual coalescing couples of cavities and the local implementation of the two criteria showed that the Thomason criterion is probably the most adapted criterion to predict the local events of coalescence in the case of the tested materials.

→ To complete this study of the void coalescence, an approach linking the local events of coalescence and the macroscopic coalescence was developed. The better current lead is based on the percolation theory of the local events of coalescence.

Chapter 5

Further work: Application to complex loading tests

The tools developed in the previous chapters were used here with the purpose of characterizing the three steps of ductile damage in DP11 samples subjected to a complex loading tests including a change of path. The DP11 material was first strained in the rolling direction and then in the perpendicular direction. The effect of such a loading on ductile damage was thus investigated.

5.1 Motivations

The main motivation of performing complex loading tests is to validate some assumptions done in this work in particular concerning the study of the void nucleation and of the void growth steps. In Section 2.3 concerning the modeling of the void nucleation, the kinematic part of the strain hardening X appears in the modified equation of the Argon's criterion. Furthermore, X is assumed to be responsible for the faster growth in the martensite specimen and in the DP samples (see Section 3.3.2). In order to experimentally check these assumptions, the kinetics of damage were investigated in DP11 samples subjected to complex loading tests. This kind of tests gives the possibility to modify the value of X.
The tensile test is not the mechanical test inducing stresses being the most representative of the forming. Cold rolling has then also been carried out to validate the consistency of the results.

5.2 Experimental set up

Complex loading tests cannot be completely achieved in *in-situ* conditions. A pre-deformation was thus applied on the initial sheet of DP11 steel before cutting the specimens introduced in Section 1.1.1.3. The tensile direction of the *in-situ* tensile tests was chosen to be perpendicular to the direction of pre-deformation as imaged in Figure 5.1.

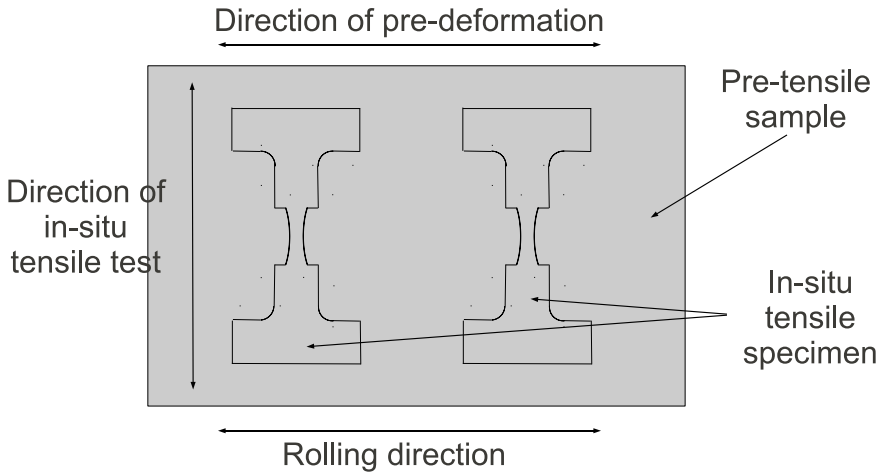

Figure 5.1: Configuration of the complex loading tests.

Two kinds of pre-deformation were applied:

- The initial DP11 steel was strained using large specimens on a conventional tensile machine along the rolling direction. The applied pre-strain had to be inferior to the necking strain to induce a uniform deformation inside the specimen. Two pre-deformations were applied in this way: a pre-strain of 5% and a pre-strain of 15%. The data acquired in the pre-strained 5% specimen is not used in this manuscript because of the presence of damage banding (other cases of damage banding were observed and more information on the effect on damage can be found in Appendix B).

- In order to have a more important pre-deformation, the initial sheet of DP11 steel was rolled until an equivalent deformation in the rolling direction of 28%.

In-situ tensile test specimens were subsequently cut in the pre-deformed materials and classical *in-situ* tensile tests (described in Section 1.1.1.3) were carried out to investigate the effect of these pre-deformations on ductile damage.

5.3 Damage characterization in DP11 specimen undergoing a complex loading test

Damage appearing during the second part of the test were analyzed using the work performed in Chapters 2, 3 and 4. The effects induced by the complex loading test on void nucleation, void growth and void coalescence were then investigated.

5.3.1 Void nucleation

The void density measured in both pre-strained and pre-rolled DP11 samples are given in Figure 5.2. The figure compares the kinetic of nucleation in a standard DP11 specimen with the pre-strain and the pre-rolled ones. The pre-deformation induces few events of nucleation. During the *in-situ* tensile test, voids nucleate faster in the pre-rolled and the pre-strained samples than in the standard specimen.

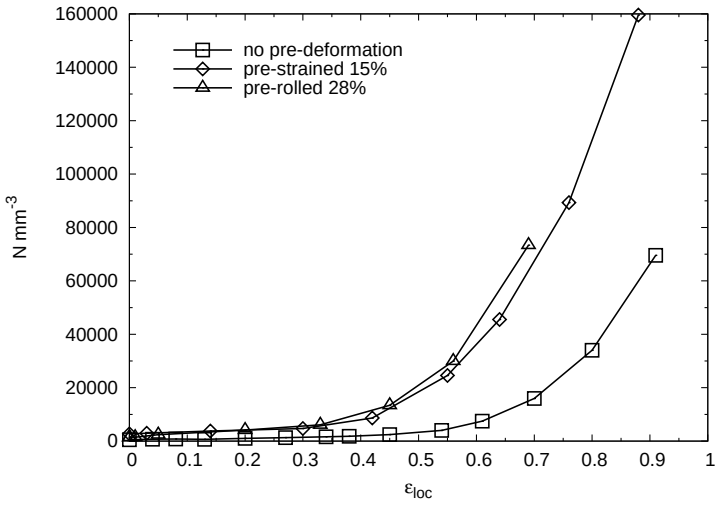

Figure 5.2: Measured void density in the pre-strained, the pre-rolled and the standard DP11 specimens.

The prediction of the kinetic of nucleation developed in Section 2.3 was then used to model the void density in these pre-deformed samples. The steel used for the pre-deformed specimens being the same as for standard specimen, the value of the ferrite/martensite interface strength σ_C was kept the same. The difference in the kinetic of void nucleation can only be a consequence of the change in the value of the kinematic part of the strain hardening X. The modeled kinetic was thus applied on the experimental data with the parameter A and N_0 initially found, the new fitting parameter being X. The modelings resulting from the fitting procedure are given in Figure 5.3 and the values of X estimated in this way for each specimen are given in Table 5.1. As expected, the values of X found for the pre-deformed samples are higher than the one initially calculated for the standard DP11 material (using the microstructural parameters of the DP11 material, see page 58). Note that the X value of the pre-rolled sample is slightly higher than the one of the pre-strain sample, the pre-deformation being higher in the pre-rolled sample.

	X (MPa)
no pre-def	200
pre-strained 15%	500
pre-rolled 28%	550

Table 5.1: Values for X estimated to fit the nucelation modeling on experimental data.

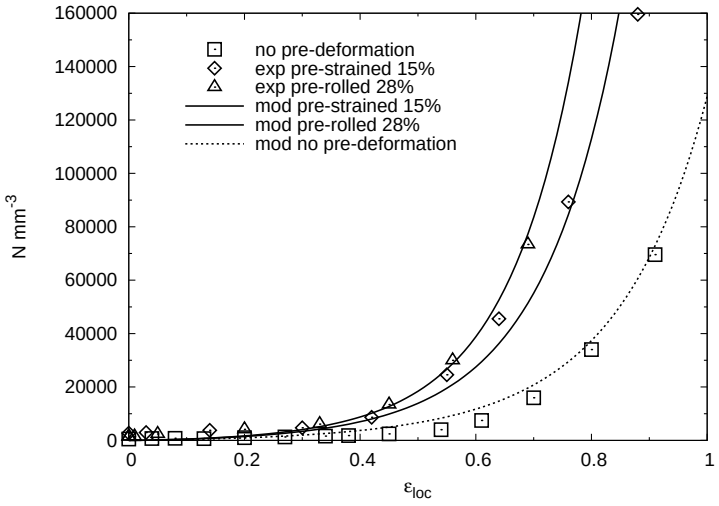

Figure 5.3: Modeling of the void density in the pre-deformed DP11 specimens.

5.3.2 Void growth

5.3.2.1 Volume change

Like the void nucleation, the step of void growth was characterized using the tools described in Chapter 3. The evolution of the equivalent diameter of the 20 largest cavities present in the studied stub-volume of the pre-deformed DP11 samples is given in Figure 5.4. As expected, the growth of the cavities in these specimens is higher than in the standard specimen. This faster growth is quantified using the parameter α_{Huang} extracted from the Huang prediction. Found values of α_{Huang} are given in table 5.2. Note that larger values of α_{Huang} are found for the pre-deformed samples and a even higher value is obtained for the pre-rolled specimen. This data confirms that the kinematic hardening has an influence on the kinetic of growth and that the pre-rolled sample has a higher value of X than the pre-deformed sample, this observation being already noted in the previous section.

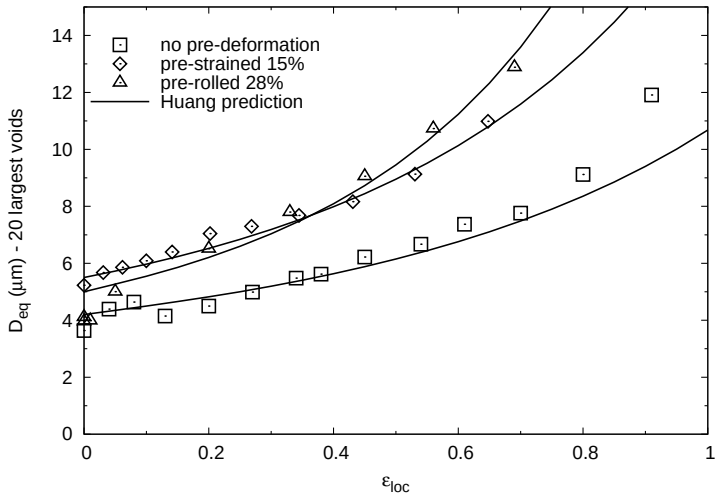

Figure 5.4: Effect of the pre-deformation on the void growth.

	α_{Huang}
no pre-def	0.55
pre-strained 15%	0.65
pre-rolled 28%	0.85

Table 5.2: Values of α_{Huang} for the pre-deformed DP11 samples.

5.3.2.2 Void shape change

Because of the the pre-deformation, the shape of the voids is modified. Figure 5.5 shows the evolution of the void dimensions of the 20 largest cavities in the pre-deformed specimens and compares them to the one of the standard DP11 specimen.

- In the pre-strained specimen, cavities are first elongated in the pre-deformation direction. Then the applied tensile deformation leads the voids to mainly grow in the tensile direction. The evolution of the void aspect ratio W (Figure 5.6) shows that the voids become as elongated as in the standard specimen.
- The initial voids in the pre-rolled specimen first have a penny-shape. The applied tensile deformation makes them mainly grow in the tensile and in the pre-rolling directions. Finally, the cavities have a less elongated shape that in the pre-strained and in the standard specimens.

5.3.3 Void coalescence

Concerning the step of void coalescence, no particular effect of the kinematic part of the strain hardening was observed in the previous work. The frequency distribution of the distance between cavities λ at the step before fracture was determined in the pre-deformed specimens and compared to the one measured in the standard specimen in Figure 5.7. The frequency distribution measured in the three specimens is quite similar. This reinforces the conclusion that kinematic hardening does not seem to have an influence on the void coalescence step.

Following the conclusions of the work presented in Chapter 4, the Thomason criterion was tested on every couple of neighboring cavities present in the studied sub-volume of the pre-deformed specimens. The graphical representation of the couples of voids at the last step of strain before fracture as well as the Thomason criterion are given in Figure 5.9. No particular difference is observed in the pre-deformed samples compared to the standard specimen. Figure 5.8 shows that the increase of the number of couples having a positive Thomason criterion occurs sooner in the pre-deformed samples than in the standard DP11 specimen. This observation is simply a consequence of the higher void density and the larger void growth and it leads to a decrease of the fracture strain.

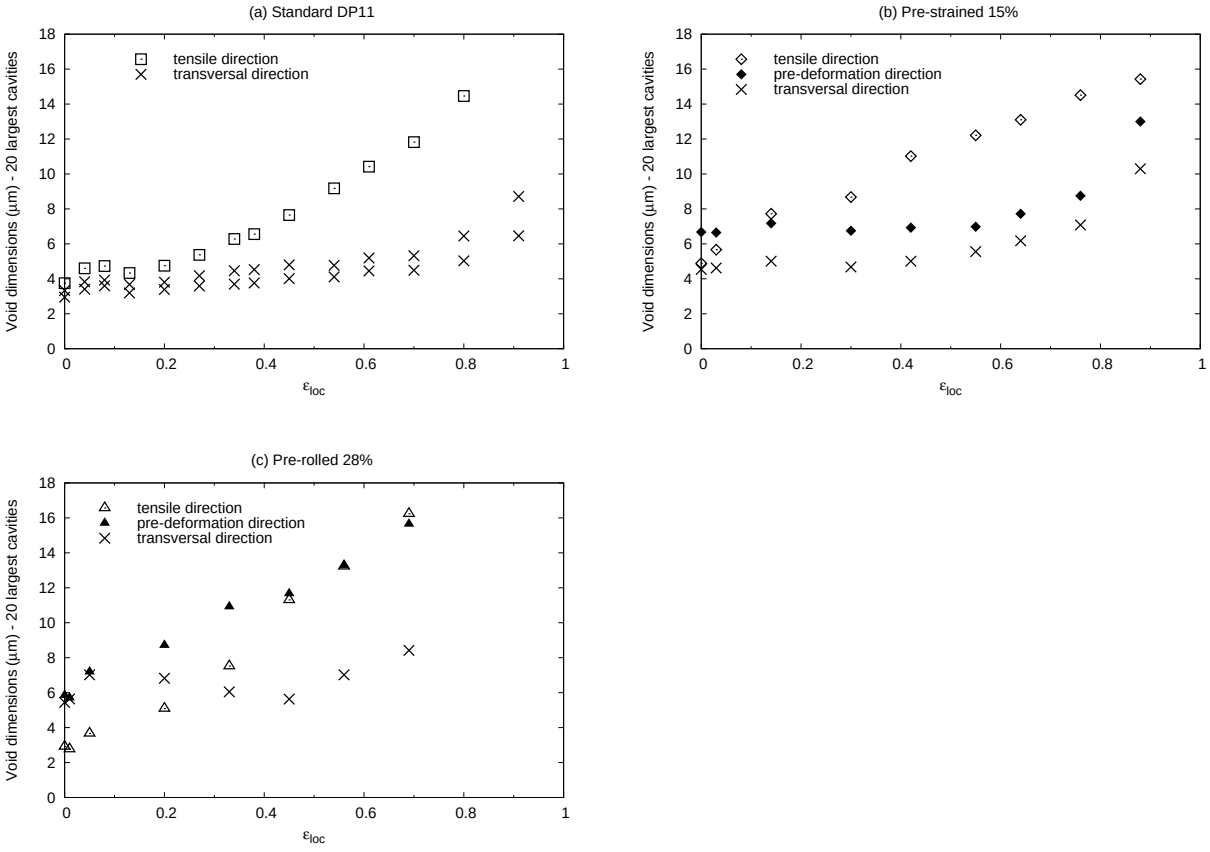

Figure 5.5: Experimental measurements of the void dimensions of the 20 largest cavities in the pre-deformed specimens.

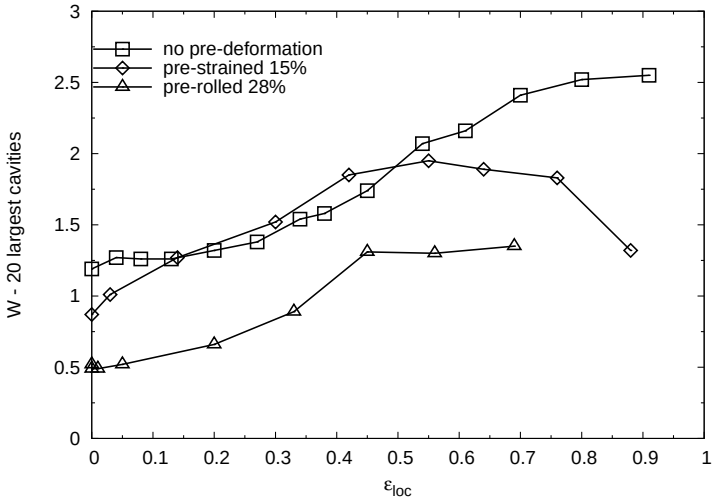

Figure 5.6: Evolution of the void aspect ratio W in the pre-deformed specimens.

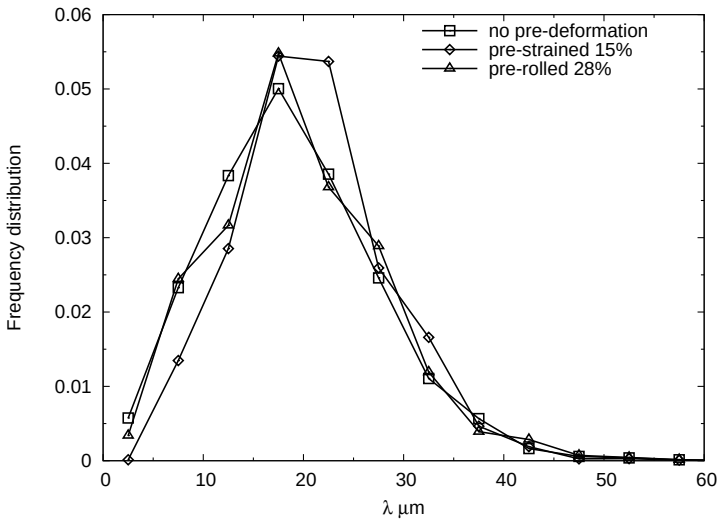

Figure 5.7: Effect of pre-deformation on the frequency distribution of λ.

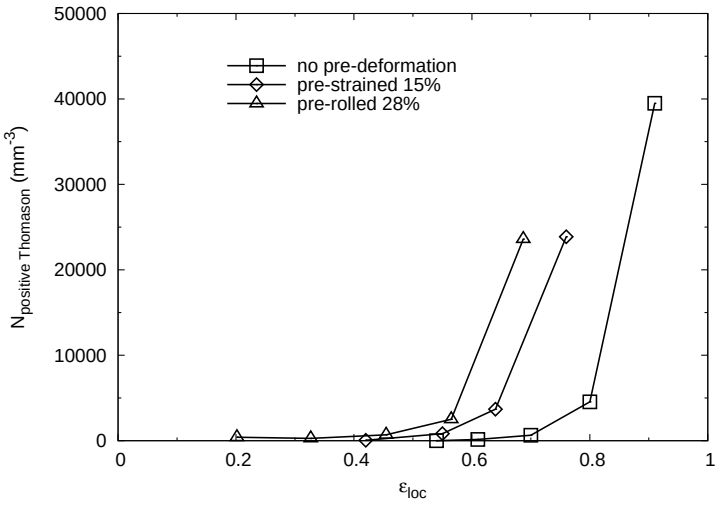

Figure 5.8: Density of couples having a positive Thomason criterion in the pre-deformed DP11 specimens.

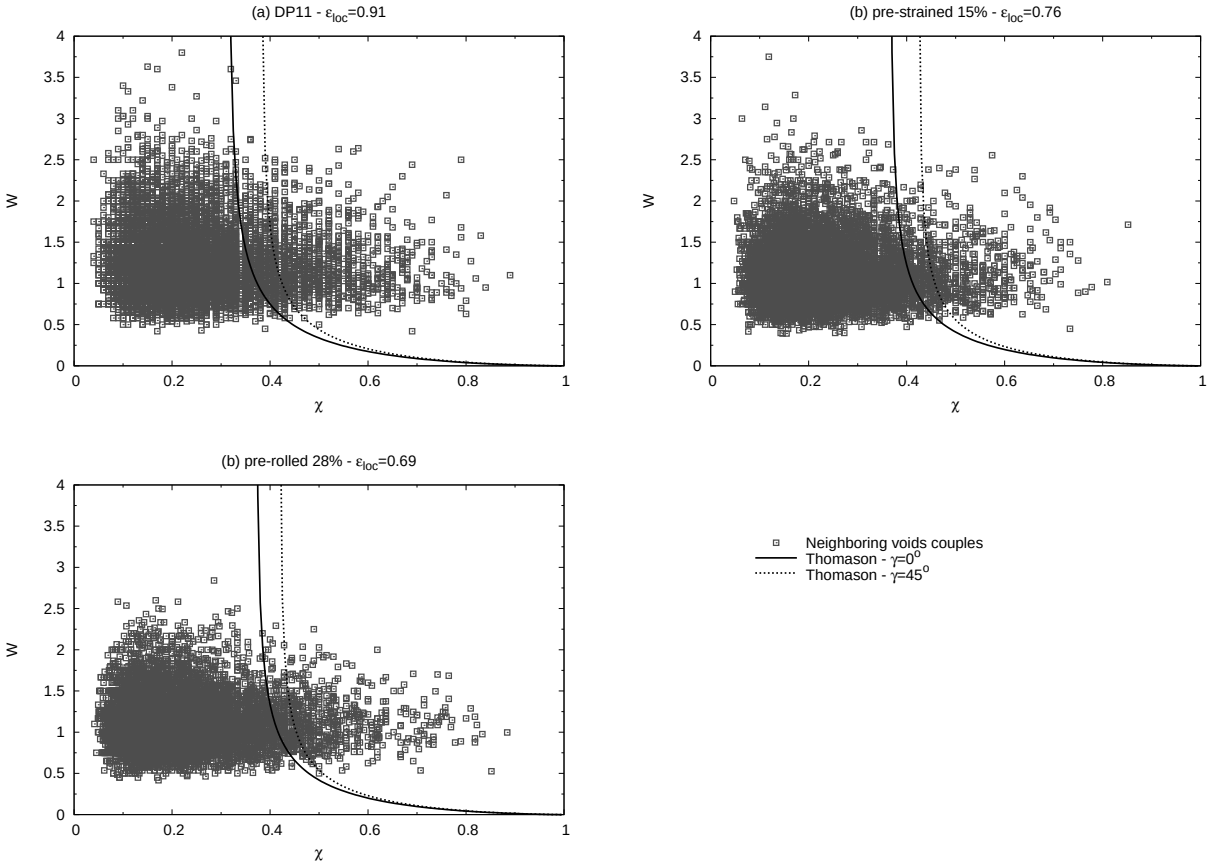

Figure 5.9: Graphical representation of the couples of neighboring voids and the Thomason criterion at the last step of strain before fracture.

5.4 Summary

Complex loading tests were performed by testing pre-strained and pre-rolled specimens of DP11 steel. The effects on ductile damage of this particular mechanical solicitation were thus investigated:

→ Complex loadings inducing a higher value of the kinematic part of the strain hardening, the assumptions concerning the involvement of X on void nucleation and void growth were confirmed. Indeed a higher value of X induces a higher void nucleation and a faster growth. However, the kinematic hardening is probably not the only catalyst for damage.

→ No influence on the step of coalescence was observed in the pre-deformed specimens. The smaller values of fracture strains in these specimens is simply due to the higher void nucleation and the faster growth.

Conclusions and perspectives

The purpose of this thesis was to characterize ductile damage in Dual-Phase steels and obtain quantitative data concerning the damage nucleation, the void growth and the coalescence. This data was then used to develop or validate analytic models concerning every steps of damage. The main contributions are described below:

- Quantitative data concerning every steps of ductile damage was obtained using X-ray tomography. The void nucleation was characterized using the number of cavities present in the studied volume, the void growth using the equivalent diameter and the main dimensions of the twenty largest voids of the volume and the void coalescence using the distance between cavities. For the first time, void coalescence was experimentally and quantitatively characterized in an industrial steel.

- The ferritic phase and the martensitic phase composing the DP steels microstructure were distinguished inside a same sample using X-ray tomography. A particular technique, the holo-tomography was used. Ferrite and martensite could only be visualized in a non-deformed sample, the contrast being lost when the specimen was strained.

- The quantitative data concerning the void nucleation was employed to developed a modeling predicting the kinetic of void nucleation in the studied steels either based on a stress criterion of decohesion or based on a strain criterion of particle fracture, depending on the observed nucleation mechanism. The ferrite / martensite interface stress of the studied DP steel was estimated using this prediction.

- By using the quantitative measurements on the void growth performed on several notched specimens, the Huang's correction of the void growth model of Rice and Tracey, which better takes into account the effect of triaxiality, was experimentally validated. The use of this model also showed that microstructural parameters not taken into account in this simple model, in particular the yield stress of the material, have an influence on the growth of cavities.

- For the first time, the Brown and Embury criterion and the Thomason criterion were experimentally tested on the strained specimen. Both criteria were locally applied on every couples of neighboring voids. This local approach showed that the Thomason criterion was the most adapted to predict the local events of coalescence.

- The effect of tempering on ductile damage was investigated using tempered DP samples. A sufficient tempering leads to a decrease of the void nucleation and the change of the nucleation mechanism. The void growth rate with strain was also reduced.

- The effect of the kinematic part of the strain hardening on damage was emphasized in this work. It was observed that kinematic hardening influences the void nucleation and accelerate the void growth. These observations were validated by performing complex loading test, this kind of test increasing the kinematic hardening.

This work clarified some points concerning the ductile damage in the DP steels. This kind of study using X-ray tomography is easy to implement to characterized damage in various materials.
Some items processed in this work can be employed for complementary investigations:

- 3D experimental data was used here to develop or validate only analytic models of ductile damage. However, this data is also adapted to work with numerical simulations. A first approach was attempted by Ben Bettaieb *et al.* [Bett 11]. Data acquired from the tomogramms can also be directly transfered to finite elements codes using dedicated plugins. The main advantage of numerical simulations is the ability to quantify the influence of some mechanical parameters. For example, the effect of the kinematic hardening could be quantitatively investigated using finite element modeling.

- The significance of the ferrite/martensite interface decohesion in the void nucleation process was emphasized in this work. The weak value of the interface strength of the studied DP11 material was the source of the high void density observed in this DP steel. Although the interface strength depends on the chemical composition of the DP steel and an investigation dedicated to this subject could propose a way of reinforcing the ferrite/martensite interface.

- Some tools were developed in this work to study and quantify the coalescence step of damage. They were applied to industrial materials which exhibit some inconveniences like the increasing number of cavities. In order to better understand the link between the local events of coalescence and the macroscopic coalescence, these tools could be used to characterize coalescence in model materials, the fabrication of which becomes easier in the recent period thanks to rapid prototyping for instance.

The final purpose of this study on damage in DP steels is to be used to design a optimum DP steel grade which exhibits the better compromise between strength and resistance to damage.

Appendix A

Macroscopic measurements

Thanks to the volumes imaged by X-ray tomography, the outer shape of the specimen is known for each step of deformation. From the evolution of the outer shape of the specimen, useful macroscopic mechanical properties, describing the tensile test (local strain, true stress) and playing an important part in damage evolution (equivalent stress, triaxiality), are calculated in this appendix.

A.1 Tensile properties measurements

A.1.1 Local deformation

The local tensile deformation in the smallest section of the specimen ε_{loc} is calculated using the areas of the initial minimal section before deformation S_0 and of the current minimal section of the characterized step of deformation S. Using this local value of the deformation is consistent in this work because damage is concentrated at the center of the specimen and only a central volume situated close to the minimal section is analyzed (as seen in Section 1.1.1.4).

$$\varepsilon_{loc} = \ln\left(\frac{S_0}{S}\right) \tag{A.1}$$

In Section 3.3.4, the lateral deformation ε_{trans} is needed. The deformations in both transversal directions ε_x and ε_y were experimentally measured in DP11 smooth and notched specimens. Figure A.1 shows the experimental measurements of ε_x and ε_y. The figure confirms that the deformation can be considered as isotropic and then:

$$\varepsilon_{trans} = -\frac{\varepsilon_{loc}}{2} \tag{A.2}$$

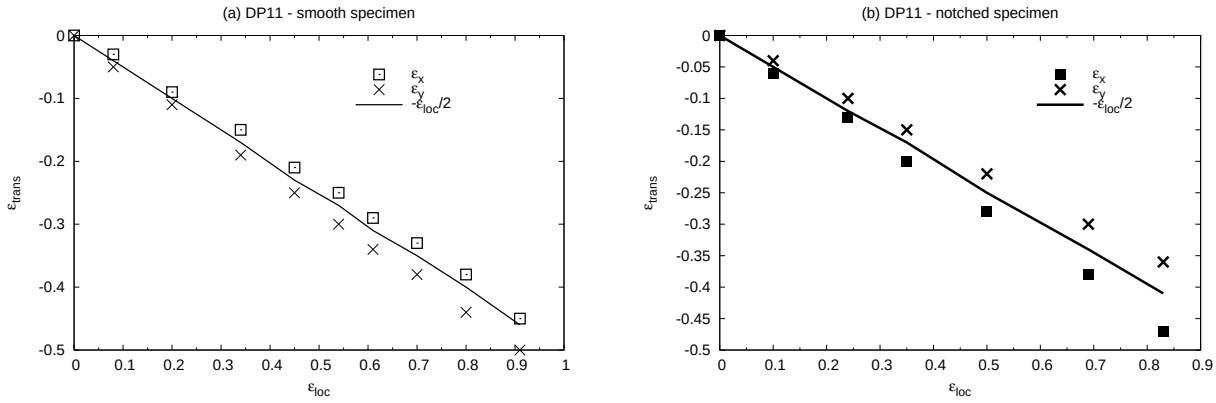

Figure A.1: Measurement of the transversal deformations in (a) a smooth specimen of DP11, (b) in a notched specimen of DP11.

A.1.2 True stress

Knowing the area of the minimal section of the specimen allows the calculation of the true stress σ_{zz} in this section using the measured force F given by the sensor during the tensile test.

$$\sigma_{zz} = \frac{F}{S} \tag{A.3}$$

The σ_{zz}-ε_{loc} curves of the five steels investigated in this work are given in Figure A.2.

A.2 Equivalent stress and triaxiality determination

A.2.1 The Bridgman analysis

In notched specimens or when necking appears during the tensile test, transversal stresses are generated in the directions perpendicular to the tensile one. These induced stresses were widely studied by Bridgman [Brid 45]. In this work, Bridgman realized a geometrical analysis of the stresses induced by the presence of a notch in a specimen. The geometric parameters involved to this study are given in Figure A.3. Resulting from this analysis, the local value of the stress triaxility T in an axisymmetric specimen at the radial coordinate a, for $0 \leq a \leq r_{Section}$ is:

$$T = \frac{1}{3} + \ln\left(\frac{{r_{Section}}^2 + 2r_{Section}R_{Notch} - a^2}{2r_{Section}R_{Notch}}\right) \tag{A.4}$$

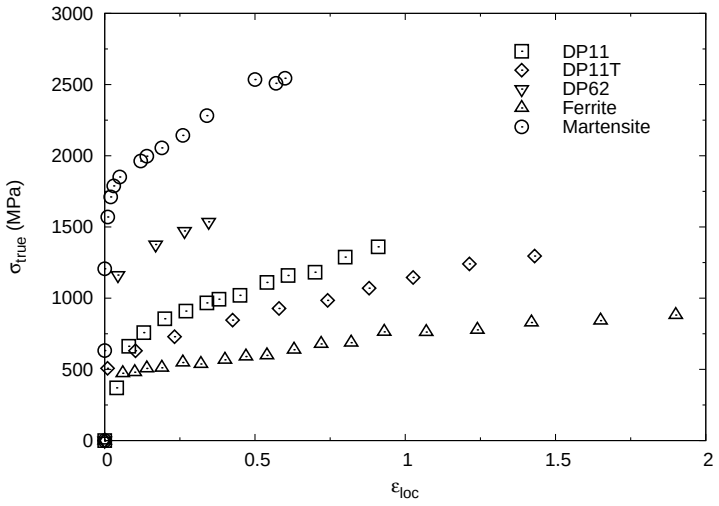

Figure A.2: Measurements of the true stress in the five studied steels.

Therefore the triaxility is maximum at the center of the specimen, where $a = 0$. The maximal value of the triaxiality in the specimen is then:

$$T = \frac{1}{3} + \ln\left(1 + \frac{r_{Section}}{2R_{Notch}}\right) \tag{A.5}$$

This formula, known to underestimate the value of the triaxiality at the center of the specimen was re-assessed by Wierzbicki and Bao [Wier 04] using numerical simulations. The result of this simulation is shown in Figure A.4. As a result of this additional work, a better expression to calculate the maximal value of the triaxialiaty is:

$$T = \frac{1}{3} + \sqrt{2}\ln\left(1 + \frac{r_{Section}}{2R_{Notch}}\right) \tag{A.6}$$

Furthermore, a more global study of Bridgman [Brid 64] evaluated from this triaxiality analysis the ratio between the true stress σ_{zz} and the equivalent stress σ_{eq}:

$$\frac{\sigma_{zz}}{\sigma_{eq}} = \left(1 + \frac{2R_{Notch}}{r_{Section}}\right)\ln\left(1 + \frac{r_{Section}}{2R_{Notch}}\right) \tag{A.7}$$

A.2.2 Experimental results

Using the acquired volumes, the values of the radius of the minimal section and of the notch radius are extracted from the outer shape of the specimen. These experimental parameters were then employed to determine the values of the equivalent stress and of the stress triaxiality for each step of deformation.

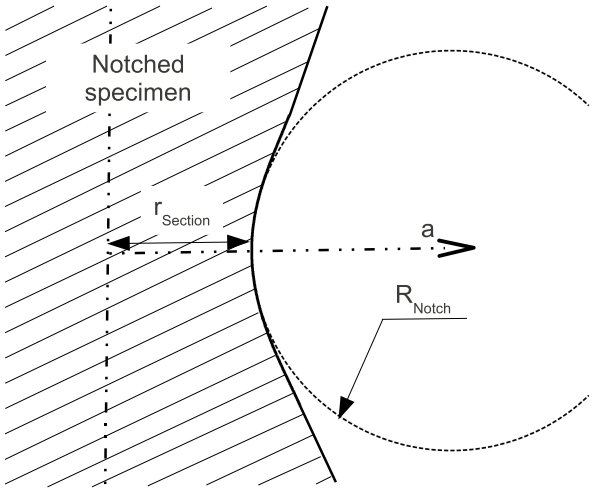

Figure A.3: Geometric parameters involved in the triaxiality calculation.

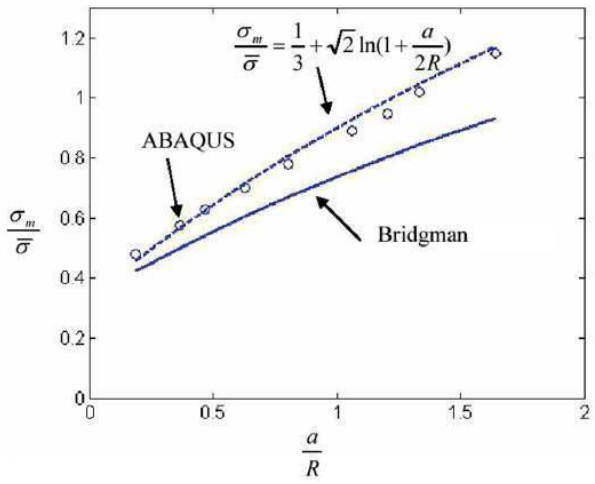

Figure A.4: Re-assessment of the Bridgman formula by Wierzbicki and Bao [Wier 04].

A.2.2.1 Triaxiality

The expression given in equation A.6 is used here to determine the value of the triaxiality for each imaged specimen. The evolutions of the triaxialiaty in a smooth and two different notched specimens of a DP11 steel are given in Figure A.5. The different geometries of notches effectively induce various ranges of triaxiality. Figure A.6 shows the triaxilities calculated from eq. (A.6) in smooth specimens of the different studied steels. In smooth specimen, initial triaxiality has to be equal to 1/3. However, the machining of the specimens can lead to a sample with a slight notch inducing a higher value of triaxiality (around 0.4 in the cases of ferrite and martensite specimens). The evolution of the triaxiality in smooth specimens is quite the same from a material to another: a parallel evolution of T is observed with the deformation except for the DP62 sample.

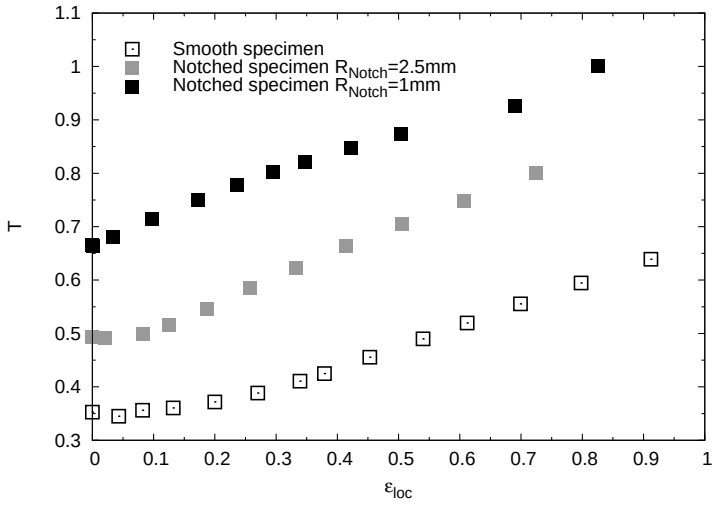

Figure A.5: Evolution of T calculated from eq. (A.6) in DP11 specimens with different notch geometries.

A.2.2.2 Equivalent stress

Figure A.7 shows the comparison between the longitudinal true stressσ_{zz} and the equivalent stress σ_{eq} in smooth and notched specimens of DP11. In the smooth specimen, differences between σ_{zz} and σ_{eq} appear when the necking starts forming and the gap between the two remains quite weak.

Since the equivalent stress is a parameter representative of the mechanical behavior of the materials frequently used in damage modelings, the experimental curves σ_{eq} vs

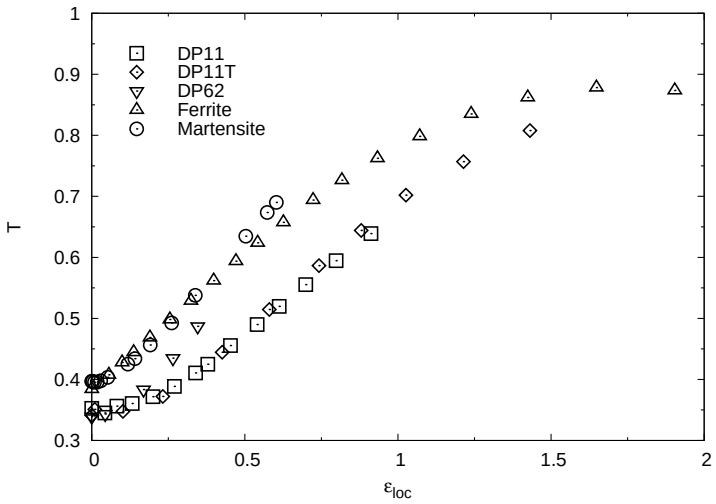

Figure A.6: Evolution of T calculated from eq. (A.6) in smooth specimen of the different studied steels.

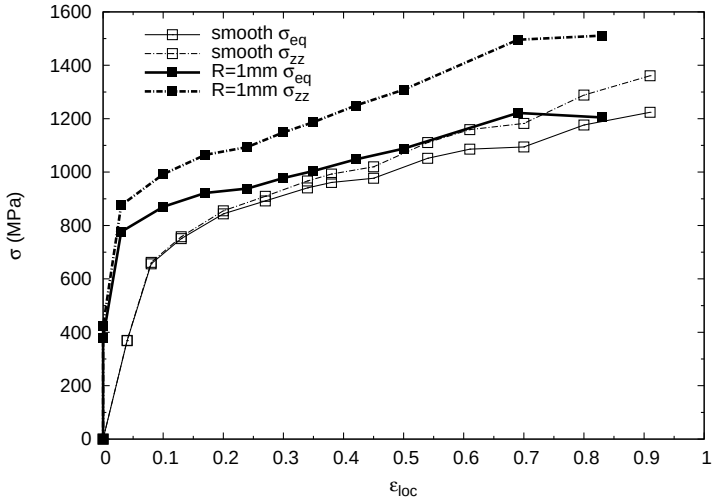

Figure A.7: Comparison of σ_{zz} and σ_{eq} for smooth and notched specimens of DP11.

ε_{loc} were fitted using a traditional power law:

$$\sigma_{eq} = k_\sigma {\varepsilon_{loc}}^n \tag{A.8}$$

Figure A.8 shows the result of these fits for each studied steel and the determined values of the parameters n and k_σ are given in Table A.1.

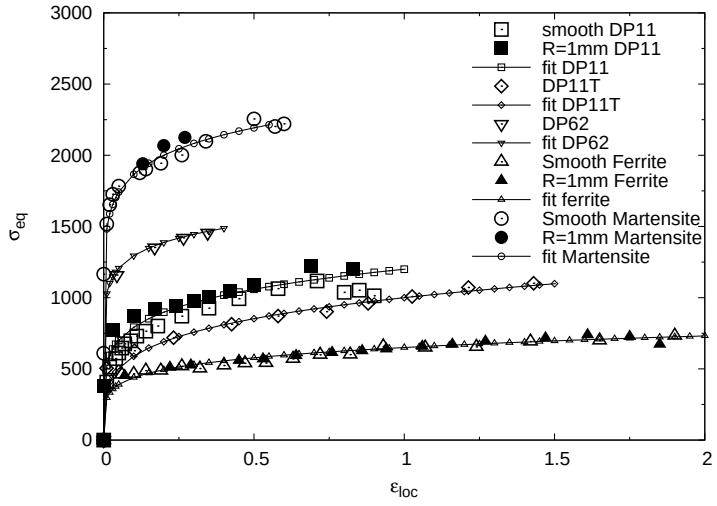

Figure A.8: σ_{eq} vs ε_{loc} curves for all studied steels.

Steel	k_σ	n
Ferrite	650	0.17
DP11	1200	0.18
DP11T	1000	0.23
DP62	1630	0.1
Martensite	2350	0.1

Table A.1: Fitted values of n and k_σ.

A.3 Validation using finite elements simulation

Since the average values of the local deformation ε_{loc} and the stress triaxiality T respectively calculated from the equations (A.1) and (A.6) were used in the modeling sections, these values have to be the calculated with a high degree of confidence. The use of the equations (A.1) and (A.6) was thus validated using numerical simulations. This work was performed by Liza Lecarme, PhD student at the Institute of Mechanics, Materials

and Civil Engineering, at the Université Catholique de Louvain, Belgium. The geometry of a smooth 3D specimen and a notched 2D axisymmetric specimen with a radius of 1mm were simulated in order to evaluate the accuracy of using the calculated values of ε_{loc} and T for the local deformation and the triaxiality in the center of the specimen required in the damage modelings. FE simulations were performed using the commercial code Abaqus and the open-source mesh generator Gmsh [Geuz 09]. The matrix of both specimens is modeled as an isotropic J2 material, with the hardening law given by experimental results for DP11 (see Figure A.8). The local effective strain ε_{center} and the stress triaxiality T are extracted from the element located at the center of the minimum section of each specimen. The values obtained from the numerical simulations are compared in Figure A.9 and Figure A.10 respectively to the ones calculated from the experimental data and using equations (A.1) and (A.6). Concerning the deformation, the agreement between the analytical solution and the numerical simulation is very good for the notched sample. In the smooth specimen, the value calculated for ε_{loc} is lower that the one given by the simulation particularly for values of the strain higher than 0.5 but the discrepancy between the two is rather small. Concerning the triaxiality, the same conclusion can be drawn: using the values calculated using equation (A.6) and the experimental measurement of the shape of the sample gives an estimation reasonably close to the numerical simulation in our case.

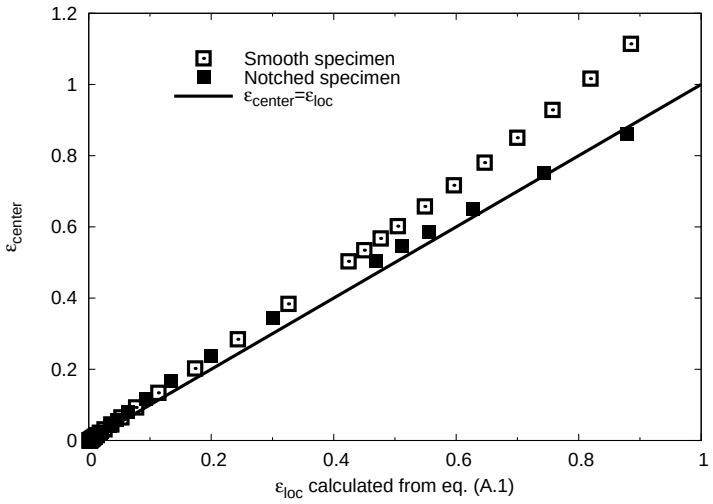

Figure A.9: Comparison of the experimental value of ε_{loc} and the one calculated at the center of the specimen using the numerical simulations.

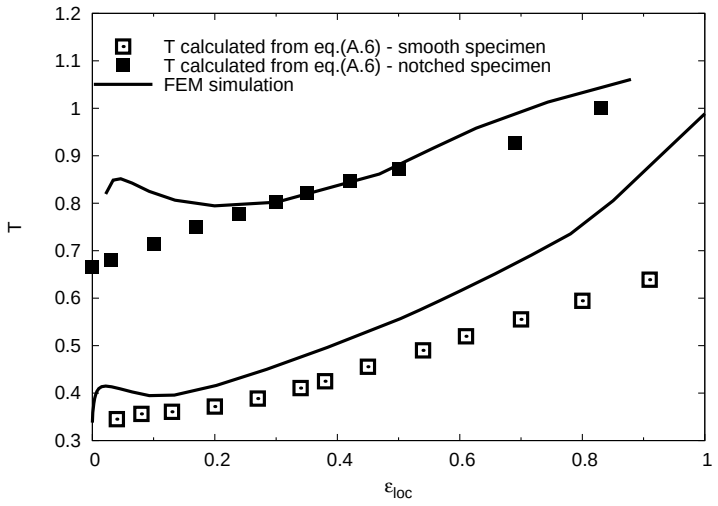

Figure A.10: Comparison of the experimental value of T and the one calculated at the center of the specimen using the numerical simulations.

A.4 Summary

The monitoring of the outer shape of the specimen during the tensile deformation brings information on the specimen geometry being not available in classical tensile tests. The minimal section and the curvature radius of the necking are then measured at every steps of deformation. This information is then employed to calculate macroscopic mechanical parameters:

→ The minimal section is used in the calculation of the mean value of the local deformation and the mean value of the true stress in this section.

→ The curvature radius of the necking area is involved in the calculation of the triaxiality. Its value is then used in the modified Bridgman's formula. The triaxiality has a major influence on damage evolution and has to be taken into account in damage modelings.

Appendix B

Influence of banded microstructure of martensite on damage in DP11 steel

Manganese segregation resulting from the solidification leads to the formation of martensite banding within the DP microstructures. The influence of these banded structures on the mechanical behavior and the resistance to damage of DP steels were studied by several authors [Han 89, Sun 02, Stau 04, Mazi 07, Avra 09a]. The presence of banded microstructures tends to decrease the ductility. Sun and Pugh [Sun 02] showed that in such microstructures, void nucleation preferentially occurs inside the martensite banding.
Some of the specimens of DP11 steel investigated in this study presented banded microstructures. They were thus used in the quantitative investigation of the effects of such microstructures on void nucleation, void growth and void coalescence.

B.1 Experimental observations

As mentioned in Section 1.1.1.3, there is no contrast between ferrite and martensite in the volumes acquired by X-ray tomography. The presence of martensitic bands inside a DP11 sample is thus detected on optical micrographies performed on the fractured specimens, like the one given in Figure B.1. An alignment of cavities correlated to the band of martensitic islands is clearly identified on this micrograph. This alignment of voids was also noticed in the tomograms, either on 2D longitudinal sections (see Figure B.2(a)) where the same voids alignment is seen, or on 3D visualizations (see Figure B.2(b)) where all the plane of cavities is visualized. Note that this plane containing the voids matches the central plane of the steel sheet.

As suggested in [Sun 02, Avra 09a], Figure B.1 shows that the preferential mechanism of nucleation within the banded martensitic microstructure is the fracture of the islands

of martensite. The consequences of the presence of this alignment of cavities on the evolution of damage is quantitatively studied in the next section.

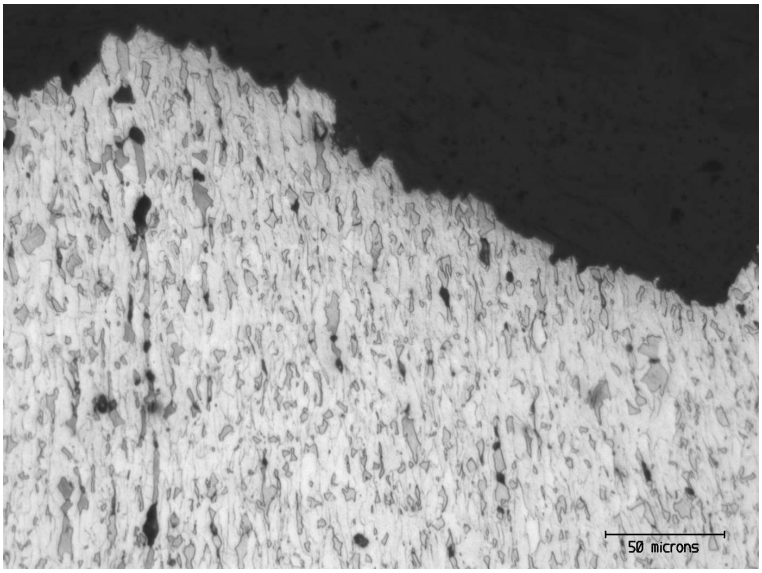

Figure B.1: Optical micrography of a fracture DP11 specimen presenting banded martensitic microstructure and damage banding.

B.2 Damage quantification in DP11 specimens presenting banded martensitic microstructure

B.2.1 Void nucleation

The void density was quantified in two specimens presenting void alignment and in two standard specimens. A projection along the tensile direction of all the voids present in each specimen is imaged in Table B.1. Damage banding is identified thanks to this kind of representation of the specimens. The evolution of the void density measured in these specimens is given in Figure B.3. The samples presenting the highest void density are the ones where banded microstructure implied banded damage. In these specimens, voids nucleate sooner than in the other samples because of the nucleation mechanism. In standard samples, cavities nucleate when a stress sufficient for the ferrite/martensite interface decohesion is reached in the material. The criterion for the nucleation inside the martensite is probably reached before the one for the interface decohesion thus explaining this difference in the strain at nucleation.

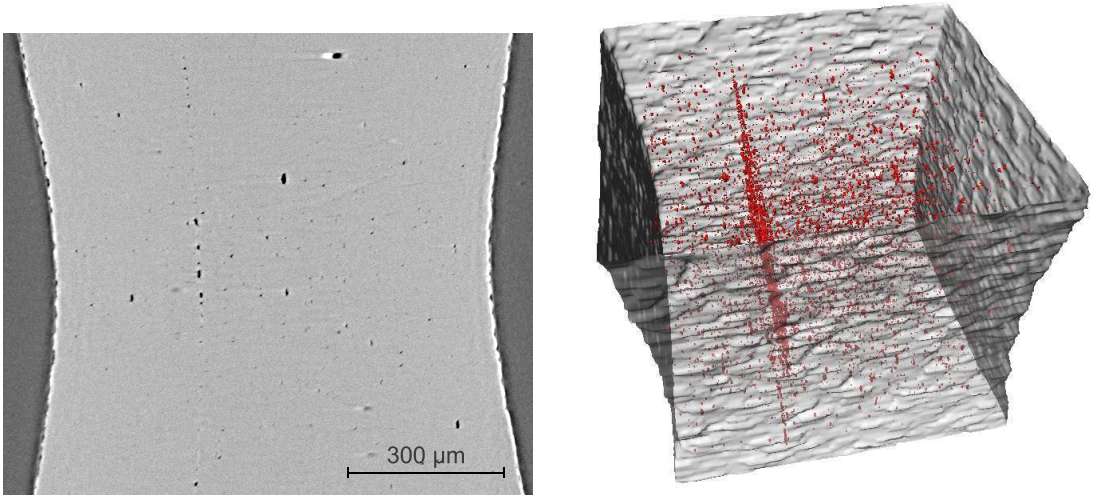

(a) (b)

Figure B.2: Damage banding observations using X-ray tomography: (a) 2D visualization of a longitudinal section inside the specimen, (b) 3D visualization of the acquired volume.

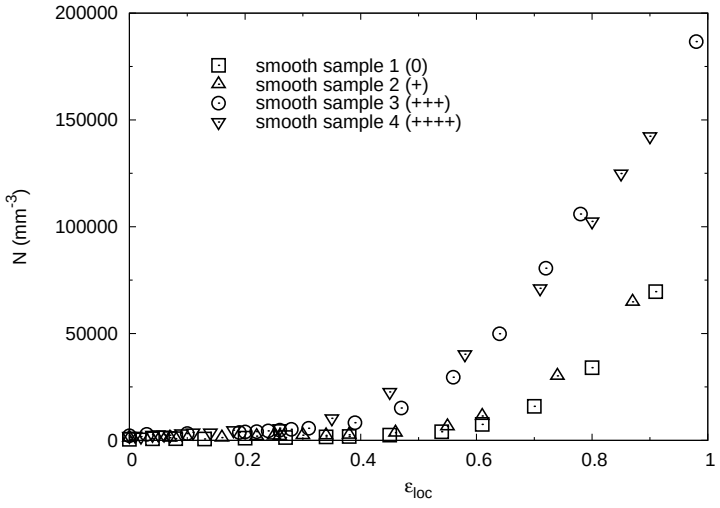

Figure B.3: Quantification of the void density in the DP11 specimens present in Table B.1.

smooth sample 1	smooth sample 2
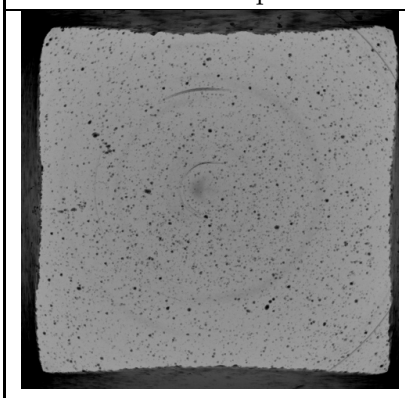	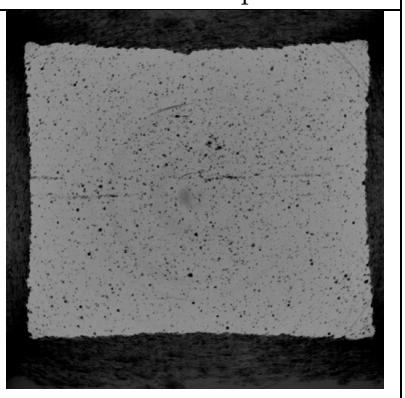
Damage banding 0	Damage banding +
smooth sample 3	smooth sample 4
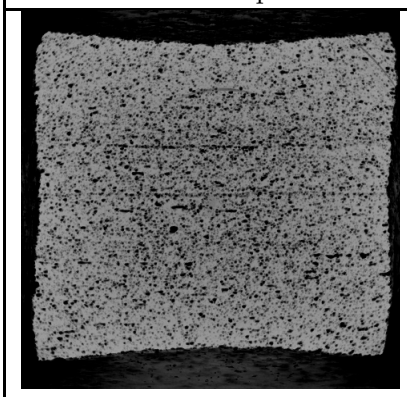	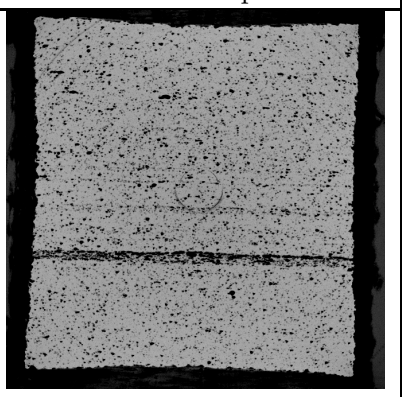
Damage banding +++	Damage banding ++++

Table B.1: Classification of the tested samples of DP11.

B.2.2 Void growth

The cavities belonging to the plane were isolated in order to study their growth kinetic. The evolution of the equivalent diameter of the largest voids present in the plane with the deformation is given in Figure B.4 and compared to the growth of cavities measured in the standard specimens.The growth of the cavities resulting from the banded martensitic microstructure is much higher than the growth of the voids in the standard specimens. Moreover, Figure B.5 shows that the growth mainly occurs in the directions included in the plane of voids contrary to the growth in standard samples which mainly occurs in the tensile direction. This phenomenon of faster and oriented growth can be partially explained by the stronger voids interactions in this plane where cavities are closer to each other.

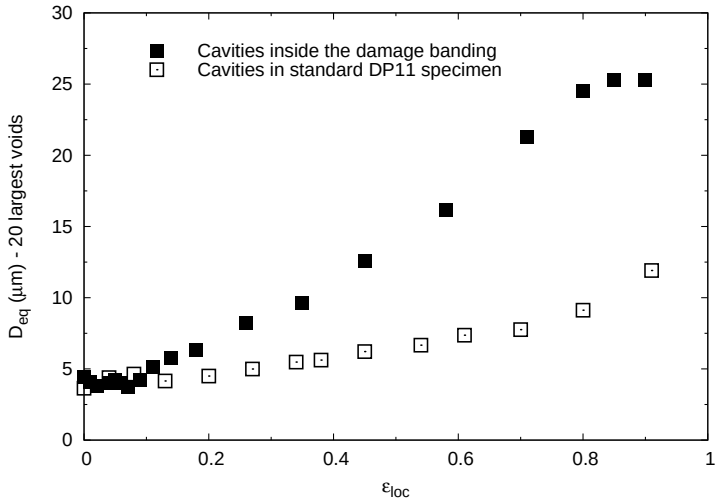

Figure B.4: Void growth in damage banding and in a standard specimen of DP11.

B.2.3 Void coalescence

An other consequence of the short distance between neighboring voids in the damage plane is that void coalescence occurs sooner in this plane than in the other parts of the specimen. 3D qualitative observations from Figure B.6 show that events of coalescence occurs in the martensite banding from $\varepsilon_{loc} = 0.35$. This is quite soon compared to standard specimens of DP11 where first events of coalescence happen for $\varepsilon_{loc} = 0.7$. The evolution of the frequency distribution of the distance between neighboring voids, given in Figure B.7, confirms this observation. The final frequency distribution of λ is reached really soon in the damage banding *i.e.* from $\varepsilon_{loc} = 0.45$. The comparison with the final frequency distribution of λ in a standard specimen of DP11 shows that cavities are really closer in the damage banding, the frequency distribution being shifted to the smallest

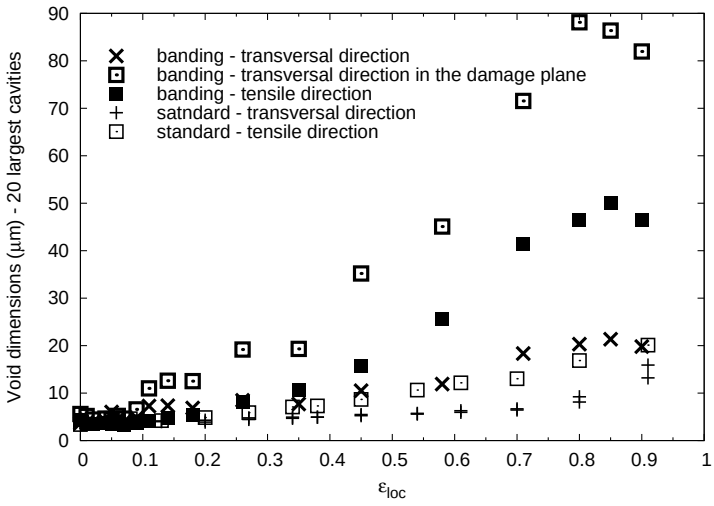

Figure B.5: Void growth in the main directions in damage banding and in a standard specimen of DP11.

values of λ.

The Thomason's criterion modified by Scheyvaerts *et al.* [Sche 11] and already used in Section 4.3.2 was also applied on the couples of neighboring cavities present in the damage banding. The density of couples of voids with a positive Thomason criterion is given in Figure B.8. It is as well compared with the density of couples of voids with a positive Thomason criterion measured in a standard DP11 specimen. Because of the higher void density and the faster growth in the damage banding, the increase of the density of couples with a positive Thomason criterion occurs sooner in the tensile test: from $\varepsilon_{loc} = 0.25$ while in standard DP11 samples, first couples of voids with positive Thomason criterion appear around $\varepsilon_{loc} = 0.8$.

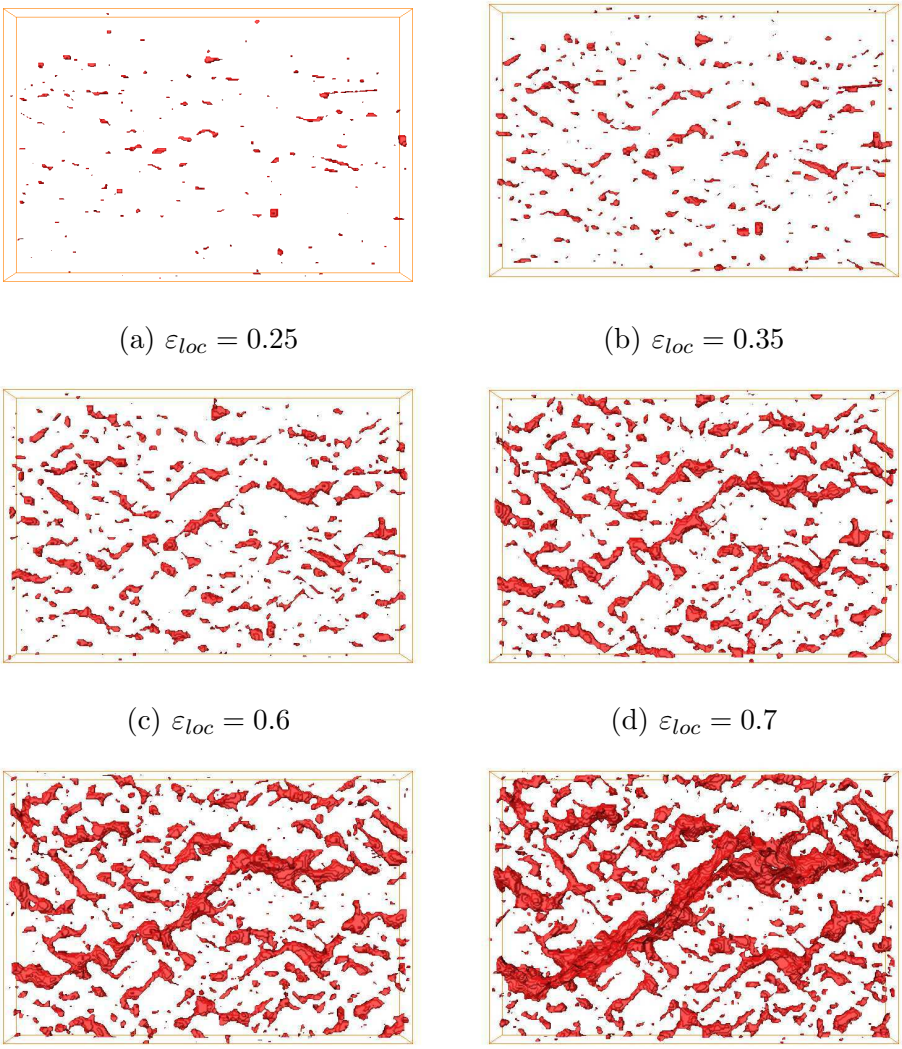

(a) $\varepsilon_{loc} = 0.25$ (b) $\varepsilon_{loc} = 0.35$

(c) $\varepsilon_{loc} = 0.6$ (d) $\varepsilon_{loc} = 0.7$

(e) $\varepsilon_{loc} = 0.8$ (f) $\varepsilon_{loc} = 0.9$

Figure B.6: 3D observations of the void coalescence in the damage banding.

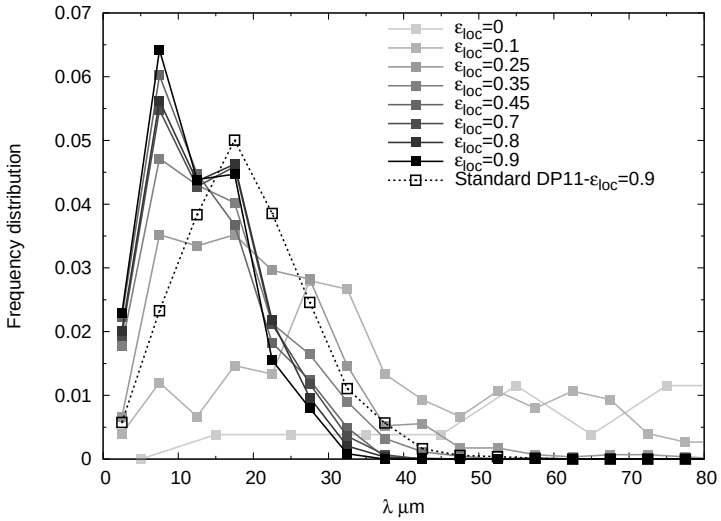

Figure B.7: Evolution of the frequency distribution of the distance between neighboring cavities in the damage banding.

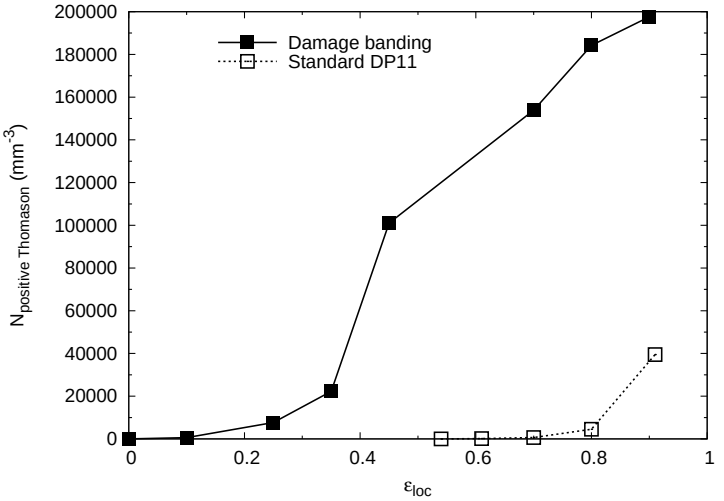

Figure B.8: Density of couples of neighboring voids having a positive Thomason criterion in the damage banding and in a standard DP11 specimen.

B.3 Summary

The present work demonstrated that the presence of banded martensitic microstructure due to the manganese segregation influences the kinetics of damage. Void nucleation and void growth are particularly concerned by this particular arrangement of the microstructure:

→ The presence of long islands of martensite induces soonest void nucleation in the martensite and leads to the formation of a plane of cavities inside the specimen. Because of the high density of cavities, the distance between voids are shorter in this area than elsewhere in the specimen.

→ Cavities present in this plane grow faster in particular in the plane directions because of the strong void interactions.

→ The mechanisms of coalescence are not directly concerned by the banded microstructure. However, void coalescence occurs sooner in this kind of microstructure because cavities are close to each other and grow faster.

Finally, the global ductility of DP steel presenting banded martensitic microstructure is affected. Even if the occurrence of damage is only locally accelerated, this is detrimental to the global sample. Such banded microstructures thus have to be averted as much as possible.

Appendix C

Résumé étendu de la thèse en français

Caractérisation de l'endommagement dans les aciers Dual-Phase à l'aide de la tomographie aux rayons X

C.1 Motivations

Dans le contexte actuel où la masse de la structure des automobiles est amenée à être réduite, il est avantageux pour les constructeurs automobiles d'utiliser des matériaux présentant de meilleures propriétés mécaniques. Des aciers à très haute résistance, dont font partie les aciers Dual-Phase (DP), ont donc été développés et sont déjà couramment utilisés dans la structure de la caisse en blanc des automobiles. Les aciers DP présentent de bonnes propriétés mécaniques grâce à leur microstructure bi-phasée constituée d'une phase molle, la ferrite, et d'une phase plus dure, la martensite. Il s'avère cependant que l'augmentation de la résistance à l'effort entraîne une diminution de la déformation à rupture. La capacité de ces matériaux à se déformer est pourtant nécessaire afin d'assurer l'étape de la mise en forme. Dans le but de continuer à améliorer la résistance des aciers DP tout en préservant leur ductilité, une meilleure compréhension des mécanismes d'endommagement menant à la rupture est nécessaire.

Dans les années soixantes, les premières études ont montré que l'endommagement ductile est physiquement divisé en trois étapes. Dans un premier temps, des cavités apparaissent là où le matériau présente des faiblesses, il s'agit de l'étape de germination de l'endommagement. Par la suite, le volume de ces cavités augmente durant la

phase de croissance jusqu'à la rupture finale du matériau liée à la coalescence des cavités.

Les récentes techniques de caractérisation, telle la tomographie aux rayons X, permettent désormais de caractériser en trois dimensions (3D), de façon qualitative et quantitative chaque étape de l'endommagement. Cette technique a ainsi été utilisée dans cette étude afin de caractériser l'endommagement ductile dans les aciers DP. Chacune des trois étapes a été quantifiée puis modélisée à l'aide de modèles analytiques issus de la littérature.

C.2 Techniques de caractérisation et matériaux étudiés

La tomographie aux rayons X

Le principe de la tomographie aux rayons X (RX) est donné par la Figure C.1. L'échantillon à imager est placé entre la source RX et le détecteur. Un nombre important de radiographies 2D est enregistré durant la rotation de l'échantillon. L'image 3D du volume caractérisé est ensuite reconstruite à partir de ces projections.

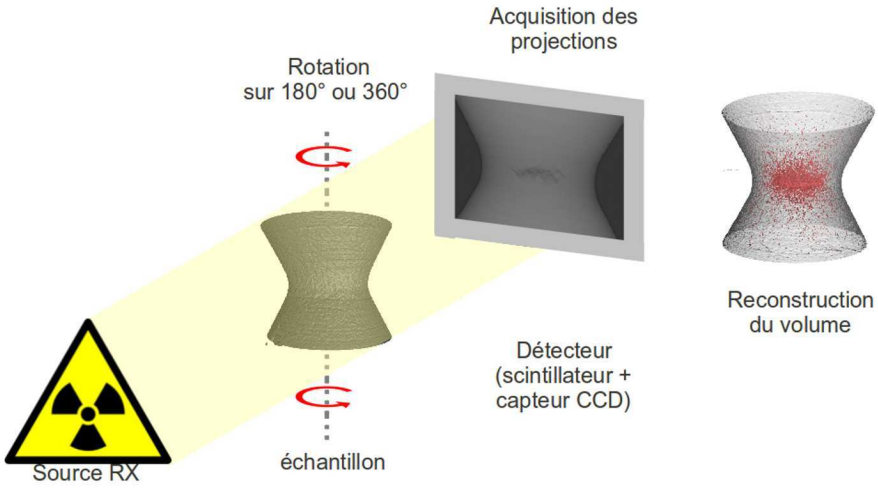

Figure C.1: Principe de la tomographie aux rayons X.

La tomographie étant une technique non-destructive, des essais de traction *in-situ* sur des éprouvettes lisses et entaillées ont été mis en œuvre. Lors de l'acquisition, la déformation était stoppée mais maintenue constante. Ces essais *in-situ* ont été réalisés à l'European Synchrotron Radiation Facility (ESRF) de Grenoble afin d'avoir une résolution et une énergie suffisante pour imager des éprouvettes d'acier ayant une section de 1×1 mm. Le contraste obtenu sur de telles images est lié au coefficient

d'absorption des rayons X du matériau traversé par le faisceau. Les cavités qui apparaissent lors de l'essai de traction ont un coefficient quasiment nul, contrairement à l'acier qui a un coefficient d'absorption élevé. On obtient donc un bon contraste entre le matériau et les cavités présentes à l'intérieur de l'éprouvette. À l'inverse, les coefficients d'absorption de la ferrite et de la martensite étant très proches, la phase ferritique ne peut pas être différenciée de la phase martensitique sur les volumes obtenus par tomographie RX.

Dans l'optique de caractériser l'endommagement, les volumes acquis lors des essais de traction *in-situ* ont été traités à l'aide du logiciel ImageJ. Les volumes ont d'abord été filtrés en utilisant un filtre médian afin de réduire le bruit de l'image, puis seuillés afin de séparer le matériau des cavités. Par la suite, l'endommagement a été caractérisé seulement dans la zone centrale de l'éprouvette où la déformation et la triaxialité sont les plus élevées. La figure C.2 montre la zone étudiée au sein de l'éprouvette. Ce sous-volume, dont le côté mesure 300 µm, doit être suffisamment grand pour être représentatif et suffisamment restreint pour considérer que la déformation et la triaxialité sont constantes au sein de cette zone. À partir de l'image 3D de l'éprouvette, la déformation ε_{loc}, la contrainte équivalente σ_{eq} et la triaxialité T dans le sous-volume ont été calculées.

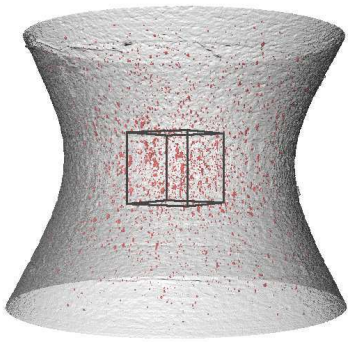

Figure C.2: Visualisation 3D du sous-volume où l'endommagement a été étudié.

Microscopie optique

La tomographie RX ne permettant pas de différencier la ferrite de la martensite, des micrographies optiques ont également été réalisées. Afin de révéler la microstructure, les échantillons ont été polis puis attaqués au Nital.

Les matériaux étudiés

Cinq aciers présentant des microstructures différentes ont été caractérisés lors de cette étude :

- Une nuance industrielle d'acier DP contenant une fraction volumique de martensite F_M de 11% et une concentration totale de carbone de 0.08%. La martensite se présente sous forme d'ilôts très durs et fragiles au sein d'une matrice ferritique plus molle. Cette nuance est appelée DP11 par la suite.

- La même nuance ayant subi un revenu de 30 minutes à 400 °C. Le revenu a pour effet d'adoucir la phase martensitique. Cet acier, appelé DP11T possède donc la même microstructure que le DP11 mais les propriétés de la phase martensitique ont été modifiées.

- Une nuance d'acier DP contenant une fraction volumique de martensite plus élevée que le DP11, F_M=62% et une concentration totale de carbone de 0.15%. La phase martensitique majoritaire est alors plus ductile que dans le DP11.

- Un acier 100% ferritique.

- Un acier 100% martensitique dont la concentration totale en carbone est de 0.1%.

Les micrographies optiques de chaucun de ces aciers sont données Figure C.3 et leurs propriétés microstructurales sont résumées dans le Tableau C.1.

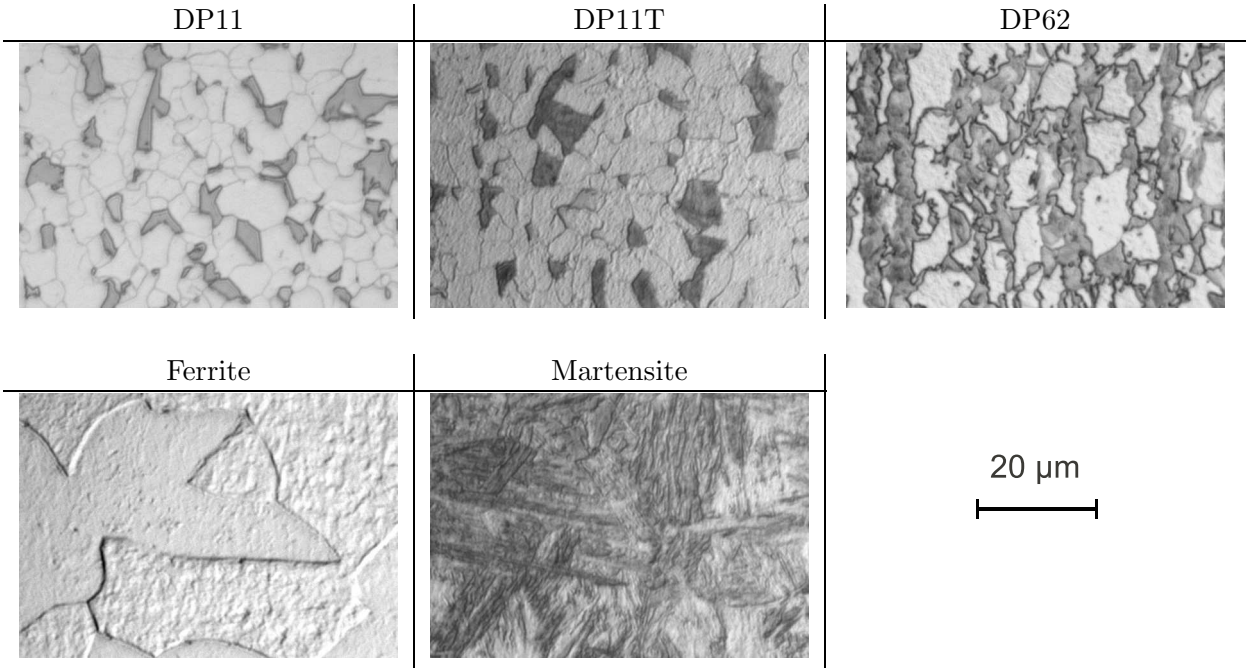

Figure C.3: Micrographies optiques des aciers étudiés.

Désignation	Dureté Vickers (20 kgf)	Type de microstructure	F_M	C_M (%m)	HV_M
DP11	180	bi-phasé	11%	0.73	830
DP11T	165	bi-phasé	11%	0.73	415
DP62	315	bi-phasé	62%	0.24	530
Ferrite	150	mono-phasé	0%	-	-
Martensite	330	mono-phasé	100%	0.1	330

Tableau C.1: Propriétés microstructurales des aciers étudiés : F_M fraction volumique de martensite, C_M concentration massique en carbone dans la martensite, HV_M dureté de la martensite.

C.3 Étude de la germination de l'endommagement

Caractérisation expérimentale

Les représentations 3D d'une même éprouvette de DP11 pour différents états de déformation sont données Figure C.4. Les cavités à l'intérieur du volume apparaissent en rouge et la forme extérieure de l'éprouvette est représentée de façon transparente en gris. La germination de nouvelles cavités est clairement visible sur ces volumes. Dans chaque sous-volume étudié, le nombre de cavités est compté à l'aide du logiciel ImageJ et la densité volumique de cavités N est calculée :

$$N = \frac{\text{nombre de cavités}}{\text{volume étudié}} \tag{C.1}$$

L'évolution de N avec la déformation est mesurée dans chaque matériau et est représentée sur la Figure C.5. La cinétique de germination quantifiée d'un matŕiaux à l'autre est trés différente. La densité de cavités est notamment particulièrement importante dans les aciers bi-phasés.

Les volumes obtenus en tomographie RX ne permettent pas de distinguer la ferrite de la martensite et donc d'identifier le mécanisme de germination. Pour cela des micrographies optiques ont été réalisées sur les éprouvettes après rupture. Ces micrographies sont données Figure C.6. Deux mécanismes de germination ont été identifiés :

- La décohésion de l'interface ferrite/martensite dans le DP11.

- La rupture de l'ilôt de martensite dans le DP11T et le DP62.

Modélisation

La cinétique de germination des cavités par décohésion de l'interface observée dans l'éprouvette de DP11 a été modélisée à l'aide du critère d'Argon [Argo 75b]. Ce critère

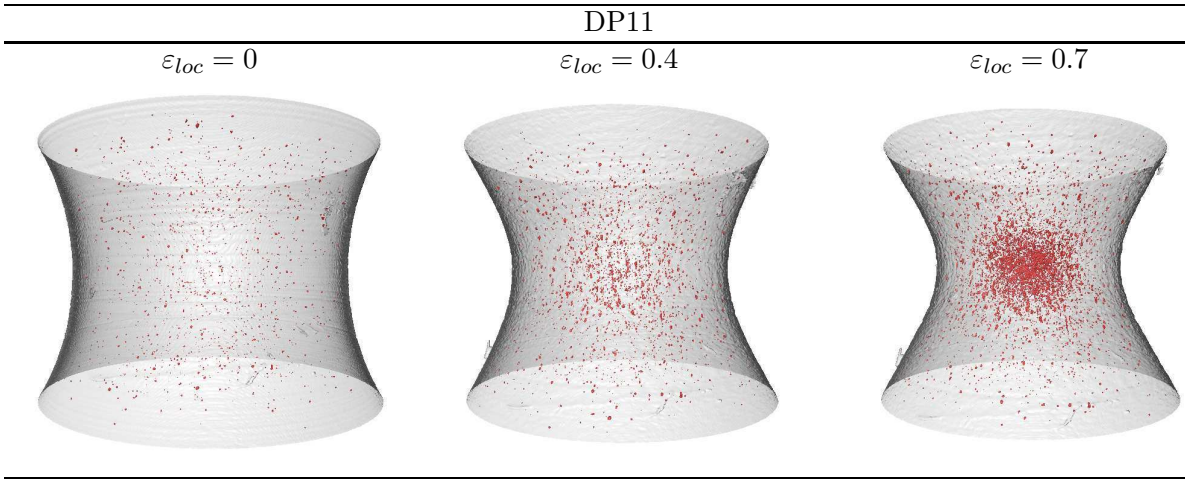

Figure C.4: Vues 3D d'une éprouvette à différents états de déformation, exemple du DP11.

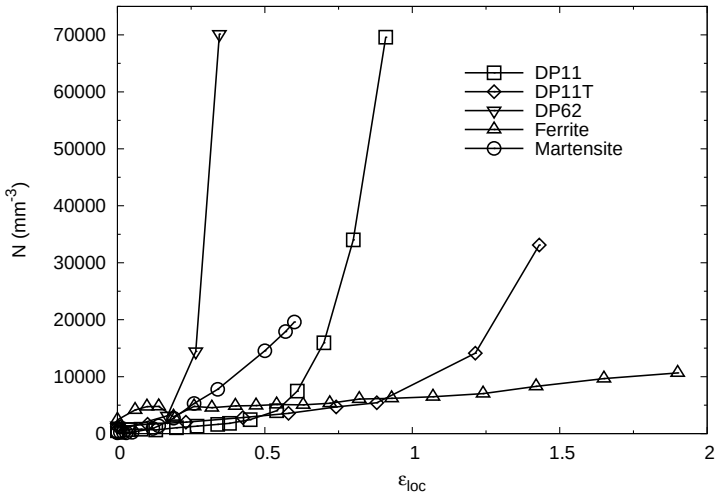

Figure C.5: Évolution de la densité volumique de cavités dans chaque acier étudié.

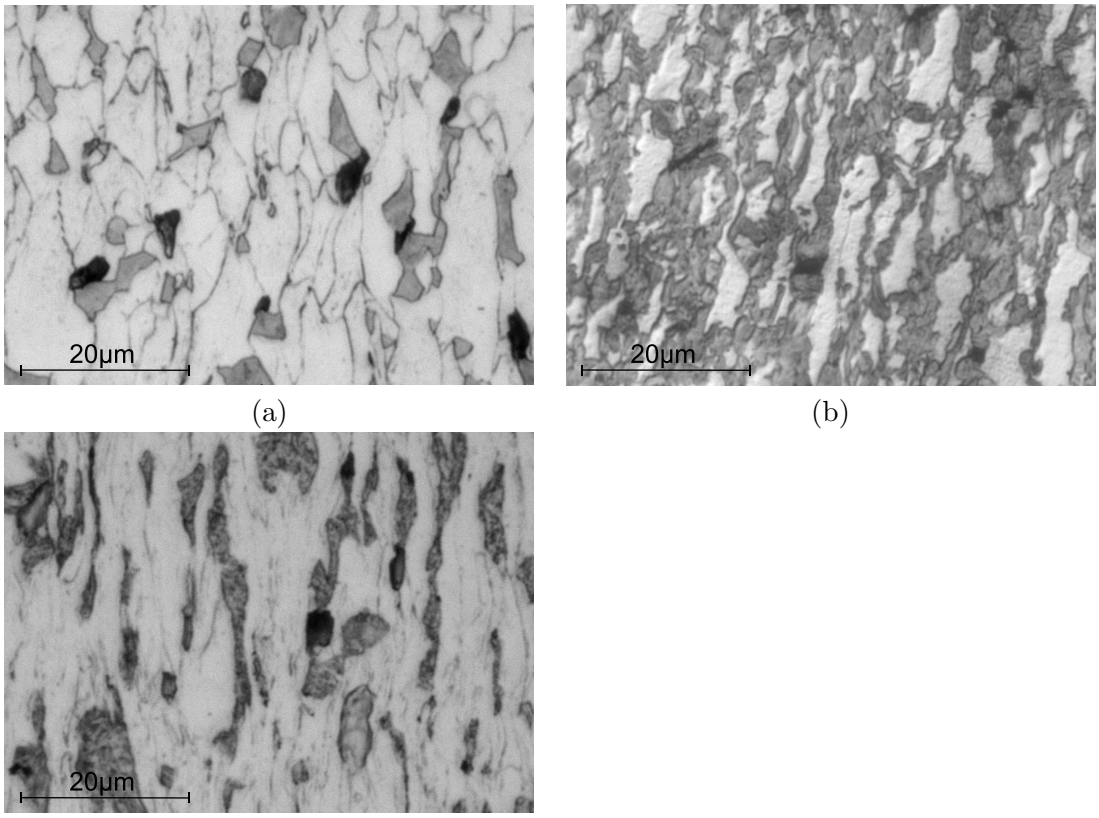

(a) (b)

(c)

Figure C.6: Mécanismes de germination identifiés dans les différents aciers bi-phasés étudiés : (a) DP11, (b) DP62, (c) DP11T.

en contrainte critique a été modifié afin de tenir compte de la triaxialité locale T_{loc} dépendant notamment de l'écrouissage cinématique :

$$\sigma_{eq}\,(1 + T_{loc}) = \sigma_C \tag{C.2}$$

avec σ_C la contrainte critique de l'interface ferrite/martensite.
Ce critère a été intégré dans l'expression donnant l'évolution de la densité de cavités :

$$\frac{dN}{d\varepsilon} = A\frac{\sigma_{eq}\,(1 + T_{loc})}{\sigma_C}\left(1 + \frac{N}{N_0}\right) \tag{C.3}$$

avec A et N_0 deux constantes utilisées pour ajuster le modèle aux données expérimentales. La Figure C.7(a) illustre l'application de ce modèle aux données expérimentales issues d'une éprouvette lisse et d'une éprouvette entaillée de DP11. Plus d'informations concernant cette modélisation sont disponibles dans [Land 10b].

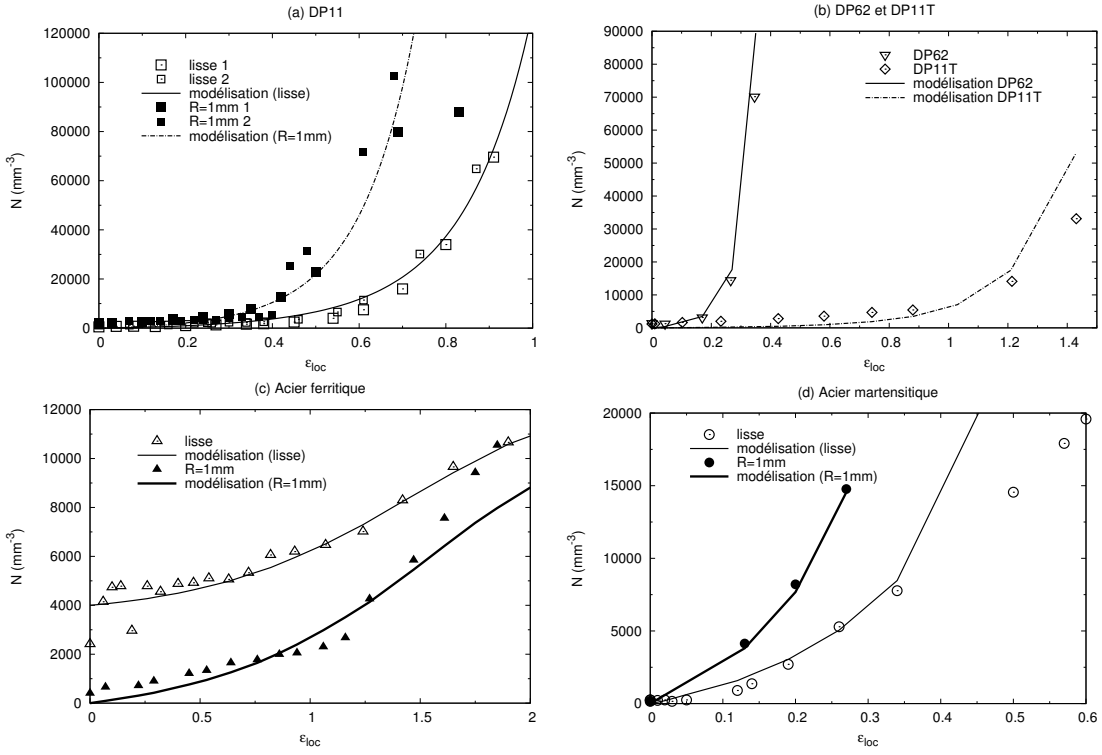

Figure C.7: Modélisation de la cinétique de germination : (a) DP11 (équation C.3), (b) DP62 et DP11T (équation C.4), (c) ferrite (équation C.4), (d) martensite (équation C.4).

Les cinétiques de germination de cavités suite à la rupture des ilôts martensitiques quantifiées dans le DP11T et le DP62 ainsi que dans les aciers mono-phasés ont quant

à elles été modélisées à l'aide d'une expression intégrant le critère de Chu et Needleman [Chu 80], qui est un critère en déformation critique.

$$N = N_0 \left(\exp\left(\frac{\varepsilon}{\varepsilon_N} \right) - 1 \right) \tag{C.4}$$

avec

$$\varepsilon_N = A \exp\left(-\beta T\right) \tag{C.5}$$

où A, N_0 et β sont des constantes utilisées pour ajuster le modèle aux données expérimentales. Cette expression est ajustée pour les différents matériaux présentant un amorçage de l'endommagement suite à la rupture d'ilôts de martensite dans les Figures C.7 (b), (c) et (d).

C.4 Étude de la croissance des cavités

Caractérisation expérimentale

Afin d'observer l'étape de croissance, une cavité issue du sous-volume d'une éprouvette de DP11 a été isolée et est représentée sur la Figure C.8 pour plusieurs états de déformation. Ces images montrent que le volume de la cavité augmente et que la cavité prend une forme plus allongée. Il est possible de quantifier le volume et la forme de chaque cavité présente dans le sous-volume étudié. Le nombre de voxels composant chaque cavité est mesuré et permet le calcul du diamètre équivalent en faisant l'hypothèse que la cavité est sphérique. Les dimensions des cavités dans les directions principales sont également mesurées.

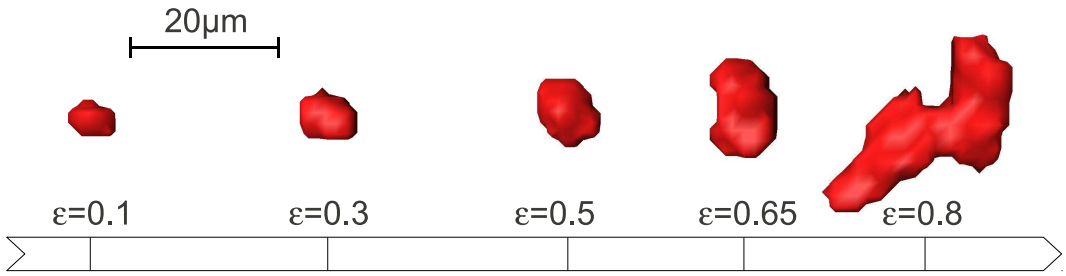

Figure C.8: Visualisation 3D d'une même cavité issue de l'éprouvette de DP11 pour différents états de déformation.

Dans les éprouvettes étudiées, il est très difficile de suivre une même cavité d'un état de déformation à l'autre à cause du nombre important de cavités germant durant l'essai

de traction. Dans l'éprouvette de DP11, l'évolution individuelle du diamètre équivalent de trois des plus grosses cavités du sous-volumes a été quantifiée et comparée à l'évolution de la moyenne du diamètre équivalent calculée sur les 20 plus grosses cavités, les 50 plus grosses cavités et la population entière du sous-volume. Ces résultats sont représentés sur la Figure C.9. Ces mesures montrent que la croissance moyenne des 20 ou des 50 plus grosses cavités du sous-volume est similaire à la croissance individuelle de chaque cavité contrairement à la population totale dont le diamètre équivalent moyen reste constant à cause de la germination importante de nouvelles cavités. Par la suite, les mesures expérimentales concernant la croissance ont été réalisées sur les 20 plus grosses cavités du sous-volume. La croissance des cavités ainsi quantifiée dans chacun des aciers étudiés est donnée Figure C.10.

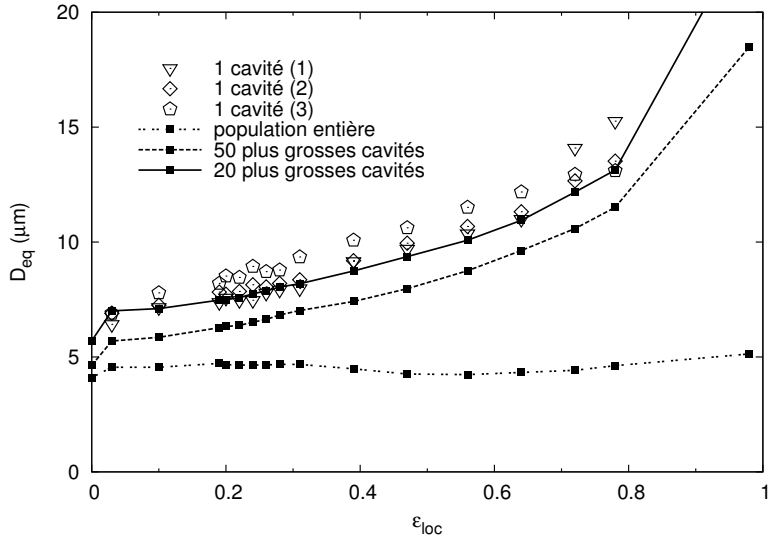

Figure C.9: Évolution de la valeur moyenne du diamètre équivalent calculée sur différents nombres de cavités : 1, les 20 plus grosses, les 50 plus grosses et la population entière.

Modélisation

Les différentes cinétiques de croissance précédemment quantifiées dans chacun des matériaux ont été modélisées à l'aide du modèle de Huang [Huan 91]:

$$\frac{dR}{R} = \alpha_{Huang} T^{0.25} \exp\left(\frac{3}{2}T\right) d\varepsilon \tag{C.6}$$

avec R le rayon des cavités, T la triaxialité et ε la déformation.
L'expression de Huang est en fait une correction du modèle de Rice et Tracey [Rice 69] dont le terme pré-exponentiel ne dépend pas de la triaxialité. Grâce à l'utilisation

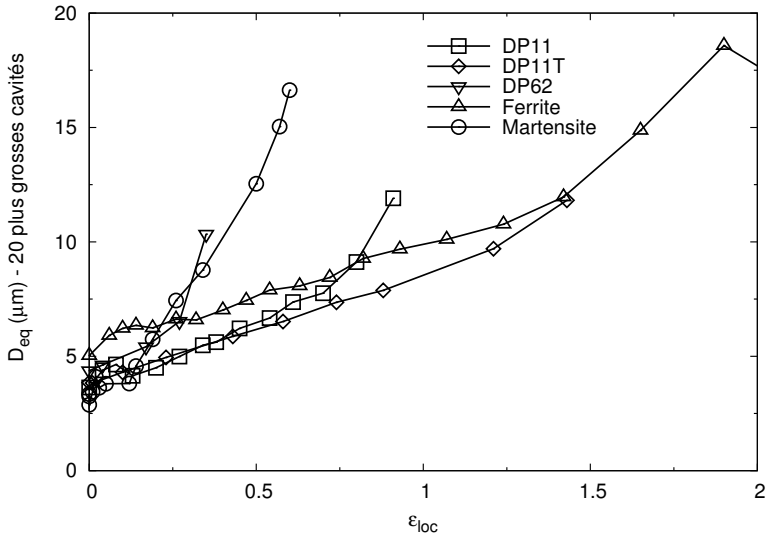

Figure C.10: Évolution du diamètre equivalent moyen calculé sur les 20 plus grosses cavités des aciers étudiés.

d'éprouvettes entaillées, cette expression corrigée a été validée par les données expérimentales de ce travail. Plus d'informations sont disponibles dans [Land 11]. Le paramètre α_{Huang} a été utilisé pour ajuster le modèle de Huang sur les données expérimentales. Un exemple de cinétique de croissance ainsi modélisée est donné pour le DP11 sur la Figure C.11(a). Une valeur différente pour α_{Huang}a été trouvé pour chaque matériau. Ces différentes valeurs peuvent s'expliquées par le fait que les aciers étudiés sont loin des conditions du modèle de Huang prévu pour des matériaux parfaitement plastiques. Nous avons notamment observé que les matériaux présentant de l'écrouissage cinématique avaient une valeur de α_{Huang} plus élevée synonyme d'une croissance plus importante. Une seconde piste est illustrée par la Figure C.11(b) où sont représentées les valeurs de α_{Huang} en fonction de k_σ issue de la modélisation de la contrainte équivalente par une simple loi puissance :

$$\sigma_{eq} = k_\sigma {\varepsilon_{loc}}^n \tag{C.7}$$

Une relation linéaire, pour l'instant non expliquée, lie les valeurs de α_{Huang} à k_σ.

Afin de modéliser le changement de forme de la cavité durant la phase de croissance, les équations du modèle de Rice et Tracey prédisant l'évolution des dimensions des cavités dans la direction de traction $R_{tensile}$ et dans la direction transverse R_{trans} ont également été utilisées avec la correction de Huang et les valeurs précédemment déterminées pour α_{Huang} :

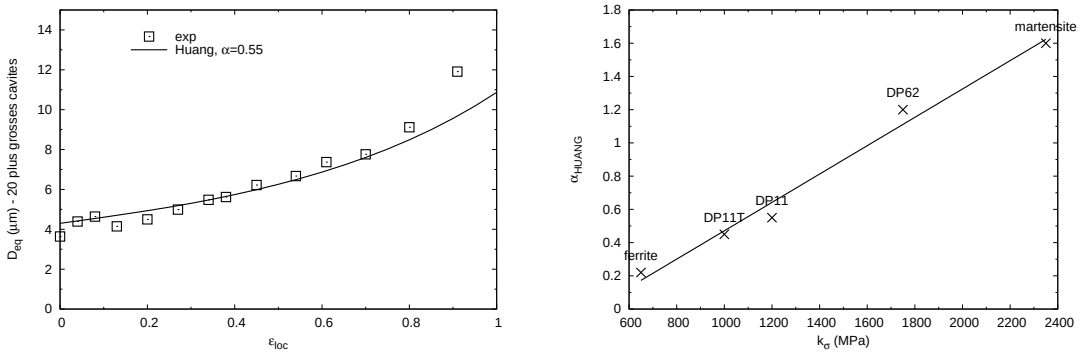

(a) (b)

Figure C.11: (a) Exemple de modélisation de la croissance des 20 plus grosses cavités dans le DP11. (b) Relation entre α_{Huang} et k_σ.

$$\begin{aligned}\frac{dR_{tensile}}{R} &= \alpha_{Huang} T^{0.25} \exp\left(\frac{3}{2}T\right) d\varepsilon_{loc} + (1+E_V)\, d\varepsilon_{loc} \\ \frac{dR_{trans}}{R} &= \alpha_{Huang} T^{0.25} \exp\left(\frac{3}{2}T\right) d\varepsilon_{loc} - \frac{1}{2}(1+E_V)\, d\varepsilon_{loc}\end{aligned} \tag{C.8}$$

avec $1+E_V$ une constante dont la valeur a été utilisée pour ajuster les courbes sur les données expérimentales.

De même, le modèle développé par Bouaziz *et al.* [Mair 08] a été utilisé avec la correction de Huang et les valeurs de α_{Huang} précédemment déterminées pour chaque matériau afin de modéliser l'évolution du rayon équivalent moyen de la population totale de cavités $\bar{R}$. [Mair 08]

$$\frac{d\bar{R}}{d\varepsilon} = \alpha_{Huang} T^{0.25} \exp\left(\frac{3}{2}T\right) \bar{R} + \frac{1}{N}\frac{dN}{d\varepsilon}\left(\bar{R} - R^\star\right) \tag{C.9}$$

avec N la densité de cavités et $R^\star$ le rayon initial des cavités.

Les résultats de ces modélisations en accord avec les données expérimentales sont présentées Figure C.12.

C.5 Étude de la coalescence des cavités

Caractérisation expérimentale

Jusqu'à présent, la coalescence a été très peu étudiée expérimentalement. Les volumes acquis lors des essais de traction *in-situ* ont montré que des événements de coalescence

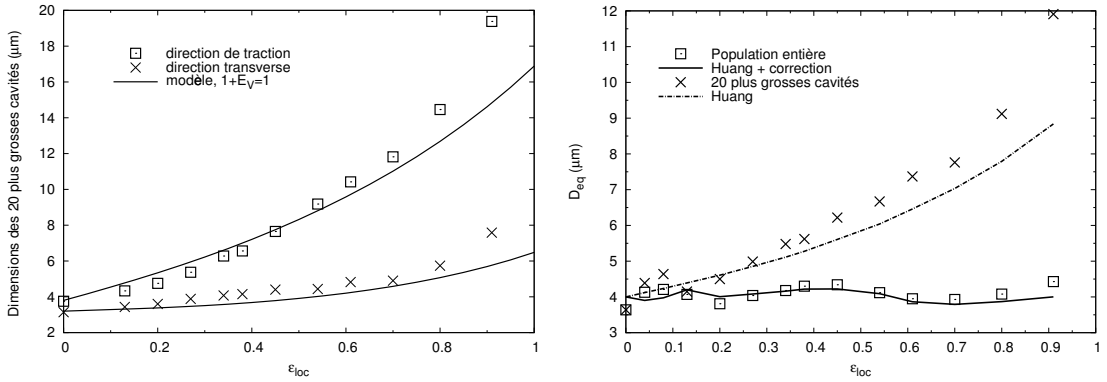

(a) (b)

Figure C.12: (a) Exemple de prédiction des dimensions moyennes des 20 plus grosses cavités du DP11 dans les directions principales. (b) Exemple de prédiction du diamètre équivalent moyen de la poulation entière de cavités du DP11.

locaux, tel celui illustré par la Figure C.13(a), intervenaient bien avant la coalescence macroscopique menant à la rupture finale et illustrée par la Figure C.13(b).

Le paramètre caracteristique contrôlant la coalescence est la distance entre les cavités λ. Dans un premier temps, la distance inter-cavités moyenne dans le sous-volume étudié λ_{mean} a été calculée à l'aide des mesures expérimentales de la densité de cavités N et du diamètre équivalent moyen D_{eq}.

$$\lambda_{mean} = \frac{1}{N^{1/3}} - D_{eq} \tag{C.10}$$

L'évolution de λ_{mean} avec la déformation est donnée pour les différents aciers étudiés sur la Figure C.14. Une mesure plus locale de la distance entre chaque cavités voisines a ensuite été effectuée à l'aide d'ImageJ. Les distributions en fréquence de λ mesurées lors du dernier état de déformation avant la rupture de chaque éprouvette sont données Figure C.15. Qu'elles soient globales ou locales, ces mesures concernant la coalescence montrent que la nature mono ou bi-phasée de la microstructure intervient au niveau de la distance inter-cavités juste avant la rupture. Dans le cas des aciers mono-phasés (ferrite ou martensite) une valeur λ_{mean} ≈30µm et des distributions similaires ont été trouvées. Il en va de même dans les aciers bi-phasés (DP11, DP11T et DP62) avec une valeur λ_{mean} ≈20µm.

La configuration géométrique des cavités voisines a également été étudiée. Il s'est avéré que la configuration expérimentale est très différente de la configuration idéale des critères de coalescence puisque deux cavités voisines ont fréquemment des tailles différentes et ne sont pas orientées perpendiculairement à la direction de traction.

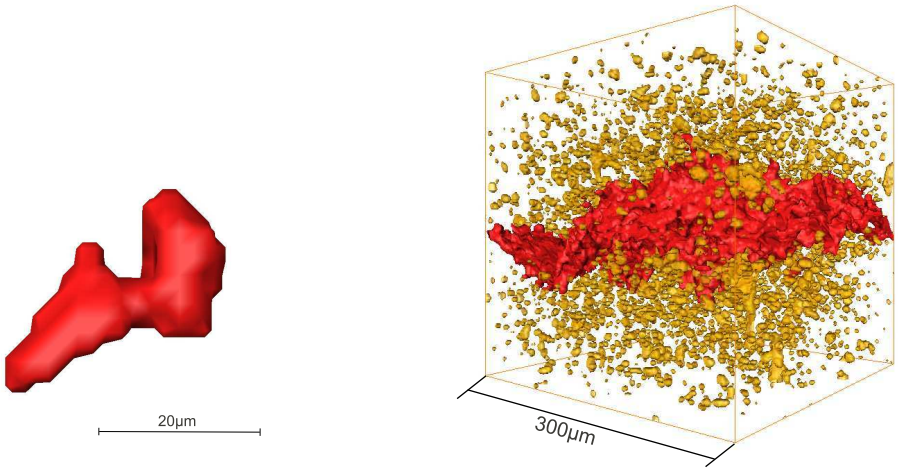

(a) (b)

Figure C.13: Vues 3D de la coalescence dans une éprouvette de DP11: (a) événement local de coalescence entre deux cavités voisines à $\varepsilon_{loc} = 0.69$, (b) Coalescence macroscopique au centre de l'éprouvette à $\varepsilon_{loc} = 0.83$ (une énorme cavité issue de la coalescence macroscopique apparait en rouge).

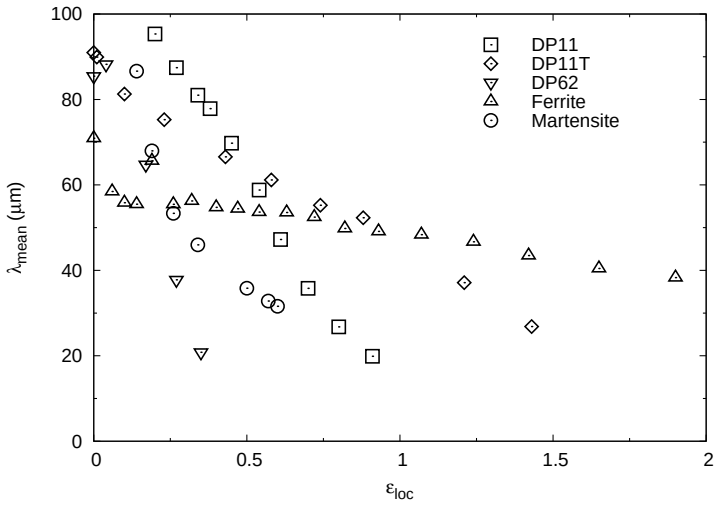

Figure C.14: Évolution de la distance moyenne inter-cavités lors de l'essai de traction des différents aciers.

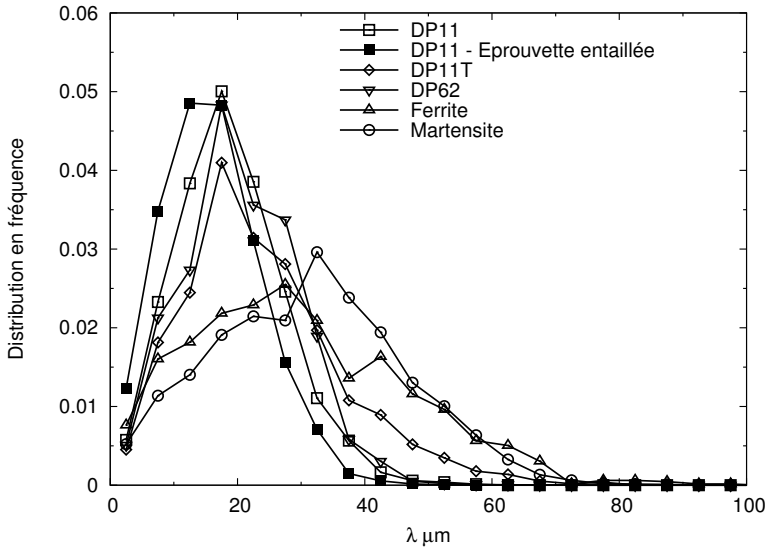

Figure C.15: Distribution finale de la distance entre les cavités λ pour chaque matériau étudié.

Modélisation macroscopique

La mesure moyenne de la distance inter-cavités a par la suite été utilisée pour l'application macroscopique des critères de coalescence de Brown et Embury [Brow 73] et de Thomason [Thom 85]. Le critère de Brown et Embury est un critère de coalescence purement géométrique basé sur la possibilité d'apparition de bandes de cisaillement à 45°entre les deux cavités. Son expression est la suivante :

$$Lx^2 = {R_{trans}}^2 + {R_{tensile}}^2 \tag{C.11}$$

avec Lx la demi distance séparant le centre des cavités, $R_{tensile}$ le rayon des cavités dans la direction de traction et R_{trans} le rayon des cavités dans la direction transversale.
Le critère de Thomason est quant à lui basé sur la striction du ligament séparant deux cavités. L'expression utilisée pour ce critère est celle développée par [Sche 11]:

(C.12)

avec $W = \frac{R_{tensile}}{R_{trans}}$, $\chi = \frac{R_t trans}{Lx}$, σ_{zz} la contrainte appliquée dans la direction de traction et σ_y^{loc} la contrainte équivalente au niveau du ligament.
Un exemple d'implémentation macroscopique du critère de Brown et Embury et du critères de Thomason sur les données expérimentales issues d'une éprouvette de DP11 est donné respectivement sur la Figure C.16(a) et (b). Les deux conditions de coalescence sont en accord avec la déformation à rupture observée expérimentalement.

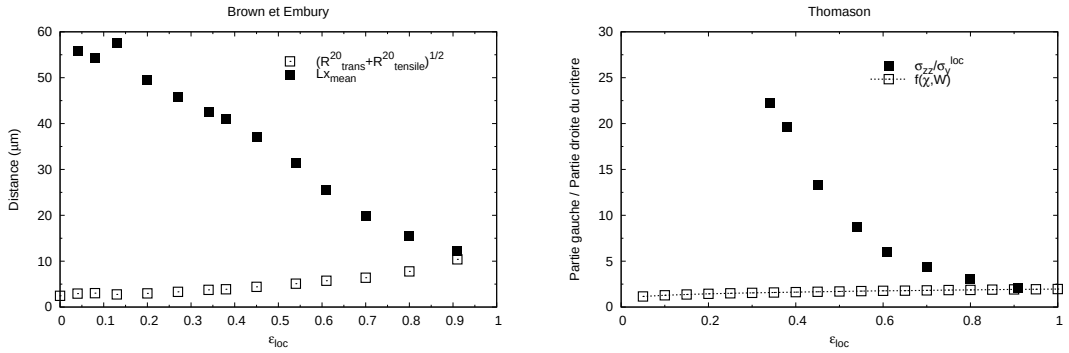

(a) (b)

Figure C.16: Application macroscopique des critères de coalescence de Brown et Embury (a) et Thomason (b) sur les données expérimentales issues de l'éprouvette de DP11.

L'intérêt d'utiliser ces critères de façon macroscopique réside dans le fait que les valeurs de χ et W peuvent être calculées à partir des modélisations de N, $R_{tensile}$ et R_{trans}. Les valeurs des déformations à rupture prédites par le critère de Brown et Embury ε_R^{BE} et le critère de Thomason $\varepsilon_R^{Thomason}$ en utilisant les modélisations présentées dans les parties précédentes sont données dans le Tableau C.2. Les valeurs prédites par les deux critères sont très proches de la déformation à rupture observée expérimentalement. Le critère de Brown et Embury et le critère de Thomason peuvent donc être tous deux utilisés pour modéliser la rupture des aciers étudiés.

	DP11	DP11T	DP62	ferrite	marteniste
ε_R^{exp}	1	1.43	0.35	2.2	0.6
ε_R^{BE} (erreur)	1.1 (+0.1)	1.45 (+0.02)	0.41 (+0.06)	2.25 (0.05)	0.6 (0)
$\varepsilon_R^{Thomason}$ (erreur)	1 (0)	1.4 (-0.03)	0.32 (-0.03)	2.7 (+0.5)	0.55 (-0.05)

Tableau C.2: Valeurs des déformations à rupture observées expérimentalement et prédites par le critère marcoscopique de Brown et Embury ε_R^{BE} et par le critère de Thomason $\varepsilon_R^{Thomason}$.

Modélisation locale

Afin de tenir compte des événements de coalescence locaux observés expérimentalement, les critères de coalescence de Brown et Embury et de Thomason ont également été appliqués localement sur chaque couple de cavités voisines en utilisant les valeurs de χ et W propres à chaque couple. Lors de cette application locale, une expression du critère

de Thomason tenant compte de l'orientation des cavités voisines γ a été utilisée :

$$\frac{\sigma_{zz}}{\sigma_y^{loc}(\gamma)} = \left(1-\chi^2(\gamma)\right)\left[0.1\left(\frac{1-\chi(\gamma)}{\chi(\gamma)W}\right)^2 + 1.2\frac{1}{\sqrt{\chi(\gamma)}}\right] \text{ for } \gamma \in \left[0:\frac{\pi}{2}\right] \qquad \text{(C.13)}$$

La Figure C.17 représente dans le plan $\chi - W$ tous les couples de cavités voisines présents dans le sous-volume étudié. Le critère de Brown et Embury ainsi que le critère de Thomason ont également été représentés. Les couples présentant les critères de coalescence positifs sont situés en haut à droite du graphe. Cinq couples ayant coalescé à l'état scanné suivant ont été marqués en rouge. Tous les cinq ont un critère de Thomason positif alors que seulement deux d'entre eux ont un critère de Brown et Embury positif. Cette dernière observation nous pousse donc à préférer le critère de Thomason pour l'application locale de la condition de coalescence.

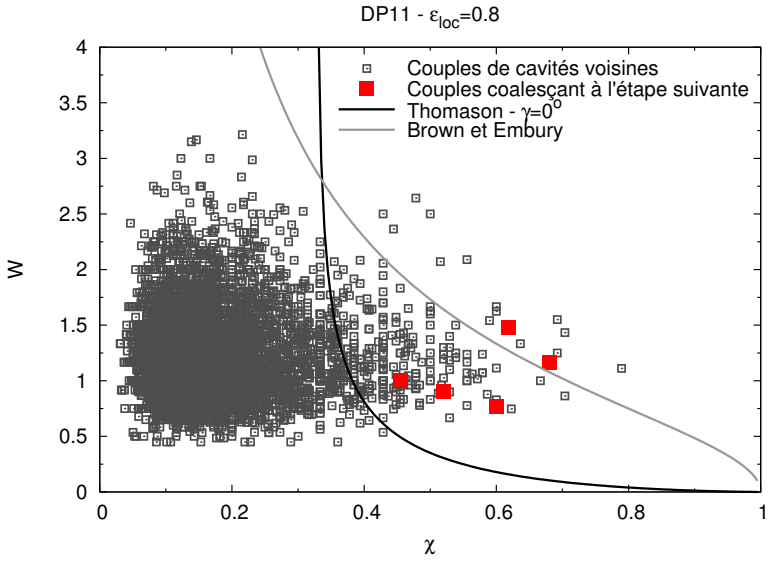

Figure C.17: Représentation graphique des couples de cavités présents dans le sous-volume étudié ainsi que des critères de Brown et Embury et Thomason.

Dans l'optique de relier les événements de coalescence locaux avec la coalescence macroscopique, la densité de couples présentant un critère de Thomason positif est représentée en fonction de la déformation pour tous les matériaux étudiés sur la Figure C.18. Juste avant la rupture des éprouvettes, une augmentation du nombre de couples avec un critère positif est observée. Une condition de coalescence macroscopique basée sur la fraction volumique de cavités impliquées dans les événements de coalescence locaux et la distance moyenne entre les cavités voisines a été mise en place dans le cas du DP11

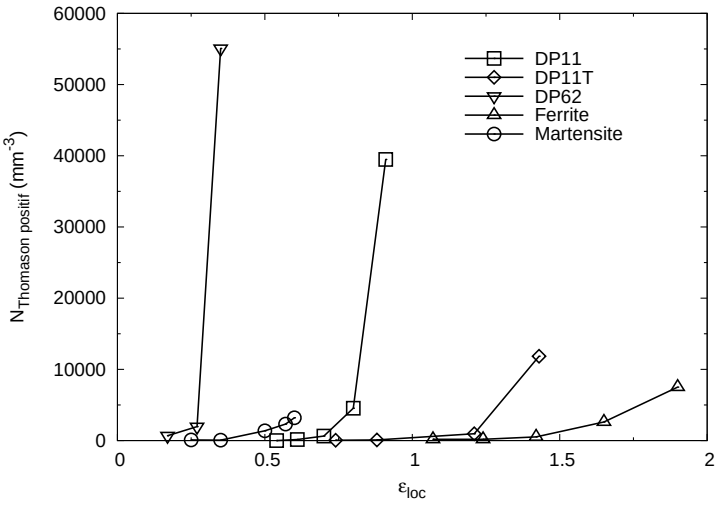

Figure C.18: Évolution de la densité de couples de cavités avec un critère de Thomason positif.

C.6 Étude de l'endommagement dans des éprouvettes pré-déformées

Afin de valider les hypothèses avancées concernant l'effet de l'écrouissage cinématique sur la germination et la croissance des cavités, l'endommagement a été étudié dans des éprouvettes d'aciers DP11 ayant subi des chargements complexes. Avant l'essai de traction *in-situ* le matériau a été déformé soit en traction, soit par laminage dans la direction perpendicualire à celle de l'essai *in-situ* comme illustré par la Figure C.19.

L'endommagement dans les éprouvettes pré-déformées a été caractérisé et modélisé lors de l'essai de traction *in-situ* comme décrit précédemment. Les cinétique de germination et de croissance de cavités quantifiées dans les éprouvettes pré-déformées et pré-laminées sont données respectivement Figure C.20 (a) et (b). Les deux étapes de germination et de croissance des cavités sont influencées : les cavités germent plus tôt et grossissent plus vite dans les éprouvettes pré-déformées. Ces effets peuvent être en partie imputés à l'augmentation de la part cinétique de l'écrouissage dans le DP11 pré-déformé.

C.7 Conclusions et perspectives

Dans cette thèse, les trois étapes de l'endommagement ductile, à savoir, la germination, la croissance et la coalescence des cavités ont été caractérisées de façon qualitative et quantitative à l'aide de la tomographie aux rayons X. Les données quantitatives ont été utilisées pour la modélisation des phénomènes d'endommagement utilisant des modéles

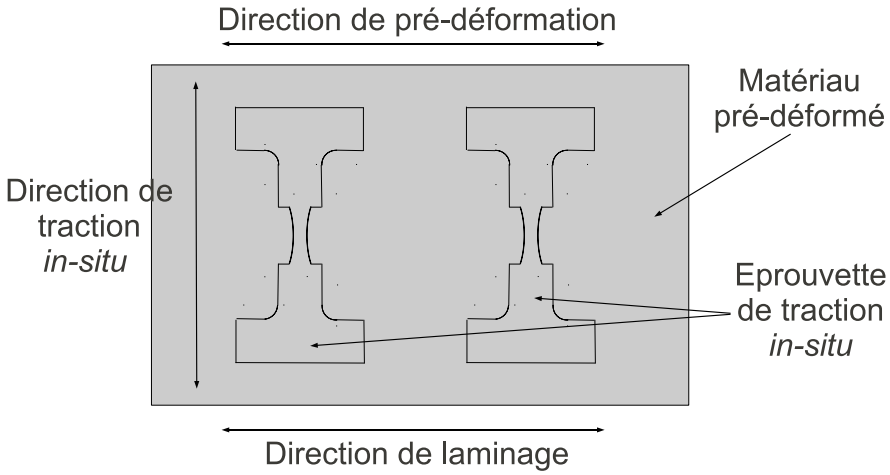

Figure C.19: Configuration des trajets de chargement complexes.

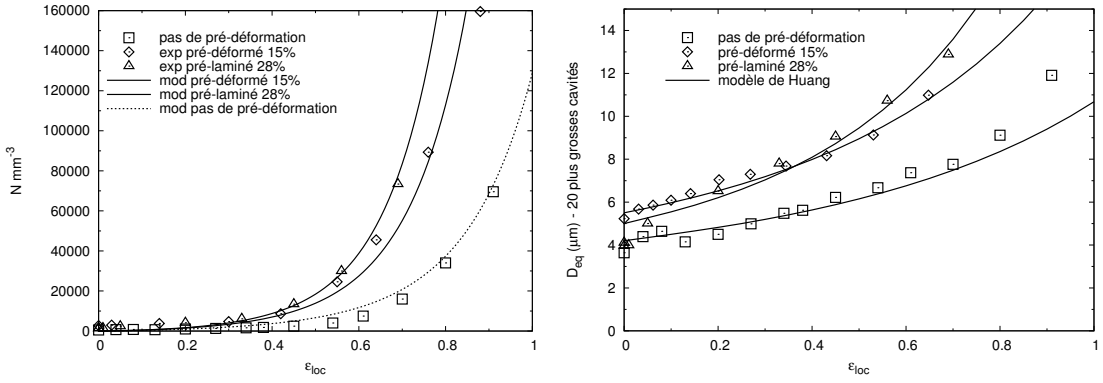

(a) (b)

Figure C.20: Effet de la pré-déformation sur les cinétiques (a) de germination et (b) de croissance.

analytiques issus de la littérature. La correction du modèle de croissance de Rice et Tracey proposée par Huang a notamment été validée à l'aide de ces données quantitatives et les critères de coalescence de Brown et Embury et de Thomason ont été appliqués localement sur les couples de cavités voisines présents dans les éprouvettes étudiées.
Les différents aciers DP étudiés ont montré que toutes les étapes de l'endommagement sont sensibles à la microstructure. Cette dernière a notamment un effet sur le mécanisme de germination et sur la cinétique de croissance. L'effet du revenu est particulièrement bénéfique puisqu'il diminue à la fois la germination et la croissance des cavités.

Lors de ces travaux, l'endommagement a seulement été modélisé à partir de modèles analytiques simples. L'utilisation des données expérimentales obtenues ici (ou celles obtenues sur d'autres matériaux) dans des simulations numériques permettrait de prendre en compte beaucoup plus de paramètres matériaux.
Enfin, coupler ces modèles d'endommagement à des modèles établissant un lien entre la microsturcture des aciers DP et leurs propriétés mécaniques permettrait de déterminer la ou les microstructures DP présentant le meilleur compromis résistance/ductilité.

References

[Abra 04] M. D. Abramoff, P. J. Magelhaes, and S. J. Ram. "Image Processing with ImageJ". *Biophotonics International*, Vol. 11, pp. 36–42, 2004.

[Alla 08] S. Allain and O. Bouaziz. "Microstrucure based modeling for the mechanical behavior of ferrite-pearlite steels suitable to capture isotropic and kinematic hardening". *Materials Science and Engineering A*, Vol. 496, pp. 329–336, 2008.

[Ando 72] M. Ando and S. Hosoya. In: G. Shinoda, K. Kohra, and T. Ichinokawa, Eds., *Proceedings of the 6th International Conference on X-ray Optics and Microanalysis*, pp. 63–68, University of Tokyo Press, Tokyo, 1972.

[Argo 75a] A. Argon and J. Im. "Separation of second phase particles in spheroidized 1045 steel, Cu-0.6pct Cr alloy, and maraging steel in plastic straining". *Metallurgical and Materials Transactions A*, Vol. 6, pp. 839–851, 1975.

[Argo 75b] A. Argon, J. Im, and R. Safoglu. "Cavity formation from inclusions in ductile fracture". *Metallurgical and Materials Transactions A*, Vol. 6, pp. 825–837, 1975.

[Asgh 09] Z. Asghar, G. Requena, H. Degischer, and P. Cloetens. "Three-dimensional study of Ni aluminides in an AlSi12 alloy by means of light optical and synchrotron microtomography". *Acta Materialia*, Vol. 57, pp. 4125 – 4132, 2009.

[Avra 09a] G. Avramovic-Cingara, Y. Ososkov, M. Jain, and D. Wilkinson. "Effect of martensite distribution on damage behaviour in DP600 dual phase steels". *Materials Science and Engineering A*, Vol. 516, pp. 7–16, 2009.

[Avra 09b] G. Avramovic-Cingara, C. A. R. Saleh, M. Jain, and D. S. Wilkinson. "Void Nucleation and Growth in Dual-Phase Steel 600 during Uniaxial Tensile Testing". *Metallurgical and Materials Transactions A*, Vol. 40A, pp. 3117–3127, 2009.

[Babo 01] L. Babout, E. Maire, J. Y. Buffiere, and R. Fougeres. "Characterization by X-ray computed tomography of decohesion, porosity growth and coalescence

in model metal matrix composites". *Acta Materialia*, Vol. 49, pp. 2055 – 2063, 2001.

[Babo 04a] L. Babout, Y. Brechet, E. Maire, and R. Fougeres. "On the competition between particle fracture and particle decohesion in metal matr composites". *Acta Materialia*, Vol. 52, pp. 4517–4525, 2004.

[Babo 04b] L. Babout, E. Maire, and R. Fougeres. "Damage initiation in model metallic materials: X-ray tomography and modelling". *Acta Materialia*, Vol. 52, pp. 2475–2487, 2004.

[Barn 84] J. T. Barnby, Y. W. Shi, and A. S. Nadkarni. "On the void growth in C-Mn structural steel during plastic deformation". *International Journal of Fracture*, Vol. 25, pp. 273–283, 1984.

[Benz 00] A. A. Benzerga. *Rupture ductile des toles anisotropes*. PhD thesis, Ecole Nationale Superieure des Mines de Paris, 2000.

[Benz 02] A. A. Benzerga. "Micromechanics of coalescence in ductile fracture". *Journal of the Mechanics and Physics of Solids*, Vol. 50, pp. 1331 – 1362, 2002.

[Benz 04a] A. A. Benzerga, J. Besson, and A. Pineau. "Anisotropic ductile fracture: Part I: experiments". *Acta Materialia*, Vol. 52, pp. 4623 – 4638, 2004.

[Benz 04b] A. A. Benzerga, J. Besson, and A. Pineau. "Anisotropic ductile fracture: Part II: theory". *Acta Materialia*, Vol. 52, pp. 4639 – 4650, 2004.

[Benz 10] A. A. Benzerga and J.-B. Leblond. "Ductile Fracture by Void Growth to Coalescence". In: *Advances in Applied Mechanics*, 2010.

[Bere 81] F. Beremin. "Cavity formation from inclusions in ductile fracture of A508 steel". *Metallurgical and Materials Transactions A*, Vol. 12, pp. 723–731, 1981.

[Bess 03] J. Besson and C. Guillemer-Neel. "An extension of the Green and Gurson models to kinematic hardening". *Mechanics of Materials*, Vol. 35, pp. 1–18, 2003.

[Bett 11] M. B. Bettaieb, X. Lemoine, O. Bouaziz, A. M. Habraken, and L. Duchene. "Numerical modeling of damage evolution of DP steels on the basis of X-ray tomography measurements". *Mechanics of Materials*, Vol. 43, pp. 139 – 156, 2011.

[Boua 04] O. Bouaziz and P. Buessler. "Iso-work increment assumption for heterogeneous material behavior modelling". *Advanced Engineering Materials*, Vol. 6, pp. 79–83, 2004.

[Bouc 08] P. Bouchard, L. Bourgeon, H. Lachaple, E. Maire, C. Verdu, R. Forestier, and R. Log. "On the influence of particle distribution and reverse loading on damage mechanisms of ductile steels". *Materials Science and Engineering: A*, Vol. 496, pp. 223 – 233, 2008.

[Brid 45] P. W. Bridgman. "Effects of High Hydrostatic Pressure on the Plastic Properties of Metals". *Reviews of Modern Physics*, Vol. 17, pp. 3–14, 1945.

[Brid 64] P. W. Bridgman. *Studies in large plastic flow and fracture*. Harvard university press, 1964.

[Bron 04] F. Bron, J. Besson, and A. Pineau. "Ductile rupture in thin sheets of two grades of 2024 aluminum alloy". *Materials Science and Engineering A*, Vol. 380, pp. 356 – 364, 2004.

[Brow 73] M. Brown and D. Embury. "A Model of Ductile Fracture in Two-Phase Materials". In: *Proceedings of 3rd international conference on strength of metals and alloys*, pp. 164 – 169, London, 1973.

[Budi 82] B. Budiansky, J. W. Hutchinson, and D. R. Slutsky. *Mechanics of Solids*, Chap. Void growth and collapse in viscous solids, pp. 13 – 45. Pergamon Press, 1982.

[Buff 10] J. Buffiere, E. Maire, J. Adrien, J. Masse, and E. Boller. "In Situ Experiments with X ray Tomography: an Attractive Tool for Experimental Mechanics". *Experimental Mechanics*, Vol. 50, pp. 289–305, 2010.

[Buff 99] J.-Y. Buffiere, E. Maire, P. Cloetens, G. Lormand, and R. Fougeres. "Characterization of internal damage in a MMC using X-ray synchrotron phase contrast microtomography". *Acta Materialia*, Vol. 47, pp. 1613–1625, 1999.

[Chae 04] D. Chae and D. A. Koss. "Damage accumulation and failure of HSLA-100 steel". *Materials Science and Engineering A*, Vol. 366, pp. 299 – 309, 2004.

[Chu 80] C. C. Chu and A. Needleman. "Void Nucleation Effects in Biaxially Stretched Sheets". *Journal of Engineering Materials and Technology*, Vol. 102, pp. 249–256, 1980.

[Cloe 99] P. Cloetens, W. Ludwig, J. Baruchel, D. Van Dyck, J. Van Landuyt, J. Guigay, and M. Schlenker. "Holotomography: Quantitative phase tomography with micrometer resolution using hard synchrotron radiation x rays". *Applied Physics Letters*, Vol. 75, pp. 2912–2914, 1999.

[Cobo 08] S. Cobo and O. Bouaziz. "Investigations and modelling of the work-hardening of as-quenched martensite". In: T. Perez, Ed., *New developments on metallurgy and applications of high strength steels, Proceedings*, pp. 909–918, Buenos Aires, 2008.

[Corb 94] S. Corbin and D. Wilkinson. "Influence of matrix strength and damage accumulation on the mechanical response of a particulate metal matrix composite". *Acta Metallurgica et Materialia*, Vol. 42, pp. 1329 – 1335, 1994.

[Cox 74] T. B. Cox and J. R. Low. "An investigation of the Plastic Fracture of AISI 4340 and 18 Nickel-200 Grade Maraging Steels". *Metallurgical Transactions*, Vol. 5, pp. 1457–1470, 1974.

[Deyb 05] S. Deyber, F. Alexandre, J. Vaissaud, and A. Pineau. "Probabilistic life of DA718 for aircraft engine disks". In: *Superalloys 718, 625, 706 and Derivatives, Proceedings*, Mineral, Metals & Mat Soc, Structural Mat Div, 2005. 6th International Symposium on Superalloys 718, 625, 706 and Derivatives, Pittsburgh, PA, OCT 02-05, 2005.

[Dube 87] E. Dubensky and D. Koss. "Void/pore distributions and ductile fracture". *Metallurgical and Materials Transactions A*, Vol. 18, pp. 1887–1895, 1987.

[Dzie 11] K. Dzieciol, A. Borbly, F. Sket, A. Isaac, M. D. Michiel, P. Cloetens, T. Buslaps, and A. Pyzalla. "Void growth in copper during high-temperature power-law creep". *Acta Materialia*, Vol. 59, pp. 671 – 677, 2011.

[El G 01] R. El Guerjouma, J. Baboux, D. Ducret, N. Godin, P. Guy, S. Huguet, Y. Jayet, and T. Monnier. "Non-destructive evaluation of damage and failure of fibre reinforced polymer composites using ultrasonic waves and acoustic emission". *Advanced Engineering Materials*, Vol. 3, pp. 601–608, 2001.

[Eshe 57] J. D. Eshelby. "The Determination of the Elastic Field of an Ellipsoidal Inclusion, and Related Problems". *Proceedings of the Royal Society of London. Series A, Mathematical and Physical Sciences*, Vol. 241, pp. 376–396, 1957.

[Ever 01] R. K. Everett, K. E. Simmonds, and A. B. Geltmacher. "Spatial distribution of voids in HY-100 steel by X-ray tomography". *Scripta Materialia*, Vol. 44, pp. 165 – 169, 2001.

[Fabr 08a] D. Fabregue and T. Pardoen. "A constitutive model for elastoplastic solids containing primary and secondary voids". *Journal of the Mechanics and Physics of Solids*, Vol. 56, pp. 719–741, 2008.

[Fabr 08b] D. Fabregue and T. Pardoen. "Corrigendum to "A constitutive model for elastoplastic solids containing primary and secondary voids"". *Journal of the Mechanics and Physics of Solids*, Vol. 56, pp. 719–741, 2008.

[Fish 81] J. R. Fisher and J. Gurland. "Void nucleation in spheroidized carbon steels Part 1: Experimental". *Metal Science*, Vol. 15, pp. 185–192, 1981.

[Flor 70] S. Floreen and H. Hayden. "Some observations of void growth during the tensile deformation of a high strength steel". *Scripta Metallurgica*, Vol. 4, pp. 87–94, 1970.

[Gamm 04] J. Gammage, D. Wilkinson, Y. Brechet, and D. Embury. "A model for damage coalescence in heterogeneous multi-phase materials". *Acta Materialia*, Vol. 52, pp. 5255 – 5263, 2004.

[Garr 07] W. M. Garrison and A. L. Wojcieszynski. "A discussion of the effect of inclusion volume fraction on the toughness of steel". *Materials Science and Engineering: A*, Vol. 464, pp. 321 – 329, 2007.

[Geni 99] M. Geni and M. Kikuchi. "Void configuration under constrained deformation in ductile matrix materials". *Computational Materials Science*, Vol. 16, pp. 391–403, 1999.

[Geuz 09] C. Geuzaine and J.-F. Remacle. "Gmsh: A 3-D finite element mesh generator with built-in pre- and post-processing facilities". *International Journal for Numerical Methods in Engineering*, Vol. 79, pp. 1309–1331, 2009.

[Golo 93] M. Gologanu, J. B. Leblond, and J. Devaux. "Approximate models for ductile metals containing non-spherical voids - Case of axisymmetric prolate ellipsoidal cavities". *Journal of Mechanics and Physic of Solids*, Vol. 41, pp. 1723–1754, 1993.

[Good 79] S. H. Goods and L. M. Brown. "Overview No. 1: The nucleation of cavities by plastic deformation". *Acta Metallurgica*, Vol. 27, pp. 1–15, 1979.

[Goun 06] M. Goune, O. Bouaziz, J. M. Pipard, and P. Maugis. "Study of the effect of cold deformation on the austenite formation". *Revue de Metallurgie - Cahiers d'informations Techniques*, Vol. 103, pp. 465–471, 2006.

[Gran 77] R. Grange, C. Hribal, and L. Porter. "Hardness of tempered martensite in carbon and low-alloy steels". *Metallurgical and Materials Transactions A*, Vol. 8, pp. 1775–1785, 1977.

[Guil 00] C. Guillemer-Neel, X. Feaugas, and M. Clavel. "Mechanical behavior and damage kinetics in nodular cast iron: Part I. Damage mechanisms". *Metallurgical and Materials Transactions A*, Vol. 31, pp. 3063–3074, 2000.

[Gurs 77] A. Gurson. "Continuum Theory of Ductile Rupture by Void Nucleation and Growth: Part I - Yield Criteria and Flow Rules for Porous Ductile Media". *Journal of Engineering Materials and Technology*, Vol. 99, pp. 2–15, 1977.

[Hamm 07] Y. Hammi and M. Horstemeyer. "A physically motivated anisotropic tensorial representation of damage with separate functions for void nucleation, growth, and coalescence". *International Journal of Plasticity*, Vol. 23, pp. 1641 – 1678, 2007.

[Han 89] S.-K. Han and H. Margolin. "Void formation, void growth and tensile fracture of plain carbon steel and a dual-phase steel". *Materials Science and Engineering: A*, Vol. 112, pp. 133 – 141, 1989.

[Helb 98] A. L. Helbert, X. Feaugas, and M. Clavel. "Effect of microstructural parameters and back stress on damage mecanisms in alpha/beta titanium alloys". *Acta Metallurgica*, Vol. 46, pp. 939–951, 1998.

[Henk 93] B. L. Henke, E. M. Gullikson, and J. C. Davis. "X-ray interactions: photoabsorption, scattering, transmission, and reflection at E=50-30000 eV, Z=1-92". *At Data Nucl Data Tables*, Vol. 54, pp. 181–342, 1993.

[Herm 80] G. T. Herman. *Image reconstruction from projections: the fundamentals of computerized tomography*. Academic Press, 1980.

[Huan 91] Y. Huang. "Accurate dilatation rates for spherical voids in triaxial stress fields". *Transactions of the ASME*, Vol. 58, pp. 1084–1086, 1991.

[Imad 03] A. Imad, J. Wilsius, M. Abdelaziz, and G. Mesmacque. "Experiments and numerical approaches to ductile tearing in an 2024-T351 aluminium alloy". *International Journal of Mechanical Sciences*, Vol. 45, pp. 1849 – 1861, 2003.

[Kadk 11] J. Kadkhodapour, A. Butz, and S. Z. Rad. "Mechanisms of void formation during tensile testing in a commercial, dual-phase steel". *Acta Materialia*, Vol. 59, pp. 2575 – 2588, 2011.

[Kane 95] N. Kanetake, M. Nomura, and T. Choh. "Continuous observation of microstructural degradation during tensile loading of particle reinforced aluminium matrix composites". *Materials Science and Technology*, Vol. 11, pp. 1246–1252, 1995.

[Kopl 88] J. Koplik and A. Needleman. "Void growth and coalescence in porous plastic solids". *International Journal of Solids and Structures*, Vol. 24, pp. 835 – 853, 1988.

[Kosc 93] J. Kosco and D. Koss. "Ductile Fracture of Mechanically Alloyed Iron-Yttria Alloys". *Metallurgical Transactions A-Physical Mettalurgy and Materials Science*, Vol. 24, pp. 681–687, 1993.

[Kuma 09] J. Kumar, B. Srivathsa, and V. Kumar. "Stress triaxiality effect on fracture behavior of IMI-834 titanium alloy: A micromechanics approach". *Materials & Design*, Vol. 30, pp. 1118 – 1123, 2009.

[Kuro 11] S. Kurosu, H. Matsumoto, A. Chiba, C. Landron, D. Fabregue, and E. Maire. "The damage process in a biomedical Co-29Cr-6Mo-0.14N alloy analyzed by X-ray tomography and electron backscattered diffraction". *Scripta Materialia*, Vol. 64, pp. 367 – 370, 2011.

[Kwon 88] D. Kwon. "Interfacial decohesion around spheroidal carbide particles". *Scripta Metallurgica*, Vol. 22, pp. 1161 – 1164, 1988.

[Land 10a] E. N. Landis and D. T. Keane. "X-ray microtomography". *Materials Characterization*, Vol. 61, pp. 1305 – 1316, 2010.

[Land 10b] C. Landron, O. Bouaziz, E. Maire, and J. Adrien. "Characterization and modeling of void nucleation by interface decohesion in dual phase steels". *Scripta Materialia*, Vol. 63, pp. 973–976, 2010.

[Land 11] C. Landron, E. Maire, O. Bouaziz, J. Adrien, L. Lecarme, and A. Bareggi. "Validation of void growth models using X-ray microtomography characterization of damage in dual phase steels". *Acta Materialia*, Vol. 59, pp. 7564 – 7573, 2011.

[Lass 06] D. Lassance, F. Scheyvaerts, and T. Pardoen. "Growth and coalescence of penny-shaped voids in metallic alloys". *Engineering Fracture Mechanics*, Vol. 73, pp. 1009–1034, 2006.

[Lebl 95] J. B. Leblond, G. Perrin, and J. Devaux. "An improved Gurson-type model for hardenable ductile metals". *European Journal of Mechanics A*, Vol. 14, pp. 499–527, 1995.

[LeRo 81] G. LeRoy, J. Embury, G. Edwards, and M. Ashby. "A model of ductile fracture based on the nucleation and growth of voids". *Acta Metallurgica*, Vol. 29, pp. 1509 – 1522, 1981.

[Li 02] Z. Li and W. Guo. "The influence of plasticity mismatch on the growth and coalescence of spheroidal voids on the bimaterial interface". *International Journal of Plasticity*, Vol. 18, pp. 249 – 279, 2002.

[Lort 10] J. Lorthios, F. Nguyen, A.-F. Gourgues, T. Morgeneyer, and P. Cugy. "Damage observation in a high-manganese austenitic TWIP steel by synchrotron radiation computed tomography". *Scripta Materialia*, Vol. 63, pp. 1220 – 1223, 2010.

[Magn 88] P. Magnusen, E. Dubensky, and D. Koss. "The effect of void arrays on void linking during ductile fracture". *Acta Metallurgica*, Vol. 36, pp. 1503 – 1509, 1988.

[Mair 08] E. Maire, O. Bouaziz, M. D. Michiel, and C. Verdu. "Initiation and growth of damage in a dual-phase steel observed by X-ray microtomography". *Acta Materialia*, Vol. 56, pp. 4954–4964, 2008.

[Mair 11] E. Maire, S. Zhou, J. Adrien, and M. Dimichiel. "Damage quantification in aluminium alloys using in situ tensile tests in X-ray tomography". *Engineering Fracture Mechanics*, Vol. 78, pp. 2679 – 2690, 2011.

[Mari 84] B. Marini. *Croissance des cavits en plasticit rupture sous chargements non radiaux et en mode mixte.* PhD thesis, Ecole Nationale Superieure des Mines de Paris, 1984.

[Mari 85] B. Marini, F. Mudry, and A. Pineau. "Ductile rupture of A508 steel under nonradial loading". *Engineering Fracture Mechanics*, Vol. 22, pp. 375 – 386, 1985.

[Mart 00] C. Martin, C. Josserond, L. Salvo, J. Blandin, P. Cloetens, and E. Boller. "Characterisation by X-ray micro-tomography of cavity coalescence during superplastic deformation". *Scripta Materialia*, Vol. 42, pp. 375 – 381, 2000.

[Mazi 07] M. Mazinani and W. J. Poole. "Effect of martensite plasticity on the deformation behavior of a low-carbon Dual-Phase steel". *Metallurgical and Materials Transactions A*, Vol. 38, pp. 328–339, 2007.

[McCl 68] F. A. McClintock. "A criterion for ductile fracture by the growth of holes". *Journal of Applied Mechanics*, Vol. 35, pp. 363–371, 1968.

[Mear 85] M. Mear and J. Hutchinson. "Influence of yield surface curvature on flow localization in dilatant plasticity". *Mechanics of Materials*, Vol. 4, pp. 395 – 407, 1985.

[Miro 04] G. Mirone. "Approximate model of the necking behaviour and application to the void growth prediction". *International Journal of Damage Mechanics*, Vol. 13, pp. 241–261, 2004.

[Need 87] A. Needleman and V. Tvergaard. "An analysis of ductile rupture modes at a crack tip". *Journal of the Mechanics and Physics of Solids*, Vol. 35, pp. 151 – 183, 1987.

[Pard 00] T. Pardoen and J. W. Hutchinson. "An extended model for void growth and coalescence". *Journal of the Mechanics and Physics of Solids*, Vol. 48, pp. 2467–2512, 2000.

[Pard 06] T. Pardoen. "Numerical simulation of low stress triaxiality ductile fracture". *Computers an Structures*, Vol. 84, pp. 1641–1650, 2006.

[Pard 98a] T. Pardoen. *Ductile fracture of cold-drawn copper bars: experimental investigation and micromechanical modelling.* PhD thesis, Université catholique de Louvain, Belgium, 1998.

[Pard 98b] T. Pardoen and F. Delannay. "Assessment of void growth models from porosity measurements in cold-drawn copper bars". *Metallurgical and Materials Transactions A*, Vol. 29, pp. 1995–1909, 1998.

[Pard 98c] T. Pardoen, I. Doghri, and F. Delannay. "Experimental and numerical comparison of void growth models and void coalescence criteria for the presiction od ductile fracture in copper bars". *Acta Materialia*, Vol. 46, pp. 541–552, 1998.

[Park 88] I. G. Park and A. W. Thompson. "Ductile fracture in spheroidized 1520 steel". *Acta Metallurgica*, Vol. 36, pp. 1653–1664, 1988.

[Perr 00] G. Perrin and J.-B. Leblond. "Accelerated void growth in porous ductile solids containing two populations of cavities". *International Journal of Plasticity*, Vol. 16, pp. 91 – 120, 2000.

[Perr 90] G. Perrin and J. Leblond. "Analytical study of a hollow sphere made of plastic porous material and subjected to hydrostatic tension-application to some problems in ductile fracture of metals". *International Journal of Plasticity*, Vol. 6, pp. 677 – 699, 1990.

[Putt 59] K. E. Puttick. "Ductile fracture in metals". *Philosophical Magazine*, Vol. 4, pp. 964–969, 1959.

[Qiu 99] H. Qiu, H. Mori, M. Enoki, and T. Kishi. "Evaluation of ductile fracture of structural steels by microvoid model". *ISIJ International*, Vol. 39, pp. 358–364, 1999.

[Raga 04] A. R. Ragab. "Prediction of ductile fracture using isotropic and kinematic hardening rules including void nucleation". *Fatigue Fracture Engineering Fracture Mechanics*, Vol. 27, pp. 99–110, 2004.

[Rice 69] J. R. Rice and D. M. Tracey. "On the ductile enlargement of voids in triaxial stress fields". *Journal of the Mechanics and Physics of Solids*, Vol. 17, pp. 201–217, 1969.

[Sche 11] F. Scheyvaerts, P. Onck, C. Tekoglu, and T. Pardoen. "The growth and coalescence of ellipsoidal voids in plane strain under combined shear and tension". *Journal of the Mechanics and Physics of Solids*, Vol. 59, pp. 373 – 397, 2011.

[Schm 82] J. Schmitt and J. Jalinier. "Damage in sheet metal forming-I. Physical behavior". *Acta Metallurgica*, Vol. 30, pp. 1789 – 1798, 1982.

[Stau 04] A. Stauffer, D. Koss, and J. McKirgan. "Microstructural banding and failure of a stainless steel". *Metallurgical and Materials Transactions A*, Vol. 35, pp. 1317–1324, 2004.

[Stau 98] C. Staub and J. C. Boyer. "A ductile growth model for elasto-plastic material". *Journal of Materials Processing Technology*, Vol. 77, pp. 9 – 16, 1998.

[Stei 88] D. L. Steinbrunner, D. Matlock, and G. Krauss. "Void formation during tensile testing of dual-phase steels". *Metallurgical Transactions A*, Vol. 19, pp. 579–589, 1988.

[Stra 03] G. Straffelini. "Ductility of materials with ferritic matrix". *Materials Science and Engineering A*, Vol. A342, pp. 251–257, 2003.

[Su 87] Y. Su and J. Gurland. "Strain partition, uniform elongation and fracture strain in dual-phase steels". *Materials Science and Engineering*, Vol. 95, pp. 151 – 165, 1987.

[Suer 10] M. Suery, J. Adrien, C. Landron, S. Terzi, E. Maire, L. Salvo, and J.-J. Blandin. "Fast in-situ X-ray micro tomography characterisation of microstructural evolution and strain-induced damage in alloys at various temperatures". *International Journal of Materials Research*, Vol. 101, pp. 1080–1088, 2010.

[Sun 02] S. Sun and M. Pugh. "Properties of thermomechanically processed dual-phase steels containing fibrous martensite". *Materials Science and Engineering A*, Vol. 335, pp. 298 – 308, 2002.

[Szew 82] A. Szewczyk and J. Gurland. "A Study of the Deformation and Fracture of a Dual-Phase Steel". *Metallurgical and Materials Transactions A*, Vol. 13, pp. 1821–1826, 1982.

[Takt 09] R. Taktak, N. Benseddiq, and A. Imad. "Analysis of ductile tearing using a local approach to fracture". *Fatigue and Fracture of Engineering Materials and Structures*, Vol. 32, pp. 525–530, 2009.

[Tana 70] K. Tanaka, T. Mori, and T. Nakamura. "Cavity Formation at Interface of a Spherical Inclusion in a Plastically Deformed Matrix". *Philosophical Magazine*, Vol. 21, p. 267, 1970.

[Tang 05] B. Tanguy and J. Besson. "Simulation of the ductile to brittle Charpy transition curve after irradiation: effect of the hardening behavior". In: G. Augusti, G. I. Schuller, and M. Ciampoli, Eds., *Proceedings of 9th international conference on structural safety and reliability*, pp. 587 – 590, Rome, 2005.

[Thev 98] P. Thevenaz, U. E. Ruttimann, and M. Unser. "A pyramid approach to subpixel registration based on intensity". *IEEE Transactions on Image Processing*, Vol. 7, pp. 27–41, 1998.

[Thom 77] A. W. Thompson and J. C. Williams. "Nuclei from ductile fracture in titanium". In: T. DMR, Ed., *Proceedings of the fourth international conference on fracture*, 1977.

[Thom 85] P. Thomason. "A three-dimensional model for ductile fracture by the growth and coalescence of microvoids". *Acta Metallurgica*, Vol. 33, No. 6, pp. 1087 – 1095, 1985.

[Thom 87] A. Thompson. "Modeling of local strains in ductile fracture". *Metallurgical and Materials Transactions A*, Vol. 18, pp. 1877–1886, 1987.

[Thom 90] P. F. Thomason. *Ductile fracture of metals*. Pergamon press, 1990.

[Toda 11] H. Toda, E. Maire, S. Yamauchi, H. Tsuruta, T. Hiramatsu, and M. Kobayashi. "In situ observation of ductile fracture using X-ray tomography technique". *Acta Materialia*, Vol. 59, pp. 1995 – 2008, 2011.

[Trac 71] D. M. Tracey. "Strain-hardening and interaction effects on the growth of voids in ductile fracture". *Engineering Fracture Mechanics*, Vol. 3, pp. 301 – 315, 1971.

[Tver 81] V. Tvergaard. "Influence of voids on shear band instabilities under plane strain conditions". *International Journal of Fracture*, Vol. 17, pp. 389–407, 1981.

[Tver 84] V. Tvergaard and A. Needleman. "Analysis of the cup-cone fracture in a round tensile bar". *Acta Metallurgica*, Vol. 32, pp. 157 – 169, 1984.

[Unde 70] E. E. Underwood. *Quantitative Stereology*. Addison-Wesley publishing company, 1970.

[Weck 07] A. Weck. *The role of coalescence on ductile fracture*. PhD thesis, McMaster University, Canada, 2007.

[Weck 08a] A. Weck and D. Wilkinson. "Experimental investigation of void coalescence in metallic sheets containing laser drilled holes". *Acta Materialia*, Vol. 56, pp. 1774 – 1784, 2008.

[Weck 08b] A. Weck, D. Wilkinson, and E. Maire. "Observation of void nucleation, growth and coalescence in a model metal matrix composite using X-ray tomography". *Materials Science and Engineering: A*, Vol. 488, pp. 435 – 445, 2008.

[Weck 08c] A. Weck, D. Wilkinson, E. Maire, and H. Toda. "Visualization by X-ray tomography of void growth and coalescence leading to fracture in model materials". *Acta Materialia*, Vol. 56, pp. 2919 – 2928, 2008.

[Wei 07] Z. Wei and R. Batra. "Damage model for anisotropic materials, and its application to analysis of stability and spallation". *International Journal of Impact Engineering*, Vol. 34, pp. 1780 – 1796, 2007.

[Wier 04] T. Wierzbicki and Y. Bao. *Bridgman Revisited: On the History Effect on Ductile Fracture*. Massachusetts Institute of Technology, Cambridge, MA, 2004.

[Wors 90] M. J. Worswick and R. J. Pick. "Void growth and constitutive softening in a periodically voided solid". *Journal of the Mechanics and Physics of Solids*, Vol. 38, pp. 601 – 625, 1990.

[Zhan 95] Z. L. Zhang and E. Niemi. "A new failure criterion for the Gurson-Tvergaard dilational constitutive model". *International Journal of Fracture*, Vol. 70, pp. 321–334, 1995.

FOLIO ADMINISTRATIF

THESE SOUTENUE DEVANT L'INSTITUT NATIONAL DES SCIENCES APPLIQUEES DE LYON

NOM : LANDRON
(avec précision du nom de jeune fille, le cas échéant)

DATE de SOUTENANCE : 21/12/11

Prénoms : Caroline

TITRE : Caractérisation de l'endommagement ductile dans les aciers Dual-Phase à l'aide de la tomographie aux rayons X

NATURE : Doctorat

Numéro d'ordre : 2011-ISAL-0147

Ecole doctorale : Ecole doctorale matériaux de Lyon

Spécialité : Matériaux

RESUME :

Dans le cadre du développement de nuances d'aciers toujours plus performantes en termes de résistance à l'effort et à l'endommagement, les aciers Dual-Phase (DP) présentent un bon compromis résistance/ductilité. Cependant, il est nécessaire de disposer de meilleures connaissances concernant les mécanismes menant à la rupture de tels aciers. Les mécanismes d'endommagement ont ainsi été étudiés dans cette thèse à l'aide de la tomographie aux rayons X. Des essais de traction in-situ ont été réalisés sur plusieurs nuances d'aciers DP, un acier ferritique et un acier martensitique afin de caractériser chaque étape de l'endommagement ductile. Des observations qualitatives et des données quantitatives concernant la germination de l'endommagement, la croissance des cavités et la coalescence ont été recueillies lors de ces essais. Ces données quantitatives ont ensuite été utilisées pour le développement et/ou la validation de modèles d'endommagement. Une prédiction de la cinétique de germination a ainsi été proposée et la version du modèle de croissance de cavités de Rice et Tracey corrigée par Huang et prenant mieux en compte l'effet de la triaxialité a été validée expérimentalement. L'étape de coalescence des cavités menant à la rupture des matériaux a pour la première fois été caractérisée de façon quantitative dans un matériau industriel et des critères de coalescence ont été appliqués localement sur les couples de cavités présentes dans le matériau. L'utilisation de ces modèles analytiques a permis une meilleure compréhension des propriétés agissant sur les phénomènes mis en jeu. L'effet de la part cinématique de l'écrouissage sur la germination et la croissance de l'endommagement a notamment été souligné et validé par des essais de chargements complexes.

MOTS-CLES :

Endommagement ductile – acier Dual-Phase – Tomographie aux rayons X- germination de cavités – croissance de cavités – coalescence – modélisation analytique

Laboratoire (s) de recherche : MATEIS – UMR 5510

Directeur de thèse: E. MAIRE, J. ADRIEN

Président de jury : A. PINEAU

Composition du jury :

A. PINEAU (Président)
X. FEAUGAS (Rapporteur)
T. PARDOEN (Rapporteur
O. BOUAZIZ (Examinateur)
E. MAIRE (Directeur)
J. ADRIEN (Co-directeur)